CONSTANT AND VARIABLE DENSITY FLOW IN POROUS MEDIA, UNDER MULTIPLE SOURCES OF UNCERTAINTY

Aronne Dell’Oca

Thesis submitted for the partial fulfilment of
PhD in Environmental and Infrastructure Engineering
29° Cycle

Tutor: Prof. Monica Riva

Politecnico di Milano

Acknowledgements

Part of this thesis has been founded by MIUR (Italian ministry of Education, Universities and Research, PRIN2010-11) project: “Hydroelectric energy by osmosis in coastal areas” and by the European Community Horizon 2020 Research and Innovation Program under Grant Agreement No. 640979.

Thanks

Thank to Monica for giving me the opportunity, the economic, technical and moral supports, the challenges and her patience. Thank to Monica for showing me that analytical stuff is not that scary if cut into pieces, nearly funny…once finished.

Thank to Alberto for believing that I am able to do it, roughly explain it and approximately to sketch it in words (to paraphrase). Thank for his patience.

Thank to Jesús for showing me how much passion and colors one can put in this ‘work’ (inappropriate term). Thank for not being patience, in his unique way on what matter.

Thank to Monica, Alberto and Jesús together for remembering me that even if one can see the ‘spherical cow’, cut it and sell it is a matter of precision, details and order.

Thank to Giovanni for the tennis games, his beautiful wedding, his delicious ‘Risotto con l’osso buco’, his shared sense that there are a lots of interesting things to enjoy away from our beloved desks. Talking about desks, thank to Monica, Alberto and Giovanni for accepting (and even sharing) the Philosophy.

Thank to Ivo for showing me that even being an ordered person the pain will not flow away. Thank for all the laughs, stupid comments and days of frustration shared together. Thank for the little things that only a true friend, sharing the same experience, can note and do. Obviously, thank for being the Cossignano’ Count, with all that means.

Thank to Giulia for helping me in being an ordered person. Thank for our successful social experiment. Thank for sharing and appreciating the needed dose of liquid happiness after another long day. Thank for the compassion shown to my living-tupperware. Thank for hating peoples that go in Sardinia on vacation. Thank for the fun.

Thank to Ivo and Giulia for all the expensive bets.

Thank to my Parents, obviously, for the support, but also for the reasonable question asked from time to time ‘So, did you get something?’. Thank to God, the spirit of the question was that of a sincere interest for my live.

Thank to my sister Silvia for being the first person who showed me that is possible to study more than half an hour without dying. Thank for your patience and support.

Thank to Veronica for not being in the field and still believing that one must be clever in order to pursue a PhD. Thank to Veronica for questioning the nature of a PhD and for starting to believe that, even if we don’t save lives, there are some responsibilities.

Thank to all the people in the department for all the lunches, breaks and funny moments shared.

Thank to all my friends. Especially to the new ones in Barcelona, who welcomed me among them and in their homes. Thank for all the fun and kindness.

Despite of all the time, experiences, freedoms, frustrations, that it took I want to say thank to the road to become a PhD, because it gave (and still gives) to me an important lesson for my live: ‘Knowledge makes fear disappear’ (Aldo Rock on radio Deejay).

ABSTRACT

In this thesis, we analyze flow and transport phenomena in porous media, for both constant and variable density conditions.

In the context of constant density condition, we focus on scenarios characterized by middle to high levels of heterogeneity in the porous media conductivity. Solutions of the flow and transport problems are obtained by means of numerical simulations. In particular, we rely on adaptive discretization technique to solve the transport problem. We adopt an anisotropic spatial and temporal discretization guided by *a posteriori* recovery error estimator. We found a satisfactory comparison between results grounded on the use of adaptive discretization and results for fixed uniform discretization, of which level of refinement is established through a convergence study.

In the context of stable variable density flow within heterogeneous porous media, we analyze the reduction of solute dispersion, respect to its equivalent for constant density condition. To highlight the interaction between the heterogeneous porous media permeability and the stabilizing effects induced by the flow and transport coupling, we decompose the velocity field as the sum of a *stationary* components, associated with the solution of the flow problem for constant density, plus a *dynamic* components, related to the coupling effects. The proposed decomposition allow us to identify and quantify the origin of the solute spread reduction. In essence, the stabilizing effects identified with the *dynamic* components leads to a regularization of the *stationary* velocity field at the solute front. This regularization of the velocity field is at the origin of the solute dispersion reduction. Then we derive an effective model satisfied by the ensemble average of the horizontal average of the concentration. The spatial averaging (upscaling) operation leads to the introduction of a dispersive flux in the effective model, allowing us to retain the effects of the unresolved details of the permeability in terms effective prediction. Ensemble averaging allow us to deal with our limited knowledge of the porous media properties. For the proposed model, we provide both semi-analytical results and Monte Carlo based solution, which compare well.

For the environmental issue of saltwater intrusion along coastal aquifer we perform a Global Sensitivity Analysis (GSA) for global descriptor of the intruding wedge with respect to typically unknown flow condition and porous media properties. In particular, we rely on variance-based Sobol’ indices to quantify the sensitivity. Due to the high computational costs associated with the numerical solution of the coupled flow and transport problems that govern the saltwater intrusion dynamics we introduce a generalized Polynomial Chaos Expansion (gPCE) of the global descriptor of interest. The gPCE allows for a direct evaluation of the Sobol’ indices and allows us to obtain probability density function (*pdf*) of the output at affordable computational costs. This task is computationally prohibitive when relying on the full numerical model. As conceptualization of seawater intrusion we take the anisotropic dispersive Henry problem. Results show that the dispersive properties of the media greatly affects mixing between salt and fresh waters, the intensity of the buoyancy effects determine the inland intrusion of the wedge and the anisotropy ratio of the media permeability dictates the variability of the vertical height of the wedge along the coast. The same kind of GSA is applied to a hydraulic fracturing operation, with the aim of define the sensitivity of the global level of contamination in a vulnerable aquifer in communication with the production aquifer. For the test case here analyzed, results shows a great level of sensitivity of the level of contamination to the aperture of the fracture and the pressure of injection of the fracturing fluid. These two applications demonstrate the benefits of carrying out GSA to aid in the understanding of system behavior and proper quantification of the sensitivity.

In the end, we propose a new GSA grounded on the first four statistical moments of the model output *pdf*. We define the sensitivity of an output with respect to an input on the base of new metrics entailing the mean, variance, skewness and kurtosis of the output. Our methodology provides a comprehensive characterization of the output sensitivity. Results show that the output sensitivity to input parameters is a function of the particular statistical moment analyzed. The application of our approach can be of interest in the context of current practices and evolution trends in factor fixing procedures (i.e., assessment of the possibility of fixing a parameter value on the basis of the associated output sensitivity), design of experiment, uncertainty quantification and environmental risk assessment, due to the role of the key features of a model output *pdf* in such analyses. We demonstrate our methodology for an analytic test function widely used as benchmark for GSA studies, in the context of variable density scenario for the critical pumping rate in coastal aquifer and regarding constant density problems, we focus on the breakthrough curve of a tracer solute at the outlet of a heterogeneous sand box.

CONTENTS

1 Thesis Introduction

Facing fluid flow and transport problems in porous media is a challenging task, usually exacerbated by the complex heterogeneous nature of the media properties (see e.g. Rubin, 2003). Numerical simulations are crucial to understand and predicted the solute behavior (de Druzey et al., 2007; Bellin et al., 1992), but retain a detailed description of the media heterogeneity and its effects, in terms of solute fate, may be a challenging task to achieve. Adaptive discretization technique represent an interesting and promising approach to simulate the concentration evolution in heterogeneous media (Esfandiar, 2015).

Depending on the scopes, available resources and knowledge about the problem, a description of the flow and transport problems in terms of average quantities (spatial and/or ensemble average) may be of interest. This goal is reached through the definition of an effective model (see e.g. Neuman and Tartakovsky, 2009; Woods et al., 2003). Usually effective model requires proper parameters, which spatial arrangement and temporal evolution are inherently related with the unresolved and typically unknown heterogeneity details. Further complexity and difficulties in describing and understanding flow and transport mechanism through an effective model arise when the flow and transport processes are coupled because of the additional features of the feedback. Analysis and understanding of the dynamics governing the effective behavior of solute transport for stable variable density flow in heterogeneous porous media is pursued in this thesis.

The manifested heterogeneous nature of porous media and the common scarcity of data for environmental related problems rend uncertain the input parameters as well as initially and boundary conditions (see e.g. Dongxiao, 2002; Rubin, 2003). Moreover, many hydrogeological application of interest are governed by complicated systems of equations, which may interact among themselves. In the light of the uncertainty and complexity associated with the solution of flow and transport in porous media, may be hard to understand and quantify which is the relative importance of input parameters in terms of investigated quantities of interest. In this thesis we firstly explore the use of variance-based Sobol' indices (Sobol, 1993) to assess the output-input sensitivity and then we propose new metrics based on the first four statistical moments of an output of interest to determine its sensitivity with respect to input parameters.

1.1 Adaptive mesh and time discretization for tracer transport in heterogeneous porous media

In the context of solute transport in heterogeneous media, is a common practice to resort numerical simulation to obtain a proper description of the solute plume evolution (see e.g. de Druzey et al., 2007; Bellin et al., 1992). In this work we focus on the description of solute transport at the continuum scale, assuming valid the advection-dispersion equation (ADE) at the local scale (see e.g. Bear and Cheng, 2011). The velocity field conserves fluid mass and Darcy's law is valid (Bear and Cheng, 2011).

As the heterogeneity in the permeability increases, variability and contrast in the flow field and in the resulting solute plume increase too. The complex evolution of the concentration field may be challenging to capture, since high gradients arise and a proper numerical discretization of the problem is required. A brute force refinement of the time and space discretization is the simplest strategy in order to reduce numerical discretization errors (e.g. Landman, 2007a). Inevitable drawback are the increase in computational cost and time to obtain the solution. A second possibility is the use of adaptive space-time discretization, which aims for discretization refinement automatically guided by the characteristic of the solution itself (Mansell et al., 2002).

In Section 2 of this work, we assess the impact of adaptive space and time discretization (Porta et al. 2012; Micheletti et al. 2010) on the modeling of tracer solute transport. Previous work demonstrated the capability of the anisotropic space-time adaptive discretization technique for tracer transport in homogenous and block-wise heterogeneous porous media (Esfandiar et al., 2014, 2015). We extend the methodology for random heterogeneous media. The adaptive discretization is guided by a suitable gradient-based recovery error estimator, which in essence optimizes the mesh and time stepping discretization according to the intensity of gradients of interest(Porta et al. 2012; Micheletti et al. 2010). We investigate two different guiding strategies for the anisotropic meshes adaptation, defining the guiding error estimator on the base of: (*i*) the concentration field only; (*ii*) both concentration and velocity field. We tested the methodologies for two dimensional synthetic cases with moderate, $\sigma_Y^2 = 1$, an high, $\sigma_Y^2 = 5$, level of heterogeneity, σ_Y^2 being the variance of Y. We found a satisfactory comparison between results for the adaptive methodologies and corresponding results for fixed space-time discretization characterized by mesh cardinality greater of order of magnitude and time step equal to the minimum allowed in the adaptive solutions. As quantities for the comparison we focus on concentration related global metric, like the scalar dissipation rate, and punctual metric like point wise break through curves.

Results encourage further developments of the adaptive methodologies in order to treat flow and transport at field scale, capturing directly the effects of detailed small-scale heterogeneity relaxing the need of an upscaled-effective descriptions.

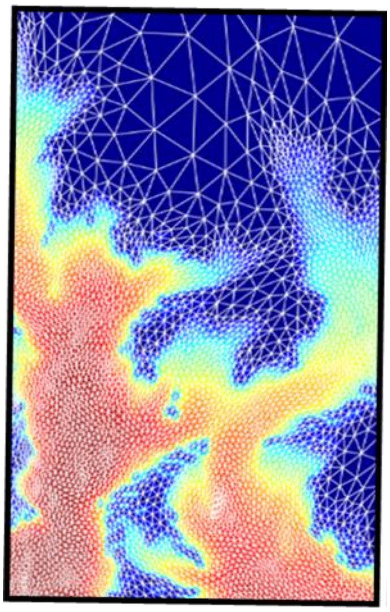

Figure 1.1. Example of a complex concentration plume developed in highly heterogeneous porous media. The resulting adapted mesh is overlapped to the normalized solute maps (logarithmic scale; red one, blue zero).

1.2 Dispersion for stable variable density flow, within heterogeneous porous media.

In the context of miscible stable variable density flow within porous media, it is well known that an increase in the intensity of the stabilizing flow components lead to a reduction in the size of the dispersion zone (see e.g. Flowers and Hunt, 2007; Hassanizadeh and Leijn, 1995;). In our work, we focus on a linear dependency of the fluid density on the dissolved solute concentration, while the viscosity is assumed constant. Such choices are consistent with the analysis of process regarding the mix between freshwater and saltwater (Abarca et al. 2007).

In Section 3 of this work, we provide a clear link between heterogeneity in the media permeability and the stabilizing mechanism which arise because of the coupling between flow and transport, in order to find an explanation of the manifested contraction of the solute dispersion zone. To do so we decompose the flow field as a *stationary* component, associated with the solution of the flow problem for constant density, plus a *dynamic* component which allow to highlight the flow and transport coupling effects. The main results is that *dynamic* fluctuation component exhibit an opposite sign respect to the *stationary* fluctuations, leading to a suppression of the velocity and concentration fluctuation in case of stable conditions. We highlight the concepts and utility of the proposed decomposition for a simple explanatory setting.

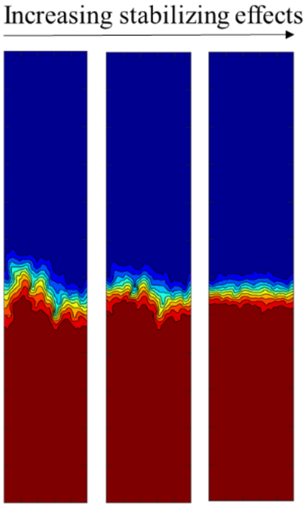

Figure 1.2. Explanatory representation of the progressive reduction of solute dispersion and of the tendency to resemble an homogenous-like behavior at the solute front, as the stabilizing effects increase. Depicted normalized solute concentration maps (red one, blue zero). Density is a linear function of concentration. The underlying heterogeneous permeability field is the same for all the three columns.

Then, we find that the same regularizing dynamics highlighted by means of the *stationary* and *dynamic* decompositions holds also in random heterogeneous media. On these bases, we firstly propose an upscaled effective model, in which the upscaling operator correspond with the lateral spatial average. We do so because in many cases just integrated measurement are available rather than pointwise measurement. Secondly, in order to accommodate our uncertainty in the permeability field and its effect on the solute concentration, we derive a model satisfied by the ensemble average of monodimensional solute profiles and for the associated variance. In the effective model appears the dispersive flux, which quantifies the level of spreading of solute and has expected decrease for increasing intensity of stabilizing buoyancy effects. We investigate the evolution of the dispersive flux for different intensity of the stabilizing effects and of the permeability heterogeneity. Both semi-analytical and Monte Carlo based results are proposed.

The proposed decomposition of the flow field and related interpretations throughout the theoretical developments, encourage its application in other set up, e.g. unstable condition, or for other coupled problems.

1.3 Variance-based Global Sensitivity Analysis for Hydrogeological Problems

In the context of hydrogeological problems the nature of the involved process, e.g. coupling between flow and transport, the mathematical formalism used for the problem description, specific problem configuration, imposed boundary and initially condition, variability and/or uncertainty in the input parameters can lead to an high level of complexity (Herman et al., 2013; Wagener et al., 2010). The problem complexity may render it difficult to understand the relationship and the sensitivity between input quantities and sought model outputs of interest (Razavi and Gupta, 2015). Anyway, understanding and quantifying properly the influence of a model parameter on investigated results is of crucial importance.

In a broad sense sensitivity analysis aims to quantify how variation in an input leads to variation in outputs. If variations in an input lead to great variation in the output, it is said that the output is highly sensitivity to the input. Different ways to define the sensitivity are available in the literature (see e.g. Pianosi et al., 2016). In Section 4 of this work we focus on variance-based Global Sensitivity Analysis (GSA) and in particular on the Sobol' indices (Sobol, 1993). Sobol' indices quantify the relative contribution to the output variance associated with the variability of an input parameter. So, the metric employed in the context of Sobol' indices to define the sensitivity between output and input is based on the variance of the output. The word global in GSA, indicates that the sensitivity is evaluated with reference to the entire parameter range of variation and not just around a single fixed value of the parameter, as in local sensitivity analysis. The beauty and power of Sobol' indices relay in their conceptual simplicity that renders them easy to interpret. On the other hand, Sobol' indices evaluation requires many model evaluations for different combination of parameters values, in order to explore the parameters space of definition.

When easy to evaluate analytical expression for the input-output relationship are not available, we must rely on numerical simulation of the problem. For complex problems, the typically high computational costs associated with a single numerical run may render it unfeasible to perform global sensitivity analysis. In order to overcome this difficulty we resort a generalized Polynomial Chaos Expansion (gPCE) surrogate modelling (see e.g. Sudret, 2008;) of output quantities of interest. Once available, the gPCE representation allow for a direct evaluation of the Sobol' indices and to derive probability density function (*pdf*) of the output at feasible computational costs. Note that *pdf* of target output allow a complete uncertainty quantification, which is useful in the context of risk assessment analysis.

We focus on two different complex hydrogeological problematics, the saltwater intrusion along coastal aquifer and the hydraulic fracturing operation in deep basins. As conceptualization of saltwater intrusion along coastal aquifer we select the dispersive anisotropic Henry problem proposed in Abarca et al. (2007), because despite its simplicity respect to a real world scenario it encapsulate important features of the typical saltwater wedge. We evaluate the sensitivity of proper dimensionless global metrics introduced to describe the overall aspect of the saltwater wedge with respect to dimensionless parameters of the problem, that summarize the intensity of the dispersive mechanism, buoyancy forces and anisotropy of the permeability formation. Regarding the analysis of hydraulic fracturing operations, we focus on a simple and preliminary conceptualization, in which an already fractured reservoir of production underlie a so called target aquifer, which is representative of water resource to preserve form contamination. We evaluate the sensitivity of the global level of contamination of the target aquifer with respect to both media properties and operational conditions. For both the scenarios the use of variance-based Sobol' indices allow for a precise quantification of the sensitivity and enrich our understanding of the system behavior. Moreover, despite the problem complexity we find a satisfactory representation of the investigated output quantities through the constructed gPCE surrogate models.

1.4 Moment-based Metrics for Global Sensitivity Analysis of Hydrogeological Systems

Despite their simplicity of interpretation variance-based sensitivity metrics, e.g. Sobol' indices, have some limitations (Borgonovo, 2007; Pianosi et al., 2016). The sensitivity is defined only in terms of process variance, which means that only the second statistical moment of the output *pdf* is tested. Moreover, considering the close link between Sobol' indices and uncertainty quantification analysis (see Saltelli et al., 2008) becomes clear that Sobol' indices are fully informative of the possibility of reduce the output uncertainty by knowing an input parameter, if the variance is a good proxy of the uncertainty, which is not the case for highly skewed and tailed *pdf*.

These criticisms of the variance-based GSA approach has lead to the definition of sensitivity analysis methodologies in which the output-input sensitivity metric entails the entire output *pdf*, and not only of the output variance, variations due to input parameters variability. Methodologies based on this last approach are said moment-independent GSA, since no particular moments of the output distribution are selected in the definition of the sensitivity. Moment-independent GSA (see e.g. Borgonovo, 2007; Pianosi and Wagner, 2015;) can be view as a more complete way of determining the output-input sensitivity respect to variance-based GSA. However two main drawbacks occurs comparing moment-independent with variance-based GSA: (*i*) in the former approach is not evident which particular feature of the *pdf* is affected by an input variation while in the second approach is explicit that it is the variance, which in particular case is a good proxy of spread of the *pdf* around its mean value; (*ii*) an accurate evaluation of entire *pdf* requires more model evaluations respect to an accurate evaluation of the process variance. The last drawback is of concern when we must rely on heavy computational model to obtain the sought output. Moreover, even if the use of a gPCE surrogate model rend the evaluation of the probability function feasible, it is expected that more accurate surrogate models are needed in order to capture the entire probability function respect to just low order statistical moments.

To overcome the disadvantages of variance-based and moment-independent GSA, in Section 5 we define a new GSA methodology based on the first four statistical moment of the output *pdf*. Our methodology allow defining the sensitivity of the output, respect to input parameters, on the base of the mean, variance, skewness and kurtosis separately. Results are easy to interpret, since each of the first statistical moments has a clear relationship with the *pdf* structure. The application of our approach can be of interest in the context of current practices and evolution trends in factor fixing procedures (i.e., assessment of the possibility of fixing a parameter value on the basis of the associated output sensitivity), design of experiment, uncertainty quantification and environmental risk assessment, due to the role of the key features of a model output *pdf* in such analyses. We test and exemplify our methodology on three testbeds: (*a*) the Hishigami test function, which is widely employed to test sensitivity analysis techniques (Borgonovo, 2007); (*b*) the evaluation of the critical pumping rate to avoid salinization of a pumping well in a coastal aquifer, as studied by Pool and Carrera (2011); and (*c*) a laboratory-scale nonreactive transport experiment where the temporal evolution of solute concentrations, $\overline{C}(t)$, is available, as studied by Esfandiar et al. (2015).

Reference

Abarca, E., Carrera, J., Sanchez-Vila, X. and Dentz, M.: Anisotropic dispersive Henry problem, Adv. Water Resour., 30(4), 913-26, http://dx.doi.org/10.1016/j.advwatres.2006.08.005, 2007.

Bear, J. and Cheng, A. H. D.: Modeling groundwater flow and contaminant transport, Springer, 2011.

Bellin, A., Salandin, P. and Rinaldo, A.: Simulation of dispersion in heterogeneous porous formations: Statistics, first-order theories, convergence of computaions, Water Resour. Res., 28, 2211-2227, 1992.

Borgonovo, E.: A new uncertainty importance measure, Reliability Eng. Syst. Safety, 92, 771–784, 2007.

de Dreuzy, J., R., Beaudoin, A. and Erhel, J.: Asymptotic dispersion in 2D heterogeneous porous media determined by parallel numerical simulations, Water Resour. Res., 43, W10439, doi:10.1029/2006WR005394, 2007.

Dongxiao, Z.: Stochastic Methods for Flow in Porous Media, San Diego:Academic Press, 2002.

Esfandiar, B., Porta, G., Perotto, S. and Guadagnini, A.: Anisotropic mesh and time step adaptivity for solute transport modeling in porous media, New Challenges in Grid Generation and Adaptivity for Scientific Computing, edited by L. Formaggia and S. Perotto, SEMA SIMAI Springer Series, vol. 5, Springer Milan, 2014.

Esfandiar, B., Porta, G., Perotto, S. and Guadagnini, A.: Impact of space-time mesh adaptation on solute transport modeling in porous media, Water Resour. Res., 51, 1315-1332, 2015.

Flowers, T. C. and Hunt, J. R.: Viscous and gravitational contributions to mixing during vertical brine transport in water-saturated porous media, Water Resour. Res., 43:W01407, doi:10.1029/2005WR004773, 2007.

Hassanizadeh, S. M. and Leijnse, A.: A non-linear theory of high-concentration-gradient dispersion in porous media, Adv. Water Resour., 18(4), 203-215, doi:10.1016/0309-1708(95)00012-8, 1995.

Herman, J. D., Kollat, J. B., Reed, P. M. and Wagener T.: From maps to movies: high-resolution time-varying sensitivity analysis for spatially distributed watershed models. Hydrol. Earth Syst. Sci., 17, 5109-5125, doi:10.5194/hess-17-5109-2013, 2013.

Micheletti, S., Perotto, S. and Farrell, P.: A recovery-based error estimator for anisotropic mesh adaptation in CFD, SEMA J., 50(1), 115-137, 2010.

Neuman, S. P. and Tartakovsky, D. M.: Perspective on theories of non-Fickian transport in heterogeneous media, Adv. Water Resour., 32(5), 670-680, 2009.

Pianosi, F. and Wagener, T.: A simple and efficient method for global sensitivity analysis based on cumulative distribution functions, Environ. Model. Softw., 67, 1-11, http://dx.doi.org/10.1016/j.envsoft.2015.01.004, 2015.

Pianosi, F., Wagener, T., Beven, K., Freer, J., Hall, J.W., Rougier, J. and Stephenson, D.B.: Sensitivity Analysis of Environmental Models: a Systematic Review with Practical Workflow, Environmental Modelling & Software, 79, 214-232, http://dx.doi.org/10.1016/j.envsoft.2016.02.008, 2016.

Pool, M. and Carrera, J.: A correction factor to account for mixing in Ghyben-Herzberg and critical pumping rate approximations of seawater intrusion in coastal aquifers, Water Resour. Res., 47, W05506, doi:10.1029/2010WR010256, 2011.

Porta, G., Perotto, S. and Ballio, F.: A space-time adaptation scheme for unsteady shallow water problems, Math. Comput. Simul., 82(12), 2929–2950, 2012.

Razavi, S. and Gupta H. V.: What do we mean by sensitivity analysis? The need for comprehensive characterization of "global" sensitivity in Earth and Environmental systems models, Water Resour. Res., 51, doi:10.1002/2014WR016527, 2015.

Rubin, Y.: Applied stochastic hydrogeology, Oxford University Press, New York, 2003.

Saltelli, A., Ratto, M., Andres, T., Campolongo, F., Cariboni, J., Gatelli, D., Saisana, M., Tarantola, S.: Global Sensitivity Analysis. The Primer. Wiley, 2008.

Sobol, I. M.: Sensitivity estimates for nonlinear mathematical models, Mathematical Modeling and Computational Experiment, 1, 407-417, 1993.

Sudret, B.: Global sensitivity analysis using polynomial chaos expansions, Reliab. Eng. & Syst. Safety, 93, 964-979, doi:10.1016/j.ress.2007.04.002, 2008.

Wagener, T., Sivapalan, M., Troch, P. A., McGlynn, B. L., Harman, C. J., Gupta, H. V., Kumar, P., Rao, P. S. C., Basu, N. B., and Wilson, J. S.: The future of hydrology: An evolving science for a changing world, Water Resour. Res., 46, W05301, doi:10.1029/2009WR008906, 2010.

Wood, B. D., Cherblanc, F., Quintard, M. and Whitaker, S.: Volume averaging for determining the effective dispersion tensor: Closure using periodic unit cells and comparison with ensemble averaging, Water Resour. Res., 39(8), 1210, 2003.

2 Adaptive mesh and time discretization for tracer transport in heterogeneous porous media

We assess the impact of adaptive anisotropic space and time discretization on the modeling of tracer solute transport in heterogeneous porous media. The heterogeneity is characterized in terms of the spatial distribution of permeability, whose natural logarithm, *Y*, has been treated as a second order stationary random process. We assume that transport of solute mass obeys an advection-dispersion equation at the continuum scale. Solution of the flow problem is obtained from the numerical solution of Darcy's law, and provides the advective velocity field. A suitable recovery-based error estimator guides the adaptive discretization. We investigate two different guiding strategies for the anisotropic meshes adaptation, defining the guiding error estimator on the basis of spatial gradients of: (*i*) the concentration only; (*ii*) both concentration and velocity components. We tested the methodologies for two dimensional synthetic cases with moderate, $\sigma_Y^2 = 1$, an high, $\sigma_Y^2 = 5$, level of heterogeneity, σ_Y^2 being the variance of *Y*. As quantities of interest, we focus on the time evolution of section-averaged and point-wise breakthrough curves, second centered spatial moment and the scalar dissipation rate. We found a satisfactory comparison between results for the adaptive methodologies and reference solutions found for fixed space-time discretization, whose resolution is established on the basis of a convergence study. Comparison of the two adaptive strategies highlights that: (*i*) defining the error estimator only in terms of concentration fields leads to some advantages in treating the solute transport in correspondence of low velocity spots, where diffusion-dispersion mechanism dominate; (*ii*) incorporation of the velocity field in the guiding error estimator leads to a better characterization of the forward fringe of the solute fronts which propagate through fast velocity channels.

2.1 Introduction

In the analysis and prediction of contaminant transport within heterogeneous porous material numerical models represent a powerful and flexible tool. One of the key challenges is the development of numerical methodologies which are suitable to approximate solute transport within media characterized by large variations of effective properties, e.g. permeability.

In this work, we focus on transport of a non-reactive solute in heterogeneous porous media at continuum scale, which is here described through an Advection Dispersion Equation (ADE) (Bear and Cheng, 2011). We therefore assume that at the continuum scale, the total effective dispersion coefficient is described as the sum of an effective diffusion and hydrodynamic dispersion, (i.e. the so called Fickian analogy, Scheidegger 1961). The effective dispersion coefficient in the ADE accounts for the enhancement of solute dispersion due to the unresolved velocity variability at scales which are not explicitly included in the model, e.g. at pore scale (see, e.g., Bear and Cheng, 2011; de Barros and Dentz, 2015). This is consistent with the idea of dispersion in capillary tubes (Taylor, 1953; Salles et al., 1993) where hydrodynamic dispersion arises from enhanced diffusion due to the presence of a spatial velocity distribution.

The advection term appearing in the ADE accommodates the resolved velocity details emerging from the solution of the flow problem, which is defined by combining the steady state fluid mass conservation and the Darcy' law. In the last two decades a considerable amount of literature focuses on the analysis of transport features which are not consistent with the ADE formulation (e.g., long tails, corresponding to long residence times of solute mass within the porous domain). This has provided motivation for the development of models which can capture non-Fickian (or so-called anomalous) transport features. These approaches include continuous time random walk (CTRW, Berkowitz et al., 2006), fractional derivatives (Zhang et al., 2012) and multi-rate mass transfer models (Haggerty et al., 2004). All of these effective formulations include nonlocal transport terms and the mathematical formulations can be related with each other (Neuman and Tartakovsky, 2012).

According to a number of recent studies, the ability of the ADE model to interpret solute transport processes in randomly heterogeneous media is largely dependent on the level of detail associated with the characterization of the system properties. For example, the results by Riva et al. (2008) suggest that, apparent non-Fickian features observed in field-scale data can be interpreted through Monte Carlo simulations of an ADE. In this context it is of paramount importance the proper characterization of the heterogeneity of hydraulic conductivity and consequently of the velocity field. The chosen space-time resolution selected to approximate the ADE can also have a considerable impact on the ability of this simple model in interpreting observed results (e.g., Rubin et al., 2003; Lawrence and Rubin, 2007). It appears then crucial to be able to approximate the ADE with a sufficiently small space-time resolution to be able to retain all the relevant details of the heterogeneous conductivity (or trasmissivity) field in input, which in turn determine the non-Fickian transport feature through the spatial organization of preferential pathways (Edery et al., 2015). In this context, the selection a priori of appropriate space and time discretization is a challenging task, particularly in highly heterogeneous media where the solute typically can travel relatively fast along preferential pathways and reside for long times in stagnant regions.

The simplest way to set up a discretization mesh is to select a fixed numerical mesh where all elements have the same spatial dimension and of the time step for all the window of simulation. In this context, an appropriate discretization grid can be selected upon resolving the numerical problem at hand on different space and time discretization, obtained through a sequential uniform refinement of the full spatial mesh and of the time step. This type of blind refinement can lead to unaffordable computational costs as the domain size increases and/or a detailed description of the tracer plume is needed. Adaptive discretization techniques provide a valuable alternative in this context. The common idea of adaptive discretization is to exploit the features of the solution in order to increase or decrease atuomatically the space and time resolution associated with the numerical approximation. As a consequence, the element and time step size and shape is not chosen a priori, but dynamically selected. Typically, this is obtained upon relying on a specific error indicator. A number of previous works provide implementation of adaptive grids in the context of numerical modeling of flow (Knupp 1996; Bresciani et al. 2012; Cao and Kitanidis, 1999; Mehl and Hill, 2002; Cirpka et al. 1999; Jayasinghe, 2015) and solute transport processes in homogenous (see e.g. in Pepper and Stephenson,1995; Pepper et al., 1999; Saaltink et al., 2004; Kavetski et al., 2002; Younes and Ackerer, 2010; and heterogeneous (see e.g. Trompert, 1993; Huang and Zhan, 2005; Gedeon and Mallants, 2012; Chueh et al., 2010; Amaziane et al. 2014; Klieber and Rivière, 2006; Mansell et al., 2002 and references therein) porous media. Recently, Amaziane et al. (2014) employ both space and time adaptive technique for simulating radionuclide transport in block wise heterogeneous media, but without incorporating the anisotropic features of the solution in guiding the spatial adaptation. Jayasinghe (2015) implement an anisotropic spatial and time step refinement for both single and two phase flow, focusing on homogenous field scale scenario. In anisotropic mesh adaptivity the size, orientation and shape of the elements are optimized to match the directional features of the problem at hand.

With respect to the above cited works, the key element of originality of our work is that we combine anisotropic mesh and time step adaptation to simulate solute transport within randomly heterogeneous media. Heterogeneity of the considered porous media is characterized here in terms of the spatial distribution of conductivity, whose natural logarithm, Y, is treated as a second-order stationary random process. By performing a verification study on a single realization of the conductivity field, our work provides an assessment of the reliability of adaptive grids to be employed within uncertainty quantification and model calibration procedures, e.g., based on Monte Carlo approaches. We focus on synthetic test cases characterized by middle to high heterogeneity, i.e. with a level of variance in Y up to five.

Our works starts from the anisotropic mesh and time step adaptive discretization technique recently devised in Esfandiar et al. (2014, 2015). The numerical technique relies on the a posteriori recovery-based error estimators for space and time discretization errors devised in Micheletti and Perotto (2010) and Porta et al. (2012a,b). In particular, Esfandiar et al. (2015) assess the impact of employing a space and time adaptation procedure in the context of parameter estimation. This is obtained upon comparing parameter estimates obtained through inverse modeling of solute transport within a block-wise heterogeneous porous medium at laboratory scale, i.e. when the domain is composed by regions of uniform properties. Results of Esfandiar et al. (2015) show that the quality of parameter estimation results improves when the space-time adaptive methodology is implemented, with respect to those obtained using fixed uniform discretization characterized by an apparently sufficient resolution.

In this paper we focus on modelling solute transport in randomly heterogeneous porous media employing the adaptive discretization technique of Esfandiar et al. (2015). As typically done, the flow problem is solved on a fixed numerical grid which is built to honor the spatial structure of the random conductivity field. The resulting velocity field may exhibit complex spatial structure, with the presence of high velocity channels and large stagnant regions that may be linked to emerging non Fickian solute transport features (Edery et al., 2015). When spatial meshes are dynamically adapted coarsening and refinement is performed at each time step. In this context, a key challenge in implementing dynamically adaptive spatial meshed is that the original velocity field needs to be projected to the adapted mesh, which can be characterized by local element sizes which may be totally unrelated to the original definition of the conductivity field. Esfandiar et al. (2014,2015) show that mesh adaptation driven by gradients of concentration leads to accurate result when the porous medium is characterized by homogeneous or block heterogeneous properties. Here, we investigate two diverse strategies guiding the anisotropic meshes adaptation. The error estimator of each of these is assessed on the basis of spatial gradients of (*i*) only solute concentration, or (*ii*) both concentration and fluid velocity components, upon following the procedure proposed in Porta et al. (2012a) to combine diverse error indicators to adapt the mesh. The idea to include the velocity components in the error estimator is consistent with the link between the spatial derivatives of the components of the velocity vector and the resulting folding, stretching, mixing and spreading of the evolving concentration plume especially for highly heterogeneous media, (see e.g. de Barros et al. 2012, Le Bronge et al., 2015).

To assess the quality of the adaptive methodologies we focus on the evolution in time of both local and spatially integrated concentration as well as global spreading and mixing indicators, i.e. the second centered spatial moment and the scalar dissipation rate.

The rest of this chapter is organized as follows. Section 2.2 describe the problem setting, while in section 2.3 the main features of the adaptive methodology proposed in Esfandair et al. (2014) are briefly recalled. Results and comparison of the adaptive space-time discretization technique are presented in section 2.5. Conclusion are drawn in section 2.6.

2.2 Problem Setting

2.2.1 Mathematical and Numerical Model

We consider a two dimensional rectangular domain, Ω, of height $H = 0.14$ *m* and width $L = 0.04$ *m*. In our reference system we indicate the horizontal and the vertical direction with *y*, *z* (see Fig. 2.1.*a*). The Advection Dispersion Equation (ADE) reads

$$\frac{\partial C}{\partial t} + \boldsymbol{v}\cdot\nabla C - \nabla\cdot\left(\boldsymbol{D}\nabla C\right) = 0 \tag{2.1}$$

where $C = C(\boldsymbol{x},t)$ [-] is the solute concentration at position $\boldsymbol{x}$ and time *t*, $\boldsymbol{v}$ [LT^{-1}] is the velocity vector of horizontal v_y and vertical v_z components, and $\boldsymbol{D}$ [L^{2}T^{-1}] is the local dispersion tensor (see Bear and Cheng, 2011) given by

$$\boldsymbol{D} = \left(\alpha_T + D_m\right)\delta_{ij} + \left(\alpha_L - \alpha_T\right)\frac{v_i v_j}{|\boldsymbol{v}|} \quad \text{with} \quad i, j = y, z \tag{2.2}$$

here α_T [L] and α_L [L] are the transverse and longitudinal dispersivity, D_m [L^{2}T^{-1}] is the molecular diffusion, δ_{ij} is the Kronecker' delta and $|\boldsymbol{v}|$ is the module of the velocity. Here we set $\alpha_T = \alpha_L = 10^{-3} m$ and $D_m = 10^{-9} m^2/s$ The imposed boundary conditions for (2.1)-(2.2) are: time varying concentration along the bottom edge, $C_{BC} = \exp(-(t-3))$; impermeable boundary along the vertical edges and a free boundary at the top, $\nabla C\cdot\mathbf{n} = 0$ (see also Figure 2.1.*c*). At initial time the concentration is zero everywhere in the domain. The advective velocity, $\boldsymbol{v}$, is here assumed steady and obeys the fluid mass conservation and the Darcy' law

$$\nabla\cdot\boldsymbol{v} = 0; \qquad \boldsymbol{v} = -\frac{\boldsymbol{K}}{\phi}\nabla h; \tag{2.3}$$

where, *h* [L] is the hydraulic head and ϕ [-] is the constant porosity, here assumed to be constant and equal to 0.35. The hydraulic conductivity of the porous medium is modelled as an isotropic stationary random field $\boldsymbol{K} = K_G \exp(Y(y,z))\mathbf{I}$ [LT^{-1}], where $\mathbf{I}$ is the identity matrix, $K_G = 10^{-9} m/s$ is the geometric mean of conductivity and *Y*(*y*, *z*) is a zero-mean second order stationary random process characterized by an isotropic exponential covariance function

$$C_{YY} = \sigma_Y^2 \exp\left(-\frac{|\boldsymbol{r}|}{l} \right) \tag{2.4}$$

where $\boldsymbol{r}$, σ_Y^2, l are the separation vector between two points, variance and correlation length of the Y process, respectively. The correlation length is fixed at $l = 0.02$ *m* and therefore we obtain $H/l = 7$ and $L/l = 2$, which are suitable for the objective of the work. Regarding the level of heterogeneity we consider two different values $\sigma_Y^2 = (1;5)$, in order to obtain an increasing level of complexity in the velocity and concentration fields. The heterogeneous conductivity fields has been generated with SGSIM (Deutsch and Journel, 1998) on a discretization grid with $n_y = 50$ element along L and $n_z = 175$ along *H.* These choice lead to a great representation of the heterogeneity in $\boldsymbol{K}$, since we set 25 element for correlation length, *l*. Hereafter we label as $\Delta\boldsymbol{K}$ the size of the square element of the mesh employed for generating $\boldsymbol{K}$. Figure 2.1.*a* depicts the selected Y realization for the test case with $\sigma_Y^2 = 5$. The imposed boundary conditions for (2.3) are: fixed head along the bottom edge, h_{BC}; no flow along the vertical edges and imposed constant vertical velocity at the top boundary equal to $v_{z,BC}$ (see also Figure 2.1.*b*). A global Péclet number can then be defined as the ratio between average diffusion-dispersion and advective time scales i.e., $Pe = lv_{z,BC} / \left(D_m + v_{z,BC}\alpha \right) = 19.9$.

The final simulation time is equal to $T = 4t_{PV}$ and $T = 2t_{PV}$ respectively for $\sigma_Y^2 = 5$ and $\sigma_Y^2 = 1$, where $t_{PV} = 200s$ is equal to the total volume of Ω occupied by the pores divided by the total imposed flowrate and it is usually defined as pore volume, and computed as $t_{PV} = \phi\left(hl\right) / \left(q_{z,BC}l\right)$.

Following Esfandiar et al. (2014, 2015), we discretize (2.1)–(2.2) by means of a stabilized finite element method, which is based on a streamline diffusion technique (Brooks and Hughes, 1991). Spatial discretization is performed upon relying on a spatial mesh $\mathfrak{T}_h = \{K\}$, i.e., a conformal discretization of Ω into triangular elements *K*. Discretization of the time window [0,*T*] is performed upon introducing the time levels $\left\{t^0 = 0,..,t^n = T\right\}$, which define the set $\{I_k\}$ of the time intervals I_k of amplitude $\Delta t^k = t^{k+1} - t^k$. Time discretization is performed through the standard θ-method (Quarteroni et al., 2007). To guarantee the unconditionally absolute stability of the θ -method, we resort to an implicit scheme and set θ= 2/3. The numerical solution of the flow problem (2.3) is obtained through a standard finite element of degree two for the pressure, which means that velocity components are obtained as piecewise linear functions, through (2.3).

Figure 2.1.*a* depicts the selected Y realization for the test case with $\sigma_Y^2 = 5$. Figure. 2.1.*b* depicts the logarithm in base ten of the module of velocity, i.e. $\log\left(|\boldsymbol{v}|\right)$, for $\sigma_Y^2 = 5$ and Fig. 2.1.*c* depicts the resulting concentration field at $t = 0.5t_{PV}$ for $\sigma_Y^2 = 5$. Fig. 2.1.*b* shows the spatial distribution of the modulus of velocity, which displays the presence of two preferential pathways characterized by large velocities, identified by a black dashed line in Fig. 2.1.*b*.

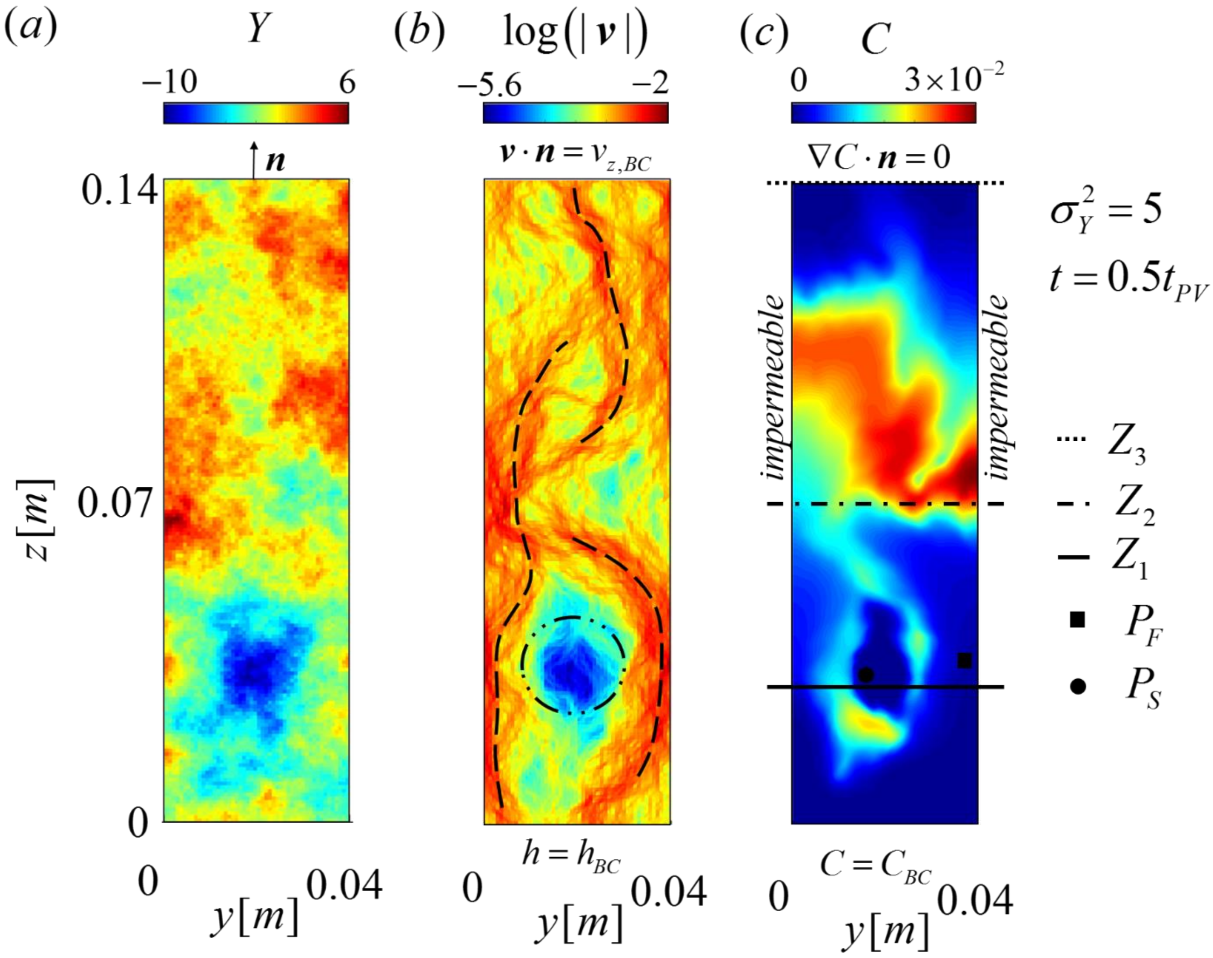

Figure 2.1. Test case for $\sigma_Y^2 = 5$: (*a*) Spatial distribution of the log-conductivity field *Y*, (*b*) spatial distribution of the velocity modulus, (*c*) solute concentration field at $t = 0.5t_{PV}$. High-velocity channels (dashed lines) and the low velocity region (dash-dotted line) are highlighted in (*b*). Location associated with section averaged concentrations $\bar{C}_1, \bar{C}_2, \bar{C}_3$ and local concentrations C_F, C_S is indicated in (*c*) (see text for definitions). Imposed boundary conditions for the flow, (*b*), and transport (*c*) problem are reported.

2.2.2 Observables

We introduce here the variables that will be considered as key target outputs of our analysis.

We consider the variation of solute concentration at specific locations within the computational domain. In particular, we consider

$$C_F(t) = C(y_F, z_F, t) \qquad C_S(t) = C(y_S, z_S, t) \tag{2.5}$$

where $P_F = (y_F, z_F)$, $P_S = (y_S, z_S)$ indicate the location in the domain where the modulus of fluid velocity is maximum and minimum respectively (i.e., subscripts *F* and *S* indicate fast and slow). For the highly heterogeneous test case, $\sigma_Y^2 = 5$, we find $y_F = 3.8\times10^{-2}m$; $z_F = 2.2\times10^{-2}m$ and $y_S = 1.5\times10^{-2}m$; $z_S = 3.6\times10^{-2}m$, see Fig. 2.1.*c*. For the middle heterogeneous case, $\sigma_Y^2 = 1$, we find $y_F = 4\times10^{-3}m$; $z_F = 6.9\times10^{-2}m$ and $y_S = 1.8\times10^{-2}m$; $z_S = 3.3\times10^{-2}m$.

Moreover, we consider spatially integrated concentrations along a section located at constant *z*

$$\overline{C}_i = \frac{1}{L}\int_L C(y,z_i,t)dy \quad i \in \{1,2,3\} \tag{2.6}$$

where $\overline{C}_1$ is evaluated at $Z_1=H/4$; $\overline{C}_2$ at $Z_2=H/2$ and $\overline{C}_3$ at $Z_3=H$ (see Fig. 2.1.*c*).

Finally, we introduce some globally integrated variables, which can quantify spreading and mixing of the plume within the domain. We consider in particular the second centred spatial moment, i.e. S_{zz}, of the concentration plume along the *z*-direction

$$S_{zz}(t) = \frac{1}{M\Omega}\int_\Omega C(\boldsymbol{x},t)\left(z - Z_{AV}(t)\right)^2 d\Omega \tag{2.7}$$

where *M* is the integral of concentration in the domain and Z_{AV} is the center of mass of the plume

$$Z_{AV}(t) = \frac{1}{M\Omega}\int_\Omega C(\boldsymbol{x},t)(z)d\Omega \tag{2.8}$$

We focus on S_{zz} due to its important role for the characterization of solute plume spreading (see e.g. Rubin 2003). Furthermore, we consider the scalar dissipation rate

$$\chi(t) = \int_\Omega \nabla C^T \boldsymbol{D} \nabla C d\Omega \tag{2.9}$$

The scalar dissipation rate, χ, quantify the rate of mixing of the plume and turn out to be crucial for the study of mixing-driven reactive transport (see e.g. de Simoni et al, 2005).

2.2.3 Fixed Uniform Discretization

We solve the transport (2.1) and flow (2.3) problems for the explained set up for fixed uniform triangular mesh with an increasing level of discretization and decreasing length of the time step. The space-time refinement is pursued until convergence is reached. As convergence criterion we impose that all the integrated quantities of interest, (2.6)-(2.9), do not exhibit a relative absolute error greater than 1% and that the pointwise breakthrough curves, (2.5), do not exhibit an absolute variation greater than 2.5×10^{-4}. As a reference grid we select a structured Cartesian grid where the distance between two nodes along the *y*, Δy, and *z*, Δz, axes is equal to $\Delta\boldsymbol{K}$. The resulting mesh, called *G*1, consist of $n_{G1} = 17500$ triangles. For the second level of discretization, we subdivide each conductivity element in four sub-element that in turn are composed of two triangles. The edges of the triangles are now $\Delta y = \Delta z = \Delta\boldsymbol{K}/2$ and G2 is made of $n_{G2} = 70000$ elements. We proceed in this way until we reach $\Delta y = \Delta z = \Delta\boldsymbol{K}/6$ for mesh G6, composed of $n_{G6} = 630000$ triangles. Regarding the time step we analyse three different values, i.e. $\Delta t_1 = 10^{-1}s$, $\Delta t_2 = 5\times10^{-2}s$ and $\Delta t_3 = 2.5\times10^{-2}s$. We verify that the quantities of interest introduced in section 4.2 are at convergence respect to the fixed mesh discretization and time stepping for G5 and $\Delta t_2 = 5\times10^{-2}s$. In the following, the results associated with G6 and $\Delta t_2 = 5\times10^{-2}s$ represent the reference solution for the fixed time-space discretization and results for the adaptive procedure will be compared against them.

2.3 Adaptive Discretization Technique

We briefly recall here the main features of the adaptive methodology. This has been previously applied to shallow water modeling (Porta et al., 2012) and computational fluid dynamics (Micheletti et al., 2010). Esfandiar et al. (2014, 2015) have applied this procedure to solute transport within homogeneous and block-wise heterogeneous porous media.

The adaptive technique is grounded on the definition of an a posteriori error estimator for the global (space-time) discretization error

$$\eta^A_{ht} = \eta^A_h + \eta_t \tag{2.10}$$

where η^A_h is an anisotropic spatial error estimator that allow to optimize the size, shape, orientation of the mesh elements and η_t is an error estimator for the time discretization. To compute both terms in (2.10) we rely on recovery-based error estimators (Zienkiewicz and Zhu, 1987), which are devised in Micheletti and Perotto (2010) and Porta et al. (2012b).

2.3.1 Anisotropic Mesh Adaptation

Let C_h be the piece-wise linear finite element approximation of the concentration C involved in the solution of (2.1). Following Porta et al. (2012a) and Micheletti and Perotto (2010), we introduce the local anisotropic estimator

$$\begin{aligned}\left[\eta^A_{K,C}(t)\right]^2 = \frac{1}{\lambda_{1,K}\lambda_{2,K}} \int_{\Delta K} \Big\{ & \lambda^2_{1,K}\left[\mathbf{r}_{1,K}\cdot\left(P_R\left(C_h(t)\right)\right) - \nabla C_h(t)\right]^2 \\ & + \lambda^2_{2,K}\left[\mathbf{r}_{2,K}\cdot\left(P_R\left(C_h(t)\right)\right) - \nabla C_h(t)\right]\Big\}\, d\Delta K \quad K \in \mathfrak{T}_h,\ \ t > 0\end{aligned} \tag{2.11}$$

where $\lambda_{i,K}$ and $\mathbf{r}_{i,K}$ (i = 1, 2) identify the eigenvalues and the eigenvectors of the tensor $\mathbf{M}_K$, defining the mapping between a reference triangle $\hat{K}$ and the generic element K of the mesh $\mathfrak{T}_h$ (see Figure 2.2.*a*). Note that $\lambda_{i,K}$ measure the length of the semiaxes of the ellipse circumscribing K, while $\mathbf{r}_{i,K}$ identify the directions of these semiaxes (Formaggia and Perotto, 2001, 2003). The quantity $P_R\left(C_h(t)\right)$ represents the recovered spatial gradient of C_h at time t. As depicted in Figure 2.2.*b*, $P_R\left(C_h\right)$ is computed as the area-weighted average of the discrete gradient $\nabla C_h(t)$ within the patch ΔK of triangles sharing at least one vertex with K. The global error a posteriori estimator associated with the finite element spatial discretization of the concentration field is computed as

$$\left[\eta^A_C(t)\right]^2 = \sum_{K\in\mathfrak{T}_h} \left[\eta^A_{K,C}(t)\right]^2 \qquad t > 0 \tag{2.12}$$

Equation (2.12) represents an anisotropic error estimate, as it directly involves the anisotropic quantities $\lambda_{i,K}$ and $\mathbf{r}_{i,K}$ identifying the size, shape, and orientation of element K. For a rigorous presentation of the error estimator (2.11)-(2.12), we refer to Porta et al. (2012) and Micheletti and Perotto (2010). The same strategy has been employed for homogeneous and block-wise heterogeneous media by Esfandiar et al. (2014, 2015). This adaptation strategy and associated results will be referred as $G_{\nabla C}$ in the following.

Along with (2.12) we consider in this work a second version of the error estimator, where our aim is to embed the spatial variability of the velocity components. Let us then assume that the field

$\tilde{\mathbf{v}}_h = \left(\tilde{u}_h, \tilde{v}_h\right)$ represents the piece-wise linear interpolation of the velocity field on the grid $\mathfrak{T}_h$. For the sake of a posteriori error estimation, we define the dimensionless components

$$U_h(\boldsymbol{x},t) = \frac{\tilde{u}_h(\boldsymbol{x},t) - \min(\tilde{u}_h(\boldsymbol{x},t))}{\max(\tilde{u}_h(\boldsymbol{x},t)) - \min(\tilde{u}_h(\boldsymbol{x},t))} \quad ; \quad V_h(\boldsymbol{x},t) = \frac{\tilde{v}_h(\boldsymbol{x},t) - \min(\tilde{v}_h(\boldsymbol{x},t))}{\max(\tilde{v}_h(\boldsymbol{x},t)) - \min(\tilde{v}_h(\boldsymbol{x},t))} \tag{2.13}$$

We then define the estimator

$$\left[\eta_{K,U}^{A}\left(t\right)\right]^2 = \begin{cases} 0,\ if\ C_{h,K} < 10^{-7} \\ \dfrac{1}{\lambda_{1,K}\lambda_{2,K}} \displaystyle\int_{\Delta K} \Big\{ \lambda_{1,K}^2 \left[\mathbf{r}_{1,K} \cdot \left(P_R\left(U_h\left(t\right)\right)\right) - \nabla U_h\left(t\right)\right]^2 \\ \qquad\qquad + \lambda_{2,K}^2 \left[\mathbf{r}_{2,K} \cdot \left(P_R\left(U_h\left(t\right)\right)\right) - \nabla U_h\left(t\right)\right] \Big\} d\Delta K,\ if\ C_{h,K} \geq 10^{-7} \end{cases} \tag{2.14}$$

Where $C_{h,K}$ represents the average concentration in the triangle *K*. We can then define an estimator $\eta_{K,V}^{A}\left(t\right)$ upon replacing *U_h* with *V_h*. From definition (2.14) it is then possible to obtain global error estimates η_V^A, η_V^A, as in (2.12). Note that estimator (2.14) is defined as a measure of the variability of the dimensionless velocity component U_h, but is conditional to the value of local concentration $C_{h,K}$. The rationale behind this choice is that our aim is at targeting those parts of the domain where solute mass is present, i.e. where transport phenomena are active at a given time. In general, a posteriori error estimation targets the estimation of the numerical error resulting from finite element approximation of a target variable (e.g., C_h in (2.12)). Quantity U_h is the result of piece-wise linear interpolation of the velocity on the grid $\mathfrak{T}_h$. In this sense, estimator (2.14) provides an a posteriori estimation of the H_1 seminorm of the interpolation error associated with quantity U_h.

Our aim is here is to embed in a single error indicator the information on the spatial distribution of concentration and on the velocity components. Following Porta et al. (2012), we then define a global error estimator

$$\left[\eta_{CUV}^{A}\left(t\right)\right]^2 = \frac{1}{3}\left(\left[\eta_C^A\left(t\right)\right]^2 + \left[\eta_U^A\left(t\right)\right]^2 + \left[\eta_V^A\left(t\right)\right]^2\right) \tag{2.15}$$

where the concentration field and the velocity components are jointly employed in order to guide the adaptive procedure. This adaptation strategy and associated results will be referred as $G_{\nabla CUV}$. Note that criterion (2.15) is provided in Porta et al. (2012a) for the solution of the shallow water equations, i.e. a system of partial differential equations. Here, we apply the same concept to the solution of the scalar equation (2.1), where the velocity components are parameters and not unknowns. The rationale behind this choice is that the solution of problem (2.1) requires to project the velocity components onto the grid employed to compute concentration, and therefore a linear interpolation between an original velocity field and the mesh where C_h is computed. Indicator (2.15) is designed to control the error associated with the solution of C_h as well as that related to the interpolation of U_h, V_h.

The final goal is to construct an anisotropic spatial grid driven by the estimator (2.12) or (2.15). In this work our goal is to fix the number of elements of the adapted grid to $N_{ele} \approx 10^4$. Let us assume here that C_h, U_h, V_h are known piece-wise linear functions on a generic grid $\mathfrak{T}_h$. Our aim is then to generate a new mesh, which is designed to minimize the chosen error, conditional to the selected number of elements. This is here obtained through an iterative procedure which relies on the metric based adaptation technique proposed in Formaggia and Perotto (2003), and then applied in diverse contexts in a number of works (e.g., Porta et al. 2012; Esfandiar et al., 2014,2015; Micheletti and Perotto, 2010). The mesh adaptation procedure can be summarized as follows:

1. Following Formaggia and Perotto (2003) we arbitrarily set a global tolerance τ and impose that the same error τ_K is assigned to each triangle K of $\mathfrak{T}_h$, i.e. upon applying the error equidistribution principle.
2. We solve a constrained local optimization problem in each tringle K of the mesh which yields the optimal values of $\lambda_{i,K}^{new}$ and $\mathbf{r}_{i,K}^{new}$ (i = 1, 2) for all triangles in the mesh $\mathfrak{T}_h$ (see e.g., Formaggia and Perotto, 2003; Micheletti and Perotto, 2010).
3. We define then the new metric tensor $\mathbf{M}_{K,0}^{new}$. To ensure that the new mesh satisfies the imposed number of triangles we apply a global and uniform rescaling the metric tensor $\mathbf{M}_{K,0}^{new}$ to obtain $\mathbf{M}_{K}^{new}$ in a way to obtain the desired cardinality for the mesh $\mathfrak{T}_h^{new}$. Note that the rescaling is assigned upon estimating the area of the elements from the optimized quantities $\lambda_{i,K}$ and $\mathbf{r}_{i,K}$, i.e. it does not require to actually generate $\mathfrak{T}_h^{new}$.
4. Once $\mathbf{M}_{K}^{new}$ is known, we generate the adapted mesh $\mathfrak{T}_h^{new}$ through the metric –based mesh generator BAMG (Hecht et al., 2010).

Some constraints are imposed to the mesh adaptation procedure, to guarantee the robustness of the methodology. Excessive element clustering is locally prevented by setting a minimum threshold $p = 10^{-9}$ value for the product $\lambda_{1,K}^{new}\lambda_{2,K}^{new}$ within the local optimization solution. This is equivalent to assign a lower limit on the element area, since $|K| = |\hat{K}|\lambda_{1,K}\lambda_{2,K}$.

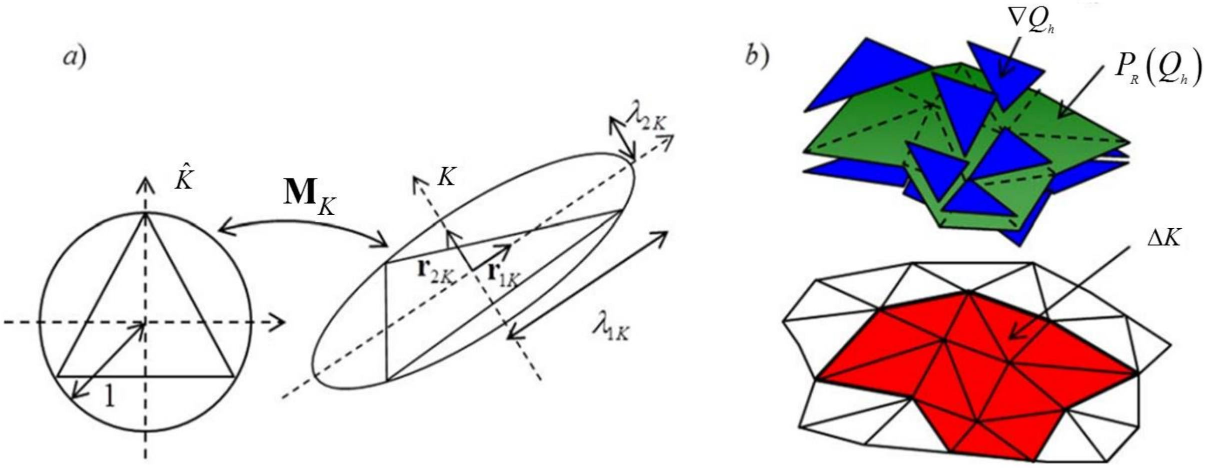

Figure 2.2. Spatial error estimator $\left[\eta_K^A(t)\right]$ in (2.12): (a) geometric definition of the anisotropic setting, and (b) definition of the recovered gradient $P_R(Q_h)$.

2.3.2 Time Step Adaptation

Time step adaptation is implemented upon relying on a recovery-based estimate of the time discretization error. We aim at predicting the time step Δt^k that can be used at each time level t^k for the subsequent time advancement. The recovery-based estimator for the time discretization error within time interval $I_{k-1} = \left[t^{k-1}, t^k\right]$ is then defined as (Porta et al., 2012; Esfandiar et al., 2014):

$$\left[\eta^t_{I_{k-1}}(\boldsymbol{x})\right]^2 = \Delta t^{k-1}\int_{I_{k-1}} \left| \frac{\partial C_R(\boldsymbol{x})}{\partial t}\Big|_{I_{k-1}} - \frac{C_h^k(\boldsymbol{x}) - C_h^{k-1}(\boldsymbol{x})}{\Delta t^{k-1}} \right|^2 dt \tag{2.16}$$

where $C_R(\boldsymbol{x})$ is a recovered solution, coinciding with the parabola which interpolates the concentration values $\left[C_h^{k-2}(\boldsymbol{x}), C_h^{k-1}(\boldsymbol{x}), C_h^k(\boldsymbol{x})\right]$ at $\left[t^{k-2}, t^{k-1}, t^k\right]$ respectively (see Figure 2.3); and $C_h^k(\boldsymbol{x})$ is the numerically computed concentration at time t^k and at point $\boldsymbol{x}$. Note that the multiplicative factor Δt^{k-1} in (2.16) renders the time error estimator dimensionless, consistent with the spatial error estimator $\eta_h^A(t)$ in (2.12) and (2.15). Note that in this work estimator (2.16) is always evaluated on the basis of the concentration *C*, since flow is steady and the fluid velocities are then constant in time. The recovery-based error estimator in (2.16) is evaluated at each vertex, i.e. V_i, of the current mesh $\mathfrak{T}_h^b$. The global time error estimator is obtained as an area weighted average

$$\left[\eta_t\right]^2 = \frac{\sum_{K\in\mathfrak{T}_h^b}\left(1/3\sum_{V_i\in K}\left[\eta^t_{I_{k-1}}(V_i)\right]^2\right)^2 |K|}{\sum_{K\in\mathfrak{T}_h^b}|K|} \tag{2.17}$$

the new time step is computed by fixing a tolerance for the time error, i.e., we impose the condition $\eta_t = \tau_t^{\Delta t} = 10^{-6}$. The error control is applied on each time slab I_{k-1}, because the global error estimator can be evaluated only at the end of the simulation when the whole time partition is known. Following Porta et al. (2012b) and Esfandiar et al. (2014), the adaptive time step is then calculated as

$$\Delta t^k = \frac{\tau_t^{\Delta t}}{\eta_t}\Delta t^{k-1} \tag{2.18}$$

The predicted time step (2.18) is constrained by a minimum, $\Delta t_{MIN} = 0.05s$, and a maximum, $\Delta t_{MAX} = 30s$ which are chosen to avoid excessive coarsening/refinement of the time discretization.

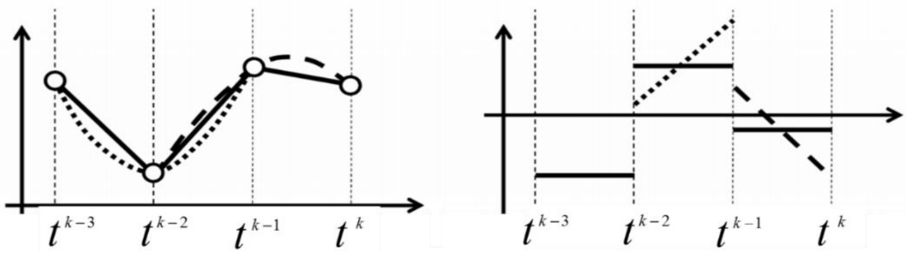

Figure 2.3. (*a*) Time derivative recovery procedure: recovered solution C_R (dotted and dashed lines) versus linear interpolant of values C_h (continuous line). (*b*) comparison between the time derivatives $\partial C_R / \partial t$ (dotted and dashed lines) and $\partial C_h / \partial t$ (continuous lines).

2.3.3 Solution adaptation procedure

We detail here all the steps which we follow to obtain the numerical solution of (2.1) through our adaptive strategy. As a first step we compute a reference velocity field upon solving the flow problem 2.(3) on a fixed uniform and sufficiently fine grid $\mathfrak{T}_h^F$, to obtain the numerical approximation of the fluid velocity field $\mathbf{v}_h\left(\mathfrak{T}_h^F\right)=u_h\left(\mathfrak{T}_h^F\right),v_h\left(\mathfrak{T}_h^F\right)$. In this study we set $\mathfrak{T}_h^F=G3$. We then detail how we employ the space time adaptive procedure for a generic time level t^k. Let us assume the concentration $C_h^k=C_h(t^k)$ and the grid $\mathfrak{T}_h^k$ are known. The adaptive solution is employed to compute C_h^{k+1}, the adapted grid $\mathfrak{T}_h^{k+1}$ and the new time level t^{k+1}. These are obtained through the following steps:

1. Obtain the velocity field $\tilde{\mathbf{v}}_h=\mathbf{v}_h\left(\mathfrak{T}_h^k\right)$ upon projecting $\mathbf{v}_h\left(\mathfrak{T}_h^F\right)=u_h\left(\mathfrak{T}_h^F\right),v_h\left(\mathfrak{T}_h^F\right)$ onto the grid $\mathfrak{T}_h^k$. This is here performed through linear interpolation.
2. Solve the transport equation (2.1) upon employing the velocity field $\tilde{\mathbf{v}}_h=\mathbf{v}_h\left(\mathfrak{T}_h^k\right)$ to determine the advective and dispersive parameters. This allows obtaining $C_h^{k+1}\left(\mathfrak{T}_h^k\right)$.
3. Apply the mesh adaptation procedure, upon relying on estimator (12) or (15) and compute $\mathfrak{T}_h^{k+1}$. As detailed in Section 2.3.2 we obtain this adapted grid so that the number of elements of $\mathfrak{T}_h^{k+1}$ is approximately equal to 10^4 elements.
4. Project the concentration fields $C_h^{k-1},C_h^k,C_h^{k+1}$ onto the new grid $\mathfrak{T}_h^{k+1}$ to obtain the adapted time step Δt^k. The next time level for the simulation is then defined as $t^{k+1}=t^k+\Delta t^k$.

The procedure is then repeated until $t^{k+1}\geq T$. Note that step 4. of the above procedure can be performed only when $k > 1$, that is the two steps $\Delta t^0,\Delta t^1$ are assigned by default to a fixed time step Δt_{MIN}, which is assigned a priori as anticipated in Section 2.3.2.

2.4 Results

This section is devoted to the comparison of numerical results for the observables described in Section 2.2.2, obtained relaying up on: (*a*) fixed time step and fixed uniform spatial discretization; space-time adaptive methodology guided by error estimators based on (*b*) the concentration fields only, i.e. (2.12) and (*c*) both the concentration and the velocity fields, i.e. (2.15). We discuss results obtained for $\sigma_Y^2=5$ (section 2.4.1), and then those obtained for $\sigma_Y^2=1$ (section 2.4.2).

2.4.1 Test case with variance of Log-conductivity: $\sigma_Y^2=5$.

The realization of the log-conductivity field is reported in Figure 2.1.a. Figure 2.1.*b* depicts the logarithm of the modulus of the velocity field, i.e. $\log\left(|\,\boldsymbol{v}\,|\right)$, as obtained from the numerical discretization on the fixed grid G3 of the flow problem. Fig. 2.1.*b* reveals the presence of two high velocity channels (see dashed curves in Fig. 2.1.*b*), which act as preferential pathways for fluid flow and are expected to largely influence transport behaviour as well. An approximately circular low velocity region is also identified, centred around location z = 0.035 m, y = 0.02 m (see dash-dotted circle in Figure 2.1.*b*). Figure 2.1.*c* depicts the resulting concentration field at $t = 0.5t_{PV}$. Before going into details, we can observe that solute mass distribution of the domain is largely influenced by the structure of the velocity field, and in particular part of the mass is delayed due to the presence of the above mentioned low velocity region.

We start our analysis by focusing on the early time behaviours of the adapted mesh and resulting concentration fields for $G_{\nabla CUV}$ and $G_{\nabla C}$, and compare the results with those obtained by the reference solution. Figure 2.4 depicts, at $t = 0.05t_{PV}$, the concentration field obtained by the three discretization strategies (Figure 2.4.*a*-*c*) and the adapted meshes (Figure 2.4.*d*-*e*). We report concentrations in logarithmic scale, given that small values of concentration are critical to evaluate early arrivals and tailing, which are often of interest in practical applications. In all panels of Figure 2.4 we focus on a limited region close to the inflow boundary. Comparison between Figure 2.4.*a*-*c* shows that the overall behavior of the solution is consistent among $G_{\nabla CUV}$, $G_{\nabla C}$ and *G*6. We note that for early times two solute finger appear, due to the channeling in the velocity field around the low velocity region zone indicated in Figure 2.4.*b*.

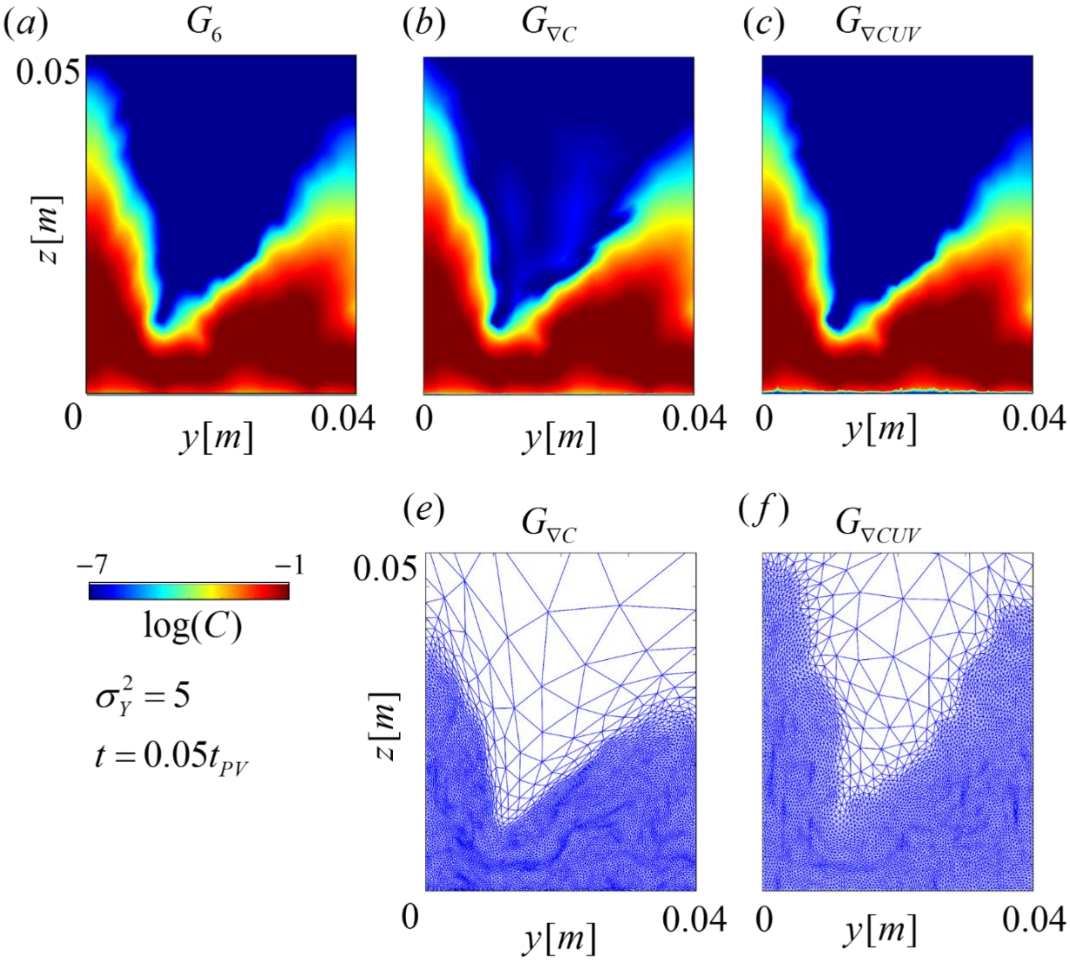

Figure 2.4. Test case with $\sigma_Y^2 = 5$: spatial distribution of the concentration field in logarithmic scale at time $t = 0.05t_{PV}$, for discretizations (*a*) *G*6; (*b*) $G_{\nabla C}$; (*c*) $G_{\nabla CUV}$ and the associated adapted meshes for (*e*) $G_{\nabla C}$; (*f*) $G_{\nabla CUV}$.

The spatial topology of the adapted grid $G_{\nabla C}$ reveals that the element dimension is relatively coarse close to the forward solute fringe (see Figure 2.4.*d*). This can be seen, e.g., in the region y=[0,0.01]m× z=[0.04,0.05]m and is justified upon observing that the concentration varies between approximately 10^{-7} and 10^{-4} in the same region, i.e. the concentration gradient is lower with respect to other portions of the domain body (see Figure 2.4.*b*). As a consequence, the log-concentration field rendered by $G_{\nabla C}$ appears to be characterized by a local loss of accuracy. We also observe that some oscillation of the order of 10^{-6}-10^{-5} appear in the solution (e.g., y ≈ 0.02 m, z ≈ 0.02 m). These are probably linked to interpolation of the solution between adapted meshes, which is associated to a small error in the presence of relatively coarse elements. The adapted mesh $G_{\nabla CUV}$ is characterized by elements of small size along the whole forward solute fringe, since the adaptation is guided also by the spatial gradients of U_h and V_h which are embedded in criterion (2.15)-(2.16). As a result, the solution yielded by $G_{\nabla CUV}$ is capable to reproduce the fine scale details of the log-concentration field which are partially lost in $G_{\nabla C}$. We also observe that the shape of the triangular elements is close to isotropic when the velocity components are considered for mesh adaptation, consistent with the isotropic model selected for the variation of the hydraulic conductivity.

Figure 2.5 depicts the log-concentration field for time $t = 1.5t_{PV}$, as given by $G6$ (*a*), $G_{\nabla C}$ (*b*) and $G_{\nabla CUV}$ (*c*). A first visual inspection reveals that the three solutions appear to be very similar: the concentration field displays smooth variations. Solute mass remains trapped in the low velocity region located in the center-bottom part of the domain (see also Figure 2.1.b), while in the upper portion of the domain ($z > 0.07$ m) the solute is uniformly distributed throughout the domain. These features of the solution are reflected in the adapted meshes. Grid $G_{\nabla C}$ is refined within the low conductivity zone where relative high concentration gradients arise (see Figure 2.5.d). Mesh $G_{\nabla CUV}$ is constituted by elements of comparable size the vast majority of the domain of the considered domain, i.e. at all locations where $C > 10^{-7}$ (see Figure 2.5.c and 2.5.e). At these late times, visually the solutions obtained for $G6$, $G_{\nabla C}$ and $G_{\nabla CUV}$ appear to be very similar, even if the adapted meshes display marked differences.

Figure 2.6 show a magnification of the log-concentration field and of the adapted grids at $t = 1.5t_{PV}$ around the low velocity area. The solution associated with mesh $G_{\nabla C}$ exhibits local variations of the order of 10^{-6}-10^{-5} which are particularly evident at $z \approx 0.015$ m, i.e. the light blue fringes of log(C) in Figure 6.*b* are not found in the reference solution (Figure 2.6.*a*) and when $G_{\nabla CUV}$ is considered. As previously noted, this observation can be linked to difference between $G_{\nabla C}$ and $G_{\nabla CUV}$ in the local dimensions of the elements of the grid. We observe that $G_{\nabla CUV}$ is composed by elements of similar size. Only mild variations in the element shape and orientation are seen in Figure 2.6.*d*, which allow to barely recognize the footprint of the concentration field on the mesh topology. On the other hand the mesh $G_{\nabla C}$ is completely tied to the concentration field gradients and displays large variations of the elements size and shape around the low velocity area.

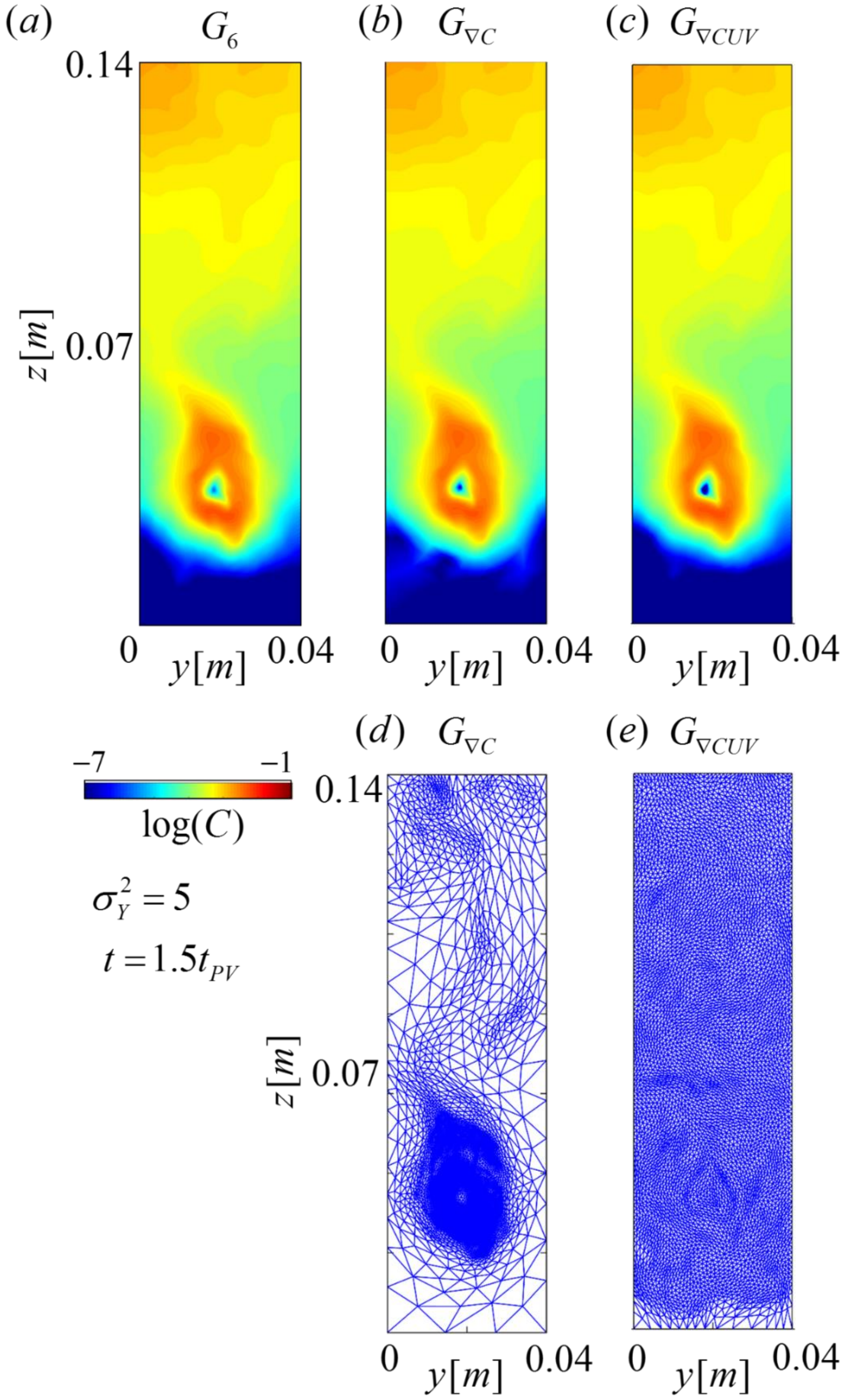

Figure 2.5. Test case with $\sigma_Y^2 = 5$: spatial distribution of the concentration field in logarithmic scale over the entire domain, Ω, at time $t = 1.5t_{PV}$, for discretizations (*a*) *G*6; (*b*) $G_{\nabla C}$; (*c*) $G_{\nabla CUV}$ and the associated adapted meshes for (*e*) $G_{\nabla C}$; (*f*) $G_{\nabla CUV}$.

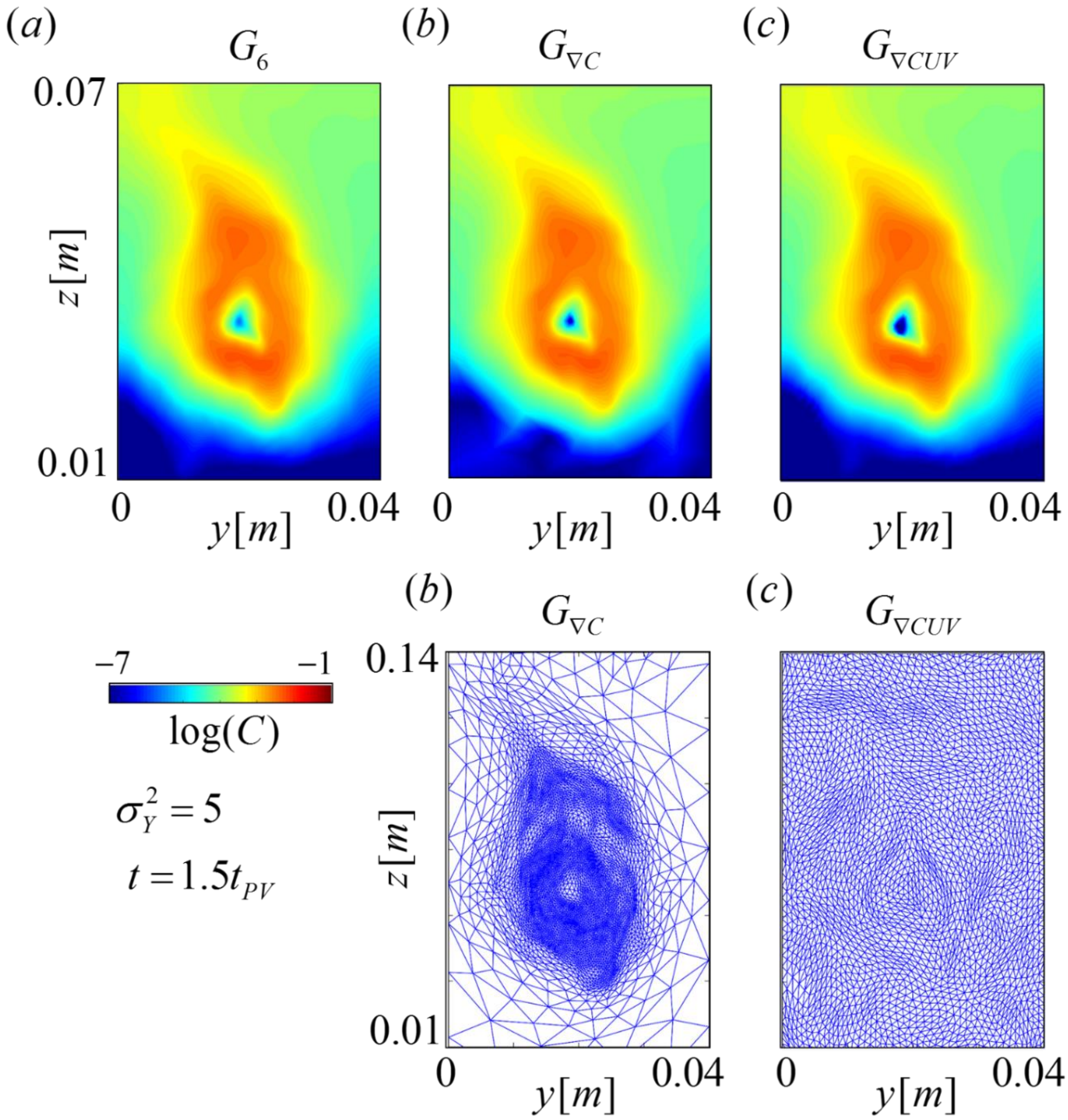

Figure 2.6. Test case with $\sigma_Y^2 = 5$: spatial distribution of the concentration field in logarithmic scale in the low velocity region indicated in Figure 1 for $t = 1.5t_{PV}$ and discretizations (*a*) *G*6; (*b*) $G_{\nabla C}$; (*c*) $G_{\nabla CUV}$ together with the associated adapted meshes for (*e*) $G_{\nabla C}$; (*f*) $G_{\nabla CUV}$

The evolution of the time step, Δt, as a function of time is depicted in Figure 7 for $G_{\nabla CUV}$ (red curve) and $G_{\nabla C}$ (blue curve). In Fig. 7 the minimum allowed time step which coincide with the one settled in $G6$, Δt_{MIN}, and the maximum, Δt_{MAX}, are also reported. At early times the time steps is identical to Δt_{MIN}, due to the rapid variation of the C field in time. As time advances, $\Delta t > \Delta t_{MIN}$ are allowed, since the solute plume spreads over a greater portion of the domain and diffusive/dispersive process gain importance leading to slower time variation of the C fields. The combination of the time step and mesh adaptivity allows obtaining a relative speed up the computational costs between $G_{\nabla CUV}$ and $G6$ equal to $CPU_{\nabla CUV/G6} = 1.27 \times 10^{-1}$, and for $G_{\nabla C}$ equal to $CPU_{\nabla C/G6} = 1.56 \times 10^{-1}$.

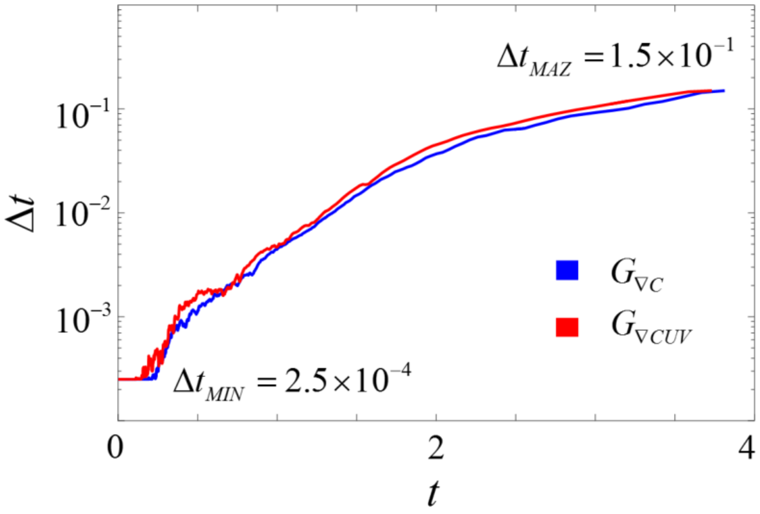

Figure 2.7. Test case with $\sigma_Y^2 = 5$: evolution of the adaptive time step, Δt, against time t. Red curve for $G_{\nabla CUV}$ and blue curve for $G_{\nabla C}$.

We now proceed to analysis the selected quantities of interest described in Section 2.2.2. Figure 2.8.*a* shows the section-averaged concentrations at locations Z_1, Z_2, Z_3 (see Fig. 2.1.*c*) evaluated for $G6$. For the sake of clarity the comparison between the results obtained with the different strategies is then reported in various subpanels, which focus on particular parts of the $\overline{C}_i(t)$ trends. The reader can note the asymmetry in all the $\overline{C}_i$, which is due to the level of heterogeneity in $\boldsymbol{K}$ (see, e.g., Edery et al., 2015). A marked tailing behavior appears at late times particularly in $\overline{C}_1$, due to the presence of the low velocity spot where solute accumulates at early times and from which are slowly released by diffusion-dispersion. Fig. 2.8.*b* shows detail of the early times behavior of $\overline{C}_1$, for $G6$ (black curve), $G1$ (green curve), $G_{\nabla C}$ (blue curve) and $G_{\nabla CUV}$ (red curve). Overall we observe that the differences between the various solutions is relatively small (of the order of 10^{-5}) when the tails of section-averaged concentrations are of concern. This can be seen for early and late solute arrivals in Fig. 2.8.*b* and 2.8.*d*, respectively. We observe that for late arrivals the fixed mesh $G1$ tends to underestimate the section average concentration, while the adaptive grids reproduce well the results given by G6. While the absolute difference between section-average concentrations is small we observe that such small variations may be important in some practical applications. The two adaptive strategies also reproduce well the peak concentration given by $G6$ while $G1$ tends to underestimate the maximum concentration by approximately 10^{-3} at both locations Z_1 and Z_2, as depicted in Figure 2.8.*c*.

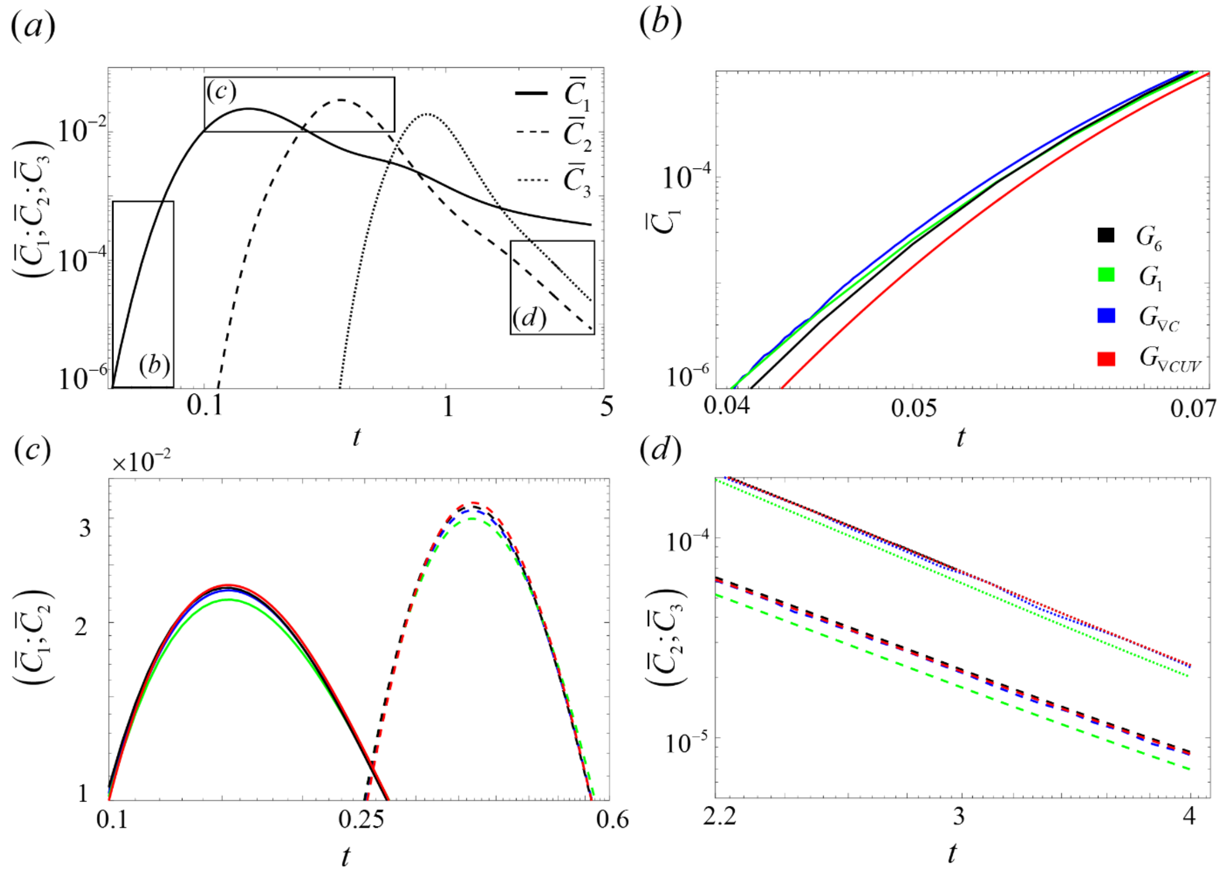

Figure 2.8. Test case with $\sigma_Y^2 = 5$: time evolution of the section-averaged concentrations $\bar{C}_1$ (continuous curves), $\bar{C}_2$ (dashed curves), and $\bar{C}_3$ (dotted curves), for (*a*) *G*6. Panels (*b*-*d*) display magnifications of specific time intervals, associated with early times (*b*), peak (*c*) and late times (*d*), as indicated in panel (*a*). In all plots black curves are associated with *G*6, green curves with *G*1, red curves with $G_{\nabla CUV}$ and blue curves with $G_{\nabla C}$.

Figure 2.9 displays the same type of comparisons obtained this time upon focusing on local values of concentrations, i.e. C_F and C_S related to the fastest and slowest flow velocity within the domain. Note that, while the two considered locations are quite close in the domain the local concentration dynamics exhibits very different characteristics at the two locations. For example C_F peaks at $t = 0.1t_{PV}$, while C_S reaches a maximum value at $t = 1.5t_{PV}$ and then slowly decreases. The delay observed in these two locations reflects the fact that transport is advection dominated at location P_F, while solute mass exchanges around location P_S are dominated by diffusion and transverse dispersion.

Fig. 2.9 show a magnification of C_F at (*b*) early, (*c*) intermediate, (*d*) and late times for *G*6 (continuous black curves), *G*1 (green curves), $G_{\nabla C}$ (blue curves) and $G_{\nabla CUV}$ (red curves). The differences between G1 and G6 are can here reach values up to 10^{-2} and are particularly evident for $t < 0.1$PV, i.e. as long as C_F increases with time (see Figure 2.9 *b*-*c*). The two adapted meshes are here in close agreement with G6. Note that at these early times the two adaptive strategies tend to predict later solute arrivals at P_F, while *G*1 predicts earlier solute arrivals (due to numerical diffusion). For $t > 0.1$PV (Figure 2.9.*c*-*d*) the difference between the solutions given by all strategies tend to reduce to values below 10^{-4}. We observe that the solution associated with $G_{\nabla C}$ displays oscillations of the order of 10^{-5} which are visible in both forward and backward tail. Such oscillations are related to the small inaccuracies noted in Figure 2.4 and 2.5, and are explained upon observing that the local element size is characterized by large variations of element size at location P_F across time.

The variation of concentration C_S (i.e., concentration at point P_S) with time is considered in Figure 2.9 *e*-*f*. Large differences appear between G1 and G6, while the adaptive strategies closely reproduce the results given by the reference solution. As a results, for instance, the arrival time of a concentration $C_S = 10^{-5}$ is largely overestimated by G1 (see Figure 2.9.*e*).

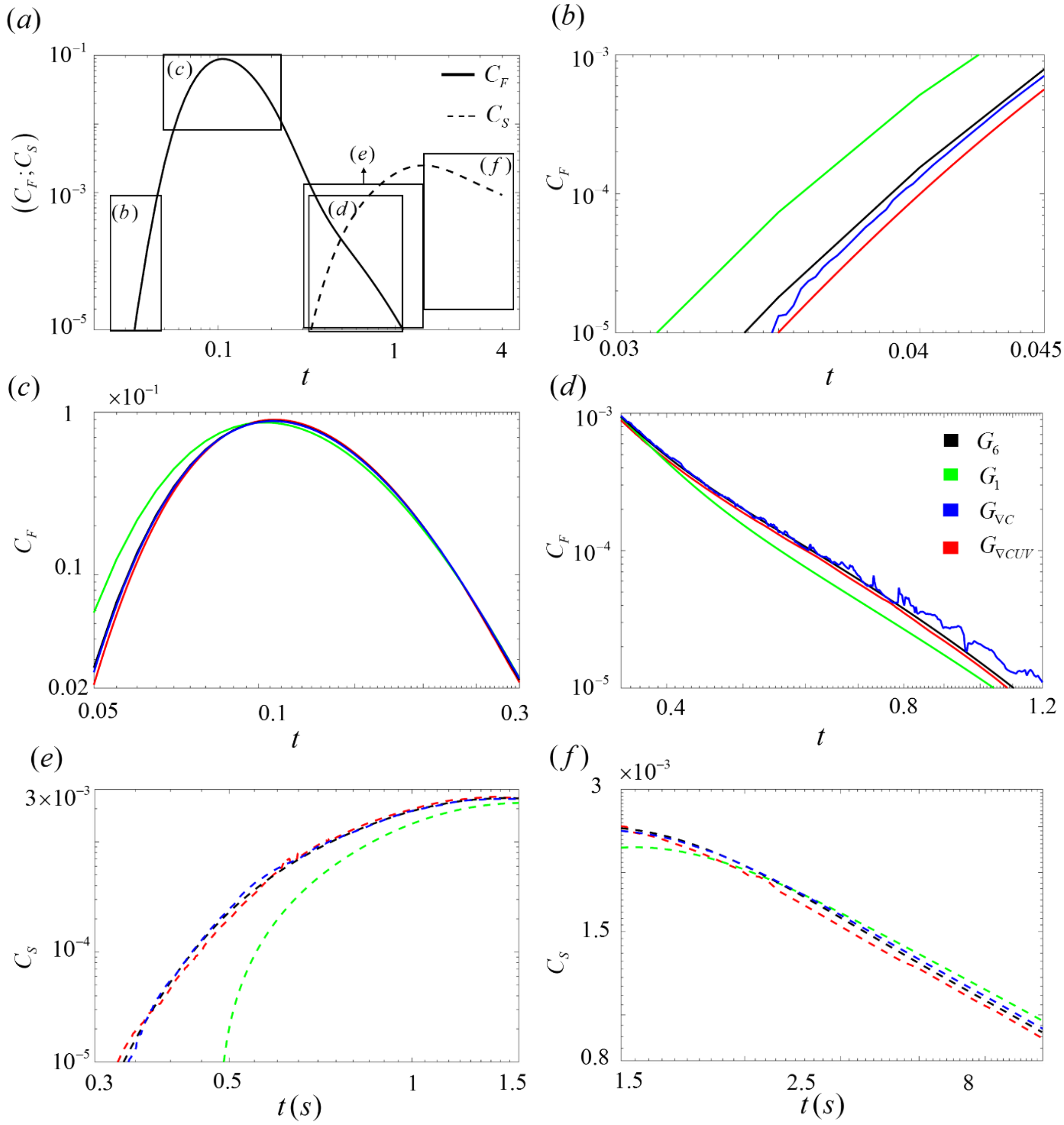

Figure 2.9. Test case with $\sigma_Y^2 = 5$: time evolution of the local concentration values C_F (continuous curves) and C_S (dashed curves), for (*a*) *G*6. Panels (*b*-*f*) display magnifications related to specific time intervals associated with C_F (*b*-*d*) and C_S (*e*-*f*) as indicated in (*a*). In all plots black curves are associated with *G*6, green curves with *G*1, red curves with $G_{\nabla CUV}$ and blue curves with $G_{\nabla C}$.

As last we consider the evolution of global indicators of spreading and mixing of solute mass in the domain, i.e. S_{zz} and χ. Fig. 2.10.*a* compare S_{zz}, evaluated with *G*6 (black curve), *G*1 (green curve), $G_{\nabla CUV}$ (red curve) and $G_{\nabla C}$ (blue curve). No great difference can be noted between the four solutions, with *G*1 which overestimates only slightly S_{zz} for $t < 0.25t_{PV}$ and then underestimates it. Fig. 2.10.*b* reveals instead a marked difference between the scalar dissipation rate χ obtained through *G*1 when compared against reference results obtained through *G*6, while $G_{\nabla C}$ and $G_{\nabla CUV}$ provide values of χ which compare extremely well with the reference solution *G*6. This result suggests that while different meshing strategies may have a reduced impact on the prediction of spreading they can heavily impact the prediction of mixing, which is crucial also with a view to the simulation of reactive processes.

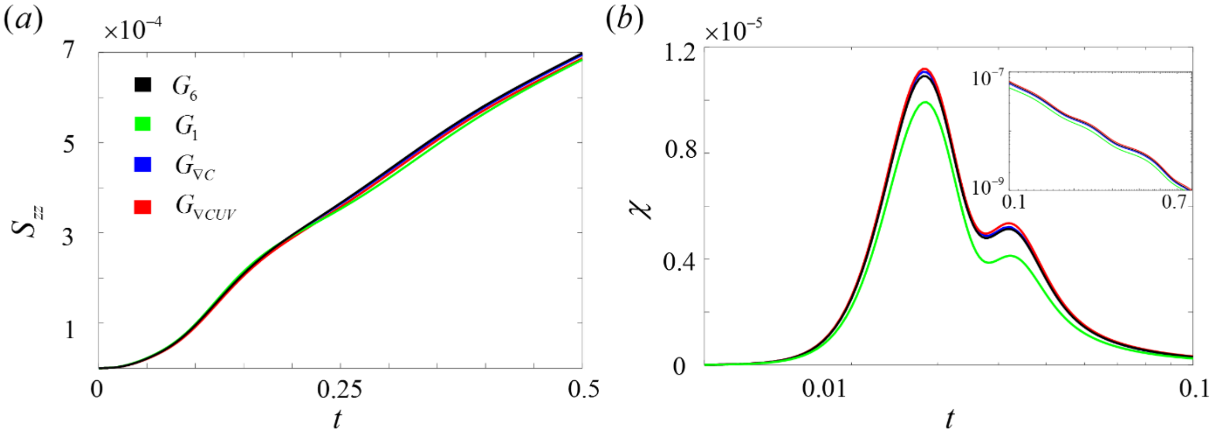

Figure 2.10. Test case with $\sigma_Y^2 = 5$: time evolution of (*a*) Second center plume spatial moment, S_{zz}, and (*b*) scalar dissipation rate, χ. Black curves are associated with *G*6, green curves with *G*1, red curves with $G_{\nabla CUV}$ and blue curves with $G_{\nabla C}$.

As a final term of comparison, Figure 2.11 depicts the global *a posteriori* error estimator (12), η_C^A, (i.e. based solely on C_h) for *G*6 (black curve), *G*1 (green curve), $G_{\nabla CUV}$ (red curve) and $G_{\nabla C}$ (blue curve). Note that the value assumed by the estimator provides an approximation of the computational error in H1 semi-norm (i.e., based on the gradients of the concentration). Inspection of Fig. 2.11 reveals that *G*1 shows the highest η_C^A for all the times. For $0.05t_{PV} < t < 1t_{PV}$, the resulting η_h^A for *G*6 is the smallest. Note that for the interval $0.05t_{PV} < t < 1t_{PV}$ the slope of the curves for $G_{\nabla C}$ and $G_{\nabla CUV}$ is smaller respect to the slope of the curve for *G*6. The smaller slope given by the adaptive procedures for the highlighted interval is due to the fact that, even if the gradients in solution are smearing out, the plume spreads across the z directions, i.e. its total size increases and the assigned number of elements N_{ele} need to cluster within an increasing area of the domain. As consequence of this dynamics, the reduction in η_C^A is less marked in the adaptive procedure when compared against the *G*6. At late times, i.e. $t > 1t_{PV}$, the elements of the adaptive grid $G_{\nabla C}$ tend to concentrate around the low velocity region (see Fig. 2.4) allowing a proper resolution of concentration gradients which arise in the low velocity spot, leading to a sensible reduction of η_C^A, i.e. a marked negative slope of the blue curve in Fig. 2.11. Interestingly, for $t < 0.05t_{PV}$, when η_C^A reaches its maximum value, the values η_C^A associated with $G_{\nabla C}$ and $G_{\nabla CUV}$ are smaller than the ones for $G6$. Moreover, inspection of the $G_{\nabla C}$ and $G_{\nabla CUV}$ meshes at times $t < 0.05t_{PV}$, reveals that almost all the N_{ele} elements are properly placed near the inlet, with elements having an average size smaller than the one of the uniform elements in $G6$. Therefore, it is reasonable to assume that at these early time adaptive grids may lead to a slightly more accurate spatial solution than the reference $G6$.

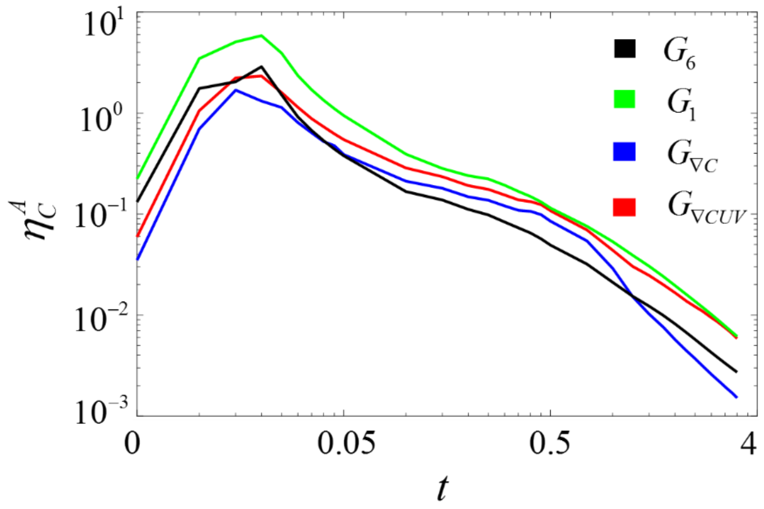

Figure 2.11. Test case with $\sigma_Y^2 = 5$: Time evolution of the a posterior estimation (2.13) of the spatial discretization error associated with concentration, t, computed for discretization $G6$ (black curve) $G1$ (green curve), $G_{\nabla CUV}$ (red curve) and $G_{\nabla C}$ (blue curve).

2.4.2 Test case with variance of Log-conductivity: $\sigma_Y^2 = 1$.

In this section we present results for the test case with $\sigma_Y^2 = 1$, to assess the sensitivity of the results to the heterogeneity of the porous medium. Note that, the Y field has been generated with the same seed number used for the case with $\sigma_Y^2 = 5$ in SGSIM and then properly rescaled to obtain the desired variance. We do not show here results related with section-averaged concentrations $\overline{C}_i$, which display a satisfactory agreement between G6 and the two adaptive strategies, while G1 provides the most flat and less picked trends also for this level of permeability heterogeneity. Figure 2.12.*a* depicts then the time evolution of the local concentrations C_S and C_F for $G6$. Note that the location of the two points P_F and P_S is not the same as in the previous case (see Section 2.2.2).

The behavior of C_S and C_F is not dramatically different, reflecting the less marked influence of the heterogeneity on the concentration. Fig. 2.12.*b* show a magnification of C_S at early times, note that the agreement between $G6, G_{\nabla C}$ and $G_{\nabla CUV}$ results is much more satisfactory than that noted for $\sigma_Y^2 = 5$ for the early times behaviour of C_S (see Fig. 2.9.*e*). A good agreement between the results obtained through $G6, G_{\nabla C}$ and $G_{\nabla CUV}$ results is obtained also for the early times in C_F (not shown) and for late times in both C_S and C_S, see Fig. 2.12.*d*. The two adaptive strategies also reproduce well the observed peak of C_F, as shown in Fig. 2.12.*c*, the same result holds for the peak of C_S (not shown). Results obtained through $G1$ display the smallest peak and heavier tails, which can be attributed to the presence of numerical dispersion.

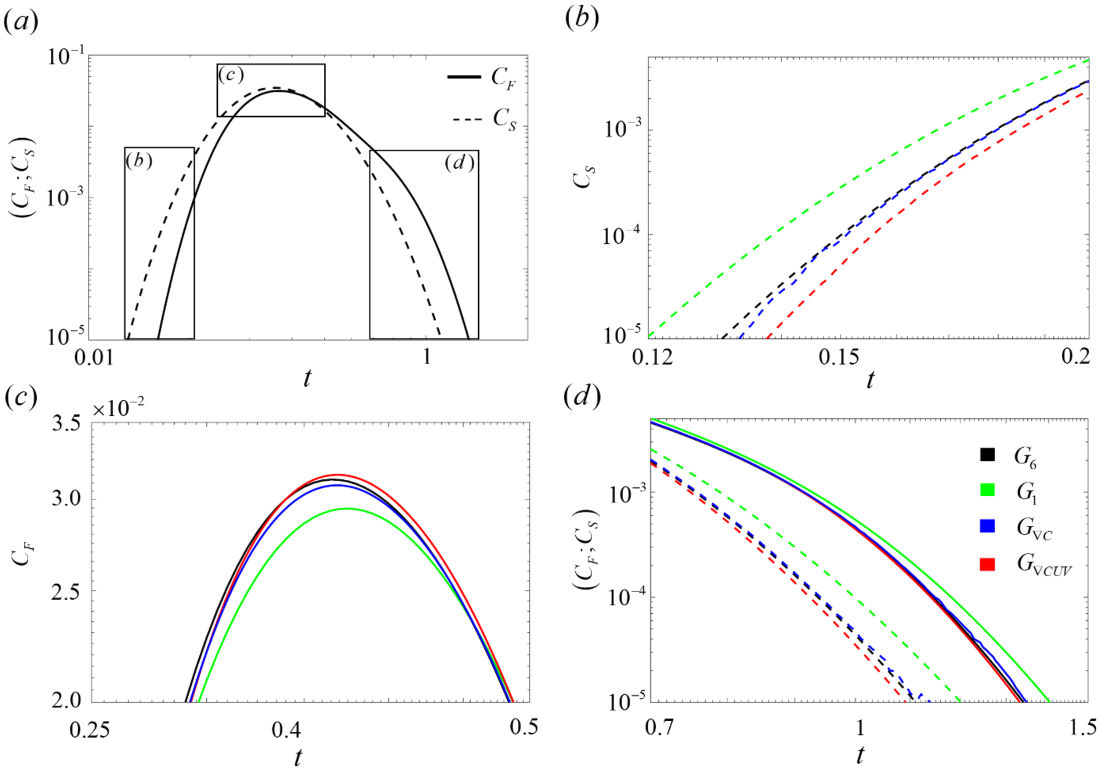

Figure 2.12. Test case with time evolution of the local concentration values C_F (continuous curves) and C_S (dashed curves), for (*a*) $G6$. Panels (*b*-*f*) display magnifications related to specific time intervals, associated with C_F (*c*-*d*) and C_S (*b*-*d*), as indicated in (*a*). Black curves are associated with $G6$, green curves with $G1$, red curves with $G_{\nabla CUV}$ and blue curves with $G_{\nabla C}$.

Figure 2.13 depicts the time evolution of (*a*) S_{zz} and (*b*) χ . As for the $\sigma_Y^2 = 5$ case, we note that the time evolution of S_{zz} and χ associated with $G_{\nabla C}$ and $G_{\nabla CUV}$ is in good agreement with the results obtained through *G*6. Fig. 13.*a*-*b* highlights that upon employing mesh G1 solute spreading S_{zz} is overestimated and the scalar dissipation rate χ is underestimated, which is related to smaller concentration gradients. The adaptive mesh $G_{\nabla CUV}$ provides the smallest S_{zz} and the highest χ values. This is in agreement with the general tendency of predicting a more compact and sharp evolution of the injected plume by using this adaptive strategy.

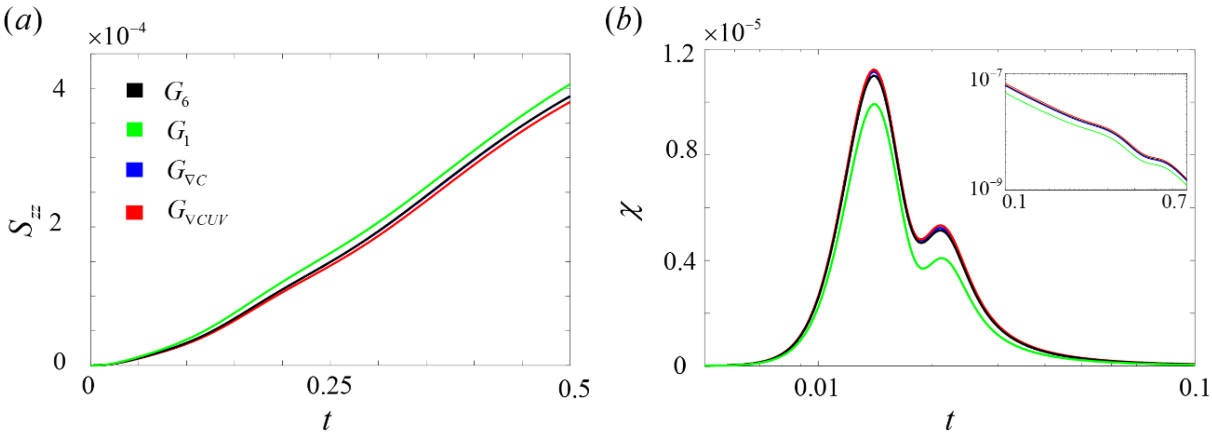

Figure 2.13. Test case with $\sigma_Y^2 = 1$: time evolution of (*a*) Second center plume spatial moment, S_{zz}, and (*b*) scalar dissipation rate, χ . Black curves are associated with *G*6, green curves with *G*1, red curves with $G_{\nabla CUV}$ and blue curves with $G_{\nabla C}$.

2.5 Conclusion

We applied a space-time adaptive methodology guided by *a posteriori* error estimator for solving solute transport in porous media with spatial distributions of log-conductivity Y characterized by middle, $\sigma_Y^2 = 1$, and high, $\sigma_Y^2 = 5$, levels of heterogeneity. The key goal of our work is to test the applicability of an automatic mesh and time step adaptation procedure to solve solute transport in such conditions. We perform a series of numerical tests and compare the results of the implemented adaptive strategies against those obtained through fixed uniform discretizations. In all adaptive simualtions the number of elements of the adapted meshes is kept constant in time, while the time step is allowed to change within two extreme values (Δt_{MIN}, Δt_{MAX}) set *a priori*. The fixed uniform discretization strategies are set such that the spatial meshes are structured and tailored on the spatial structure of the conductivity field and the time step is fixed to the minimum value employed for the fixed uniform discretizations, Δt_{MIN}. Our results lead to the following major conclusions:

- For the highest considered levels of heterogeneity, the convergence of the numerical results as quantified by local and spatially averaged indicators is achieved for a grid ($G6$) whose element size is six time smaller than ΔK, i.e. the size of elements employed to build the log-conductivity field. This result indicates that in general it may not be appropriate to routinely employ the same spatial discretization to describe the random conductivity field and numerically approximate solute mass transport.
- We implement two different strategies to guide the space adaptive procedure. In the first strategy, labeled $G_{\nabla C}$, the mesh is adapted only on the basis of the spatial gradients of the concentration field. In the second strategy, labeled $G_{\nabla CUV}$, we combine both the concentration and the velocity components. Both these adaptive strategies can reproduce the results obtained through $G6$ and a fixed time step equal to Δt_{MIN} in terms of section-averaged and local concentration values, as well as global spreading and mixing metrics. This result is achieved upon reducing the computational cost by approximately one order of magnitude.
- The two adaptive strategies lead to different meshing of the computational domain along time. When both velocity and concentration are included in the mesh adaptation strategy the mesh tends to cover more uniformly the region of the domain where solute mass is present. In spite of the difference in the spatial distribution of the elements, the two strategies yield to very similar results as for what concern spatially averaged concentration and global mixing and spreading. The key difference is that local concentration values obtained through $G_{\nabla C}$ exhibit numerical oscillations where the location of interest falls within coarse meshed subregions of the domain. These oscillations are of the order of 10^{-5}. This highlights the importance of controlling the maximum element size, when such low values of concentration are of interest.
- Evolution of the $G_{\nabla CUV}$ and $G_{\nabla C}$ meshes suggests that the former is more appropriate to capture the fast dynamics, i.e. the advective transport of solute through fast velocity channels, while the second is particularly able to grasp the slow transport mechanism which occurs in low velocity spots.
- Results obtained upon employing to solve the transport problem the same grid used to discretize the log-conductivity field ($G1$) are compared to those yielded by the mesh adaptation strategy. Mild differences can be observed when section-averaged concentration and global solute spreading are considered. On other hand, the discretization strategy matters most when local concentration values and global mixing are of concern. This result suggests

that mesh adaptation techniques may be suited to simulation of reactive transport processes. Note that mesh $G1$ is characterized by approximately the same number of elements as that assigned to the adaptive grids.

Reference

Amaziane, B., Bourgeois, M. and El Fatini, M.: Adaptive mesh refinement for a finite volume method for flow and transport of radionuclides in heterogeneous porous media, Oil & Gas Science and Technology – Rev. IFP Energies nouvelles, 69(4), 687-699, 2014.

Bear, J. and Cheng, A. H. D.: Modeling groundwater flow and contaminant transport, Springer, 2011.

Bresciani, E., Davy, P. and Dreuzy, J.: A finite volume approach with local adaptation scheme for the simulation of free surface flow in porous media, Int. J. Numer. Anal. Methods Geomech., 36(13), 1574-1591, 2012.

Bolster, D., Valdés-Parada, F. J., Le Borgne, T., Dentz, M. and Carrera, J.: Mixing in confined stratified aquifers, J. Contam. Hydrol., 120-121, 198-212, 2011.

Cao, J., and Kitanidis, P. K.: Adaptive-grid simulation of groundwater flow in heterogeneous aquifers, Adv. Water Res., 22(7), 681-696, 1999.

Chueh, C. C., Secanell, M., Bangerth, W. and Djilali, N.: Multi-level adaptive simulation of transient two-phase flow in heterogeneous porous media, J. Comp. Fluid, 39, 1585-1596, 2010.

Cirpka, O. A., Frind, E. O. and Helming, R.: Streamline-oriented grid generation for transport modelling in two-dimensional domains including wells, Adv. Water Resour., 22(7), 697-710, 1999.

Dentz, M. and de Barros, F. P. J.: Mixing-scale dependent dispersion for transport in heterogeneous flows, J. Fluid Mech., 777, 178-195, 2015.

Deutsch, C. V. and Journel, A. G.: GSLIB: Geostatisitcal Software Library and User's Guide, 2nd Ed, New York, Oxford Univerity Press, 1998.

de Barros, F. P. J. and Dentz, M.: Pictures of blockscale transport: Effective versus ensemble dispersion and its uncertainty, Adv. Water Resour., 91, 11-22, 2016.

de Barros, F. P. J., Dentz, M., Koch, J. and Nowak, W.: Flow topology and scalar mixing in spatially heterogeneous flow fields, Geophys. Res. Lett., 39(8), 2012.

De Simoni, M., Carrera, J., Sánchez-Vila, X. and Guadagnini, A.: A procedure for the solution of multicomponent reactive transport problems, Water Resour. Res., 41, W11410, 2005.

Edery, Y., Guadagnini A., Scher, H., and Berkowitz, B.: Origins of anomalous transport in heterogenoues media: Structural and dynamic controls, Wtaer Resour. Res., 50, 1490-1505, 2014.

Esfandiar, B., Porta, G., Perotto, S. and Guadagnini, A.: Anisotropic mesh and time step adaptivity for solute transport modeling in porous media, New Challenges in Grid Generation and Adaptivity for Scientific Computing, edited by L. Formaggia and S. Perotto, SEMA SIMAI Springer Series, vol. 5, Springer Milan, 2014.

Esfandiar, B., Porta, G., Perotto, S. and Guadagnini, A.: Impact of space-time mesh adaptation on solute transport modeling in porous media, Water Resour. Res., 51, 1315-1332, 2015.

Formaggia, L. and Perotto, S.: New anisotropic a priori error estimates, Numer. Math., 89(4), 641-667, 2001.

Formaggia, L. and Perotto, S.: Anisotropic error estimates for elliptic problems, Numer. Math., 94(1), 67-92, 2003.

Gedeon, M., and Mallants, D.: Sensitivity analysis of a combined groundwater flow and solute transport model using local-grid refinement: A case study, Math. Geosci., 44(7), 881-899, 2012.

Huang, W., and Zhan, X.: Adaptive moving mesh modeling for two dimensional groundwater flow and transport, AMS Contemporary Mathematics, vol. 383, pp. 239–252, Am. Math. Soc., Providence, R. I., 2005.

Jayasinghe, Y. S.: A space-time adaptive method for flows in oil reservoirs. PhD Theses, Boston, 2015.

Kavetski, D., Binning, P. and Sloan, S. W.: Adaptive backward Euler time stepping with truncation error control for numerical modelling of unsaturated fluid flow, Int. J. Numer. Methods Eng., 53(6), 1301-1322, 2002.

Klieber, W. and Rivière, B.: Adaptive simulations of two-phase flow by discontinuous Galerkin methods, Comput. Methods Appl. Mech. Engrg., 196, 404-419, 2006.

Knupp, P.: A moving mesh algorithm for 3-d regional groundwater flow with water table and seepage face, Adv. Water Res., 19(2), 83-95, 1996.

Le Borgne, T., Dentz, M. and Villermaux, E.: The lamellar description of mixing in porous media, J. Fluid Mech., 770, 458-498, 2015.

Le Borgne, T., Dentz, M., Bolster, D., Carrera, J., de Dreuzy, J. R. and Davy, P.: Non-Fickian mixing: Temporal evolution of the scalar dissipation rate in porous media, Adv. Water Resour., 33(12), 1468-1475, 2010.

Mansell, R., Ma, L., Ahuja, L. and Bloom, S.: Adaptive grid refinement in numerical models for water flow and chemical transport in soil, Vadose Zone J., 1(2), 222-238, 2002.

Mehl, S., and Hill, M. C.: Development and evaluation of a local grid refinement method for block-centered finite-difference groundwater models using shared nodes, Adv. Water Res., 25(5), 497-511, 2002.

Micheletti, S. and Perotto, S.: Anisotropic adaptation via a Zienkiewicz-Zhu error estimator for 2d elliptic problems, Numerical Mathematics and Advanced Applications 2009, edited by G. Kreiss, P. Lotstedt, A. Målqvist, and M. Neytcheva, pp. 645-653, Springer Berlin Heidelberg, 2010.

Micheletti, S., Perotto, S. and Farrell, P.: A recovery-based error estimator for anisotropic mesh adaptation in CFD, SEMA J., 50(1), 115-137, 2010.

Pepper, D. and Stephenson, D.: An adaptive finite-element model for calculating subsurface transport of contaminant, Ground Water, 33(3), 486-496, 1995.

Pepper, D. W., Chen, Y. T. and Li, L.: Subsurface transport modeling using adaptive finite elements, Water Pollution 99 paper presented at 5th International Conference on Water Pollution: Modeling, Measuring, and Prediction. Lemnos, Greece, 1999.

Porta, G. M., Bijeljic, B., Blunt, M. J. and Guadagnini A.: Continuum-scale characterization of solute transport based on pore-scale velocity distributions, Geophys. Res. Lett., 42, 7537-7545, 2015.

Porta, G., Chaynikov, S., Riva, M. and Guadagnini, A.: Upscaling solute transport in porous media from the pore scale to dual-and multicontinuum formulations, Water Resour. Res., 49, 2025-2039, 2013.

Porta, G., Perotto, S. and Ballio, F.: Anisotropic mesh adaptation driven by a recovery-based error estimator for shallow water flow modeling, Int. J. Numer. Methods Fluids, 70(3), 269–299, 2012a,

Porta, G., Perotto, S. and Ballio, F.: A space-time adaptation scheme for unsteady shallow water problems, Math. Comput. Simul., 82(12), 2929–2950, 2012b.

Quarteroni, A., Sacco, R. and Saleri, F.: Numerical Mathematics vol. 37, Springer, Berlin, 2007.

Rubin, Y., Sun, A., Maxwell, R. and Bellin, A.: The concept of block-effective macrodispersivity and a unified approach for grid-scale- and plume-scale-dependent transport, J. Fluid Mech., 395, 161-180, 1999.

Rubin, Y.: Applied Stochastic Hydrology, Oxford University press, 391p, 2003.

Saaltink, M. W., Carrera, J. and Olivella, S.: Mass balance errors when solving the convective form of the transport equation in transient flow problems, Water Resour. Res., 40, W05107, 2004.

Wood, B. D., Cherblanc, F., Quintard, M. and Whitaker, S.: Volume averaging for determining the effective dispersion tensor: Closure using periodic unit cells and comparison with ensemble averaging, Water Resour. Res., 39(8), 1210, 2003.

Younes, A. and Ackerer, P.: Solving the advection-diffusion equation with the Eulerian-Lagrangian localized adjoint method on unstructured meshes and non uniform time stepping, J. Comput. Phys., 208(1), 384-402, 2005.

Younes, A., and Ackerer, P.: Empirical versus time stepping with embedded error control for density-driven flow in porous media, Water Resour. Res., 46, W08523, 2010.

Zienkiewicz, O. C. and Zhu, J. Z., 1987. A simple error estimator and adaptive procedure for practical engineering analysis. Int. J. Numer. Methods Eng. 24 (2), 337-357.

3 Dispersion for stable variable density flow, within heterogeneous porous media

We present an investigation on the nature of the processes underpinning the reduced spreading documented in stable variable density flow through heterogeneous porous media in contrast to constant density flow. We do so by decomposing velocity and pressure as the sum of a stationary (or static) and a dynamic component. The former corresponds to the solution of the constant density flow problem, while the latter accounts for the effects induced by density variability. We focus on a stable flow configuration and analyse the longitudinal spread of saltwater injected from the bottom of a heterogeneous porous medium column initially fully saturated by freshwater. We apply a perturbation expansion approach and derive the equations satisfied by section-averaged concentrations and by their ensemble mean values. These formulations are respectively characterized by the appearance of a *single realization* and *ensemble* dispersive flux, which we analyze through the formulations of appropriate closure equations. Semi-analytical and numerical solutions of the two types of averaged equations as well as of the associated closure formulations are evaluated and analyzed. Our formulations and associated results enable us to discriminate the relative importance on the density-driven solute displacement associated with (*a*) the covariance of the heterogeneous permeability, (*b*) the cross-covariance between permeability and concentration, which is in turn linked to the coupling of the flow and transport problems, and (*c*) the cross-covariance between the *dynamic* and *stationary* velocity fields. This work has been conducted in collaboration with Prof. Jesùs Carrera (GHS UPC-CSIC, IDAEA, CSIC, Barcelona, Spain)

3.1 Introduction

Proper understanding and quantification of the feedback between space-time variability of fluid density and the ensuing flow and transport is relevant for a variety of environmental and industrial problems. These include, e.g., coastal aquifer management (e.g. Abarca et al., 2007; Dentz et al., 2006; Held et al., 2005; Kerrou and Renard, 2010; Riva et al., 2015; Werner et al., 2013;), enhanced oil recovery strategies (e.g. Hagoort, 1980; Monger et al., 1991; Di Donato et al., 2007; Spagnuolo et al., 2015, 2016;), design and engineering of safe CO_2 disposal protocols (e.g. Woumeni and Vauclin, 2006; Dentz and Tartakovsky, 2009; Pool et al., 2013;) as well as the quantification of solute transport in fractured media in the context of site remediation and/or groundwater source protection (e.g. Tenchine and Gouze, 2005; Bouquain et al., 2011;). In this framework, the effect of density contrasts between miscible fluids has been seen to influence the spreading of contaminants both along directions parallel (e.g. D'angelo et al., 2008; Flowers and Hunt, 2007; Menand and Woods, 2005; Zoia et al., 2009;); and normal to mean flow velocity (e.g. OOstrom et al., 1992a, b; Simmons et al., 2001; Diersch and Kolditz, 2002; Welty et al., 2003; Nick et al., 2009; Konz et al., 2009; Woumeni and Vauclin, 2006; Alkindi et al., 2011; Strake et al., 2006;). A notable feature is that settings associated with variable density are characterized by reduced spreading with respect to constant density for stable configuration (where the light fluid lies above the dense fluid), and by enhanced spreading for unstable configurations.

Reduced spreading is typically attributed to the stabilizing effects associated with variable density. A local increase in velocity causes a perturbation in the concentration front that does not affect velocities in constant density settings, but the ensuing density increase drags down the fluid, resulting in a reduction of the velocity surge and of the overall spreading. This stabilizing effect has been documented in nearly homogenous (e.g. Buès and Aachib, 1991; Hassanizadeh and Leijnse, 1995; Jiao and Hötzl, 2004; Kempers and Haas, 1994; Moser, 1995; Watson et al., 2002;) as well as in heterogeneous (e.g. Loggia et al., 1996; Kretz et al., 2003;) porous media.

The complexity of the pore scale geometry and flow patterns ultimately governs the variability of solute concentration (e.g. Rhodes et al., 2009; Siena et al., 2014;). A common practice to address this complexity relies on decomposing the velocity and concentration fields in terms of the sum of a mean value and a zero-mean fluctuation (perturbation). This decomposition is non-unique and can be performed by considering spatial (e.g. Bianchi Janetti et al., 2015; Davit et al., 2013; Porta et al., 2015; Whitaker, 1999;), temporal (e.g. Bolster et al., 2009; Dentz and Carrera, 2005; Pool et al., 2013;) or ensemble (e.g. Cushman et al., 2002; Dongxiao, 2002; Morales et al., 2006a, b; Naff, 1990; Neuman and Taratkovsky, 2009;) averaging techniques. Regardless the nature of this decomposition, a key research goal is the formulation and solution of an effective model satisfied by a representative (mean/average) concentration. A term which is commonly denoted as dispersive flux, and is given by the divergence of the average of the cross product between velocity and concentration fluctuations, typically arises in such effective models. Even if, under some conditions, the dispersive flux can be written in a Fickian format, e.g. introducing macrodisperion coefficients (Gelhar and Axness, 1983), its nature is fundamentally advective since it describe the advective transport component of the effective concentration due to concentration and velocity fluctuations.

Here, we focus on the interaction between the effects of (*a*) buoyancy and (*b*) heterogeneity induced by the spatial variability of permeability, on density-dependent flow and transport behavior. Our key aim is to provide a physically-based quantitative analysis of the above documented reduction of the width of the dispersion zone stable flow configurations. The essence of the issue is summarized in Fig. 3.1, which is obtained using the procedures described in Section 3.2. Salt water is continuously injected within a porous domain initially saturated with fresh water and whose permeability, $k(\mathbf{x})$, is modeled as a random function. A . realization of $Y(\mathbf{x}) = \ln k(\mathbf{x})$ is displayed in Figure 3.1a. Figures 3.1b, 3.1c, and 3.1d display a snapshot of solute concentration, for three different values of the density contrast, quantified through the gravity number, N_g, which reflects the relative importance of buoyancy and viscous forces (see Section 3.2.1 for additional details). These plots highlight two major patterns: (*a*) the progressive reduction of the width of the dispersion zone and (*b*) the tendency of the concentration profile to resemble a configuration typical of homogenous media for increasing values of N_g, i.e., strength of the stabilizing effect. It is then natural to ask: (*a*) Can we detect the basic physical mechanisms at the heart of this behavior? (*b*) What is the feedback between the effects of buoyancy and physical heterogeneity of the domain in the concentration distribution? and (*c*) Can we quantify the relative importance of buoyancy and permeability heterogeneity on the pattern of the spreading process observed? These are precisely the key questions we address in this work.

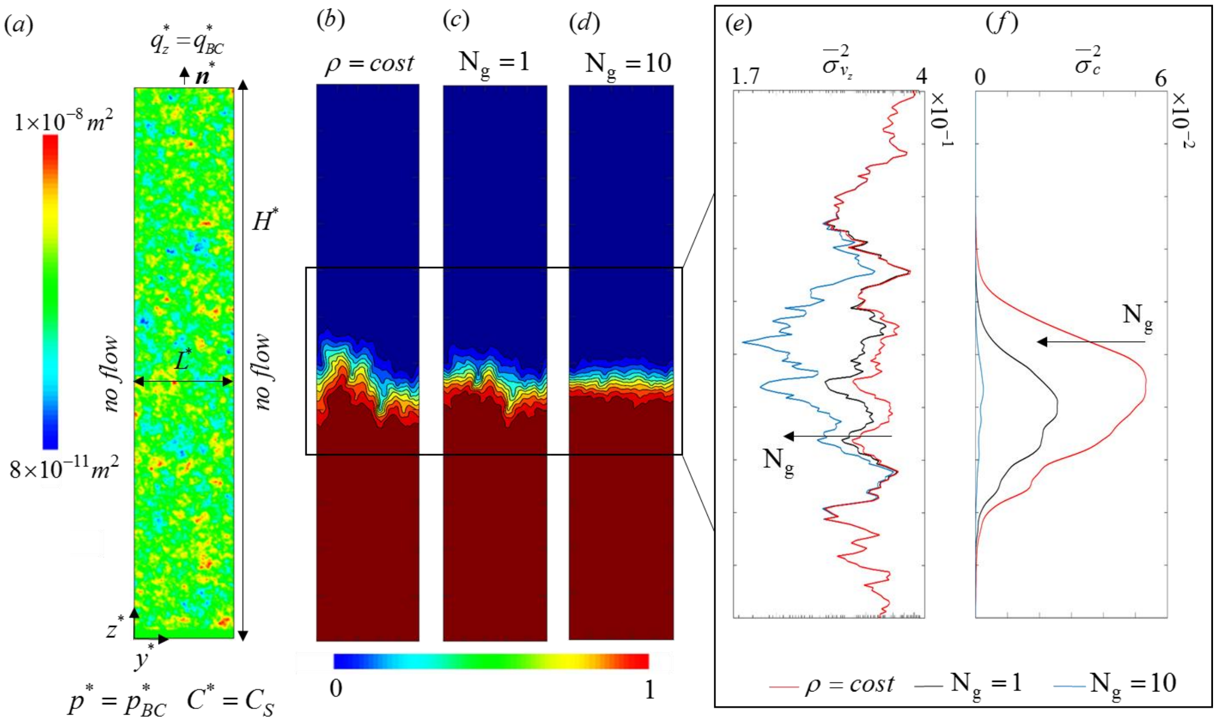

Figure 3.1. (*a*) Flow and transport problem set-up. Sample contour plot of the permeability field for $\sigma_Y^2 = 0.5$. Sample contour plots of normalized concentration for (*b*) constant density, N_g = (*c*) 1 and (*d*) 10. Magnification at solute front of (*e*) spatial variance of the vertical velocity, i.e. $\overline{\sigma}^2_{v_z}$, (*f*) spatial variance of concentration, i.e. $\overline{\sigma}^2_C$.

Previous studies have addressed these questions. Hassanizadeh and Lejnse (1995) proposed an extension of Fick's law to model the local dispersive flux, i.e. the dispersive flux appearing in the upscaled (from pore- to continuum-scale) transport equation. The authors modelled the local dispersive flux as a nonlinear function of the local concentration gradient through the introduction of a coefficient of proportionality, termed β by the authors. This model has been shown to accurately reproduce a set of laboratory experiments in homogenous media under a stable configuration (Watson et al., 2002;), as well as breakthrough curves obtained from a suite of two-dimensional numerical simulations in heterogeneous media (Landman et al., 2007;). However a clear and unambiguous link between the parameter β and the underlying physical processes is still lacking. Watson et al. (2002) and Landman et al. (2007b) observed that β depends on the mean flow rate.

Landman et al. (2007) observed also a clear dependence of β on the fluid density contrast in heterogeneous formation. Landman et al. (2007) also report two additional models based on homogenization theory: one from continuum-continuum (Darcy) scale, one from pore to continuum scale (see also Demidov, 2006;). Both models render a good reproduction of the numerical results of Landman et al. (2007b) provide relative simple nonlinear relationship between the dispersive flux and the concentration gradient of the section-averaged concentration.

Welty and Gelhar (1991) derive an analytical expression for the asymptotic (long-time) longitudinal macro-dispersivity, under the assumption that the velocity field is a second-order stationary random process. The authors show that macro-dispersion is a function of the gradient of the ensemble mean concentration, flow rate, displacement distance, gravity, fluid density and viscosity and log permeability correlation scale and variance. However, as we highlight in section 3.2, the velocity field cannot be stationary in a variable density problem, due to the coupling between flow and transport equations.

The objective of this work is precisely to obtain an upscaled equation for transport in a variable density context and, specifically, to highlights the factors and mechanism which control the dispersive flux, in order to explain the reduced solute dispersion that is observed under stable displacement conditions.

3.2 Methodology

We start by deriving the equation satisfied by section-averaged concentrations in the setting of Figure 3.1, which naturally leads to an effective one-dimensional model. This equation includes a term, called *single realization* dispersive flux, which enables us to embed the effect of the spatial heterogeneity of $\boldsymbol{k}$ in a simple one-dimensional (along the mean flow direction). The *single realization* dispersive flux can be related to the temporal derivative of the second centered spatial moment of concentration gradients, which can in turn be viewed as a measure of the width of the spreading zone (e.g. Bolster et al., 2009). Then, we leverage on this one-dimensional (section-averaged) model and average it in the probability space, to take into account our incomplete knowledge of the permeability field, *k*. The ensuing model includes an *ensemble* dispersive flux that enables us to encapsulate the effect of the uncertainty in the spatial arrangement of $\boldsymbol{k}$ on the mean concentration distribution.

An important point in common between the works of Gelhar and Welty (1991), Landam et al (2007a, b) and our work is that the stabilizing buoyancy effects take place because the heterogeneity of the medium, this observation being lacking in the study of Hassanizadeh and Lejnse (1995). In this context, Landman et al. (2007a) report a reduction of the effectiveness of the stabilizing effects as the permeability heterogeneity increase. We seek to provide a theoretical analysis supporting and quantifying this behavior.

3.2.1 Flow and transport Model

Fluid flow in porous media is described by conservation of mass and Darcy's law,

$$\frac{\partial \phi \rho^*}{\partial t^*} + \nabla^* \cdot \left(\rho^* \boldsymbol{q}^* \right) = 0 \ ; \ \boldsymbol{q}^* = -\frac{\boldsymbol{k}^*}{\mu^*} \cdot \left(\nabla^* p^* + \rho^* g^* \nabla^* z^* \right) \qquad , \qquad (3.1)$$

where ρ^* [ML^{-3}], μ^* [M T^{-1} L^{-1}] and p^* [M T^{-2} L^{-1}] are fluid density, viscosity, and pressure, respectively; g^* [LT^{-2}] is the gravitational acceleration; z^* [L] is elevation; $\boldsymbol{q}^*$ [L T^{-1}] is Darcy's flux; $\boldsymbol{k}^*$ [L^2] is the permeability tensor and ϕ [-] is porosity.

Solute transport is governed locally by the advection-dispersion equation

$$\frac{\partial \left(\phi \rho^* C^* \right)}{\partial t^*} + \nabla^* \cdot \left(\rho^* \boldsymbol{q}^* C^* \right) - \nabla^* \cdot \left(\phi \rho^* \boldsymbol{D}^* \cdot \nabla^* C^* \right) = 0 \qquad . \qquad (3.2)$$

Here C^* [-] is the solute concentration, and $\boldsymbol{D}^*$ [L T^{-2}] is the local dispersion tensor, modeled as

$$\boldsymbol{D}^* = \left(D_m^* + \alpha_T{}^* \left| \boldsymbol{v}^* \right| \right) \mathbf{I} + \left(\alpha_L{}^* - \alpha_T{}^* \right) \frac{\boldsymbol{v}^* \boldsymbol{v}^*}{\left| \boldsymbol{v}^* \right|} \qquad , \qquad (3.3)$$

where D_m^* is the molecular diffusion; $\alpha_T{}^*$ and $\alpha_L{}^*$ [L] respectively are transverse and longitudinal dispersivities; $\mathbf{I}$ is the identity matrix and $\boldsymbol{v}^*$ [L T^{-1}] is the mean fluid velocity defined as

$$\boldsymbol{v}^* = \boldsymbol{q}^* / \phi \qquad . \qquad (3.4)$$

In the following we neglect D_m^* in (3.3) because its contribution to the dispersion tensor is usually negligible (see Landman et al., 2007a).

We focus on a stable density-dependent problem within a heterogeneous porous media, Ω, of width, W^* [L], and height, H^* [L], depicted in Fig. 3.1. In our set-up Darcy's flux $\boldsymbol{q}^*$ has components q_z^* and q_y^* along the vertical z^*- and horizontal y^*- directions, respectively (see Fig. 3.1). Initially, the column is filled by freshwater with density ρ_f^* . At time $t \geq 0$ seawater with density ρ_s^* and concentration C_s is injected at the bottom of the column, $z^* = 0$. Remaining boundary conditions are: (1) no flow at $y^* = 0, W^*$; (2) constant pressure $p^* = p_{BC}{}^*$ at $z^* = 0$; (3) prescribed vertical flux, $q_z{}^* = q_{BC}{}^*$, and solute mass flux $\left(\boldsymbol{q}^* C^* - \boldsymbol{D}^* \cdot \nabla^* C^*\right) \cdot \boldsymbol{n}^* = q_{BC}{}^* C^*$ at $z^* = H^*$, where $\boldsymbol{n}^*$ is a unit vector pointing outwards.

Closure of the system (3.1)–(3.4) is obtained by assuming viscosity to be constant and expressing ρ^* as a linear function of C^* (e.g. Abarca et al., 2007)

$$\rho^* = \rho_f^* + \beta^* C^* \quad , \tag{3.5}$$

where $\beta^* = \left(\rho_s^* - \rho_f^*\right) / C_s$. In the following we assume isotropic dispersivity, $\alpha_T{}^* = \alpha_L{}^* = \alpha^*$, so (3.3) reduces to

$$\boldsymbol{D}^* = \alpha^* \, |\boldsymbol{v}^*| \, \mathbf{I} \quad . \tag{3.6}$$

The problem lacks a well-defined characteristic distance because L^* and W^* will be assumed large enough to not affect the solution. Therefore, we adopt $\sqrt{\tilde{k}^*}$, k^* being the geometric mean of the permeability field, as characteristic distance, which leads to the following dimensionless quantities

$$\begin{gathered} y = \frac{y^*}{\sqrt{\tilde{k}^*}}; \quad z = \frac{z^*}{\sqrt{\tilde{k}^*}}; \quad \nabla = \sqrt{\tilde{k}^*} \nabla^*; \quad t = \frac{t^*}{\sqrt{\tilde{k}^*} / v_{z,BC}{}^*}; \quad \boldsymbol{q} = \frac{\boldsymbol{q}^*}{v_{z,BC}{}^*}; \quad \boldsymbol{v} = \frac{\boldsymbol{v}^*}{v_{z,BC}{}^*}; \\ \rho = \frac{\rho^*}{\Delta\rho^*}; \quad p = \frac{p^*}{p_c^*}; \quad \boldsymbol{k} = \frac{\boldsymbol{k}^*}{\tilde{k}^*}; \quad C = \frac{C^*}{C_s} \end{gathered} \tag{3.7}$$

with $\Delta\rho^* = \rho_s^* - \rho_f^*$, $v_{z,BC}{}^* = q_{BC}{}^* / \phi$ and p_c^* being a characteristic pressure. Using (3.7), eqs. (3.1), (3.2), (3.5) and (3.6) can be written in dimensionless form as

$$\frac{\partial \phi \rho}{\partial t} + \nabla \cdot \left(\rho \boldsymbol{q}\right) = 0 \;\; ; \;\; \boldsymbol{q} = -\boldsymbol{k} \cdot \left(\mathrm{N}_p \nabla p + \mathrm{N}_g \rho \nabla z\right) \tag{3.8}$$

$$\rho\phi \frac{\partial C}{\partial t} + \rho \boldsymbol{q} \cdot \nabla C - \nabla \cdot \left(\rho \phi \boldsymbol{D} \cdot \nabla C\right) = 0 \tag{3.9}$$

$$\rho = \rho_f + C \qquad \text{with } \rho_f = \rho_f^* / \Delta\rho \tag{3.10}$$

$$\boldsymbol{D} = \frac{|\boldsymbol{v}|}{\mathrm{Pe}} \mathbf{I} \tag{3.11}$$

where $\mathrm{N}_p = \sqrt{\tilde{k}^*} p_c^* / \mu^* v_{z,BC}{}^*$, $\mathrm{Pe} = \sqrt{\tilde{k}^*} / \alpha^*$ and $\mathrm{N}_g = \Delta\rho^* \tilde{k}^* g^* / \mu^* v_{z,BC}{}^*$ are, respectively, dimensionless group for the pressure, Péclet and gravity numbers. The latter expresses the intensity of buoyancy over viscosity effects. In the following, we set the characteristic pressure p_c^* such that $\mathrm{N}_p = 1$. Note that such choice is allowed, since the problem is independent from the value of pressure but is its gradient that matter.

3.2.2 Numerical solution

We solve the flow and transport problem described above by means of the widely tested code SUTRA (Voss and Provost, 2002;) to evaluate the relative importance of all the terms in our subsequent derivations and to assess the validity of the approximations involved in our analytical derivations. Heterogeneity is modeled by treating the dimensionless permeability $\boldsymbol{k}$ as an isotropic random field $\boldsymbol{k} = \exp(Y(y,z))\mathbf{I}$, where $Y(y, z)$ is a zero-mean second order stationary random process characterized by an isotropic exponential covariance function

$$C_{YY}(\boldsymbol{r}^*) = \sigma_Y^2 \exp(-|\boldsymbol{r}^*|/l^*) \tag{3.12}$$

$\boldsymbol{r}^*$ [L], σ_Y^2 [-] and l^* [L] being the separation vector between two points, variance and correlation length of *Y*, respectively. In the numerical simulation we set $\phi = 0.35$, k^* = 10^{-9} m^2, H^* = 0.3 m, D^* = 0.05 m (i.e. D^*/H^* = 6; $H^*/\sqrt{k}$ ≈ 9500; $D^*/\sqrt{k^*}$ ≈ 1600), $l = l^*/\sqrt{k^*}$ = 79 (i.e., H^*/l^* =120; D^*/l^* = 20), $\mathrm{Pe} = 0.25$ ($l^*/\alpha^* = 20$) and $\rho_f = 40$.

The domain is discretized by a regular mesh of square elements. We performed a set of preliminary simulations aimed at testing the influence of space and time grid discretization on the quantities of interest (namely, horizontal mean concentration, *single realization* and *ensemble* dispersive flux and velocity covariance). Accurate results at an affordable CPU time have been obtained with a spatial grid formed by 100 × 600 elements (i.e., $\Delta z^* = \Delta y^* = 0.0005m$) and dimensionless time step $\Delta t = 2.8$. In this work we investigate four scenarios characterized by diverse levels of heterogeneity of the permeability field , i.e. $\sigma_Y^2 = (0.1; 0.5)$, combined with diverse intensity of buoyancy effects quantified by $\mathrm{N_g} = (0.1;1)$. Our numerical result are ground on 1000 Monte Carlo (MC) numerical simulations for each parameter set investigated. Moreover, we derive, at second order in the permeability fluctuations, semi-analytical solution for the quantities of interest described in Section 3.2.4. Note that the level of heterogeneity investigated in this chapter are clearly lower respect to the level investigated in chapter 2. This choice has been dictated by our main interest in the understanding of the basic mechanisms at the origin of the solute spread reduction for stable variable density flow within heterogeneous porous media. Anyway, the reader can note that our setting allow to grasp the effects of varying σ_Y^2 and/or $\mathrm{N_g}$, in terms solute spreading behavior, enhancing our understanding of the system behavior as its heterogeneity level increase and of the resulting effectiveness of the stabilizing forces (see Section 3.3), .

3.2.3 Section Average Concentration

Point concentration values $C(y,z,t)$ are seldom available from laboratory or field experiments, Boso et al. (2013), while section-average concentration profiles can be monitored (e.g. Ciriello et al., 2013; Gramling et al., 2002; Landman et al., 2007a; Menand and Woods, 2005;). Therefore, we focus on the cross-section (or horizontal) average concentration, $\overline{C}(z,t)$, where the overbar indicates the horizontal averaging operator defined as

$$\overline{\Theta} = \frac{1}{W}\int_0^W \Theta(y)dy \quad , \tag{3.13}$$

where Θ is any generic quantity (a parameter or a state variable). In the following, we derive the equation satisfied by $\overline{C}(z,t)$ invoking the Boussinesq approximation (e.g. Dentz et al., 2006; Diersch and Kolditz, 2002;), i.e. assuming that $\nabla \cdot \boldsymbol{q} >> \frac{\phi}{\rho}\frac{\partial \rho}{\partial t} + \boldsymbol{q} \cdot \frac{\nabla \rho}{\rho} \approx \nabla \cdot \left(\rho \phi \boldsymbol{D} \cdot \nabla C\right)$. Under this hypothesis (3.8) and (3.9) can be simplified as

$$\nabla \cdot \boldsymbol{v} = 0; \quad \boldsymbol{q} = -\boldsymbol{k} \cdot \left(\nabla p + \mathrm{N_g} \rho \nabla z\right) \quad , \tag{3.14}$$

$$\frac{\partial C}{\partial t} + \boldsymbol{v} \cdot \nabla C - \nabla \cdot \left(\boldsymbol{D} \cdot \nabla C\right) = 0 \quad . \tag{3.15}$$

Note that $\boldsymbol{k}$ is spatially variable and all remaining variables (i.e., $\boldsymbol{v}$, $\boldsymbol{q}$, p, ρ, C and $\boldsymbol{D}$) are both the spatially and temporally variable.

We decompose each variable in (3.14)-(3.15) as the sum of a horizontal spatial mean and a (spatial) zero-mean fluctuation (along the y-direction), i.e.

$$p=\overline{p}+p';\; C=\overline{C}+C';\; \boldsymbol{k}=\mathbf{I}+k'\mathbf{I};\; \rho=\overline{\rho}+\rho';\; \boldsymbol{v}=\overline{\boldsymbol{v}}+\boldsymbol{v}';\boldsymbol{D}=\overline{\boldsymbol{D}}+\boldsymbol{D}' \tag{3.16}$$

where it should be clear that horizontal averages depend on (z,t), while fluctuations depend on (y,z,t). Further, according to (3.11)

$$\overline{\rho}=\rho_f+\overline{C};\quad \rho'=C' \quad . \tag{3.17}$$

At second order in the perturbations, horizontal average concentration, $\overline{C}(z,t)$, satisfies (see A.3.4 in Appendix A.3),

$$\frac{\partial\overline{C}}{\partial t}+\frac{\partial\overline{C}}{\partial z}-\frac{1}{\mathrm{Pe}}\frac{\partial^2\overline{C}}{\partial z^2}+\frac{\partial\overline{v_z'C'}}{\partial z}=0 \quad , \tag{3.18}$$

where $\overline{v_z'C'}$ is the *single realization* dispersive-flux which reads (see A.3.11a)

$$\overline{v_z'C'}=-\int_0^t\int_0^H \overline{v_z'(z,t)v_z'(\xi,\tau)}\; G_z^T(z,t,\xi,\tau)\frac{\partial\overline{C}(\xi,\tau)}{\partial\xi}d\xi d\tau \quad . \tag{3.19}$$

Here $G_z^T(z,t;\xi,\tau)$ is the deterministic Green's function introduced in (A.3.10) and $\overline{v'_z(z,t)v'_z(\xi,\tau)}$, defined in (A.3.11b), is the horizontal mean of $v'_z(y,z,t)v'_z(y,\xi,\tau)$, i.e. the product between vertical velocity fluctuations evaluated at the same horizontal location and diverse vertical positions and times. The term $\overline{v_z'C'}$ in (3.18) embeds the effect of permeability fluctuations on the section average concentration. $\overline{C}(z,t)$ (e.g. de Barros and Dentz, 2015;).

In order to highlight the effect of density variations on $C(y,z,t)$, we decompose the velocity fluctuations vector as the sum of (*a*) a *stationary* component, $\boldsymbol{v}^{st}{}'(z,y)$, which corresponds to the solution of (3.14) with constant density, $\rho=\rho_f$, and a *dynamic* component, $\boldsymbol{v}^{dy}{}'(z,y,t)$, accounting for the stabilizing buoyancy effects due to density variations, i.e.

$$\boldsymbol{v}'(y,z,t)=\boldsymbol{v}^{st}{}'(y,z)+\boldsymbol{v}^{dy}{}'(y,z,t) \quad . \tag{3.20}$$

The expressions of the vertical components of $\boldsymbol{v}^{st}{}'(z,y)$ and $\boldsymbol{v}^{dy}{}'(z,y,t)$ are derived in Appendix C.3, (C.3.10)-(C.3.11). Here, we briefly elucidate the benefit of the proposed decomposition (3.20) by focusing on a simple heterogeneous domain formed by a single semi-circular inclusion of high permeability (in red in Fig.s 3.2*a*-3.2*c*), $\boldsymbol{k}(y,z)=10\mathbf{I}$ within a uniform porous media with $\boldsymbol{k}(y,z)=\mathbf{I}$. The remaining relevant key dimensionless quantities are set as $\mathrm{N_g}=0.35$, Pe = 0.25, ϕ = 0.35, ρ_f = 40. Figures 3.2*a*, 3.2*b* and 3.2*c* respectively depict $\boldsymbol{v}^{st}{}'(y,z)$, $\boldsymbol{v}^{dy}{}'(y,z,t)$ and $\boldsymbol{v}'(y,z,t)$ at t = 664. The total velocity field $\boldsymbol{v}(y,z,t)$ is reported in Fig. 3.2*d* together with the concentration field. As an additional term of comparison, Fig. 3.2*e* depicts $\boldsymbol{v}(y,z)$ and $C(y,z,t)$ computed for a tracer solute with $\rho=\rho_f$ (i.e., with constant density) at the same dimensionless time. Figures 3.2*d* and 3.2*e* clearly show that the dispersion of the solute decreases when density effects are considered. The reduction of solute dispersion for the stable variable density scenario is strictly linked to the resulting velocity distribution. Figure 3.2*a* highlights that vertical *stationary* flow fluctuations, $v_z^{st}{}'(y,z)$, are positive in the high permeability zone causing the solute to advance within this area.

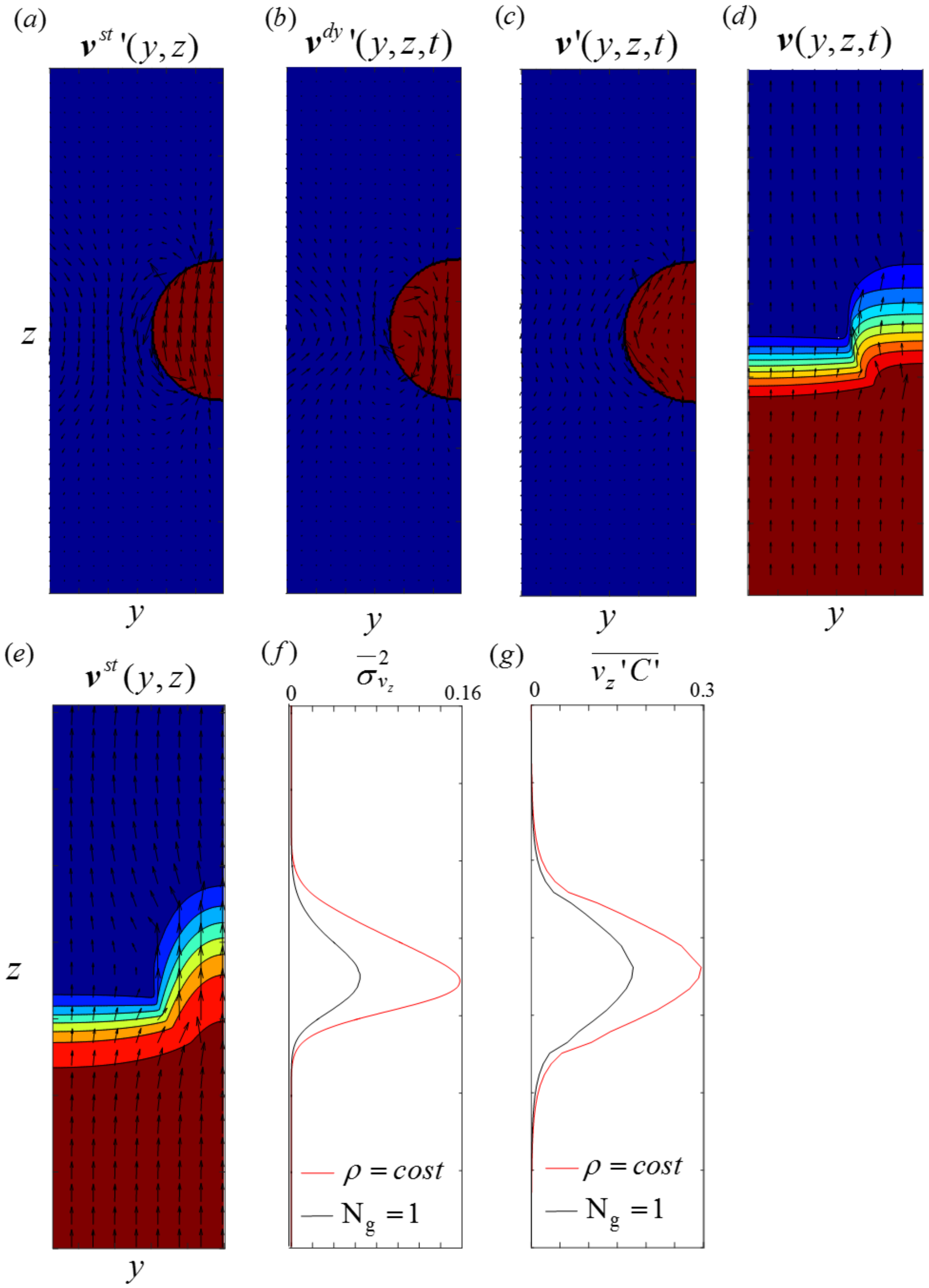

Figure 3.2. (*a*) $\boldsymbol{v}'^{st}(y,z)$, (*b*) $\boldsymbol{v}'^{dy}(y,z,t)$ and (*c*) $\boldsymbol{v}'(y,z,t)$ for the variable density flow problem. The underlying $\boldsymbol{k}(y,z)$ field is also reported. Velocity, $\boldsymbol{v}(y,z,t)$, and concentration, $C(y,z,t)$, for (*d*) variable density and (*e*) tracer case. (*f*) Vertical distribution of the variance of vertical velocity, i.e. $\overline{\sigma}^2_{v_z}$, and (*g*) *single realization* dispersive flux (3.19), i.e. $\overline{v_z'C'}$ for the tracer (red curve) and variable density (black curve) case. All the curves have been evaluated at t = 664.

This generates positive density fluctuations, $\rho'(y,z,t)$, which, due to the buoyancy term, trigger negative vertical *dynamic* flow fluctuations, $v_z^{dy}{}'(y,z,t)$ (see Fig. 3.2*b*). The opposite occurs in the portion of the domain adjacent to the high permeability inclusion. Since $v_z^{st}{}'(y,z)$ and $v_z^{dy}{}'(y,z,t)$ have opposite signs the total vertical flow fluctuation $v_z{}'(y,z,t)$ is smaller than its constant density counterpart (compare Fig. 3.2*c* and Fig. 3.2*a*). Ultimately, the velocity field at the solute front is more uniform in the variable density problem than in the tracer case (compare the velocity fields in Figs. 3.2*d* and 3.2*e*) causing a less solute dispersion in the former than in the latter case. This observation is further supported by Fig. 3.2*f* where the vertical distribution of the variance of the vertical velocity for the tracer case, i.e. $\overline{\sigma}^2_{v_z^{st}}(z) = \overline{v_z^{st}{}'(z)^2}$, is compared against the counterpart evaluated for the variable density case, $\overline{\sigma}^2_{v_z}(z,t) = \overline{v_z{}'(z,t)^2}$.

Figure 3.2*g* reports the *single realization* dispersive flux (3.19) computed for the tracer (red curve) and the variable density (black curve) case. One can clearly note the reduction of the *single realization* dispersive flux for the variable density scenario. The basic mechanisms highlighted in this section for a relatively simple heterogeneous configuration are at the bases of the observed reduction in solute spreading observed for stable variable density flow versus the outcomes relative to tracer cases within heterogeneous porous media. In section 3.3 we will further investigate this phenomenon for randomly heterogeneous porous media.

3.2.4 Ensemble Analysis

Here we treat *k* as a second order stationary random field and we derive the equation satisfied by the ensemble mean of the section average concentration, $\left\langle \overline{C}(z,t) \right\rangle$, where $\langle\ \rangle$ indicates the ensemble mean operator. This analysis allows us to link the statistical features of $\left\langle \overline{C}(z,t) \right\rangle$ to the ones of the permeability field. The equation satisfied by $\left\langle \overline{C}(z,t) \right\rangle$ results from ensemble averaging (3.18)

$$\frac{\partial\langle\overline{C}\rangle}{\partial t} + \frac{\partial\langle\overline{C}\rangle}{\partial z} - \frac{1}{\mathrm{Pe}}\frac{\partial^2\langle\overline{C}\rangle}{\partial z^2} = -\frac{\partial\left\langle\overline{v_z{}'C'}\right\rangle}{\partial z} \qquad , \tag{3.21}$$

where $\left\langle\overline{v_z{}'C'}\right\rangle$ is the *ensemble* dispersive-flux defined in (B.3.6) as

$$\left\langle \overline{v_z{}'(z,t)C'(z,t)} \right\rangle = -\int_0^t \int_0^H \left\langle \overline{v_z{}'(z,t)v_z{}'(\xi,\tau)}\ \right\rangle G_z^T(z,t,\xi,\tau)\, d\xi\, d\tau \frac{\partial\left\langle \overline{C}(z,t) \right\rangle}{\partial z} \qquad . \tag{3.22}$$

Here $\left\langle \overline{v'_z(z,t)v'_z(\xi,\tau)} \right\rangle$ is the horizontal spatial mean of $\left\langle v'_z(y,z,t)v'_z(\eta = y,\xi,\tau) \right\rangle$ which is the covariance between the vertical velocity fluctuation at *z* at time *t*, and its counterpart evaluated at ξ at time τ, both at the same horizontal coordinate y. The *ensemble* dispersive flux takes into account the effect of the spatial heterogeneity of *k* in all the *ensemble* of realizations on the evaluation of the *ensemble* mean of the section average concentration. Note that, even if the *ensemble* dispersive flux as been localized both in space and time, a Fickian-type expression characterized by a constant coefficient of dispersion can not be introduced since the results of the convolution between the horizontal average of the velocity covariance and the Green' function vary both in space and time. As discussed by Morales et al., (2006a, b), *ensemble* dispersive-flux does not quantify a physical spreading of $C(y,z,t)$, as the *single realization* dispersive flux does. It allows to accommodate the lack of knowledge of k, and therefore of the velocity field, on the prediction of $C(y,z,t)$ through $\langle \overline{C} \rangle$. Note that, due to the imposed boundary conditions for the flow and transport problems and under the validity of the Boussinesq' assumption, no additional uncertainty and artificial spreading (see e.g. de Barros and Dentz, 2015;) arise due to the variability of the center of mass of the solute fronts which is always the same for each single realization.

Equation (3.22) highlights the key role of velocity field statistics in controlling the ensemble dispersive flux. In Appendix D.3 we show that the velocity covariance, $\left\langle \overline{v'_z(z,t)v'_z(\xi,\tau)} \right\rangle$, can be decomposed as the sum of four terms, involving stationary and dynamic velocity fluctuations, as defined in (3.20). In particular, we obtain (see (D.3.12))

$$\left\langle \overline{v'_z(z,t)v'_z(\xi,\tau)} \right\rangle = \left\langle \overline{v_z^{st}{}'(z)v_z^{st}{}'(\xi)} \right\rangle + \left\langle \overline{v_z^{st}{}'(z)v_z^{dy}{}'(\xi,\tau)} \right\rangle + \left\langle \overline{v_z^{dy}{}'(z,t)v_z^{st}{}'(\xi)} \right\rangle + \left\langle \overline{v_z^{dy}{}'(z,t)v_z^{dy}{}'(\xi,\tau)} \right\rangle =$$

$$= \mathbf{A}\left\{ \left\langle \overline{Y(z)Y(\xi)} \right\rangle \right\} + \frac{\mathrm{N_g}}{\phi}\mathbf{B}\left\{ \left\langle \overline{Y(z)C'(\xi,\tau)} \right\rangle \right\} + \frac{\mathrm{N_g}}{\phi}\mathbf{C}\left\{ \left\langle \overline{C'(z,t)Y(\xi)} \right\rangle \right\} + \left(\frac{\mathrm{N_g}}{\phi} \right)^2 \mathbf{D}\left\{ \left\langle \overline{C'(z,t)C'(\xi,\tau)} \right\rangle \right\} , \tag{3.23}$$

where $\mathbf{A}\{\ \}$, $\mathbf{B}\{\ \}$, $\mathbf{C}\{\ \}$, $\mathbf{D}\{\ \}$ are operators defined in Appendix D.3 (see, (D.3.8)-(D.3.11)). Equation (3.23) highlights that while the horizontal spatial mean of *stationary-stationary* term, $\left\langle \overline{v_z^{st}{}'(z)v_z^{st}{}'(\xi)} \right\rangle$, depends on the covariance of the log-permeability field, both *stationary-dynamic*, $\left\langle \overline{v_z^{st}{}'(z)v_z^{dy}{}'(\xi,\tau)} \right\rangle$, and *dynamic-stationary*, $\left\langle \overline{v_z^{dy}{}'(z,t)v_z^{st}{}'(\xi)} \right\rangle$, counterparts depends on the cross covariance between permeability and concentration $\left\langle \overline{Y(z)C'(\xi,\tau)} \right\rangle$ and quasi-linearly proportionality respect to $\mathrm{N_g}$ (note that $\left\langle \overline{Y(z)C'(\xi,\tau)} \right\rangle$ depends on $\mathrm{N_g}$, see (E.3.5)), while the *dynamic-dynamic* component, $\left\langle \overline{v_z^{dy}{}'(z,t)v_z^{dy}{}'(\xi,\tau)} \right\rangle$, is a function of the covariance of the concentration field, $\left\langle \overline{C'(z,t)C'(\xi,\tau)} \right\rangle$ and exhibit a quasi linearly proportionality respect to $\mathrm{N_g}^2$ (note that $\left\langle \overline{C'(z,t)C'(\xi,\tau)} \right\rangle$ depends on $\mathrm{N_g}$, see (F.3.6)). The main features of these covariances and related consequence on the solute transport behavior are analyzed in Section 3.3.1.

3.3 Results

The illustration of our results is organized as follows. We analyze the four velocity covariance terms appearing in (3.23) and identify the cause of reduction of the *ensemble* dispersive flux (3.22) in Section 3.3.1. We investigate the features of spatial mean of cross-covariance $\left\langle \overline{Y(z)C'(\xi,\tau)} \right\rangle$ between permeability and concentration fluctuations in Section 3.3.2.

In this section MC based results are presented for all the quantities. Moreover, we derive semi-analytical solution for all the quantities here presented (see Section 3.2 and Appendix A.3-F.3). Due to the coupled nature of the problem at hand, semi-analytical solutions of the quantities presented in Section 3.3 must be sought by a numerical and iterative procedure, e.g. $\left\langle \overline{v_z'(z,t)C'(z,t)} \right\rangle$ and $\partial\left\langle \overline{C}(z,t) \right\rangle / \partial z$ depends non linearly on each others (see (B.3.4)-(B.3.7)). Since the iterative strategy requires a computational effort, which is comparable with the one associated with the MC simulations, we take advantage of the MC resulting $\partial\left\langle \overline{C}(z,t) \right\rangle / \partial z$ to numerically resolve expressions detailed throughout Appendix A.3-F.3 and presented in follow. Main simplifications invoked in our semi-analytical derivation are: (*i*) the second order approximation in the log conductivity fluctuations, see (A.3.5), (C.3.1), (C.3.2); (*ii*) the use of 1D Green' function associated with the flow, see (D.3.4), and transport, see (A.3.10), problems even if the set-up is 2D; (*iii*) the use of already available analytical solution for the cross-covariance between log conductivity and hydraulic head derived in Dagan,(1984) for mean uniform steady-state flow in an infinite two-dimensional domain, see also (E.3.5), in the evaluation of the cross-covariance between permeability and concentration; (*iv*) the approximation of the contribution of $\left\langle \overline{v_z^{st}{}'(z)v_z^{st}{}'(\xi)} \right\rangle$ in (3.22) as $\sigma_Y^2 l$, which corresponds to the asymptotic value of macro dispersion derived in Gelhar and Axness, 1983. The main purpose of our semi-analytical derivation is not the correct prediction of $\left\langle \overline{C}(z,t) \right\rangle$, but to enrich and support our understating of the interplay between permeability and stabilizing effects at the origin of the solute spread reduction in case of stable flow within heterogeneous media. Our semi-analytical treatment help to grasp the impact of varying N_g and σ_Y^2 on the system behavior in terms of flow structure and resulting solute spreading.

Note that for exposition purpose, we present just our Monte Carlo numerical results for the four velocity covariance in (3.23) and $\left\langle \overline{Y(z)C'(\xi,\tau)} \right\rangle$, corresponding semi-analytical results compare well (details not shown) and support associated discussions. We present our numerical and semi-analytical results for the *ensemble* dispersive flux $\left\langle \overline{v'_z(z,t)C'(z,t)} \right\rangle$ and concentration covariance in Section 3.3.3.

3.3.1 Covariance of Vertical Velocity

The covariance of the vertical velocity components (3.23) plays a critical role in determining the mean solute transport behavior, as highlighted by (3.22). Here, we compare the results obtained for the constant and variable density scenarios to elucidate and quantify the origin of the reduced solute spreading documented in Fig. 3.1.

Figures 3.3*a* and 3.3*c* respectively depict the velocity variance, $\left\langle \overline{v_z{}'^2(z,t)} \right\rangle$, and the mean concentration gradient, $-\partial \left\langle \overline{C}(z,t) \right\rangle / \partial z$, for $\mathrm{N_g} = 1$ and $\sigma_Y^2 = 0.1$ at three dimensionless times $t_1 = 2.2 \times 10^3$, $t_2 = 4.4 \times 10^3$, and $t_3 = 6.6 \times 10^3$. Corresponding depictions are shown in Figs. 3.3*b* and 3.3*d* for $\mathrm{N_g} = 0.1$ and $\sigma_Y^2 = 0.1$, in Figs 3.3*e* and 3.3*g* for $\mathrm{N_g} = 1$ and $\sigma_Y^2 = 0.5$ and in Figs 3.3*f* and 3.3*h* for $\mathrm{N_g} = 0.1$ and $\sigma_Y^2 = 0.5$. Figure 3.3 confirms that vertical velocity is a non-stationary stochastic process. Non-stationary is clearly manifested at the solute fronts, where the salinity variations induce stabilizing buoyancy effects. The occurrence of the local minima in $\left\langle \overline{v_z{}'^2(z,t)} \right\rangle$ and peaks of $-\partial \left\langle \overline{C}(z,t) \right\rangle / \partial z$ peaks is evident for $\mathrm{N_g} = 1$. Decreasing the intensity of buoyancy effect (i.e. for $\mathrm{N_g} = 0.1$) and/or increasing the permeability field heterogeneity leads to a reduction of smallest and largest values of $\left\langle \overline{v_z{}'^2(z,t)} \right\rangle$ and $-\partial \left\langle \overline{C}(z,t) \right\rangle / \partial z$, respectively. We remark that the behavior of these two quantities is strongly related. Increasing $\left\langle \overline{v_z{}'^2(z,t)} \right\rangle$, the vertical velocity fluctuation $v_z{}'(y,z,t)$ increases as well as the solute spreading. This in turns involves a decrease of the mean concentration gradient, $-\partial \left\langle \overline{C}(z,t) \right\rangle / \partial z$, and therefore gives rise to less steep $\left\langle \overline{C}(z,t) \right\rangle$ profiles.

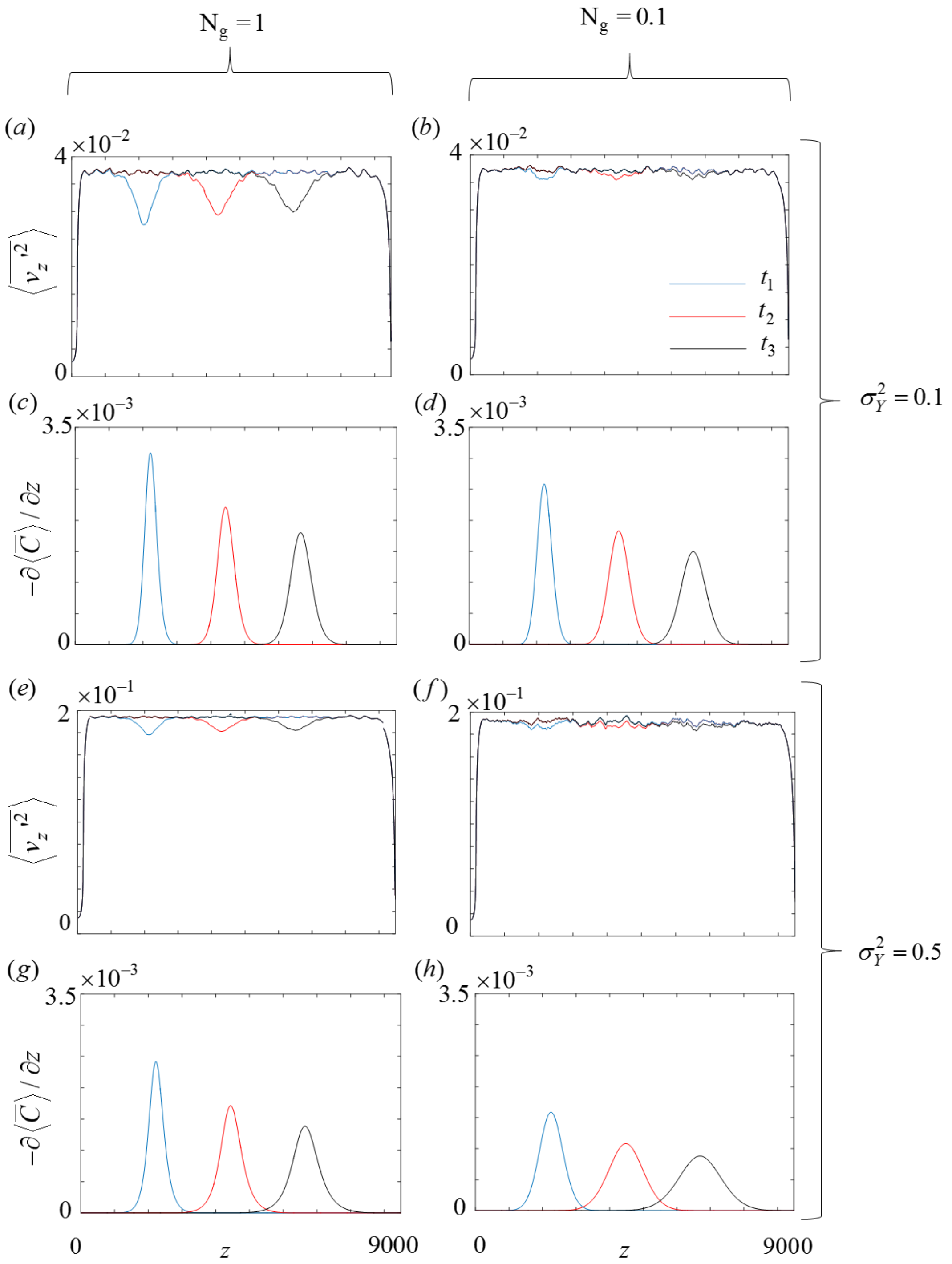

Figure 3.3. Section average vertical velocity variance , $\left\langle \overline{v_z{}'^2(z,t)} \right\rangle$, and gradient of ensemble concentration $-\partial \left\langle \overline{C}(z,t) \right\rangle / \partial z$ for (*a*), (*c*) for $\sigma_Y^2 = 0.1$ and $N_g = 1$, (*b*) , (*d*) $\sigma_Y^2 = 0.1$ and $N_g = 0.1$, (*e*), (*g*) $\sigma_Y^2 = 0.5$ and $N_g = 1$, (*f*) , (*h*) $\sigma_Y^2 = 0.5$ and $N_g = 0.1$. All curves have been evaluated at three dimensionless time t_1, t_2, t_3.

We have shown in (3.23) that the vertical velocity covariance, $\left\langle \overline{v_z'(z,t)v_z'(\xi,\tau)} \right\rangle$, can be decomposed as the sum of four components. Figure 3.4*a* depicts the dependence of $\left\langle \overline{v_z'(z,t)v_z'(\xi,\tau)} \right\rangle$ (red curve) and its constant density counterpart $\left\langle \overline{v_z^{st}{}'(z)v_z^{st}{}'(\xi)} \right\rangle$ (black curve) on ξ for N_g = 1, $\sigma_Y^2 = 0.1$, $t = \tau = t_2 = 4.4\times10^3$ and $z = z_2 = 4.27\times10^3$, which corresponds to the location where $-\partial\left\langle \overline{C}(z,t) \right\rangle / \partial z$ attains its maximum value. We note that (*i*) the peak displayed by $\left\langle \overline{v_z'(z,t)v_z'(\xi,\tau)} \right\rangle$ at $\xi = z$ is smaller than that of $\left\langle \overline{v_z^{st}{}'(z)v_z^{st}{}'(\xi)} \right\rangle$, a finding which is consistent with the above discussion about the effect of density on the vertical velocity variance; (*ii*) these two covariances tend to coincide, i.e. $\left\langle \overline{v_z'(z,t)v_z'(\xi,\tau)} \right\rangle \approx \left\langle \overline{v_z^{st}{}'(z)v_z^{st}{}'(\xi)} \right\rangle$, for $\xi > z$; and (*iii*) $\left\langle \overline{v_z'(z,t)v_z'(\xi,\tau)} \right\rangle$ becomes smaller than $\left\langle \overline{v_z^{st}{}'(z)v_z^{st}{}'(\xi)} \right\rangle$ for $\xi \le z$, $\left\langle \overline{v_z^{st}{}'(z)v_z^{st}{}'(\xi)} \right\rangle$ and $\left\langle \overline{v_z'(z,t)v_z'(\xi,\tau)} \right\rangle$ respectively attaining positive and negative values. This anti-correlated behavior is linked to the *dynamic* and *stationary* velocity components and to the cross-correlation between *Y* and *C*, as we clarify in Section 3.3.2. As expected, $\left\langle \overline{v_z'(z,t)v_z'(\xi,\tau)} \right\rangle$ and $\left\langle \overline{v_z^{st}{}'(z)v_z^{st}{}'(\xi)} \right\rangle$ tends to coincide when $\mathrm{N_g}$ decrease (see Fig. 3.4*b*), because the intensity of the stabilizing buoyancy effects decreases.

In order to help the comprehension of the following discussions, we recall that the velocity fluctuations for our setup can be written as (see (C.3.5)-(C.3.6))

$$v_z^{st}{}'(y,z) = Y(y,z) - \frac{1}{\phi}\frac{\partial p^{st}{}'(y,z)}{\partial z} \tag{3.24}$$

$$v_z^{dy}{}'(y,z,t) = -\frac{1}{\phi}\left(\frac{\partial p^{dy}{}'(y,z,t)}{\partial z} + \mathrm{N_g}\,\rho'(y,z,t)\right) \tag{3.25}$$

where, similar to (3.20), we decompose pressure fluctuation $p'(y,z,t)$ as the sum of a *stationary*, $p^{st}{}'(y,z)$ (see (C.3.12)-(C.3.14)), and a *dynamic*, $p^{dy}{}'(y,z,t)$ (see (C.3.10)-(C.3.14)), component. A numerical analysis of (3.24)-(3.25) (details not shown) reveals that $Y(y,z) >> \partial p^{st}{}'(y,z)/\partial z\phi$ and $\mathrm{N_g}\,\rho'(y,z,t) >> \partial p^{dy}{}'(y,z,t)/\partial z\phi$. Therefore, a rough simplification of (3.24)-(3.25) read

$$v_z^{st}{}'(y,z) = Y(y,z) \tag{3.26}$$

$$v_z^{dy}{}'(y,z,t) = -\frac{\mathrm{N_g}\,\rho'(y,z,t)}{\phi} \tag{3.27}$$

While (3.26)-(3.27) show a clear dependence of $v_z^{st}{}'(y,z)$ on the fluctuation *Y*(*y*,*z*) of the permeability field, the behavior of $v_z^{dy}{}'(y,z,t)$ depends on that of $\rho'(y,z,t)$, through the multiplying factor $\left(-\mathrm{N_g}/\phi\right)$. In order to further clarify the behavior of $v_z^{dy}{}'$ we note that $\rho'(y,z,t) = C'(y,z,t)$, see (3.10) and according to (A.3.8), decomposition (3.20) and simplifications (3.26)-(3.27), we rewrite (3.27) as

$$v_z^{dy}{}'(y,z,t) \simeq -\frac{\mathrm{N_g}}{\phi}\rho'(z,y,t) \simeq \frac{\mathrm{N_g}}{\phi}\int_0^t\int_\Omega\left[Y(\eta,\xi) - \frac{\mathrm{N_g}}{\phi}\rho'(\eta,\xi,\tau)\right]\frac{\partial\overline{C}(\xi,\tau)}{\partial\xi}G^T(y,z,t;\xi,\eta,\tau)\,d\eta\, d\xi\, d\tau \tag{3.28}$$

Equation (3.28) shows that $v_z^{dy}\,'(y,z,t)$ is a non-local quantity which nature is rooted in the coupling between transport and flow. Equation (3.28) shows that three effects are involved in determining $v_z^{dy}\,'(y,z,t)$: (*i*) permeability fluctuations triggers density variations; (*ii*) in turn stabilizing buoyant term acts in reducing them, with an intensity proportional to $\mathrm{N_g}$ and to the density fluctuation themselves; (*iii*) triggering and stabilizing competing mechanisms are weighted by the mean density gradient, which behavior is a net results of the competition between these two opposite mechanisms (see Fig. 3.3 and relative discussion). Even if based on rough approximations equations (3.26) and (3.28) help in understand the following discussion about the behavior of the velocity covariance in (3.23) as a function of $\mathrm{N_g}$ and σ_Y^2.

Figure 3.4*c* depicts $\left\langle \overline{v_z^{dy}\,'(z,t) v_z^{st}\,'(\xi)} \right\rangle$ versus ξ for $\mathrm{N_g} = 1$, $\sigma_Y^2 = 0.1$, $z = z_2$ and $t = t_2$. This cross-covariance is always negative and attains its largest (absolute) values mainly for $z \leq \xi$. This finding suggests that the stabilizing *dynamic* fluctuation arising at a given space-time location (z, t) is strongly correlated with the *stationary* velocity fluctuations occurring at points which lie upstream (in space) and manifest at earlier times. This result is consistent with our discussion in Section 3.2.3 according to which positive values of *stationary* velocity fluctuations, $v_z^{st}\,'(\xi)$, favour solute to advance within the domain, thus originating positive density fluctuations, $\rho'(z \geq \xi, t)$. These, in turn, trigger negative *dynamic* velocity fluctuations, $v_z^{dy}\,'(z \geq \xi, t)$ (see also (C.3.6)). The same type of reasoning also holds when values of $v_z^{st}\,'(\xi)$ are negative, because in this case positive values of $v_z^{dy}\,'(z \geq \xi, t)$ are promoted. Corresponding results for $\mathrm{N_g} = 0.1$ are depicted in Fig. 3.4.*d.* A comparison against the setting characterized by $\mathrm{N_g} = 1$ reveals: (*i*) a quasi linear dependence of $\left\langle \overline{v_z^{dy}\,'(z,t) v_z^{st}\,'(\xi)} \right\rangle$ in $\mathrm{N_g}$, consistent with the presence of the multiplying factor involving directly $\mathrm{N_g}$ in both (3.23) and (3.28) and with the further dependence on $\mathrm{N_g}$ of the stabilizing buoyant term and of the mean concentration gradients in the convolution presented in (3.28); (*ii*) a different rate of decrease of the correlation for $(z \leq \xi)$, which is related to the dependence of $\left\langle \overline{v_z^{dy}\,'(z,t) v_z^{st}\,'(\xi)} \right\rangle$ on $-\mathrm{N_g} \left\langle \overline{C'(z,t) Y'(\xi)} \right\rangle / \phi$ (see (D.3.9)) and to the fact that a diminished stabilizing buoyancy effects leads to a correlation between $C'(z \geq \xi, t)$ and $Y(\xi)$ which persists over larger distances because perturbations at the solute front are more sensible to the underlying permeability organization than in the case of higher stabilizing effects (i.e. for higher $\mathrm{N_g}$; see Fig. 3.1 and Section 3.3.2 for additional discussion).

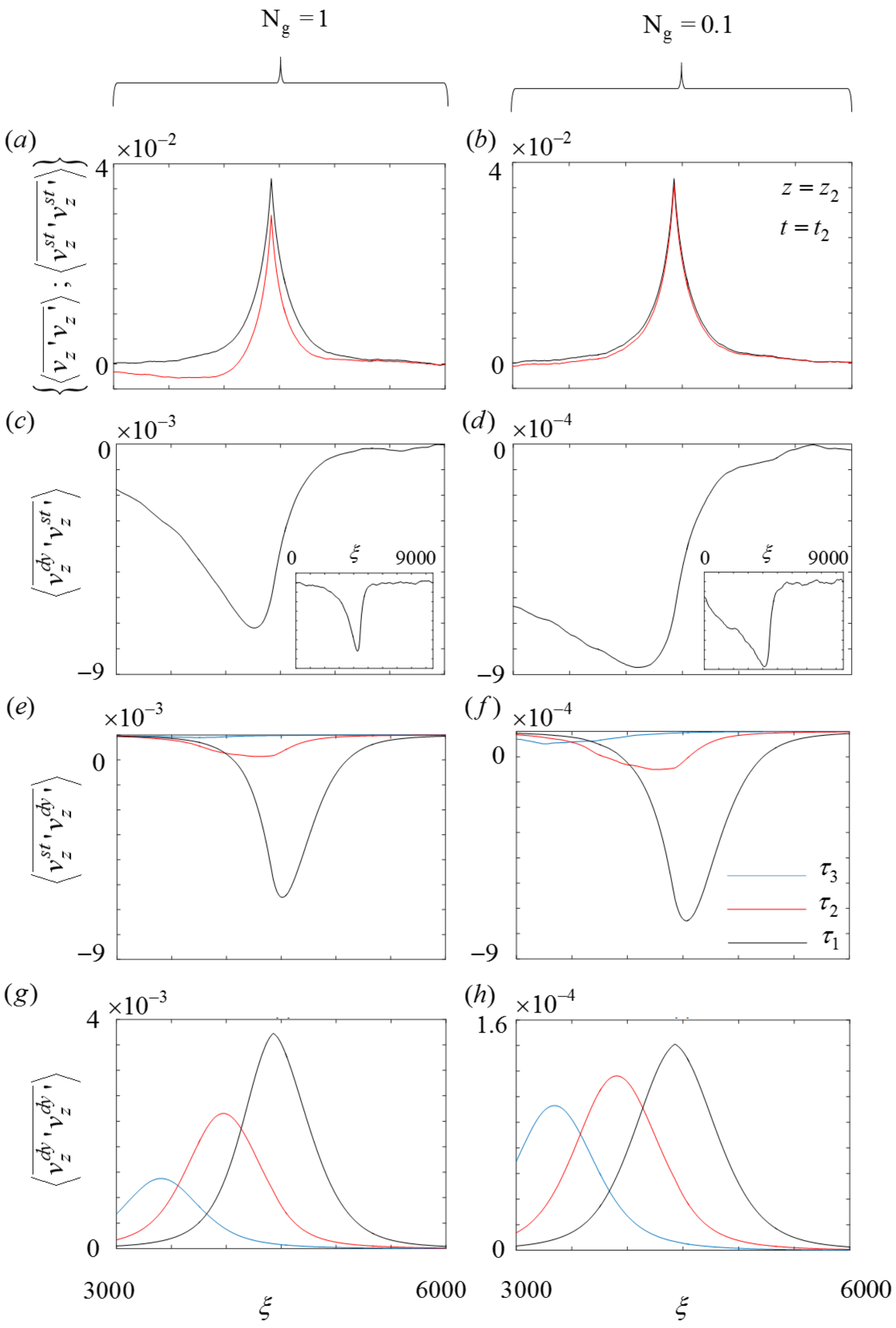

Figure 3.4. Section average vertical velocity covariance components: (*a*, *b*) $\left\langle \overline{v_z{}'(z,t)v_z{}'(\xi,\tau)} \right\rangle$ (red curve) and, $\left\langle \overline{v_z^{st}{}'(z)v_z^{st}{}'(\xi)} \right\rangle$ (black curve), (*c*, *d*) $\left\langle \overline{v_z^{dy}{}'(z,t)v_z^{st}{}'(\xi)} \right\rangle$, inserts show the entire vertical domain, (*e*, *f*) $\left\langle \overline{v_z^{st}{}'(z)v_z^{dy}{}'(\xi,\tau)} \right\rangle$, (*g*, *h*) $\left\langle \overline{v_z^{dy}{}'(z,t)v_z^{dy}{}'(\xi,\tau)} \right\rangle$ versus ξ for $\sigma_Y^2 = 0.1$ and $\mathrm{N_g} = 1$ (left column) $\mathrm{N_g} = 0.1$ (right column). In (*a*)-(*h*) $z = z_2 = 4.27\times10^3$,and $t = t_2 = 4.4\times10^3$; in (*e*)-(*h*) $\tau_1 = 4.4\times10^3$, $\tau_2 = 3.9\times10^3$, $\tau_3 = 3.3\times10^3$.

Figures 3.4*e, f* depict $\left\langle \overline{v_z^{st}{}'(z)v_z^{dy}{}'(\xi,\tau)} \right\rangle$ versus ξ for $\sigma_Y^2 = 0.1$, $z = z_2$, $t = t_2$ and three values of τ when when $N_g = 1$ and 0.1, respectively. The clear negative correlation of $\left\langle \overline{v_z^{st}{}'(z)v_z^{dy}{}'(\xi,\tau)} \right\rangle$ along the $(\xi \geq z; \tau = t)$ segment and its rapid decay in the region $(\xi \leq z; \tau \leq t)$ are explained by considering that *stationary* components are linked with (*a*) the *dynamic* velocity components arising at points which lie downstream along the mean flow direction (i.e. for $z \geq \xi$ for $\tau = t$; see also Section 3.2.3), and (*b*) with the observation that *dynamic* fluctuations in the region $(\xi \leq z; \tau \leq t)$ are, in a mean sense, less sensitive to the fluctuations of the *stationary* flow field arising at locations downstream of ξ. This rapid decaying of $\left\langle \overline{v_z^{st}{}'(z)v_z^{dy}{}'(\xi,\tau)} \right\rangle$ at $(\xi \leq z; \tau \leq t)$ is a result of (*i*) the coupling between flow and transport (as documented by the dependency of $v_z^{dy}{}'$ on ρ' in (3.25)), and (*ii*) the nature of the transport problem for which, in a mean sense and at first order (see also (A.3.8)-(A.3.10)), the density perturbation are mainly dictated by the perturbations in the velocity which has been already experienced, i.e. the Green' function of the transport problem, (A.10), is non zero mainly for the space-time coordinates $(\xi \leq z; \tau \leq t)$. As a consequence, fluctuations $v_z^{dy}{}'$, which are rooted in the coupled nature of flow and transport, are less sensitive to the corresponding *stationary* flow perturbation, $v_z^{st}{}'$, which occur at forward (in space and time along the mean flow direction) locations.

The covariance component $\left\langle \overline{v_z^{st}{}'(z)v_z^{dy}{}'(\xi,\tau)} \right\rangle$ can be seen as an indication of the extent in space and time of the region within which the *stationary* velocity fluctuation can induce *dynamic* perturbation of the flow, an effect which is mainly felt at spatial locations $\xi > z$ (i.e., ξ downstream of *z*). At the same time, the term $\left\langle \overline{v_z^{dy}{}'(z,t)v_z^{st}{}'(\xi)} \right\rangle$ evidences the strength of the effect of *stationary* velocity perturbations at $\xi < z$ (i.e., considering locations ξ upstream of *z*) in triggering *dynamic* fluctuations at (*z* ; *t*). These reasoning are supported by the observations that a change in the value of N_g induces a quasi linear variation of the magnitude of $\left\langle \overline{v_z^{st}{}'(z)v_z^{dy}{}'(\xi,\tau)} \right\rangle$ and $\left\langle \overline{v_z^{dy}{}'(z,t)v_z^{st}{}'(\xi)} \right\rangle$, the shape of these spatial cross-covariances respectively being insensitive and sensitive to N_g, i.e. to the intensity of stabilizing buoyancy effects. The similar shapes observed for $\left\langle \overline{v_z^{st}{}'(z)v_z^{dy}{}'(\xi,\tau)} \right\rangle$ in the plots of Fig. 3.4*e, f* is due to the fact that the *stationary* velocity fluctuations trigger *dynamic* fluctuations in a way which is independent of the effects of density (as rendered by N_g). The latter only affect the relative strength of $\left\langle \overline{v_z^{st}{}'(z)v_z^{dy}{}'(\xi,\tau)} \right\rangle$.

Figures 3.4*g, h* depict $\left\langle \overline{v_z^{dy}{}'(z,t)v_z^{dy}{}'(\xi,\tau)} \right\rangle$ versus ξ for $z = z_2$, $t = t_2$ and three values of τ when $N_g = 1$ and 0.1, respectively. This covariance represents the correlation between the *dynamic* velocity components and, as expected, is positive. It can then be noted that $\left\langle \overline{v_z^{dy}{}'(z,t)v_z^{dy}{}'(\xi,\tau)} \right\rangle$ exhibit a dependence on N_g with a power different from two (compare Figs. 3.4*g* and 3.4*h*) according with equation (3.28), which highlights that variations of N_g affects $v_z^{dy}{}'$ also through the buoyant term and the mean concentration gradient in convolution (3.28) ,determining a deviation from a pure square dependence of $\left\langle \overline{v_z^{dy}{}'(z,t)v_z^{dy}{}'(\xi,\tau)} \right\rangle$ on N_g.. We note that the quantities $\left\langle \overline{v_z^{dy}{}'(z,t)v_z^{st}{}'(\xi)} \right\rangle$,

$\left\langle \overline{v_z^{st}{}'(z) v_z^{dy}{}'(\xi,\tau)} \right\rangle$ and $\left\langle \overline{v_z^{dy}{}'(z,t) v_z^{dy}{}'(\xi,\tau)} \right\rangle$ display a behavior which is qualitatively similar to what illustrated above at all space-time locations (*z*, *t*) investigated (details not shown).

Figure 3.5 depicts results analogous to those of Fig. 3.4 for $\sigma_Y^2 = 0.5$. As expected we found a linear proportionality of $\left\langle \overline{v_z^{st}{}'(z) v_z^{st}{}'(\xi)} \right\rangle$ in σ_Y^2 (see e.g. Rubin, 2003). Increasing the heterogeneity of the permeability field increases also $\left\langle \overline{v'_z(z,t) v'_z(\xi,\tau)} \right\rangle$, (note the vertical scales in Figs. 3.4*a* and 3.5*a*). Moreover, assigned N_g, we found that the relative damping of the buoyant term on the permeability induced fluctuations diminish as σ_Y^2 increase, i.e. $\left\langle \overline{v'_z(z,t) v'_z(\xi,\tau)} \right\rangle$ and $\left\langle \overline{v_z^{st}{}'(z) v_z^{st}{}'(\xi)} \right\rangle$ in Fig. 5*a-b* are closer than results depicted in Fig. 4.*a-b*. This behaviour is essentially due to the relative diminished capability of the negative cross-covariance $\left\langle \overline{v_z^{dy}{}'(z,t) v_z^{st}{}'(\xi)} \right\rangle$ and $\left\langle \overline{v_z^{st}{}'(z) v_z^{dy}{}'(\xi,\tau)} \right\rangle$ of stabilizing the flow. In order to clarify this tendency, we provide here an explanation, based on rough assumptions: (*i*) neglecting the buoyant term on the right hand side of (3.28); (*ii*) approximating $\partial \overline{C}(\xi,\tau)/\partial\xi$ in (3.28) with a Gaussian bell that spread according to the macro-dispersion coefficients for tracer case (see Gelhar and Axness, 1983); (*iii*) multiplying (3.28) by $v_z^{st}{}'(z)$ as treated in (3.26); (*iv*) applying both spatial and ensemble expectation, after some manipulation we get:

$$\left\langle \overline{v_z^{st}{}'(z) v_z^{dy}{}'(z,t)} \right\rangle \simeq \frac{\mathrm{N_g}}{\phi} \int_0^t \int_\Omega \sigma_Y \exp\left(-\frac{(\xi-\tau)^2}{4l\sigma_Y^2\tau} \right) \frac{\exp}{\sqrt{4\pi l\tau}} \left(-\frac{|z-\xi|}{l} \right) G_z^T(z,t;\xi,\tau)\, d\xi\, d\tau \qquad (3.29)$$

which highlight a sublinear grow of the cross-covariance of vertical velocity in σ_Y^2, for a fixed N_g. Note that the first and second assumptions can be view as we are disregarding the buoyant stabilizing effects, in terms of the regularization of the density perturbations and the associated steepening of the mean concentration gradients, which spreading rate is surely smaller than the one dictated by the macro-dispersion coefficient for the tracer case. The spirit of (3.29) is not that of provide an exact results, but to clarify the effects of varying the permeability variance. Recalling (3.22) and (3.23), the sublinear dependence in σ_Y^2 for the cross-covariance between *dynamic* and *stationary* components, compared with the linear scaling of the *stationary* velocity covariance in σ_Y^2, suggests that the effective stabilization of the flow field, and therefore of the solute front, performed by $\left\langle \overline{v_z^{dy}{}'(z,t) v_z^{st}{}'(\xi)} \right\rangle$ and $\left\langle \overline{v_z^{st}{}'(z) v_z^{dy}{}'(\xi,\tau)} \right\rangle$ decrease as the porous media heterogeneity increases.

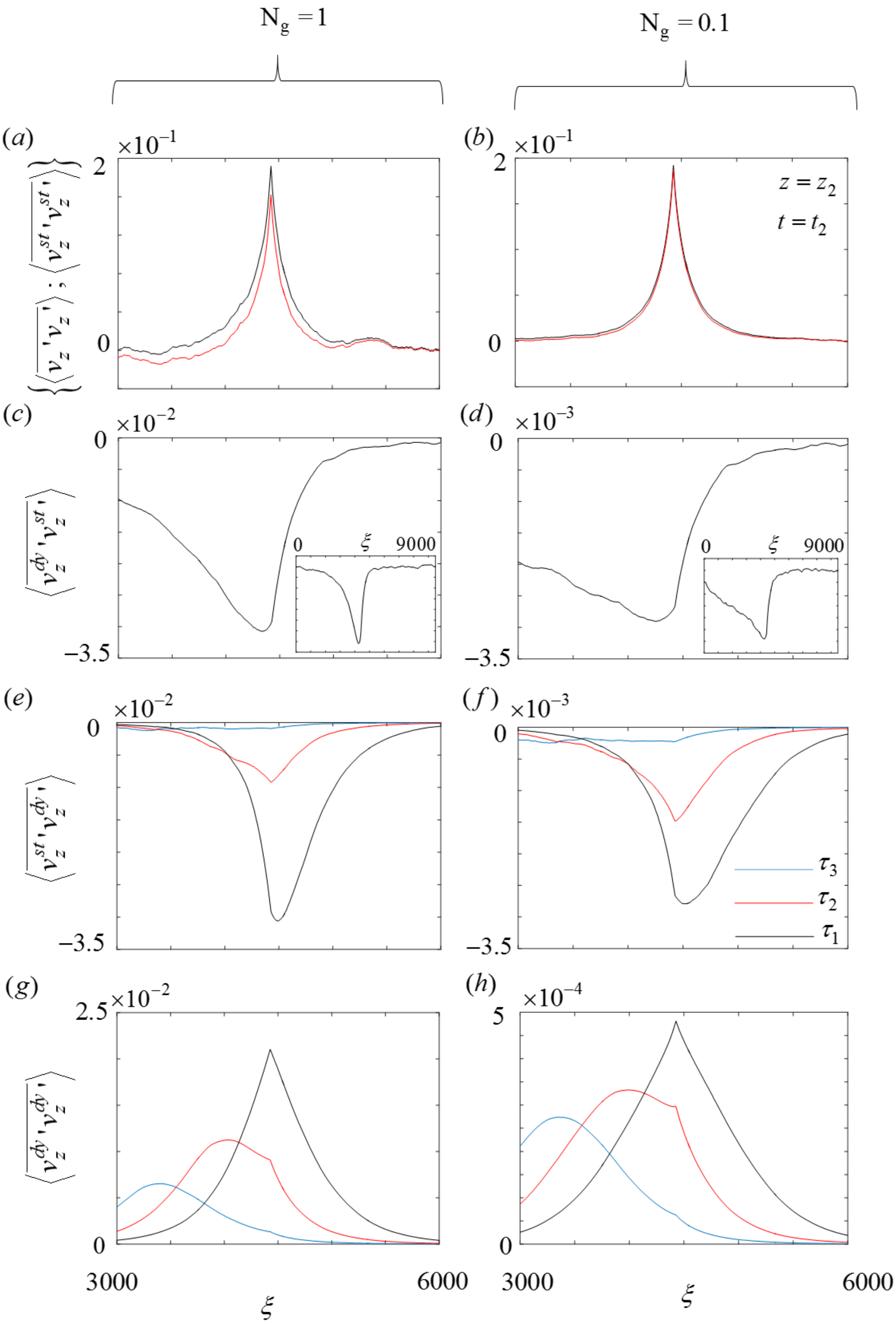

Figure 3.5. Section average vertical velocity covariance components: (*a*, *b*) $\left\langle \overline{v_z'(z,t) v_z'(\xi,\tau)} \right\rangle$ (red curve) and, $\left\langle \overline{v_z^{st}{}'(z) v_z^{st}{}'(\xi)} \right\rangle$ (black curve), (*c*, *d*) $\left\langle \overline{v_z^{dy}{}'(z,t) v_z^{st}{}'(\xi)} \right\rangle$, inserts show the entire vertical domain, (*e*, *f*) $\left\langle \overline{v_z^{st}{}'(z) v_z^{dy}{}'(\xi,\tau)} \right\rangle$, (*g*, *h*) $\left\langle \overline{v_z^{dy}{}'(z,t) v_z^{dy}{}'(\xi,\tau)} \right\rangle$ versus ξ for $\sigma_Y^2 = 0.5$ and $\mathrm{N_g} = 1$ (left column) $\mathrm{N_g} = 0.1$ (right column). In (*a*)-(*h*) $z = z_2 = 4.27 \times 10^3$,and $t = t_2 = 4.4 \times 10^3$; in (*e*)-(*h*) $\tau_1 = 4.4 \times 10^3$, $\tau_2 = 3.9 \times 10^3$, $\tau_3 = 3.3 \times 10^3$.

According to (3.22)-(3.23), the two negative cross-covariances $\left\langle \overline{v_z^{dy}{}'(z,t) v_z^{st}{}'(\xi)} \right\rangle$ and $\left\langle \overline{v_z^{st}{}'(z) v_z^{dy}{}'(\xi,\tau)} \right\rangle$ cause the reduction of the *ensemble* dispersive flux observed in a variable density problem as compared to the uniform density setting. It can then be concluded that the main contribution to the reduction of the covariance $\left\langle \overline{v_z{}'C'} \right\rangle$ in (3.22) stems from $\left\langle \overline{v_z^{dy}{}'(z,t) v_z^{st}{}'(\xi)} \right\rangle$. This result can be interpreted by considering the nature of the transport problem under study in which the expected average evolution of the concentration at (*z*, *t*) is affected by the perturbations that the velocity field experiences at $(z=\xi; t=\tau)$ (as seen from (3.22)) and by those already experienced, i.e. for times $\tau \le t$ and locations $\xi \le z$. These effects are encapsulated in the Green's function $G_z^T(z,t;\xi,\tau)$ (A.10) which displays a peak at $(z=\xi; t=\tau)$ and decays for $(\xi \le z; \tau \le t)$. Note that $\left\langle \overline{v_z^{dy}{}'(z,t) v_z^{st}{}'(\xi)} \right\rangle$ exhibits long negative tails precisely in the space-time region $(\xi \le z; \tau \le t)$, these tails producing an effects which is opposite to the one produced by $\left\langle \overline{v_z^{st}{}'(z) v_z^{st}{}'(\xi)} \right\rangle$ for $\xi \le z$. Note that both $\left\langle \overline{v_z^{st}{}'(z) v_z^{st}{}'(\xi)} \right\rangle$ and $\left\langle \overline{v_z^{dy}{}'(z,t) v_z^{st}{}'(\xi)} \right\rangle$ do not depend on τ.

The contribution of the cross-covariance $\left\langle \overline{v_z^{st}{}'(z) v_z^{dy}{}'(\xi,\tau)} \right\rangle$ in the convolution (3.23) is very small. This is so because (*i*) its marked negative tail for $\xi \ge z$ at $t=\tau$ is practically weighted by $G_z^T(z,t;\xi,\tau)$ solely at $(z=\xi; t=\tau)$, and (*ii*) the cross-covariance $\left\langle \overline{v_z^{dy}{}'(z,t) v_z^{st}{}'(\xi)} \right\rangle$ rapidly decays for $\tau < t$ (see e.g. Fig. 3.4*f*). From a physical point of view, one can see that the convolution between $G_z^T(z,t;\xi,\tau)$ and $\left\langle \overline{v_z^{dy}{}'(z,t) v_z^{st}{}'(\xi)} \right\rangle$ accommodates for about half of the reduction of the correlation between the concentration and velocity fluctuations at $(\xi = z; \tau = t)$ and for the reduction of correlation in $(\xi < z; \tau < t)$. The effect of the convolution in this latter (space-time) region is that of a net reduction of the memory of concentration perturbation on the experienced velocity field due to the stabilizing effects of the density driven scenario. The convolution of $G_z^T(z,t;\xi,\tau)$ and $\left\langle \overline{v_z^{st}{}'(z) v_z^{dy}{}'(\xi,\tau)} \right\rangle$ essentially accounts for about half of the reduction of the correlation between concentration and velocity at $(z=\xi; t=\tau)$. This reduction is due to the negative correlation between *stationary* and *dynamic* velocities at $(z=\xi; t=\tau)$. Otherwise, the contribution of $\left\langle \overline{v_z^{st}{}'(z) v_z^{dy}{}'(\xi,\tau)} \right\rangle$ in the convolution (3.23) is small for $(z \ne \xi; t \ne \tau)$. The latter outcome is consistent with previous observation that the behavior of $\left\langle \overline{v_z^{st}{}'(z) v_z^{dy}{}'(\xi,\tau)} \right\rangle$ is related to the way *stationary* velocity fluctuations act in triggering stabilizing *dynamic* velocity components at downstream locations, as described in Section 3.2.3.

3.3.2 Cross Covariance between Concentration and Permeability

In this section we analyze the section-averages cross-covariance between permeability and concentration, $\left\langle \overline{Y(z)C'(\xi,\tau)} \right\rangle$. This quantity quantifies the way permeability and concentration fluctuations are related and plays an important role in the velocity and concentration covariances, as detailed in Appendices D.3 and F.3.

Figure 3.6 depicts $\left\langle \overline{Y(z)C'(\xi,\tau)} \right\rangle$ versus ξ when $z = z_2 = 4.27\times 10^3$ (black curves) and versus z when $\xi = \xi_2 = z_2$ (red curves) at time $\tau = t_2 = 4.4\times 10^3$ for $\sigma_Y^2 = 0.1$ when $\mathrm{N_g} = 1$ (Fig. 3.6*a*) or 0.1 (Fig. 3.6*b*). A corresponding depiction for $\sigma_Y^2 = 0.5$ and $\mathrm{N_g} = 1$, or 0.1 is illustrated in Fig. 3.6*c*, *d*. Results obtained for $\left\langle \overline{Y(z = z_2)C'(\xi,\tau)} \right\rangle$ (blues curves) and $\left\langle \overline{Y(z)C'(\xi = \xi_2, \tau = t_2)} \right\rangle$ (green curves) when $\mathrm{N_g} = 0$ are also included. In general, fixing *z* in $\left\langle \overline{Y(z)C'(\xi,\tau)} \right\rangle$ highlight how permeability fluctuations, *Y*(*z*), are correlated with concentration fluctuation, $C'(\xi,\tau)$, at (ξ,τ) space-time coordinates. The opposite holds when we choose to fix (ξ,τ), i.e. we highlight how concentration fluctuation $C'(\xi,\tau)$ are affected by the permeability fluctuation at various *z* space coordinates. It can be noted that: (*a*) peak values of $\left\langle \overline{Y(z)C'(\xi,t_2)} \right\rangle$ do not take place at the selected reference locations ξ_2 or z_2; (*b*) values of $\left\langle \overline{Y(z_2)C'(\xi,t_2)} \right\rangle$ at $\xi > z_2$ are larger than those at $\xi < z_2$, implying that $Y(z_2)$ influences $C'(\xi,t_2)$ at downstream (i.e. when $\xi > z_2$) locations along the direction of the mean flow more than it does at $\xi < z_2$. This behavior can be explained by noticing that only small amounts of solute (i.e. $C'(\xi > z_2, t_2) < 0$) are advected within low permeability regions, where $Y(z_2) < 0$, the opposite being observed for regions where $Y(z_2) > 0$. According to the same mechanism, $C'(\xi_2, t_2)$ is highly correlated with $Y(z)$ when $z < \xi_2$ (see red curve in Fig. 3.6). In summary, it can be seen that Fig. 3.6 suggests that permeability at a given location highly influences concentration at downstream positions. This result also implies that, in a mean sense, permeability data are expected to be beneficial to a reduction of the uncertainty on solute transport behavior at downstream location (along the mean flow direction), concentration measurements conveying relevant information to infer permeability within upstream zones.

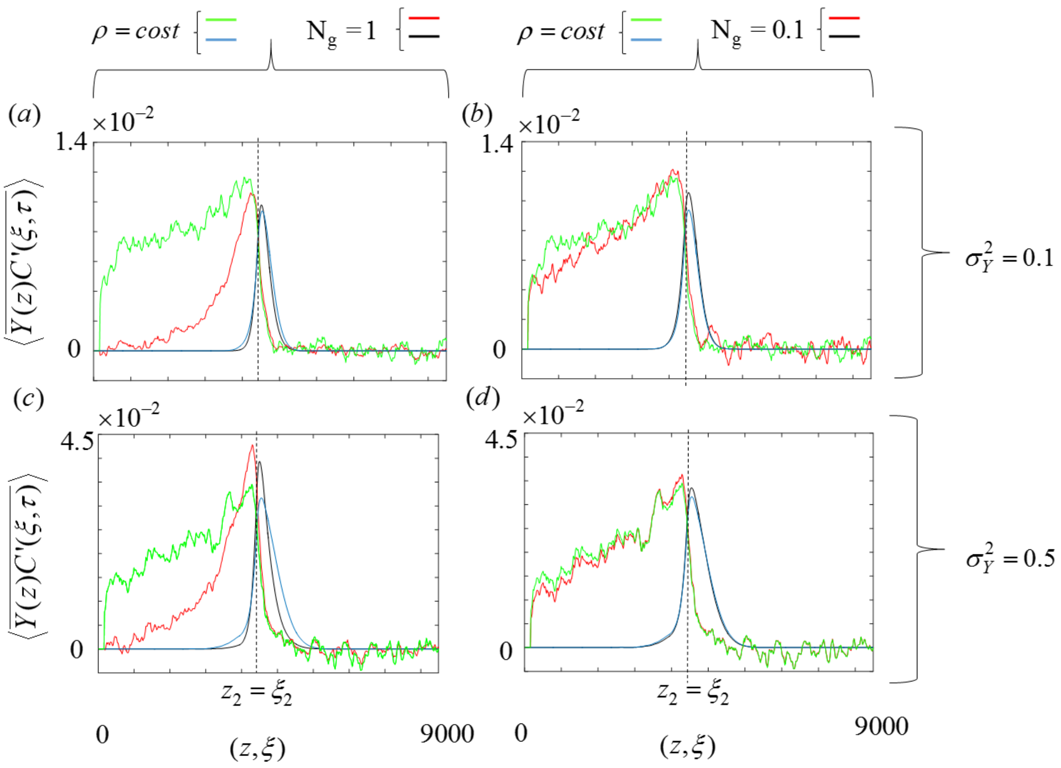

Figure 3.6. Section average log permeability and concentration cross-covariance, $\langle \overline{Y(z)C'(\xi,\tau)} \rangle$, versus ξ when $z = z_2 = 4.27\times10^3$ (black curves) and versus z when $\xi = \xi_2 = 4.27\times10^3$ (red curves) at time $\tau = t_2 = 4.4\times10^3$ for $\sigma_Y^2 = 0.1$ and 0.5 setting (*a*,*c*) $N_g = 1$ (*b*,*d*) $N_g = 0.1$. The results obtained for the tracer case (i.e. $\rho = cost$) are also reported for $\langle \overline{Y(z_2)C'(\xi,t_2)} \rangle$ (blues curves) and $\langle \overline{Y(z)C'(\xi_2,t_2)} \rangle$ (green curves).

One can note that $\langle \overline{Y(z)C'(\xi_2,t_2)} \rangle$ values for the density uniform case are larger than their counterparts associated with the variable density scenario (compare green and red curves in Fig. 3.6). The reduction of $\langle \overline{Y(z)C'(\xi_2,t_2)} \rangle$ for the variable density scenario is linked to the effects of the last terms on the right hand side of (E. 3.5), which cause a decrease of correlation between permeability and concentration associated with the emerging stabilizing effects. This term depends linearly on N_g and vanishes for the uniform density. From a physical point of view, the stabilizing buoyancy effect tends to reduce the concentration variability causing a reduction of the cross-correlation between log permeability and concentration. As a consequence, when buoyancy effects increase concentration profiles in heterogeneous domains tend to display a regular shape, which is akin to the one observed in homogeneous media (see the exemplary setting in Fig. 3.1). Values of $\langle \overline{Y(z)C'(\xi,\tau)} \rangle$ in density-driven flows tend to coincide with those associated with uniform density scenarios for increasing σ_Y^2 and/or decreasing N_g because of the decreasing stabilizing effect due to gravity.

Comparison of Figs. 3.4*c*-*d* and Fig. 3.4*a*, *b* reveal that the shape of $\langle \overline{v_z^{dy}{}'(z,t)v_z^{st}{}'(\xi)} \rangle$ and $\langle \overline{v_z^{st}{}'(z)v_z^{dy}{}'(\xi,\tau)} \rangle$ is respectively similar to that of $\langle \overline{C'(z,t)Y(\xi)} \rangle$ and $\langle \overline{Y(z)C'(\xi,\tau)} \rangle$. This numerical result is in agreement with our analytical solution (D.3.8)-(D.3.9), according to which $\left\langle \overline{v_z^{dy}{}'(z,t)v_z^{st}{}'(\xi)} \right\rangle \propto -\mathrm{N_g} \left\langle \overline{C'(z,t)Y(\xi)} \right\rangle / \phi$ and $\left\langle \overline{v_z^{st}{}'(z)v_z^{dy}{}'(\xi,\tau)} \right\rangle \propto -\mathrm{N_g} \left\langle \overline{Y(z)C'(\xi,\tau)} \right\rangle / \phi$. We remark that our analysis of the cross-covariance between permeability and concentration leads to conclusions which are consistent with those stemming from our discussion about velocity covariances because for the scenario here investigated the characteristics of Y mainly dictate the behavior of $v_z^{st}{}'$, C' being clearly related with $v_z^{dy}{}'$.

We now provide an analysis of the occurrence of the negative values of $\left\langle \overline{v'_z(z,t_2)v'_z(\xi,t_2)} \right\rangle$ observed in Fig. 3.4*a* for the set of spatial coordinates $\tilde{\xi} = \left\{ \xi < z_2 \mid \left\langle \overline{v'_z(z_2,t_2)v'_z(\xi,t_2)} \right\rangle < 0 \right\}$. As discussed in Sections 3.2.1 and 3.3.1, negative velocity correlations are mainly due to $\left\langle \overline{v_z^{dy}{}'(z_2,t_2)v_z^{st}{}'(\tilde{\xi})} \right\rangle$, contributions of $\left\langle \overline{v_z^{st}{}'(z_2)v_z^{dy}{}'(\tilde{\xi},t_2)} \right\rangle$ being negligible (compare black curves in Fig. 3.4.*c* and Fig. 3.4*e*). As noted above (see Fig. 3.4 and related comments), positive (negative) values of Y induce positive (negative) values of $v_z^{st}{}'$ and $v_z{}'$. This is so because the stabilizing effect of $v_z^{dy}{}'$ tends to decrease the intensity of $v_z{}'$ (with respect to the uniform density case) without altering its sign for the investigated values of N_g. Positive (negative) fluctuations $v_z{}'(\tilde{\xi},t_2)$ generate positive (negative) values of C' at $\xi \geq \tilde{\xi}$ as well as at z_2, thus promoting stabilization of flow through the term $v_z^{dy}{}'(z_2,t_2)$ which is associated with a negative (positive) sign. If this stabilizing effect due to gravity is not negligible with respect to the enhancement of velocity fluctuation due to heterogeneity, the resulting field of $v_z{}'(z_2,t_2)$ is characterized by an opposite sign with respect to $v_z{}'(\tilde{\xi},t_2)$. Interesting for $\xi > z_2$ Negative vertical velocity covariances do not appear in the variable density configuration, because the negative contribution of $\left\langle \overline{v_z^{st}{}'(z_2)v_z^{dy}{}'(\xi > z_2,t)} \right\rangle$ vanishes for $\xi < z_2$ approximately in the same way as the $\left\langle \overline{v_z^{st}{}'(z_2)v_z^{st}{}'(\xi)} \right\rangle$.

3.3.3 Ensemble Dispersive Flux and Concentration Variance

Here we analyze the *ensemble* dispersive flux, $\left\langle \overline{v_z{}'(z,t)C'(z,t)} \right\rangle$ introduced in (3.21)-(3.22). We recall (3.22)-(3.23), (D.3.12), (E.3.3), (E.3.5), (F. 3.4) and (F.3.6) and remark that $\left\langle \overline{v_z{}'(z,t)C'(z,t)} \right\rangle$ depends non-linearly on the mean concentration gradient, $\partial \left\langle \overline{C}(z,t) \right\rangle / \partial z$. This observation is consistent with previous analytical and numerical results (see, e.g. Welty and Gelhar, 1991; Landman et al., 2007a, b;). The root of this non-linear dependency lay in the coupling between flow and transport problems and in particular is due to the stabilizing buoyant term in the *dynamic* velocity fluctuations, which by itself depends on the mean concentration gradient. A clear definition of the non linear dependency is hard to track through out (3.22)-(3.23), (D.3.12), (E.3.3), (E.3.5), (F. 3.4) and (F.3.6). Interested readers may refers to Landman et al. 2007b who provided relative simple expression, valid for large travel times.

Figures 3.7*a* and 3.7*b* respectively depict the dependence on z of $\left\langle \overline{v_z{}'(z,t)C'(z,t)} \right\rangle$ and of the concentration variance, $\sigma_c^2(z,t) = \left\langle \overline{C'(z,t)^2} \right\rangle$, at five selected times, for $\sigma_Y^2 = 0.1$ and $\mathrm{N_g} = 0$ (blue curves), 0.1 (red curves), and 1.0 (black curves) as a result of the numerical Monte Carlo simulations (continuous curves) performed. The semi-analytical solutions of (3.22) and (F.3.6) are also depicted (dashed curves). Corresponding results for $\sigma_Y^2 = 0.5$ are depicted in Figs. 3.6*c*, *d*. From Fig. 3.7 it can be noted that our semi-analytical solution captures quite accurately the Monte Carlo numerical results despite the strong assumptions at its basis.

Values of $\left\langle \overline{v_z\,'(z,t)C\,'(z,t)} \right\rangle$ and $\sigma_c^2(z,t)$ in Figs. 3.6*a*, *d* decrease in time and/or for increasing $\mathrm{N_g}$ suggesting that $\left\langle \overline{C}(z,t) \right\rangle$ can be considered as a good approximation of $\overline{C}(z,t)$ as well as of the (random) concentration, $C(y,z,t)$, (*a*) at late times when the solute front has sampled the overall *k* variability and fluctuations along the transverse direction tend to be smoothed out due to mixing, and/or (*b*) for large values of $\mathrm{N_g}$, because the solute front in heterogeneous domains tends to resemble the pattern documented in homogenous media. Increasing the heterogeneity of the permeability field, both $\left\langle \overline{v_z\,'(z,t)C\,'(z,t)} \right\rangle$ and $\sigma_c^2(z,t)$ increase and the regularizing ability of the stabilizing buoyancy effects for a given $\mathrm{N_g}$ tends to decrease (see Section 3.3.1). This finding is in agreement with that of Landman 2007a, which on the base of experimental results (see Fig. 13 of Landman 2007a) shows that the relative reduction of the solute spreading in case of stable flow respect to the tracer case scenario, assigned $\mathrm{N_g}$, diminish as σ_Y^2 increase.

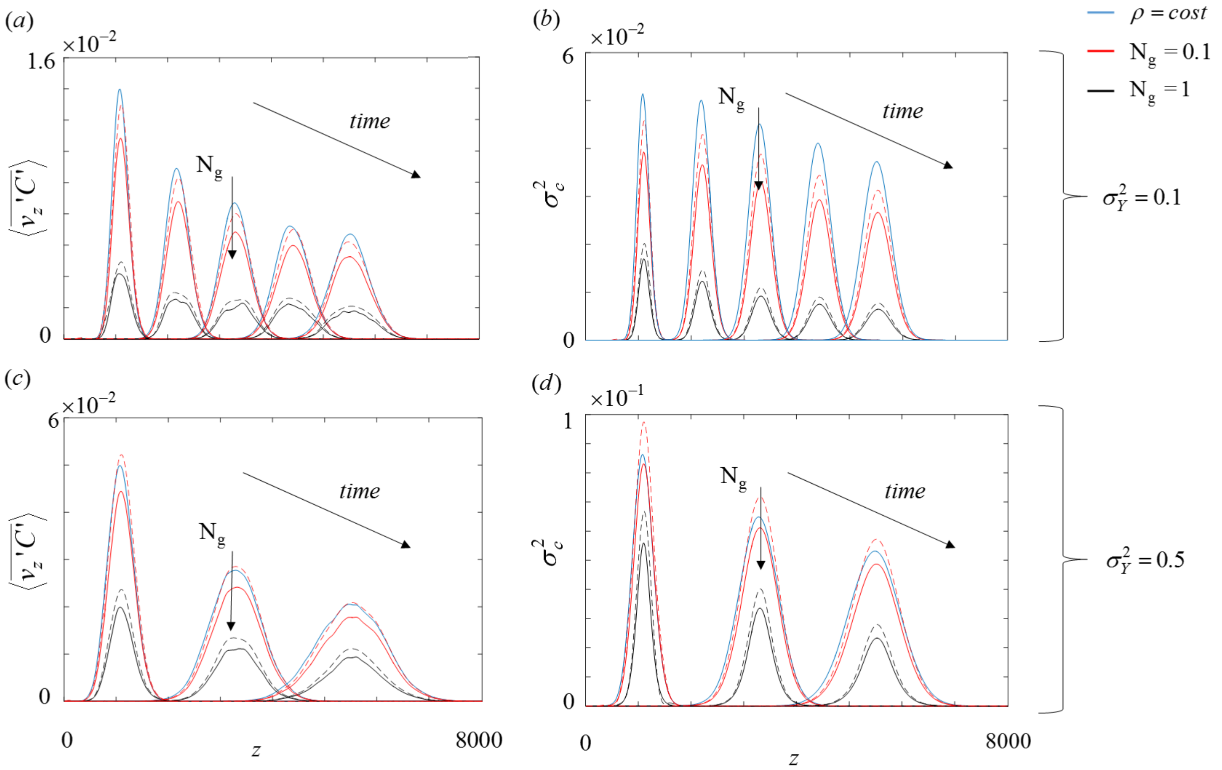

Figure 3.7. Section average ensemble dispersive flux, $\left\langle \overline{v_z\,'(z,t)C\,'(z,t)} \right\rangle$, and concentration variance, $\sigma_c^2(z,t) = \left\langle \overline{C\,'(z,t)^2} \right\rangle$, for $\mathrm{N_g} = 1$, (black curves), $\mathrm{N_g} = 0.1$, (red curves), $\rho = cost$, (blue curves), (*a*)-(*b*) for $\sigma_Y^2 = 0.1$ and (*c*)- (*d*) for $\sigma_Y^2 = 0.5$. Numerical Monte Carlo and semi-analytical results are reported by solid and dashed curves, respectively.

3.4 Conclusions

We analyze the occurrence, for stable variable density flow in heterogeneous porous media, of the solute spreading reduction and tendency to a more homogeneous-like behavior of the resulting concentration profile respect to corresponding results for the constant density counterpart case. That is, density dependence leads to sharper concentration fronts than constant density.

The main finding of this work is that the reduction of dispersion and contraction of the concentration profile are due to a reorganization of the velocity field. In particular we observed a reduction of the velocity variance and a shrink of the spatial extension of velocity correlation. The reduction in both variance and correlation distance of velocity causes a reduction of the dispersive flux.

Even if the regularization of the velocity field as responsible for the reduction of the solute dispersion was something to be expected (similar observations has been done for immiscible flow in Neuweiler et al., 2003), its proper quantification and understanding is a difficult task, due to the heterogeneous nature of permeability and the coupling between flow and transport.

We faced this challenge by decomposing the variable density flow field, and its fluctuations, in a *stationary* component, i.e. $v_z^{st}\,'$, associate with the solution of the flow problem for constant density, plus a *dynamic* component, i.e. $v_z^{dy}\,'$, which take into account the coupling between transport and flow. The introduced decomposition of the velocity field allowed for a better understanding of the interplaying and triggering mechanism, which occurs between permeability, velocity, and concentration, which is a crucial aspect for coupled problem as the one here analyzed.

Similarly to tracer transport scenario, we found that the dispersive flux is a function of the velocity covariance. The origin of the solute dispersion reduction has been linked, both from a mathematical and physical point of view, to the negative $\left\langle \overline{v_z^{st}\,'(z) v_z^{dy}\,'(\xi,\tau)} \right\rangle$ and $\left\langle \overline{v_z^{dy}\,'(z,t) v_z^{st}\,'(\xi)} \right\rangle$ velocity cross-covariance, which are to be subtracted from the of the *stationary* velocity covariance, $\left\langle \overline{v_z^{st}\,'(z) v_z^{st}\,'(\xi)} \right\rangle$. The two cross-covariance essentially describe the interplay between permeability induced *stationary* fluctuation, which promote solute spreading, and the stabilizing buoyancy induced *dynamic* perturbation, which suppress solute dispersion.

Interestingly, we found that the shape of $\left\langle \overline{v_z^{dy}\,'(z,t) v_z^{st}\,'(\xi)} \right\rangle$ varies with the intensity of the ratio between buoyant and viscous forces, i.e. N_g, and with σ_Y^2. In particular the rate of correlation of $\left\langle \overline{v_z^{dy}\,'(z,t) v_z^{st}\,'(\xi)} \right\rangle$ increases as σ_Y^2 increases and/or N_g decreases, because density fluctuations are more sensitive to the underlying permeability variations as the regularization of the flow field pursued by the buoyant components decrease. On the other hand, the shape of $\left\langle \overline{v_z^{st}\,'(z) v_z^{dy}\,'(\xi,\tau)} \right\rangle$ remains virtually unaffected by the permeability variance and N_g, suggesting that *stationary* fluctuations trigger *dynamic* components in the same fashion. Instead, the absolute values of both $\left\langle \overline{v_z^{dy}\,'(z,t) v_z^{st}\,'(\xi)} \right\rangle$ and $\left\langle \overline{v_z^{st}\,'(z) v_z^{dy}\,'(\xi,\tau)} \right\rangle$ scale approximately linearly with N_g and sublinealry with σ_Y^2. This contrast with the well-known linear scaling in σ_Y^2 of $\left\langle \overline{v_z^{st}\,'(z) v_z^{st}\,'(\xi)} \right\rangle$. Therefore the relative importance of the stabilizing components induced by density variations decreases as the media becomes more heterogeneous.

The resulting reduction of the dispersive flux for stable flow, in comparison with the value obtained for constant density flow, increases with the relative importance of the stabilizing effects, i.e. high N_g and low σ_Y^2. In terms of solute concentration behavior, the contraction of the dispersive flux leads to concentration profile that resemble an homogenous like solution, even if the underlying permeability is still heterogeneous.

Future studies will focus on the triggering mechanism and interplay between flow and transport in order to analyze the transverse dispersion and the possibility of enrich our understanding for unstable conditions.

Appendix A.3 Section average concentration and effective dispersive flux

Substituting (3.16)-(3.17) in (3.15), applying spatial mean operator (3.13) and making use of the first of (3.14) we obtain that, for the problem set up presented in Fig. 3.1, the horizontal spatial average concentration, $\overline{C}(z,t)$, satisfies the following equation

$$\frac{\partial \overline{C}}{\partial t}+\overline{v}_z\frac{\partial \overline{C}}{\partial z}-\frac{\partial}{\partial z}\left(\overline{D_{zz}}\frac{\partial \overline{C}}{\partial z}\right)+\frac{\partial \overline{v_z'C'}}{\partial z}-\frac{\partial}{\partial z}\left(\overline{D_{zz}'\frac{\partial C'}{\partial z}}\right)=0 \tag{A.3.1a}$$

where

$$\overline{v_z'C'}=\frac{1}{D}\int_0^D v_z'(y,z,t)C'(y,z,t)dy\,;\qquad \overline{D_{zz}'\frac{\partial C'}{\partial z}}=\frac{1}{D}\int_0^D D_{zz}'(y,z,t)\frac{\partial}{\partial z}C'(y,z,t)dy\,. \tag{A.3.1b}$$

The last term of (A.3.1a) A numerically analysis of (A.3.1a) (details not shown) allows to recognize that, for the test cases considered in this work, it is possible to neglect and to approximate $\overline{D_{zz}}(z,t)$ by $1/\mathrm{Pe}$, yielding

$$\frac{\partial \overline{C}}{\partial t}+\overline{v}_z\frac{\partial \overline{C}}{\partial z}-\frac{1}{\mathrm{Pe}}\frac{\partial^2 \overline{C}}{\partial z^2}+\frac{\partial \overline{v_z'C'}}{\partial z}=0 \quad . \tag{A.3.2}$$

Applying (3.13) to the first of (3.14) and making use of (3.16)-(3.17), yields

$$\nabla\cdot\overline{\left(\overline{\boldsymbol{v}}(z,t)+\boldsymbol{v}'(z,t)\right)}=\frac{\partial \overline{v}_z(z,t)}{\partial z}=0 \quad , \tag{A.3.3}$$

i.e. the spatial mean vertical velocity is constant and equal to the prescribed flux divided by porosity, which equals 1 in dimensionless form. Making use of (A.3.3), Equation (A.3.2) simplifies as

$$\frac{\partial \overline{C}}{\partial t}+\frac{\partial \overline{C}}{\partial z}-\frac{1}{\mathrm{Pe}}\frac{\partial^2 \overline{C}}{\partial z^2}+\frac{\partial \overline{v_z'C'}}{\partial z}=0 \quad , \tag{A.3.4}$$

where $\overline{v_z'C'}$ is the *effective* dispersion flux discussed in section 3.2.2. Closure of (A.3.4) is obtained upon writing $\overline{v_z'C'}$ as function of $\overline{C}$. Subtracting (A.3.4) from (3.15) and neglecting terms involving the product of fluctuations we get

$$\frac{\partial C'}{\partial t}+\frac{\partial}{\partial z}C'-\frac{1}{\mathrm{Pe}}\nabla^2 C'=-\boldsymbol{v}'\cdot\nabla\overline{C}+\nabla\cdot\left(\boldsymbol{D}'\nabla\overline{C}(z,t)\right) \tag{A.3.5}$$

Our numerical simulations show that $-\boldsymbol{v}'\cdot\nabla\overline{C}>>\nabla\cdot\left(\boldsymbol{D}'\nabla\overline{C}\right)$ (details not shown), therefore (A.3.5) simplifies as

$$\frac{\partial C'}{\partial t}+\frac{\partial}{\partial z}C'-\frac{1}{\mathrm{Pe}}\nabla^2 C'=-v_z'\frac{\partial}{\partial z}\overline{C} \tag{A.3.6}$$

Equation (A.3.6) is subject to the following initial and boundary conditions

$$\begin{aligned}
&C'(y,z,t)=0 \quad \textit{for } z=0; \qquad C'(y,z,t)-\frac{1}{\mathrm{Pe}}\frac{\partial C'(y,z,t)}{\partial z}=0 \quad \textit{for } \ z=H;\\
&\frac{\partial C'(y,z,t)}{\partial y}=0 \quad \textit{for } \ y=0,W; \quad C'(y,z,t)=0 \qquad \textit{for } \ t=0 \ \ (y,z)\in\Omega;
\end{aligned} \tag{A.3.7}$$

Note that these are homogeneous. Therefore, (A.3.6)-(A.3.7) is driven by the rhs of (A.3.6). Its solution can be expressed in terms of G^T, Green's function that satisfies (A.3.6) with the source term replaced by $\delta(\eta-y)\delta(\xi-z)\delta(t-\tau)$ subject to homogeneous initial and boundary conditions, as

$$C'(z,y,t)=-\int_0^t\int_\Omega v_z'(\eta,\xi,\tau)\frac{\partial}{\partial\xi}\overline{C}(\xi,\tau)G^T(y,z,t;\xi,\eta,\tau)d\eta d\xi d\tau \quad , \tag{A.3.8}$$

Multiplying (A.3.8) by $v_z'(y,z,t)$ and applying (3.13) we derive the expression for the *effective* dispersive flux as

$$\overline{v_z'(z,t)C'(z,t)}=-\int_0^t\int_\Omega \overline{v_z'(z,t)G^T(z,t;\eta,\xi,\tau)}\, v_z'(\eta,\xi,\tau)\frac{\partial\overline{C}(\xi,\tau)}{\partial\xi}d\eta d\xi d\tau \quad , \tag{A.3.9a}$$

with

$$\overline{v_z'(z,t)G^T(z,t;\eta,\xi,\tau)}=\frac{1}{D}\int_0^D v_z'(y,z,t)G^T(y,z,t;\eta,\xi,\tau)dy \quad . \tag{A.3.9b}$$

In order to further simplify our analysis, we follow Bolster et al. (2009, 2011) and consider a 1D problem (along the vertical z-direction) within a semi-infinite domain, $z\in[0,\infty)$. Under this hypothesis a close analytical expression of G^T can be derived as (see Leij and Van Genuchten, 2000)

$$G^T(y,z,t;\xi,\eta,\tau)=\delta(y-\eta)G_z^T(z,t;\xi,\tau)$$

$$\text{with}\quad G_z^T(z,t;\xi,\tau)=\sqrt{\frac{\text{Pe}}{4\pi(t-\tau)}}\left[e^{-\text{Pe}\left(\frac{(z-\xi-t+\tau)^2}{4(t-\tau)}\right)}-e^{\text{Pe}\left(z-\frac{(\xi+z+t-\tau))^2}{4(t-\tau)}\right)}\right] \quad , \tag{A.3.10}$$

where $\delta(y-\eta)$ is the Dirac’ delta function. Making use of (A.3.10) equation (A.3.9) simplifies as

$$\overline{v_z'(z,t)C'(z,t)}=-\int_0^t\int_0^H \overline{v_z'(z,t)v_z'(\xi,\tau)}\, G_z^T(z,t,\xi,\tau)\frac{\partial\overline{C}(\xi,\tau)}{\partial\xi}d\xi d\tau \tag{A.3.11a}$$

with

$$\overline{v_z'(z,t)v_z'(\xi,\tau)}=\frac{1}{D}\int_0^D v_z'(y,z,t)v_z'(y,\xi,\tau)dy \tag{A.3.11b}$$

Note that, by virtue of (A.3.10), $\eta = y$, so that only the product of velocity fluctuations along the vertical is retained in (A.3.11).

Appendix B.3 Ensemble average of horizontal spatial mean concentration

We derive the equation satisfied by the ensemble average of horizontal spatial mean concentration, $\left\langle\overline{C}(z,t)\right\rangle$ by introducing the following decomposition:

$$\overline{C}(z,t)=\left\langle\overline{C}(z,t)\right\rangle+C(z,t) \quad , \qquad \overline{v}(z,t)=\hat{v}_z(z,t)+\left\langle\overline{v}(z,t)\right\rangle \quad , \tag{B.3.1}$$

$$\overline{C}=\left\langle\overline{C}\right\rangle+\hat{C}\,, \qquad \overline{v}=\hat{v}_z+\left\langle\overline{v}\right\rangle \quad , \tag{B.3.1}$$

where $\hat{C}(z,t)$ and $\hat{v}_z(z,t)$ respectively indicate fluctuations of $\overline{C}(z,t)$ and $\overline{v}(z,t)$ around their ensemble mean, i.e. $\langle\hat{C}\rangle=\langle\hat{v}\rangle=0$. Introducing (B.3.1) into (A.3.2) and applying the ensemble mean operator yields

$$\frac{\partial\langle\bar{C}\rangle}{\partial t}+\frac{\partial}{\partial z}\left(\langle\bar{v}_z\rangle\langle\bar{C}\rangle\right)-\frac{1}{\mathrm{Pe}}\frac{\partial^2\langle\bar{C}\rangle}{\partial z^2}+\frac{\partial}{\partial z}\left[\langle\hat{v}_z\hat{C}\rangle+\langle\overline{v_z' C'}\rangle\right]=0 \qquad . \tag{B.3.2}$$

Note that, as discussed in Appendix A.3, the spatial mean vertical velocity is constant and equal to the velocity fixed at top boundary in Fig. 3.1, i.e.

$$\bar{v}_z(z,t)=\langle\bar{v}_z(z,t)\rangle=1 \qquad ; \qquad \hat{v}_z(z,t)=0 \qquad . \tag{B.3.3}$$

Making use of (B.3.3), equation (B.3.2) becomes

$$\frac{\partial\langle\bar{C}(z,t)\rangle}{\partial t}+\frac{\partial\langle\bar{C}(z,t)\rangle}{\partial z}-\frac{1}{\mathrm{Pe}}\frac{\partial^2\langle\bar{C}(z,t)\rangle}{\partial z^2}=-\frac{\partial\langle\overline{v_z'(z,t)C'(z,t)}\rangle}{\partial z} \tag{B.3.4}$$

The *ensemble* dispersive flux $\langle\overline{v_z'(z,t)C'(z,t)}\rangle$ in (B.3.4) can be computed applying the ensemble operator to (A.3.11) as

$$\begin{aligned}\langle\overline{v_z'(z,t)C'(z,t)}\rangle &= -\int_0^t\int_0^H\left\langle\overline{v_z'(z,t)v_z'(\xi,\tau)}\,\frac{\partial\bar{C}(\xi,\tau)}{\partial\xi}\right\rangle G_z^T(z,t,\xi,\tau)\,d\xi\, d\tau \\ &= -\int_0^t\int_0^H\langle\overline{v_z'(z,t)v_z'(\xi,\tau)}\rangle\frac{\partial\langle\bar{C}(\xi,\tau)\rangle}{\partial\xi}G_z^T(z,t,\xi,\tau)\,d\xi\, d\tau \\ &\quad -\int_0^t\int_0^H\left\langle\overline{v_z'(z,t)v_z'(\xi,\tau)}\,\frac{\partial\hat{C}(\xi,\tau)}{\partial\xi}\right\rangle G_z^T(z,t,\xi,\tau)\,d\xi\, d\tau\end{aligned} \tag{B.3.5}$$

Neglecting terms involving products of fluctuations larger than two, (B.3.5) becomes

$$\langle\overline{v_z'(z,t)C'(z,t)}\rangle=-\int_0^t\int_0^H\langle\overline{v_z'(z,t)v_z'(\xi,\tau)}\rangle\frac{\partial\langle\bar{C}(\xi,\tau)\rangle}{\partial\xi}G_z^T(z,t,\xi,\tau)\,d\xi\, d\tau \qquad . \tag{B.3.6}$$

Equation (B.3.6) clearly elucidates that the ensemble dispersive flux is a non-local quantity in time and space since it depends on velocity cross-covariances and concentration gradients evaluated along the full domain at all times $\tau\le t$. A (partial) localization of (B.3.6) is offered by

$$\langle\overline{v_z'(z,t)C'(z,t)}\rangle=\int_0^t\int_0^H\langle\overline{v_z'(z,t)v_z'(\xi,\tau)}\rangle G_z^T(z,t,\xi,\tau)\,d\xi\, d\tau\,\frac{\partial\langle\bar{C}(z,t)\rangle}{\partial z} \tag{B.3.7}$$

Appendix C.3 Velocity and pressure Fluctuations

First order approximation of velocity fluctuation components $v_y'(y,z,t)$ and $v_z'(y,z,t)$ defined in (3.16) are derived by subtracting the spatial mean of vertical velocity (recall that $\bar{v}_z(z,t)=1$) from the second of (3.14), approximating the permeability fluctuation as $k'(y,z)=\exp(Y(y,z))-1\approx Y(y,z)$ and neglecting terms involving products of fluctuations larger than one. Following this procedure we obtain

$$v_y'(y,z,t) = -\frac{1}{\phi}\frac{\partial p'(y,z,t)}{\partial y} \tag{C.3.1}$$

$$v_z'(y,z,t) = Y(y,z) - \frac{1}{\phi}\left(\frac{\partial p'(y,z,t)}{\partial z} + \mathrm{N_g}\,\rho'(y,z,t)\right) \quad , \tag{C.3.2}$$

Recalling the *stationary* and *dynamic* decomposition introduced in (3.20) and remembering (B.3.3) we rewrite (C.3.1)-(C.3.2) as

$$v_y^{st}\,'(y,z) = -\frac{1}{\phi}\frac{\partial p^{st}\,'(y,z)}{\partial y} \tag{C.3.3}$$

$$v_y^{dy}\,'(y,z,t) = -\frac{1}{\phi}\frac{\partial p^{dy}\,'(y,z,t)}{\partial y} \tag{C.3.4}$$

$$v_z^{st}\,'(y,z) = Y(y,z) - \frac{1}{\phi}\frac{\partial p^{st}\,'(y,z)}{\partial z} \tag{C.3.5}$$

$$v_z^{dy}\,'(y,z,t) = -\frac{1}{\phi}\left(\frac{\partial p^{dy}\,'(y,z,t)}{\partial z} + \mathrm{N_g}\,\rho'(y,z,t)\right) \quad , \tag{C.3.6}$$

where p_0^{st} is obtained by solving (3.9)-(3.12) within an homogeneous system, i.e. $\boldsymbol{k}(y,z) = \mathbf{I}$ and considering a fluid with constant density equal to ρ_f, $p_0^{dy} = p_0 - p_0^{st}$, $\rho_0^{dy} = \rho_0 - \rho_f$, $p^{st}\,'(y,z)$ and $p^{dy}\,'(y,z,t)$ are *stationary* and *dynamic* pressure (random) fluctuations which expressions are evaluated in the following. Note that from (B.3) we can also write

$$\overline{v}_z(z,t) = 1 = \overline{v}_z^{st}(z) + \overline{v}_z^{dy}(z,t) = \overline{v}_z^{st} \qquad i.e. \qquad \overline{v}_z^{dy}(z,t) = 0 \tag{C.3.7}$$

which justify simplification in (C.3.6). Using (C.3.3) and (C.3.5) and the fact that $\boldsymbol{v}^{st}$ is divergence free, we write the equation for $p^{st}\,'(y,z)$ as

$$\nabla^2 p^{st}\,'(y,z) = \phi\frac{\partial Y(y,z)}{\partial z} \tag{C.3.8}$$

Note that (C.3.8) is the conventional first order approximation to the equation of (constant density) flow through heterogeneous media. Considering the problem set up of Fig. 3.1, equation (C.3.8) is subjected to the following boundary conditions

$$p^{st}\,'(y,z) = 0 \quad for\ z = 0; \quad \frac{\partial p^{st}\,'(y,z)}{\partial z} = 0 \quad for\ z = H \ ; \frac{\partial p^{st}\,'(y,z)}{\partial y} = 0 \quad for\ \ y = 0, D \tag{C.3.9}$$

Solution of (C.3.8)-(C.3.9) is

$$p^{st}\,'(y,z) = \phi\int_{\Omega}\frac{\partial}{\partial\xi}Y(\eta,\xi)\,G^F(y,z;\eta,\xi)\,d\eta\, d\xi \tag{C.3.10}$$

where $G^F(y,z;\eta,\xi)$ is the flow Green's function that satisfies (C.3.8)-(C.3.9) with the source term replaced by $\delta(\eta - y)\delta(\xi - z)$ subject to homogeneous boundary conditions.

Proceeding in a similar way, we derive the equation satisfy by pressure perturbation

$$\nabla^2 p'(y,z,t) = \phi\frac{\partial}{\partial z}Y(y,z) - \mathrm{N_g}\frac{\partial}{\partial z}\rho'(y,z,t) \quad . \tag{C.3.11}$$

Subtracting (C.3.8) from (C.3.11) and making use of (3.17) we obtain the equation satisfied by the dynamic pressure fluctuation

$$\nabla^2 p^{dy}{}'(y,z,t) = -\,\mathrm{N_g}\,\frac{\partial C'(y,z,t)}{\partial z} \quad , \tag{C.3.12}$$

subject to the following boundary conditions

$$p^{dy}{}'(y,z) = 0 \quad \textit{for } z = 0; \; \frac{\partial p^{dy}{}'(y,z)}{\partial z} = 0 \quad \textit{for } z = H \; ; \frac{\partial p^{dy}{}'(y,z)}{\partial y} = 0 \quad \textit{for } \; y = 0, D \tag{C.3.13}$$

Solution of (C.3.12)-(C.3.13) is given by

$$p^{dy}{}'(y,z,t) = -\mathrm{N_g}\int_{\Omega} \frac{\partial C'(\eta,\xi,t)}{\partial \xi} G^F(y,z;\eta,\xi)\,d\eta\, d\xi \tag{C.3.14}$$

Appendix D.3 Covariance of Vertical Velocity

Making use of (3.20) the horizontal spatial mean of the covariance of vertical velocity components can be written as

$$\left\langle \overline{v'_z(z,t)v'_z(\xi,\tau)} \right\rangle = \left\langle \overline{v_z^{st}{}'(z)v_z^{st}{}'(\xi)} \right\rangle + \left\langle \overline{v_z^{st}{}'(z)v_z^{dy}{}'(\xi,\tau)} \right\rangle + \left\langle \overline{v_z^{dy}{}'(z,t)v_z^{st}{}'(\xi)} \right\rangle + \left\langle \overline{v_z^{dy}{}'(z,t)v_z^{dy}{}'(\xi,\tau)} \right\rangle \tag{D.3.1}$$

Equation (D.3.1) elucidates that $\left\langle \overline{v'_z(z,t)v'_z(\xi,\tau)} \right\rangle$ can be decomposed as the sum of four terms, a *stationary* covariance $\left\langle \overline{v_z^{st}{}'(z)v_z^{st}{}'(\xi)} \right\rangle$, a *dynamic* covariance, $\left\langle \overline{v_z^{dy}{}'(z,t)v_z^{dy}{}'(\xi,\tau)} \right\rangle$, and two terms involving *stationary* and *dynamic* velocity fluctuations, $\left\langle \overline{v_z^{st}{}'(z)v_z^{dy}{}'(\xi,\tau)} \right\rangle$ and $\left\langle \overline{v_z^{dy}{}'(z,t)v_z^{st}{}'(\xi)} \right\rangle$ (called rispectivly *stationary-dynamic* and *dynamic-stationary* velocity covariances). Exploiting (C.3.5)-(C.3.6) and remembering (3.11) $\left\langle \overline{v_z^{st}{}'(z)v_z^{dy}{}'(\xi,\tau)} \right\rangle$ can be written as

$$\begin{aligned} \left\langle \overline{v_z^{st}{}'(z)v_z^{dy}{}'(\xi,\tau)} \right\rangle &= -\frac{1}{\phi}\left[\frac{\partial}{\partial \xi}\left\langle \overline{Y(z)p^{dy}{}'(\xi,\tau)} \right\rangle - \frac{1}{\phi}\frac{\partial^2}{\partial z \partial \xi}\left\langle \overline{p^{st}{}'(z)p^{dy}{}'(\xi,\tau)} \right\rangle \right] \\ &\quad -\frac{\mathrm{N_g}}{\phi}\left[\left\langle \overline{Y(z)C'(\xi,\tau)} \right\rangle - \frac{1}{\phi}\left\langle \overline{\frac{\partial p^{st}{}'(z)}{\partial z}C'(\xi,\tau)} \right\rangle \right] \end{aligned} \tag{D.3.2}$$

The first term on r.h.s of (D.3.2) can be computed, making use of (C.3.14), as

$$\begin{aligned} -\frac{1}{\phi}\frac{\partial}{\partial \xi}\left\langle \overline{Y(z)p^{dy}{}'(\xi,\tau)} \right\rangle &= -\frac{1}{\phi}\frac{1}{D}\int_0^D \frac{\partial}{\partial \xi}\left\langle Y(z,y)p^{dy}{}'(\xi,y,\tau) \right\rangle dy \\ &= \frac{\mathrm{N_g}}{\phi}\frac{1}{D}\int_0^D\int_0^H\int_0^D \frac{\partial}{\partial \hat{\xi}}\left\langle Y(z,y)C'(\hat{\eta},\hat{\xi},\tau) \right\rangle \frac{\partial}{\partial \xi} G^F(y,\xi;\hat{\eta},\hat{\xi})\,d\hat{\eta}\,d\hat{\xi}\,dy \end{aligned} \tag{D.3.3}$$

We then approximate $G^F(y,\xi;\hat{\eta},\hat{\xi})$ as

$$G^F(y,\xi;\hat{\eta},\hat{\xi}) = \delta(y-\hat{\eta})G^F(\xi;\hat{\xi}) \tag{D.3.4a}$$

with (Butkovskiy and Longdon, 1982)

$$G^F(\xi;\hat{\xi}) = \begin{cases} \ln\dfrac{H}{H-\xi} - 2\sum\limits_{n=1}^{\infty} I_0\left(\lambda_n,\hat{\xi}\right)\left[\dfrac{K_0\left(\lambda_n,H\right)}{I_0\left(\lambda_n,H\right)} I_0\left(\lambda_n,H-\xi\right) - K_0\left(\lambda_n,H-\xi\right)\right] & if \quad 0 \le \xi \le H-\hat{\xi} \\ \ln\dfrac{H}{\hat{\xi}} - 2\sum\limits_{n=1}^{\infty} I_0\left(\lambda_n,H-\xi\right)\left[\dfrac{K_0\left(\lambda_n,H\right)}{I_0\left(\lambda_n,H\right)} I_0\left(\lambda_n,\hat{\xi}\right) - K_0\left(\lambda_n,\hat{\xi}\right)\right] & if \quad H-\hat{\xi} \le \xi \le H \end{cases} \tag{D.3.4b}$$

Here I_0 and K_0 are the modified Bessel function of first and second kind respectively and $\lambda_n = n\pi / H$. Making use of (D.3.4a)-(D.3.4b), equation (D.3.3) becomes

$$\begin{aligned} -\frac{1}{\phi}\frac{\partial}{\partial\xi}\left\langle \overline{Y(z)p^{dy}\,'(\xi,\tau)} \right\rangle &\approx \frac{\mathrm{N_g}}{\phi}\frac{1}{D}\int_0^H\int_0^D \frac{\partial}{\partial\hat{\xi}}\left\langle Y(z,y)C'(\hat{\eta}=y,\hat{\xi},\tau)\right\rangle \frac{\partial}{\partial\xi}G^F(\xi;\hat{\xi})dyd\hat{\xi} \\ &= \frac{\mathrm{N_g}}{\phi}\int_0^H \frac{\partial}{\partial\hat{\xi}}\left\langle \overline{Y(z)C'(\hat{\xi},\tau)} \right\rangle \frac{\partial}{\partial\xi}G^F(\xi;\hat{\xi})d\hat{\xi} \end{aligned} \tag{D.3.5}$$

Adopting the same strategy allows to obtain the following expressions for the remaining terms of (D.3.2)

$$\begin{aligned} \frac{1}{\phi^2}\frac{\partial^2}{\partial z\partial\xi}\left\langle \overline{p^{st}\,'(z)p^{dy}\,'(\xi,\tau)} \right\rangle &= \frac{1}{\phi^2}\frac{1}{D}\int_0^D \frac{\partial^2}{\partial z\partial\xi}\left\langle p^{st}\,'(y,z)p^{dy}\,'(y,\xi,\tau)\right\rangle dy \\ &= -\frac{\mathrm{N_g}}{\phi}\frac{1}{D}\int_0^D\int_0^D\int_0^H\int_0^D\int_0^H \frac{\partial^2}{\partial\tilde{\xi}\partial\xi}\left\langle Y(\tilde{\eta},\tilde{\xi})C'(\eta,\xi,\tau)\right\rangle \frac{\partial}{\partial\xi}G^F(y,\xi;\eta,\xi)\frac{\partial}{\partial z}G^F(y,z;\tilde{\eta},\tilde{\xi})d\eta d\xi dy d\tilde{\eta} d\tilde{\xi} \\ &\approx -\frac{\mathrm{N_g}}{\phi}\frac{1}{D}\int_0^H\int_0^D\int_0^H \frac{\partial^2}{\partial\tilde{\xi}\partial\xi}\left\langle Y(y,\tilde{\xi})C'(y,\xi,\tau)\right\rangle \frac{\partial}{\partial\xi}G^F(\xi;\hat{\xi})\frac{\partial}{\partial z}G^F(z;\tilde{\xi})dyd\widehat{\xi d\tilde{\xi}} \\ &= -\frac{\mathrm{N_g}}{\phi}\int_0^H\int_0^H \frac{\partial^2}{\partial\tilde{\xi}\partial\xi}\left\langle \overline{Y(\tilde{\xi})C'\widehat{(\xi,\tau)}} \right\rangle \frac{\partial}{\partial\xi}G^F(\xi;\hat{\xi})\frac{\partial}{\partial z}G^F(z;\tilde{\xi})d\widehat{\xi d\tilde{\xi}} \end{aligned} \tag{D.3.6}$$

and

$$\begin{aligned} \frac{\mathrm{N_g}}{\phi^2}\frac{\partial}{\partial z}\left\langle \overline{p^{st}\,'(z)C'(\xi,\tau)} \right\rangle &= \frac{\mathrm{N_g}}{\phi}\frac{1}{D}\int_0^D\int_0^D\int_0^H \frac{\partial}{\partial\tilde{\xi}}\left\langle Y(\tilde{\eta},\tilde{\xi})C'(y,\xi,\tau)\right\rangle \frac{\partial}{\partial z}G^F(y,z;\tilde{\eta},\tilde{\xi})d\tilde{\eta}d\tilde{\xi}dy \\ &\approx \frac{\mathrm{N_g}}{\phi}\frac{1}{D}\int_0^D\int_0^H \frac{\partial}{\partial\tilde{\xi}}\left\langle Y(y,\tilde{\xi})C'(y,\xi,\tau)\right\rangle \frac{\partial}{\partial z}G^F(z;\tilde{\xi})d\tilde{\xi}dy \\ &= \frac{\mathrm{N_g}}{\phi}\int_0^H \frac{\partial}{\partial\tilde{\xi}}\left\langle \overline{Y(\tilde{\xi})C'(\xi,\tau)} \right\rangle \frac{\partial}{\partial z}G^F(z;\tilde{\xi})d\tilde{\xi} \end{aligned} \tag{D.3.7}$$

Substituting (D.3.5)-(D.3.7) into (D.3.2) we finally obtain

$$\left\langle \overline{v_z^{st}{}'(z)v_z^{dy}{}'(\xi,\tau)} \right\rangle \approx \frac{\mathrm{N_g}}{\phi} \left\{ \begin{array}{l} -\left\langle \overline{Y(z)C'(\xi,\tau)} \right\rangle - \\ -\int\limits_0^H \int\limits_0^H \frac{\partial^2}{\partial\tilde{\xi}\partial\xi} \left\langle \overline{Y(\tilde{\xi})C'(\xi,\tau)} \right\rangle \frac{\partial}{\partial z} G^F(z;\tilde{\xi}) \frac{\partial}{\partial\xi} G^F(\xi;\hat{\xi}) d\xi d\tilde{\xi} \\ +\int\limits_0^H \frac{\partial}{\partial\tilde{\xi}} \left\langle \overline{Y(\tilde{\xi})C'(\xi,\tau)} \right\rangle \frac{\partial}{\partial z} G^F(z;\tilde{\xi}) d\tilde{\xi} + \\ +\int\limits_0^H \frac{\partial}{\partial\hat{\xi}} \left\langle \overline{Y(z)C'(\hat{\xi},\tau)} \right\rangle \frac{\partial}{\partial\xi} G^F(\xi;\hat{\xi}) d\hat{\xi} \end{array} \right\} \qquad \text{(D.3.8)}$$

Equation (D.3.8) highlights that $\left\langle \overline{v_z^{st}{}'(z)v_z^{dy}{}'(\xi,\tau)} \right\rangle$ depends linearly on the dimensionless group $\mathrm{N_g}/\phi$ and it is a function of the cross-covariance $\left\langle \overline{Y(z)C'(\xi,\tau)} \right\rangle$.

In a similar way $\left\langle \overline{v_z^{dy}{}'(z,t)v_z^{st}{}'(\xi)} \right\rangle$ becomes:

$$\left\langle \overline{v_z^{dy}{}'(z,t)v_z^{st}{}'(\xi)} \right\rangle \approx \frac{\mathrm{N_g}}{\phi} \left\{ \begin{array}{l} -< \overline{C'(z,t)Y(\xi)} > - \\ -\int\limits_0^H \int\limits_0^H \frac{\partial^2}{\partial\tilde{\xi}\partial\xi} \left\langle \overline{Y(\tilde{\xi})C'(\xi,t)} \right\rangle \frac{\partial}{\partial z} G^F(z;\xi) \frac{\partial}{\partial\xi} G^F(\xi;\tilde{\xi}) d\xi d\tilde{\xi} + \\ +\int\limits_0^H \frac{\partial}{\partial\hat{\xi}} \left\langle \overline{C'(z,t)Y(\hat{\xi})} \right\rangle \frac{\partial}{\partial\xi} G^F(\xi;\hat{\xi}) d\hat{\xi} + \\ +\int\limits_0^H \frac{\partial}{\partial\hat{\xi}} \left\langle \overline{Y(\xi)C'(\hat{\xi},t)} \right\rangle \frac{\partial}{\partial z} G^F(z;\hat{\xi}) d\hat{\xi} \end{array} \right\} \qquad \text{(D.3.9)}$$

and the *dynamic*-*dynamic* velocity covariance, $\left\langle \overline{v_z^{dy}{}'(z,t)v_z^{dy}{}'(\xi,\tau)} \right\rangle$, can be written as

$$\left\langle \overline{v_z^{dy}{}'(z,t)v_z^{dy}{}'(\xi,\tau)} \right\rangle \approx \left(\frac{\mathrm{N_g}}{\phi} \right)^2 \left\{ \begin{array}{l} \left\langle \overline{C'(z,t)C'(\xi,\tau)} \right\rangle + \\ +\int\limits_0^H \int\limits_0^H \frac{\partial^2}{\partial\tilde{\xi}\partial\hat{\xi}} \left\langle \overline{C'(\hat{\xi},t)C'(\tilde{\xi},\tau)} \right\rangle \frac{\partial}{\partial z} G^F(z;\hat{\xi}) \frac{\partial}{\partial\xi} G^F(\xi;\tilde{\xi}) d\tilde{\xi} d\hat{\xi} \\ -\int\limits_0^H \frac{\partial}{\partial\hat{\xi}} \left\langle \overline{C'(\hat{\xi},t)C'(\xi,\tau)} \right\rangle \frac{\partial}{\partial z} G^F(z;\hat{\xi}) d\hat{\xi} - \\ -\int\limits_0^H \frac{\partial}{\partial\hat{\xi}} \left\langle \overline{C'(\hat{\xi},\tau)C'(z,t)} \right\rangle \frac{\partial}{\partial\xi} G^F(\xi;\hat{\xi}) d\hat{\xi} \end{array} \right\}$$

(D.3.10)

Equation (D.3.10) highlights that $\left\langle \overline{v_z^{dy}{}'(z,t)v_z^{dy}{}'(\xi,\tau)} \right\rangle$ depends linearly on the dimensionless group $\left(\mathrm{N_g}/\phi\right)^2$ and it is a function of $\left\langle \overline{C'(z,t)C'(\xi,\tau)} \right\rangle$, i.e. the horizontal spatial mean of concentration covariance.

Finally the *stationary*-*stationary* velocity covariance becomes

$$\left\langle \overline{v_z^{st}\,'(z) v_z^{st}\,'(\xi)} \right\rangle \approx \left\{ \begin{array}{l} \left\langle \overline{Y(z)Y(z)} \right\rangle + \\ + \int_0^H \int_0^H \frac{\partial^2}{\partial\hat{\xi}\partial\tilde{\xi}} \left\langle Y(\hat{\xi})Y(\tilde{\xi}) \right\rangle \frac{\partial}{\partial\xi} G^F(\xi;\hat{\xi}) \frac{\partial}{\partial z} G^F(z;\tilde{\xi}) d\hat{\xi} d\tilde{\xi} - \\ - \int_0^H \frac{\partial}{\partial\hat{\xi}} \left\langle \overline{Y(z)Y(\hat{\xi})} \right\rangle \frac{\partial}{\partial\xi} G^F(\xi;\hat{\xi}) d\hat{\xi} - \\ - \int_0^H \frac{\partial}{\partial\hat{\xi}} \left\langle Y(\xi)Y(\hat{\xi}) \right\rangle \frac{\partial}{\partial z} G^F(z;\hat{\xi}) d\hat{\xi} \end{array} \right\} \tag{D.3.11}$$

Note that $\left\langle \overline{v_z^{st}\,'(z) v_z^{st}\,'(\xi)} \right\rangle$ is a function of the covariance of *Y*.

We now introduce the following notation

$$\begin{aligned} \left\langle \overline{v'_z(z,t) v'_z(\xi,\tau)} \right\rangle &= \mathbf{A}\left\{ \left\langle \overline{Y(z)Y(\xi)} \right\rangle \right\} + \left(\frac{\mathrm{N_g}}{\phi} \right) \mathbf{B}\left\{ \left\langle \overline{Y(z)C'(\xi,\tau)} \right\rangle \right\} + \\ &+ \left(\frac{\mathrm{N_g}}{\phi} \right) \mathbf{C}\left\{ \left\langle \overline{C'(z,t)Y(\xi)} \right\rangle \right\} + \left(\frac{\mathrm{N_g}}{\phi} \right)^2 \mathbf{D}\left\{ \left\langle \overline{C'(z,t)C'(\xi,\tau)} \right\rangle \right\} \end{aligned} \tag{D.3.12}$$

where operators $\mathbf{A}\{\ \}$, $\mathbf{B}\{\ \}$, $\mathbf{C}\{\ \}$, $\mathbf{D}\{\ \}$ are respectively defined by the terms in parenthesis right hand side of (D.3.11), (D.3.8), (D.3.9) and (D.3.10). As highlighted by (D.3.12), in order to determine $\left\langle \overline{v'_z(z,t) v'_z(\xi,\tau)} \right\rangle$ we need to derive the equations satisfied by the cross covariances $\left\langle \overline{C'(z,t)Y(\xi)} \right\rangle$ and $\left\langle \overline{C'(z,t)C'(\xi,\tau)} \right\rangle$. These expressions are derived in Appendix E.3 and F.3, respectively.

Appendix E.3 Cross covariance between permeability and concentration

In this section we derive the horizontal spatial mean of cross-covariance between the log permeability and concentration, i.e. $\left\langle \overline{Y(z)C'(\xi,\tau)} \right\rangle$. Multiplying (A.3.8) by $Y(y,z)$, applying (3.13) and the ensemble average operator, making use of (A.3.10) and disregarding products of fluctuations larger than two, we obtain

$$\begin{aligned} \left\langle \overline{Y(z)C'(\xi,\tau)} \right\rangle &= \frac{1}{D} \int_0^D \left\langle Y(z,y) C'(\eta = y, \xi, \tau) \right\rangle dy \\ &= -\frac{1}{D} \int_0^t \int_0^H \int_0^D \left\langle Y(z,y) v_z\,'(y,\hat{\xi},\hat{\tau}) \right\rangle \frac{\partial}{\partial\hat{\xi}} \left\langle \overline{C}(\hat{\xi},\hat{\tau}) \right\rangle G_z^T(\xi,\tau,\hat{\xi},\hat{\tau}) d\hat{\xi} d\hat{\tau} dy \\ &= -\int_0^t \int_0^H \left\langle \overline{Y(z) v_z\,'(\hat{\xi},\hat{\tau})} \right\rangle \frac{\partial}{\partial\hat{\xi}} \left\langle \overline{C}(\hat{\xi},\hat{\tau}) \right\rangle G_z^T(\xi,\tau,\hat{\xi},\hat{\tau}) d\hat{\xi} d\hat{\tau} dy \end{aligned} \tag{E.3.1}$$

Recalling (C.3.5)-(C.3.6), equation (E.3.1) becomes

$$\left\langle \overline{Y(z)C'(\xi,\tau)} \right\rangle = -\int_0^t \int_0^H \frac{\partial}{\partial \hat{\xi}} \left\langle \overline{C}(\hat{\xi},\hat{\tau}) \right\rangle G_z^T(\xi,\tau,\hat{\xi},\hat{\tau})$$
$$\left\{ \left\langle \overline{Y(z)Y(\hat{\xi})} \right\rangle - \frac{\mathrm{Re}}{\phi} \frac{\partial}{\partial \hat{\xi}} \left\langle \overline{Y(z)p^{st}{}'(\hat{\xi})} \right\rangle - \frac{\mathrm{N_g}\,\beta}{\phi} \left\langle \overline{Y(z)C'(\hat{\xi},\hat{\tau})} \right\rangle - \frac{\mathrm{Re}}{\phi} \frac{\partial}{\partial \hat{\xi}} \left\langle \overline{Y(z)p^{dy}{}'(\hat{\xi},\hat{\tau})} \right\rangle \right\} d\hat{\xi}\, d\hat{\tau} \tag{E.3.2}$$

A numerically analysis of (E.3.2) (details not shown) shows that, for the test cases considered in this work, it is possible to disregard the last term on the r.h.s. of (E.3.2). Introducing the operator $\mathbf{F}\{\ \}$ defined as

$$\mathbf{F}\left\{ \Theta(z;\xi,\hat{\tau}) \right\} = -\int_0^t \int_0^H \Theta(z;\xi,\hat{\tau}) G_z^T(\xi,\tau,\hat{\xi},\hat{\tau}) \frac{\partial}{\partial \hat{\xi}} \left\langle \overline{C}(\hat{\xi},\hat{\tau}) \right\rangle d\hat{\xi}\, d\hat{\tau} \qquad , \tag{E.3.3}$$

we rewrites (E.3.2) as

$$\left\langle \overline{Y(z)C'(\xi,\tau)} \right\rangle + \frac{\mathrm{N_g}}{\phi} \mathbf{F}\left\{ \left\langle \overline{Y(z)C'(\hat{\xi},\hat{\tau})} \right\rangle \right\} = \mathbf{F}\left\{ \left\langle \overline{Y(z)Y(\hat{\xi})} \right\rangle \right\} - \frac{1}{\phi} \mathbf{F}\left\{ \frac{\partial}{\partial \hat{\xi}} \left\langle \overline{Y(z)p^{st}{}'(\hat{\xi})} \right\rangle \right\} \tag{E.3.4}$$

Equation (E.3.4) furnishes the link amongst the cross-covariance between the permeability and the concentration field, $\left\langle \overline{Y(z)C'(\xi,\tau)} \right\rangle$, and (*i*) the covariance of the underlying permeability field, $\left\langle \overline{Y(z)Y(\xi)} \right\rangle$, (*ii*) the cross-covariance between *stationary* pressure and permeability, i.e. $\left\langle \overline{Y(z)p^{st}{}'(\xi)} \right\rangle$. Introducing the dimensionless hydraulic head, *h*, defined as $h = p^{st} / g\rho_f + z$, with $g = \sqrt{\tilde{k}^*} g^* / v^2{}_{z,BC}{}^*$ being the dimensionless gravity, (E.3.4) can be written as

$$\left\langle \overline{Y(z)C'(\xi,\tau)} \right\rangle = \mathbf{F}\left\{ \left\langle \overline{Y(z)Y(\hat{\xi})} \right\rangle \right\} - \frac{\mathrm{C}}{\phi} \mathbf{F}\left\{ \frac{\partial}{\partial \hat{\xi}} \left\langle \overline{Y(z)h'(\hat{\xi})} \right\rangle \right\} - \frac{\mathrm{N_g}}{\phi} \mathbf{F}\left\{ \left\langle \overline{Y(z)C'(\hat{\xi},\hat{\tau})} \right\rangle \right\} \tag{E.3.5}$$

where $\left\langle \overline{Y(z)h'(\hat{\xi})} \right\rangle$ is the cross-covariance between permeability and hydraulic head in case of constant density and $\mathrm{C} = \rho_f^* \sqrt{\tilde{k}^*} g^* / v^2{}_{z,BC}{}^* \Delta\rho$ is constant of conversion between the dimensionless pressure and hydraulic head. The last term on right hand side of (E.3.5) take into account the stabilizing buoyancy effects which reduce the correlation between permeability and concentration, see Section 3.3.2.

Appendix F.3 Concentration Covariance

In this section we derive the equation satisfied by the horizontal spatial mean of concentration covariance, $\left\langle \overline{C'(z,t)C'(\xi,\tau)} \right\rangle$. Multiplying (A.3.8) by $C'(\eta,\xi,\tau)$, taking the ensemble mean operator, making use of (A.10) and neglecting terms involving power of fluctuations larger than two we obtain

$$\left\langle C'(z,y,t)C'(\xi,\eta,\tau)\right\rangle = -\int_0^H\int_0^t \left\langle v_z'(\hat{\eta}=\eta,\hat{\xi},\hat{\tau})C'(z,y,t)\right\rangle)\frac{\partial}{\partial\hat{\xi}}\left\langle\overline{C}(\hat{\xi},\hat{\tau})\right\rangle G_z^T(\xi,\tau,\hat{\xi},\hat{\tau})\,d\hat{\xi}\,d\hat{\tau} \qquad \text{(F.3.1)}$$

The term $\left\langle\overline{C'(z,t)C'(\xi,\tau)}\right\rangle$ is defined as

$$\left\langle\overline{C'(z,t)C'(\xi,\tau)}\right\rangle = \frac{1}{D}\int_0^D \left\langle C'(\eta=y,\xi,\tau)C'(z,y,t)\right\rangle dy \qquad \text{(F.3.2)}$$

Recalling (C.3.5)-(C.3.6), equation (F.3.2) becomes

$$\left\langle\overline{C'(z,t)C'(\xi,\tau)}\right\rangle = -\int_0^H\int_0^t \frac{\partial}{\partial\hat{\xi}}\left\langle\overline{C}(\hat{\xi},\hat{\tau})\right\rangle G_z^T(\xi,\tau,\hat{\xi},\hat{\tau})$$

$$\left(\left\langle\overline{Y(\hat{\xi})C'(z,t)}\right\rangle - \frac{1}{\phi}\frac{\partial}{\partial\hat{\xi}}\left\langle\overline{C'(z,t)p^{st}{}'(\hat{\xi})}\right\rangle - \frac{\mathrm{N}_g}{\phi}\left\langle\overline{C'(z,t)C'(\hat{\xi},\hat{\tau})}\right\rangle - \frac{1}{\phi}\frac{\partial}{\partial\hat{\xi}}\left\langle\overline{C'(z,t)p^{dy}{}'(\hat{\xi},\hat{\tau})}\right\rangle\right)d\hat{\xi}\,d\hat{\tau}$$

(F.3.3)

A numerically analysis of (F.3.3) (details not shown) shows that, for the test cases considered in this work, it is possible to disregard the last term on the r.h.s. of (F.3.3). Introducing the operator $\mathbf{H}\{\ \}$ defined as

$$\mathbf{H}\left\{\Theta(z,t;\xi,\hat{\tau})\right\} = -\int_0^t\int_0^H \Theta(z,t;\xi,\hat{\tau})G_z^T(\xi,\tau,\hat{\xi},\hat{\tau})\frac{\partial}{\partial\hat{\xi}}\left\langle\overline{C}(\hat{\xi},\hat{\tau})\right\rangle d\xi\,d\hat{\tau} \qquad \text{(F.3.4)}$$

equation (F.3.3) becomes

$$\left\langle\overline{C'(z,y,t)C'(\xi,\eta,\tau)}\right\rangle = \mathbf{H}\left\{\left\langle\overline{Y(\hat{\xi})C'(z,t)}\right\rangle\right\} - \frac{1}{\phi}\mathbf{H}\left\{\frac{\partial}{\partial\hat{\xi}}\left\langle\overline{C'(z,t)p^{st}{}'(\hat{\xi})}\right\rangle\right\} - \frac{\mathrm{N_g}}{\phi}\mathbf{H}\left\{\left\langle\overline{C'(z,t)C'(\hat{\xi},\hat{\tau})}\right\rangle\right\}$$

(F.3.5)

The last term in (F.3.5) present the effects of the stabilizing buoyancy effects which leads to a reduction in the concentration variance, see Section 3.3.3. Finally, making use of (C.3.10) and (D.3.4a), equation (F.3.5) can be written as

$$\left\langle\overline{C'(z,y,t)C'(\xi,\eta,\tau)}\right\rangle + \frac{\mathrm{N_g}}{\phi}\mathbf{H}\left\{\left\langle\overline{C'(z,t)C'(\hat{\xi},\hat{\tau})}\right\rangle\right\} =$$

$$\mathbf{H}\left\{\left\langle\overline{Y(\hat{\xi})C'(z,t)}\right\rangle\right\} - \mathbf{H}\left\{\frac{\partial}{\partial\hat{\xi}}\int_0^H\frac{\partial}{\partial\tilde{\xi}}\left\langle\overline{C'(z,t)Y(\tilde{\xi})}\right\rangle G^F(\hat{\xi};\tilde{\xi})\,d\tilde{\xi}\right\} \qquad \text{(F.3.6)}$$

References

Abarca, E., Carrera, J., Sanchez-Vila, X. and Dentz, M.: Anisotropic dispersive Henry problem, Adv. Water Resour., 30(4),913-26, http://dx.doi.org/10.1016/j.advwatres.2006.08.005, 2007.

Alkindi, A., Al-Wahaibi, Y., Bijelic, B. and Muggeridge, A.: Investigation of longitudinal and transverse dispersion in stable displacements with high viscosity and density contrast between the fluids, J. Contam. Hydrol., 120-121, 170-183, doi:10.1016/j.jconhyd.2010.06.006, 2011.

Bear, J. and Cheng, A.: Modelling Groundwater Flow and Transport, New York: Springer, p. 834, 2011.

Bianchi Janetti, E., Riva, M. and Guadagnini, A.: Three-Phase Permeabilities: Upscaling, Analytical Solutions and Uncertainty Analysis in Elementary Pore Structures, Transp. Porous. Med., 106, 259-283, doi 10.1007/s11242-014-0400-x, 2015.

Bolster, D., Neuwlier, I., Dentz, M. and Carrera, J.: The impact of buoyancy on front spreading in heterogeneous porous media in two-phase immiscible flow, Water Resour. Res., 47:W02508, doi:10.1029/2010WR009399, 2011.

Bolster, D., Dentz, M. and Carrera, J.: Effective two phase flow in heterogeneous media under temporal pressure fluctuations, Water Resour. Res., 45:W05408, doi:10.1029/2008WR007460, 2009.

Boso, F., de Barros F. P. J., Fiori, A. and Bellin, A.: Performance analysis of statistical spatial measures for contaminant plume characterization toward risk-based decision making, Water Resour. Res., 49, 3119-3132, doi:10.1002/wrcr.20270, 2013.

Bouquain, J., Meheust, Y. and Davy, P.: Horizontal pre-asymptotic solute transport in a plane fracture with significant density contrasts, J. Contam. Hydrol., 120-121, 184-197, doi:10.1016/j.jconhyd.2010.08.002, 2011.

Buès, M. A. and Aachib, M.: Influence of the heterogeneity of the solutions on the parameters of miscible displacement in saturated porous medium, Exp. Fluids, 11(1), 25-32, 1991.

Ciriello, V., Guadagnini, A., Di Federico, V., Edery, Y. and Berkowitz, B.: Comparative analysis of formulations for conservative transport in porous media through sensitivity-based parameters calibration, Water Resour. Res., 49, 5206-5220, doi: 10.1002/wrcr.20395, 2013.

Cushman, J. H., Bennethum, L. S. and Hu, B. X.: A primer on upscaling tools for porous media, Adv. Water Res., 25, 1043-1067, 2002.

D'Angelo, M. V., Auradou, H., Allain, C., Rosen, M. and Hulin, J. P.: Dispersion enhancement and damping by buoyancy driven flows in two-dimensional networks of capillaries, Phys. Fluids, 20, 034107, http://dx.doi.org/10.1063/1.2899635, 2008.

Dagan, G.: Solute transport in heterogeneous porous formations, J. Fluid Mech., 145, 151-177, 1984.

Davit, Y., Bell, C. G., Byrne, H. M., Chapman, L. A. C., Kimpton, L. S., Lang, G. E., Leonard, K. H. L., Oliver, J. M., Pearson, N. C., Shipley, R. J., Waters, S. L., Whiteley, J. P., Wood, B. D., Quintard M.: Homogenization via formal multiscale asymptotics and volume averaging: how do the two techniques compare?, Adv. Water Resour., 62, 178-206, http://dx.doi.org/10.1016/j.advwatres.2013.09.006, 2013.

de Barros, F. P. J. and Dentz, M.: Pictures of blockscale transport: Effective versus ensemble dispersion and its uncertainty, Adv. Water Resour., 91, 11-22, doi:10.1016/j.advwaters.2016.03.004, 2015.

De Loubens, R. and Ramakrishnan, T. S.: Analysis and computation of gravity-induced migration in porous media, J. Fluid Mech., 675, 60-86, http://dx.doi.org/10.1017/S0022112010006440, 2011.

Demidov, D.: Mathematical modelling of nonlinear brine transport processes, Ph.D. Thesis, Kazan State Univeristy, Russia, 2006.

Dentz, M. and Carrera, J.: Effective solute transport in temporally fluctuating flow through heterogeneous media, Water Resour. Res., 41:W08414, doi:10.1029/2004WR003571, 2005.

Dentz, M., Tartakovsky, D. M., Abarca, E., Guadagnini, A., Sanchez-Vila, X. and Carrera, J.: Variable-density flow in porous media, J. Fluid Mech., 561, 209-35, http://dx.doi.org/10.1017/S0022112006000668, 2006.

Dentz, M. and Tartakovsky, D. M.: Abrupt-Interface Solution for Carbon Dioxide Injection into Porous Media, Transp. Porous Med., 79, 15-27, doi10.1007/s11242-008-9268-y, 2009.

Di Donato, G., Lu, H., Tavassoli, Z. and Blunt, M. J.: Multirate-Transfer dual porosity modelling of gravity drainage and imbibition, SPE Journal, 12(01), 77-88, http://dx.doi.org/10.2118/93144-PA, 2007.

Diersch, H. J. and Kolditz, O.: Variable-density flow and transport in porous media: approaches and challenges, Adv. Water Resour., 25(8-12), 899-944, doi:10.1016/S0309-1708(02)00063-5, 2002.

Dongxiao, Z.: Stochastic Methods for Flow in Porous Media, San Diego:Academic Press, 2002.

Edery, Y., Guadagnini, A., Scher, H. and Berkowitz, B.: Origins of anomalous transport in heterogenous media: Structural and dynamic controls, Water Resour. Res., 50, 1490-1505. doi:10.1002/2013WR015111, 2014.

Egorov, A. G., Demidov, D. E. and Schotting R. J.: On the interaction between gravity forces and dispersive brine fronts in micro-heterogeneous porous media, Adv. Water Resour., 28(1), 55-68, doi: 10.1016/j.advwatres.2004.09.004, 2005.

Flowers, T. C. and Hunt, J. R.: Viscous and gravitational contributions to mixing during vertical brine transport in water-saturated porous media, Water Resour. Res., 43:W01407, doi:10.1029/2005WR004773, 2007.

Ghelar, L. and Axness, A.: Three-dimensional stochastic analysis of macrodispersion in aquifers. Water Resour Res 1983;19(1):161–180.

Gramling, C. M., Harvey, C. F. and Meigs, L. C.: Reactive transport in porous media: A comparison of model prediction with laboratory visualization, Environ. Sci. Technol., 36, 2508-2514, doi:10.1021/es0157144, 2002.

Hagoort, J.: Oil recovery by gravity drainage. SPE Journal, 20(03), 139-150, http://dx.doi.org/10.2118/7424-PA, 1980.

Hassanizadeh, S. M. and Leijnse, A.: A non-linear theory of high-concentration-gradient dispersion in porous media, Adv. Water Resour., 18(4), 203-15, doi:10.1016/0309-1708(95)00012-8, 1995.

Held, R., Attinger, S. and Kinzelbach, W.: Homogenization and effective parameters for the Henry problem in heterogeneous formations, Water Resour. Res., 41, 1-14, http://dx.doi.org/10.1029/2004WR003674, 2005.

Jiao, C. Y. and Hötzl, H.: An experimental study of miscible displacements in porous media with variation of fluid density and viscosity, Transp. Porous Med., 54, 125-44, doi:10.1023/A:1026383019300, 2004.

Landman, A. J., Johannsen, K. and Schotting, R. J.: Density-dependent dispersion in heterogeneous porous media. Part I: A numerical study, Adv. Water Resour., 30(12), 2467-2480. doi:10.1016/j.advwatres.2007.05.016, 2007a.

Landman, A. J., Schotting, R. J., Egorov, A. and Demidov, D.: Density-dependent dispersion in heterogeneous porous media Part II: Comparison with nonlinear models, Adv. Water Resour., 30(12), 2481-2498, doi:10.1016/j.advwatres.2007.05.017, 2007b.

Leij, F. J. and Van Genuchten, M. T.: Analytical modeling of nonaqueous phase liquid dissolution with Green's function, Transp. Porous Med., 38, 141-166, doi:10.1023/A:1006611200487, 2000.

Loggia, D., Rakotomalala, N., Salin, D. and Yortsos, Y. C.: Phase diagram of miscible displacements in layered porous media, Europhys Lett., 36, 105-110, doi:10.1029/2001WR001244, 1990.

Kempers, L. J. T. M. and Haas, H.: The dispersion zone between fluids with different density and viscosity in a heterogeneous porous medium, J. Fluid Mech., 267, 299-324, http://dx.doi.org/10.1017/S0022112094001199, 1994.

Kerrou, J. and Renard, P.: A numerical analysis of dimensionality and heterogeneity effects on advective dispersive seawater intrusion processes, Hydrol. J., 18, 55-72, http://dx.doi.org/10.1007/s10040-009-0533-0, 2010.

Kretz, V., Berest, P., Hulin, J. P. and Salin, D.: An experimental study of the effects of density and viscosity contrasts on macrodispersion in porous media, Water Resour. Res., 39(2), 1032-1040, doi:10.1029/2001WR001244, 2003.

Konz, M., Younes, A., Ackerer, P., Fahs, M., Huggenberger, P. andZechner, E.: Variable-density flow in heterogeneous porous media - Laboratory experiments and numerical simulations, J. Contam. Hydrol., 108(3-4), 168-175, http://dx.doi.org/10.1016/j.jconhyd.2009.07.005, 2009.

Menand, T. and Woods, A. W.: Dispersion, scale, and time dependence of mixing zones under gravitationally stable and unstable displacements in porous media, Water Resour. Res., 41:W05014, http://dx.doi.org/10.1029/2004WR003701, 2005.

Monger, T. G., Ramos, J. C. and Thomas, J.: Light oil recovery from cyclic CO2 injection: influence of low pressure, impure CO2 and reservoir gas, SPE Reservoir Engineering, 6, 25-32, http://dx.doi.org/10.2118/18084-PA, 1991.

Morales-Casique, E., Neuman, S. P. and Guadagnini, A.: Non-local and localized analyses of non-reactive solute transport in bounded randomly heterogeneous porous media: Theoretical framework, Adv. Water Resour., 29, 1238-1255, 2006a.

Morales-Casique, E., Neuman, S. P. and Guadagnini, A.: Non-local and localized analyses of non-reactive solute transport in bounded randomly heterogeneous porous media: Computational analysis, Adv. Water Resour., 29, 1399-141, 2006b.

Moser, H.: Einfluß der Salzkonzentration auf die hydrodynamische Dispersion im porösen Medium, Mitteilung nr. 128, Technische Universität, Berlin, 1995.

Naff, R. L.: On the nature of the dispersive flux in saturated heterogeneous porous media, Water Resour. Res., 26(5), 1013-1026, 1990.

Neuman, S. P. and Tartakovsky, D. M.: Perspective on theories of non-Fickian transport in heterogeneous media, Adv. Water Resour., 32(5), 670-680, 2009.

Neuweiler, I., Attinger, S., Kinzelbach, W. and King, P.: Large scale mixing for immiscible displacement in heterogeneous porous media, Transp. Porous Med., 51(3), 287-314, doi:10.1023/A:1022370927468, 2003.

Nick, H. M., Schotting, R., Gutierrez-Neri, M. and Johannsen, K.: Modelling transverse dispersion and variable density flow in porous media, Transp. Porous Med., 78, 11-35, doi:10.1007/s11242-008-9277-x, 2009.

Oostrom, M., Dane, J. H., Güven, O. and Hayworth, J. S.: Experimental investigation of dense solute plumes in an unconfined aquifer model, Water Resour. Res., 28(9), 2315-2326, doi:10.1029/92WR01265, 1992a.

Oostrom, M., Hayworth, J. S., Dane, J. H. and Güven, O.: Behavior of dense aqueous leachate plumes in homogeneous porous media, Water Resour. Res., 28(8), 2123-2134, doi:10.1029/92WR00711, 1992b.

Pool, M., Carrera, J., Vilarrasa, V., Silva, O. and Ayora, C.: Dynamics and design of systems for geological storage of dissolved CO2, Adv. Water Resour., 62, 533-542, 2013.

Pool, M., Post, V. E. A. and Simmons, C. T.: Effects of tidal fluctuations and spatial heterogeneity on mixing and spreading in spatially heterogeneous coastal aquifers, Water Resour. Res., , 51(3), 1570-1585, doi:10.1002/2014WR016068, 2015.

Porta, G. M., Bijeljic, B., Blunt, M. J. and Guadagnini, A.: Continuum-scale characterization of solute transport based on pore-scale velocity distributions, Geophy. Res. Lett., 42(18), 7537-7545, doi:10.1002/2015GL065423, 2015.

Rhodes, M. E., Bijeljic, B. and Blunt, M. J.: A rigorous pore-to-field scale simulation methodology for single-phase flow based on continuous time random walk, SPE Journal, 14(1), 88-94, doi: 10.2118/106434-MS, 2009.

Riva, M., Guadagnini, A. and Dell'Oca A.: Probabilistic assessment of seawater intrusion under multiple sources of uncertainty, Adv. Water Resour., 75, 93-104, http://dx.doi.org/10.1016/j.advwatres.2014.11.002, 2015.

Sanchez-Vila, X., Fernàndez-Garcia, D. ans Guadagnini, A.: Interpretation of column experiments of transport of solutes undergoing an irreversible bimolecular reaction using a continuum approximation, Water Resour. Res., 46:W12510, doi:10.1029/2010WR009539, 2010.

Sebben, M. L., Werner, A. D. and Graf, T.: Seawater intrusion in fractured aquifers: A preliminary numerical investigation using a fractured Henry problem, Adv. Water Resour., 85, 93-108, doi:10.1016/j.advwatres.2015.09.013, 2015.

Siena, M., Guadagnini, A., Riva, M., Bijelijic, B., Perreira Nunes, J. P. and Blunt M. J.: Statistical scaling of pore-scale Lagrangian velocities in natural porous media, Phys. Rev. E, 90:023013, doi:10.1103/PhysRevE.90.023013, 2014.

Simmons, C. T., Fenstemaker, T. R. and Sharp, J. M.: Variable density groundwater flow and solute transport in heterogeneous porous media: Approaches, resolutions and future challenges, J. Contam. Hydrol., 52(1-4), 245-275, doi:10.1016/S0169-7722(01)00160-7, 2001.

Spagnuolo, M., Callegaro, C., Masserano, F., Nobilli, M., Sabatino, R. and Blunt M. J.: Low salinity waterflooding: from single well chemical tracer test interpretation to sector model forecast scenarios, SPE Improved Oil Recovery Conference, 11-13 April, Tulsa, Oklahoma, USA, 2016.

Spagnuolo, M,. Callegaro, C., Guadagnini, A. and Sabatino, R.: Low salinity waterflooding for enhanced oil recovery – stochastic model calibration and uncertainty quantification, IOR 2015 – 18th European Symposium on Improved Oil Recovery, Dresden, Germany, 2015.

Starke, B. and Koch, M.: Laboratory experiments and Monte Carlo simulations to validate a stochastic theory of density-dependent macrodispersion, CMWRXVI, 2006.

Sun, T., Mehmani, Y., Bhagmane, J. and Balhoff, M. T.: Pore to continuum upscaling of permeability in heterogeneous porous media using mortars, Int. J. Oil, Gas and Coal Technology, 5(2-3), 2012.

Tenchine, S. and Gouze, P.: Density contrast effects on tracer dispersion in variable aperture fractures, Adv. Water Resour., 28, 273-289, http://dx.doi.org/10.1016/j.advwatres.2004.10.009, 2015.

Voss, C. I. and Provost, A. M.: SUTRA, a model for saturate–unsaturated variable density groundwater with solute or energy transport, U. S. Geol. Surv. Water Resour. Invest. Rep., 02-4231, 2002.

Watson, S. J., Barry, D. A., Schotting, R. J. and Hassanizadeh, S. M.: Validation of classical density-dependent solute transport theory for stable, high concentration-gradient brine displacements in coarse and medium sands, Adv. Water Resour., 25, 611-35, doi:10.1016/S0309-1708(02)00022-2, 2002.

Welty, C. and Gelhar, L.: Stochastic analysis of the effect of fluid density and viscosity variability on macrodispersion in heterogeneous porous media, Water Resour. Res., 27(8), 2061-75, doi:10.1029/91WR00837, 1991.

Welty, C., Kane, III A. C. and Kaufman, L. J.: Stochastic analysis of transverse dispersion in density-coupled transport in aquifers, Water Resour. Res., 39(6):1150, doi:10.1029/2002WR001631, 2003.

Werner, A. D., Bakker, M., Post, V. E. A., Vandenbohede, A., Lu, C., Ataie-Ashtiani, B., Simmons, C. T. and Barry, D. A.: Seawater intrusion processes, investigation and management: recent advances and future challenges. Adv. Water Resour., 51, 3-26, http://dx.doi.org/10.1016/j.advwatres.2012.03.004, 2013.

Whitaker, S.: The Method of Volume Averaging, Kluwer, Dordrecht 1999.

Whitaker, S.: Flow in porous media I: a theoretical derivation of Darcy' law, Transp. Porous Med., 1, 3-25, 1986.

Woumeni, R. S. and Vauclin, M.: A field study of the coupled effects of aquifer stratification, fluid density, and groundwater fluctuations on dispersivity assessment, Adv. Water Resour., 29(7), 1037-1055, doi:10.1016/j.advwatres.2005.09.002, 2006.

Xu, X., Chen, S. and Zhang, D.: Convective stability analysis of the long-term storage of carbon dioxide in deep saline aquifers, Adv. Water Resour., 29(3), 397-407, doi:10.1016/j.advwatres.2005.05.008, 2005.

Zoia, A., Latrille, C., Beccantini, A. and Cartadale, A.: Spatial and temporal features of density-dependent contaminant transport: experimental investigation and numerical modelling, J. Contam. Hydrol., 109(1-4), 14-26, doi:10.1016/j.jconhyd.2009.07.006, 2009.

4 Variance-based Global Sensitivity Analysis of Hydrogeological Systems: Probabilistic Assessment of Seawater Intrusion under multiple sources of uncertainty

In this chapter, we perform variance-based Global Sensitivity Analysis (GSA) of complex hydrogeological systems. In particular we rely on the variance-based Sobol' indices to quantify the sensitivity of model output respect to model parameters. These last indices quantify the relative contribution of uncertain model inputs to the total variance of the model output of interest. Sobol' indices of a parameter close to zero means that the overall contribute of that parameter to the output variability, as quantified by the variance, is small. The opposite holds for parameter with Sobol' index close to one. Following these statements it is customary to determine the influence of a parameter, on the output, on the base of the associated Sobol' index. In this work, Sobol' indices are evaluated upon representing the investigated model output through a generalized Polynomial Chaos Expansion (gPCE) representation. The latter also serves as a surrogate model of the model output allowing to compute and analyze the probability density function (*pdf*) of the output in a Monte Carlo framework at an affordable computational cost. Such task may be impossible to achieve relaying on the complete mathematical description and associated numerical implementation for the complex problems analyzed in this work.

As first case of interest, we select the environmental issue of saltwater intrusion along coastal aquifer (Werner et al., 2013). The dependency of the density on the solute concentration rend coupled the flow and transport problems, leading to high level of nonlinearity in system. These aspects rend hard to understand clearly the influence of an input over an output quantity of interest. Moreover, the computational costs of the full numerical emulator are typically high for such coupled problem rendering unfeasible the uncertainty propagation within a Monte Carlo framework. These aspects motivate us to perform a GSA, relaying on a gPCE representation. The details about the evaluation of the Sobol' indices, construction of the gPCE and interpretation of the GSA results are described in the following, with reference to the scenario of seawater intrusion along coastal aquifers.

In Appendix B.4 we evaluate Sobol' indices, through the same procedure employed for the seawater intrusion problem, in the context of hydraulic fracturing operation in deep basins. The aim is to investigate model parameters influence over possible negative environmental consequences related with the hydraulic fracturing technology.

4.1 Introduction

Saltwater intrusion (SWI) is a critical and widespread contamination problem in coastal aquifers. The complex interactions between fresh and salt water, with particular emphasis on management issues, has been the subject of active and intense research, including, e.g., a recent series of works highlighted in a special issue of Hydrogeology Journal (Special issue on: Saltwater and freshwater interactions in coastal aquifers, 2010, Vol 18, No 1).

Analytical or semi-analytical solutions of SWI problems have been mainly developed for homogeneous aquifers and consider saltwater and fresh water as immiscible fluids separated by a sharp interface (e.g., Reilly and Goodman, 1985; Bear et al., 1999; Bear and Cheng, 2010; Bruggeman, 1999). Within this context, Dagan and Zeitoun (1998) illustrate a first attempt to analyze the effect of aquifer heterogeneity on SWI. These authors consider a vertical cross section of a confined aquifer with randomly layered permeability distribution and show that the variability of the position of the salt - fresh water interface (particularly the location of the toe) is markedly influenced by the permeability variance and integral scale. Al-Bitar and Ababou (2005) adopt a vertically-integrated sharp interface approach and analyze the effects of variability of aquifer properties on the saltwater wedge through numerical simulations within horizontal two-dimensional randomly heterogeneous unconfined aquifer. Chang and Yeh (2010) employ a spectral approach and determine the mean interface position and its associated variability due to heterogeneity of aquifer conductivity and to the spatial variability of recharge for an unconfined horizontal aquifer model.

A realistic approach dealing with SWI should explicitly account for the occurrence of a transition zone where variable density flow is coupled with a transport model. This coupling makes it difficult to obtain analytical solutions of SWI scenarios. Henry (1964) presents a semi-analytical solution for steady-state variable density flow taking place along a two-dimensional vertical cross-section in a homogeneous isotropic coastal aquifer. Since this is the only analytical solution available, it has been widely used as a benchmark problem to SWI numerical approaches (e.g., Simpson and Clement, 2004; Werner et al., 2013). Dentz et al. (2006) present a methodology conducive to an analytical solution of the Henry's problem in dimensionless form. The Henry's problem has limited use in practical applications because it considers only diffusion while dispersion is not simulated. Abarca et al. (2007) modified the Henry's problem upon introducing anisotropy in the conductivity tensor and a dispersion tensor to improve the representation of wide transition zones of the kind observed in several field sites. Held et al. (2005) investigated the Henry's problem within a randomly heterogeneous aquifer. Making use of the homogenization theory, these authors found that the effective conductivity and dispersion coefficients are not affected by density effects, the effective dispersivity being close to its local counterpart. Otherwise, Kerrou and Renard (2010) showed that macrodispersion coefficients differ from their local counterparts in two- and three-dimensional heterogeneous scenarios. The effect of density contrast on effective parameters has also been analyzed by Jiang et al. (2013) by way of a stationary spectral approach. A discussion of current challenges in modeling density driven flows in the subsurface is offered by Werner et al. (2013).

Here we consider the anisotropic dispersive Henry's problem introduced by Abarca et al. (2007). As key sources of model uncertainty we consider the following dimensionless parameters: (*i*) the gravity number, expressing the relative importance of buoyancy and viscous forces; (*ii*) the anisotropy ratio between aquifer vertical and horizontal permeabilities; (*iii*) the longitudinal and (*iv*) transverse Péclet numbers, quantifying the relative importance of the longitudinal and transverse dispersion on solute transport. These are critical in governing the general dynamics of density dependent flow and transport processes (see e.g., Kretz et al., 2003; Menand and Woods, 2005; Dentz et al., 2006; Abarca et al., 2007). We then focus on a number of dimensionless global quantities (GQs) which are controlled by these parameters and are relevant to describe key features of the saltwater wedge and the width of the mixing zone. These global descriptors, as well as all system states such as pressure, concentration and velocity distributions within in the aquifer, are affected by uncertainty due to the lack of knowledge of the characteristic model parameters (e.g., Rubin, 2003). Proper quantification of the uncertainty associated with the characterization of these GQs is of critical relevance for the management of coastal aquifers.

Propagation of model parameter uncertainty to a given quantity of interest can be quantified through a Global Sensitivity Analysis (GSA). Here, we employ a variance-based GSA which allows assessing the relative impact of the model uncertain input parameters on the variability of model outputs (Archer et al., 1997). We base our analysis on the Sobol' indices (Sobol, 2001), which are widely used sensitivity metrics and do not require any linearity assumptions in the underlying mathematical model of the system behavior.

Estimation of the Sobol' indices is traditionally performed by Monte Carlo (MC) sampling in the uncertain parameter space. Therefore their computation can become highly demanding in terms of CPU time when the dimension of the parameters space and the degree of complexity of the problem increase. In this context, estimation of the Sobol' indices is practically unfeasible in SWI problems because of the coupled nature of the flow and transport problems. We circumvent this problem upon relying on a generalized Polynomial Chaos Expansion (gPCE) approximation of the target GQs (e.g., Ghanem and Spanos, 1991; Le Maître and Knio, 2010;). This approach allows obtaining a surrogate model for a given quantity of interest and enables one to calculate the Sobol' indices analytically via a straightforward post-processing analysis (e.g. Crestaux et al., 2009; Sudret, 2008;). Examples of application of this technique include the study of flow and transport in heterogeneous porous media (e.g. Laloy et al., 2013). Formaggia et al. (2013) and Porta et al. (2014) demonstrate the reliability and computational efficiency of gPCE-based approaches in highly non-linear systems under the effect of mechanical and geochemical compaction processes.

The work is organized as follows. Section 4.2 presents the complete flow and transport mathematical model, the key dimensionless parameters governing the process and the global descriptors of interest. Section 4.3 is devoted to a brief description of the methodology we employ to perform GSA and to derive the gPCE surrogate model. Section 4.4 presents the setting analyzed and some details of the full and surrogate system models. In Section 4.5 we show the main results of our analysis in terms of the relative contribution of the uncertain parameters to the variance of each of the global quantities analyzed. We then study the joint and marginal probability density functions (*pdfs*) of these global quantities. We remark that these tasks are computationally unaffordable by making use of the complete system model, while they can be performed by means of the gPCE surrogate model. Moreover, our relying on the gPCE allows obtaining analytical expressions for the marginal *pdf* of the global quantities of interest.

4.2 Complete model and definition of the global quantities of interest

We consider the anisotropic dispersive Henry's problem introduced by Abarca et al. (2007). The setting is a modification of the original Henry's problem (Henry, 1964) and enables one to describe seawater intrusion in coastal aquifers in a way which renders vertical salinity distributions that mimic field evidences. Saltwater intrusion is modeled across a vertical cross-section of a homogeneous aquifer under isothermal conditions (see Figure 4.1). Fluid flow is governed by the mass balance and Darcy equations, i.e.

$$\frac{\partial(\phi\rho)}{\partial t} + \nabla\cdot(\rho\boldsymbol{q}) = 0\,; \quad \boldsymbol{q} = -\frac{\boldsymbol{k}}{\mu}\cdot\left(\nabla p + \rho g \nabla z\right) \tag{4.1}$$

where $\boldsymbol{q}$ [L T^{-1}] is specific discharge vector with components q_x and q_z respectively along x- and z-directions (see Figure 1); $\boldsymbol{k}$ [L^2] is the homogeneous and anisotropic diagonal permeability tensor with components $k_{11} = k_x$ and $k_{22} = k_z$, respectively along directions x and z; ϕ [-] is the porosity of the medium; μ [M L^{-1} T^{-1}] and ρ [M L^{-3}] respectively are dynamic viscosity and density of the fluid; p [M L^{-1} T^{-2}] is pressure; and g [L T^{-2}] is the gravitational constant. Solute transport is described by the advection-dispersion equation

$$\frac{\partial(\phi\rho C)}{\partial t}+\nabla\cdot(\rho C\boldsymbol{q})-\nabla\cdot\left[\rho\boldsymbol{D}\cdot\nabla C\right]=0 \tag{4.2}$$

Here C [-] is solute concentration and $\boldsymbol{D}$ [L^2 T^{-1}] is the dispersion tensor, whose entries are defined as

$$D_{xx}=\phi D_m+\left(\alpha_L\frac{q_x^2}{|\boldsymbol{q}|}+\alpha_T\frac{q_z^2}{|\boldsymbol{q}|}\right);\quad D_{zz}=\phi D_m+\left(\alpha_L\frac{q_z^2}{|\boldsymbol{q}|}+\alpha_T\frac{q_x^2}{|\boldsymbol{q}|}\right);\quad D_{xz}=D_{zx}=(\alpha_L-\alpha_T)\frac{q_x q_z}{|\boldsymbol{q}|} \tag{4.3}$$

where D_m is the molecular diffusion coefficient and α_L and α_T [L] respectively are the longitudinal and transverse dispersivity coefficients, which are considered as uniform in the system. Since molecular diffusion is commonly neglected in transport settings taking place in porous media under the conditions we consider (e.g. Fetter, 1999;), in the following we disregard the contribution of D_m in (4.3). Initial conditions corresponding to freshwater hydrostatic pressure distribution are set in the system. No-flow conditions are imposed at the bottom and top of the domain; constant freshwater influx, q_f, is prescribed along the inland boundary (x = 0), where C = 0; saltwater hydrostatic pressure distribution is imposed along the seaside boundary, $x = l$ (i.e., $p = \rho_s\, g\, (d - z)$, ρ_s being density of seawater) where the salt mass flux is set as

$$(\boldsymbol{q}C-\boldsymbol{D}\cdot\nabla C)\cdot\boldsymbol{n}=\begin{cases} q_x C & if \quad q_x>0 \\ q_x C_s & if \quad q_x<0 \end{cases} \qquad x=l \tag{4.4}$$

$\boldsymbol{n}$ and C_s respectively being the normal vector pointing outward from the aquifer and the concentration of salt in seawater (salinity). According to (4.4) water entering and leaving the system has salt concentration C_s and C, respectively. Key features and limitations of this schematization are illustrated in Abarca et al. (2007).

Closure of the system (4.1)-(4.4) is obtained upon specifying a constitutive relationship between fluid properties, ρ and μ, and salt concentration. For the range of concentrations typically associated with SWI (e.g. Bear and Cheng, 2011;), viscosity can be assumed as constant and the following linear relationship can be employed to describe the evolution of ρ with C

$$\rho=\rho_f+\left(\rho_s-\rho_f\right)\frac{C}{C_s} \tag{4.5}$$

ρ_f being the freshwater density.

Introducing the following dimensionless quantities

$$x'=\frac{x}{d};\quad z'=\frac{z}{d};\quad \nabla'=d\nabla\ ;\ t'=\frac{t}{d/q_f}\ ;\ \boldsymbol{q}'=\frac{\boldsymbol{q}}{q_f}\ ;\ \rho'=\frac{\rho}{\rho_s-\rho_f}=\frac{\rho}{\Delta\rho}\ ;\ p'=\frac{p}{\Delta\rho q_f^2} \tag{4.6}$$

equation (4.1) can be rewritten in dimensionless form as

$$\frac{\partial(\phi\rho')}{\partial t'}+\nabla'\cdot(\rho'\boldsymbol{q}')=0\,;\qquad \boldsymbol{q}'=-\boldsymbol{\Upsilon}N_g\left(\frac{q_f^2}{gd}\nabla' p'+\rho'\nabla' z'\right) \tag{4.7}$$

where $\boldsymbol{\Upsilon}$ is a diagonal matrix with entries $\Upsilon_{11}=1$ and $\Upsilon_{22}=r_k$, $r_k=k_z/k_x$ being the permeability anisotropy ratio, q_f^2 / gd is a representative Froude number, and $N_g = g\Delta\rho k_x / q_f \mu$ is the gravity number (e.g., Kempers and Haas, 1994; Menand and Woods, 2005).

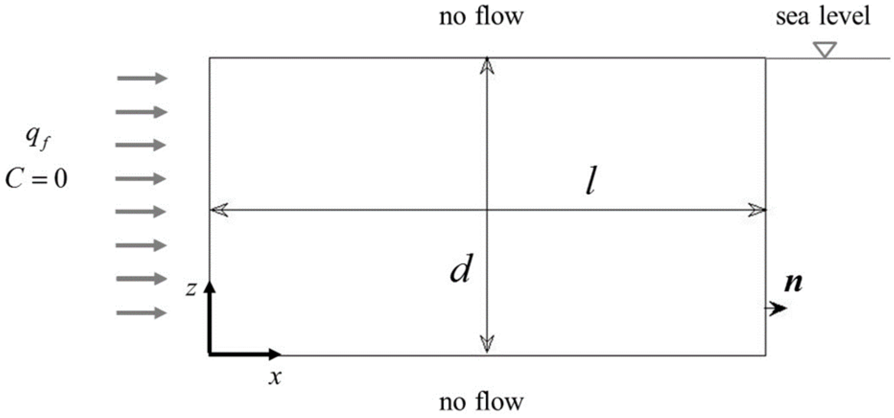

Figure 4.1. Scheck of the flow and transport test problem for the anisotropic dispersive Henry' problem here considered as conceptualization of seawater intrusion along coastal aquifer.

The transport equation can be written in dimensionless form as

$$\frac{\partial(\phi\rho' C')}{\partial t'} + \nabla' \cdot (\rho' C' \boldsymbol{q}') - \nabla' \cdot \left[\rho' \boldsymbol{D}' \cdot \nabla' C'\right] = 0 \tag{4.8}$$

with

$$D'_{xx} = \frac{1}{Pe_L}\frac{q'^2_x}{|\boldsymbol{q}'|} + \frac{1}{Pe_T}\frac{q'^2_z}{|\boldsymbol{q}'|}; \quad D'_{zz} = \frac{1}{Pe_L}\frac{q'^2_z}{|\boldsymbol{q}'|} + \frac{1}{Pe_T}\frac{q'^2_x}{|\boldsymbol{q}'|}; \quad D'_{xz} = D'_{zx} = \left(\frac{1}{Pe_T} - \frac{1}{Pe_L}\right)\frac{q'_x q'_z}{|\boldsymbol{q}'|} \tag{4.9}$$

where $Pe_L = d / \alpha_L$ and $Pe_T = d / \alpha_T$ are longitudinal and transverse Péclet number, respectively, and $C' = C / C_s$. Equations (4.7)-(4.9) highlight that the problem under investigation is governed by eight dimensionless quantities, i.e., ϕ, r_k, $\rho_f / \Delta\rho$, N_g, Pe_L, Pe_T, C_s and q_f^2 / gd.

Since point-wise measurements of state variables (e.g., salt concentration, velocity and pressure values) in SWI problems are usually scarce due to technical and economic constraints (e.g., Boso et al., 2013) in our study we focus on a global description of the process by considering dimensionless global quantities, GQs, that enable us to describe the overall seawater intrusion process. A similar approach has also been adopted by Abarca et al., 2007. The four GQs of interest (note that each GQ is rendered dimensionless by normalization through *d*) are depicted graphically in Figure 4.2 and defined in the following.

- The dimensionless toe penetration, *LT*. This corresponds to the inland penetration, measured along the bottom of the domain, of the 50% C' isoline. This metric characterizes the inland extent of the saltwater wedge.
- A measure, *LS*, of the spread of solute at the toe of the saltwater wedge. This is defined as the dimensionless distance, evaluated along the bottom of the domain, between the 20% and 80% C' isolines.
- The dimensionless average width of the mixing zone, *WD*. Here WD is evaluated as the average of *wmz*(*x*') within the region 0.2×*LT* ≤ *x*' ≤ 0.8×*LT; wmz*(*x*') being the dimensionless vertical distance between the 25% and 75% C' isolines (in case the 75% C' isoline has

intruded the domain up to a distance less than 0.8×*LT*, we consider *wmz*(*x*') as the vertical distance between the 25% C' isoline and the bottom of the aquifer).

- The dimensionless sinking of the saltwater wedge at the seaside boundary, *LY*. This is quantified as the dimensionless vertical distance between the bottom of the aquifer and the 50% C' contour curve at the seaside boundary.

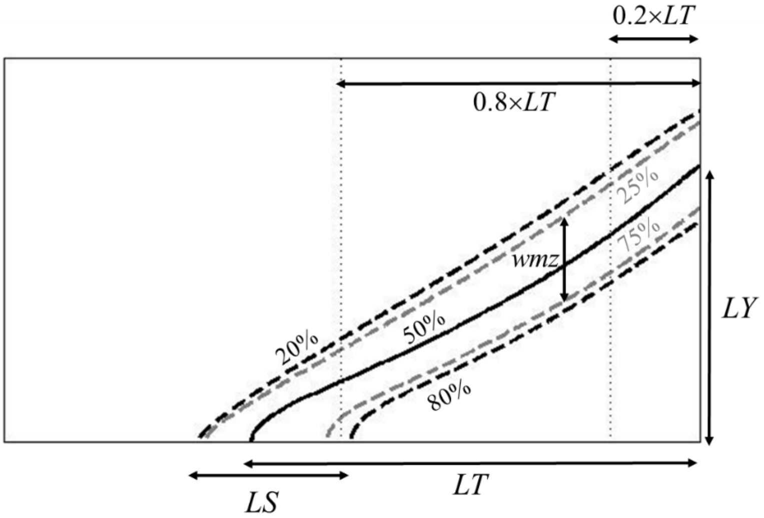

Figure 4.2. Schematic description of the target GQs. Iso-concentration line C' = 20% and 80% (dashed black), 25% and 75% (dashed grey), and 50% (solid black) are depicted.

4.3 Uncertainty quantification via global sensitivity analysis and generalized Polynomial Chaos Expansion

In this section we introduce the Sobol' indices that will be used to investigate the way lack of knowledge of key parameters appearing in the problem formulation (4.6)-(4.9) propagates to the selected global descriptors. We also briefly describe the way we alleviate the computational burden by introducing a surrogate model of the coupled flow-transport problem illustrated in Section 4.2.

As seen in previous Section 4.2, the seawater intrusion problem is governed by eight dimensionless quantities. Amongst these, we consider as uncertain the following four parameters: (*i*) the permeability anisotropy ratio , r_k , (*ii*) the longitudinal, Pe_L , and transverse, Pe_T , Péclet numbers, expressing the effect of the longitudinal and transverse dispersivity, and (*iii*) the gravity number, N_g , quantifying the relative importance of buoyancy and viscous forces. Uncertainty in these quantities is associated with our imperfect knowledge of the aquifer hydraulic (i.e., permeability tensor components) and dispersive parameters related to saltwater spreading in the system at the scale of observation.

We collect the four uncertain quantities N_g, r_k, Pe_L and Pe_T in a random parameter vector $\mathbf{x} \equiv (x_1, ..., x_N$; with $N = 4$) and treat each x_n as an independent random variable. The occurrence of correlation among entries of $\mathbf{x}$ could be included in the methodology (see, e.g., Li et al., 2009;). However, this would require the knowledge of the marginal probability density functions of the uncertain parameters and the associated correlation matrix. The type of correlations which can be found in the literature, e.g., between α_L and α_T (i.e., between Pe_L and Pe_T) are purely empirical and not generally supported by theoretical arguments. Due to the general lack of prior information on **x**, we also assume that each x_n can be described by a uniform distribution within the interval $\Gamma_n = [x_{n,min}, x_{n,max}]$.

This study is based on a global sensitivity analysis (GSA) which is performed through the evaluation of the variance-based Sobol' indices (e.g., Sobol, 1993; Archer et al., 1997;). The latter provide a description of the way the variability of a given quantity of interest, quantified in terms of its total variance, is affected (separately and jointly) by the random parameters collected in **x**. Sobol' indices provide generally robust results, as these are not constrained by any linearity assumption on the underlying mathematical model (Saltelli et al., 2006;) a feature which is particularly critical in a complex system of the kind we investigate.

A target quantity $y(\boldsymbol{x})$, representing a given GQ, which depends on N independent random variables can be decomposed as

$$y(\boldsymbol{x}) = y_0 + \sum_{x_i=1}^{N} y_{x_i}(x_i) + \sum_{x_i<x_j} y_{x_i,x_j}(x_i,x_j) + \ldots + y_{x_1,x_2,\ldots,x_N}(x_1,x_2,\ldots,x_N) \tag{4.10}$$

where

$$\begin{aligned} y_0 &= \int_{\Gamma} y(\boldsymbol{x})\rho_{\Gamma}(\boldsymbol{x})d\boldsymbol{x} \\ y_{x_i}(x_i) &= \int_{\Gamma\sim x_i} y(\boldsymbol{x})\rho_{\Gamma\sim x_i}(\boldsymbol{x})d\boldsymbol{x}_{\sim x_i} - y_0 \\ y_{x_i,x_j}(x_i,x_j) &= \int_{\Gamma\sim x_i,x_j} y(\boldsymbol{x})\rho_{\Gamma\sim x_i,x_j}(\boldsymbol{x})d\boldsymbol{x}_{\sim x_i,x_j} - y_{x_i i}(x_i) - y_{x_j}(x_j) - y_0 \end{aligned} \tag{4.11}$$

and so on. Here, $\rho_{\Gamma}(\boldsymbol{x})$ is the *pdf* of $\boldsymbol{x}$, $\Gamma = [\Gamma_{x_1} \times \ldots \Gamma_{x_N}]$ is the parameters space, $\int_{\Gamma\sim x_i} y(\boldsymbol{x})\rho_{\Gamma\sim x_i}(\boldsymbol{x})d\boldsymbol{x}_{\sim x_i}$ represents integration of $y(\boldsymbol{x})$ over the space of all entries of vector **x** excluding x_i, $\rho_{\Gamma\sim x_i}$ being the corresponding *pdf*. Note that y_0 in (4.10) is the mean of $y(\boldsymbol{x})$. The Sobol' index $S_{x_{i_1}, x_{i_2}, \ldots, x_{i_s}}$, embedding the mixed effects of $x_{i_1}, x_{i_2}, \ldots, x_{i_s}$ (Sobol, 1993, 2001;), is defined as

$$S_{x_{i_1}, x_{i_2}, \ldots, x_{i_s}} = \frac{1}{V_y} \int_{\Gamma_{x_{i_1}, x_{i_2}, \ldots, x_{i_s}}} y_{x_{i_1}, x_{i_2}, \ldots, x_{i_s}}(x_{i_1}, x_{i_2}, \ldots, x_{i_s})\rho_{\Gamma_{x_{i_1}, x_{i_2}, \ldots, x_{i_s}}}(\boldsymbol{x})dx_{i_1}\ldots dx_{i_s} \tag{4.12}$$

V_y being the total variance of $y(\boldsymbol{x})$, i.e.

$$V_y = \int_{\Gamma} y(\boldsymbol{x})^2 p_{\Gamma}(\boldsymbol{x})\, d\boldsymbol{x} - y_0{}^2 \tag{4.13}$$

From (4.12), the principal sensitivity index of x_n, denoted as S_{x_n}, describes the contribution of only x_n (without considering interactions with the other parameters) on the total variance, V_y. The overall contribution of parameter x_n to V_y is then given by the total sensitivity index

$$S_{x_i}^{T} = S_{x_i} + \sum_{x_j} S_{x_i,x_j} + \sum_{x_j,x_k} S_{x_i,x_j,x_k} + \ldots \tag{4.14}$$

and includes S_{x_n} and all the joint terms where x_n appears. Denoting by $S_{x_n}^{L}$ the contribution to S_{x_n} of the linear term associated with x_n, $S_{x_n}^{NL} = \left(S_{x_n}^{T} - S_{x_n}^{L}\right)$ represents the total contribution of non-linear terms involving x_n, i.e., $S_{x_n}^{NL}$ indicates the degree of nonlinearity of the input-output mapping of $y(\boldsymbol{x})$ with respect to x_n.

Computing the indices (4.12) requires multiple integrations of the model response $y(\boldsymbol{x})$ for diverse combinations of the uncertain parameters. This is typically achieved by numerical Monte Carlo simulation and the associated computational cost can be very high, depending on model complexity and on the number of random parameters considered, see Sudret, (2008).

The generalized Polynomial Chaos Expansion (gPCE) (e.g. Ghanem and Spanos, 1991; Le Maître and Knio, 2010; Sudret, 2008; Xiu and Karniadakis, 2002;) can be employed to build surrogate models of target quantities at a relatively affordable computational cost (see, e.g. Ciriello et al., 2013; Fajaouri et al., 2011; Formaggia et al., 2013; and references therein). As such, the gPCE approximation can be used to ascertain the way uncertainty associated with unknown model parameters propagates to system states of interest. In this context, the gPCE of $y(\boldsymbol{x})$ can be constructed as a spectral expansion of $y(\boldsymbol{x})$ in terms of a set of orthonormal polynomials representing a basis of the probabilistic space Γ within which an approximation of the model response surface is built. The specific family of polynomials which can be used depends on the probability distribution of the uncertain model parameters considered. Since each x_n is here assumed to be uniformly distributed, we adopt the family of multivariate Legendre polynomials (Xiu and Karniadakis, 2002;). The way a multidimensional Legendere polynomial is constructed starting from univariate Legendre polynomials is described by Gautschi (2004) to which we refer for additional details. The gPCE approximation of $y(\boldsymbol{x})$ can be constructed as

$$y(\boldsymbol{x}) \simeq \beta_0 + \sum_{i=1}^{N} \sum_{\boldsymbol{p}\in\Im_i} \beta_{\boldsymbol{p}} \psi_{\boldsymbol{p}}(\boldsymbol{x}) + \sum_{i=1}^{N} \sum_{j=1}^{N} \sum_{\boldsymbol{p}\in\Im_{i,j}} \beta_{\boldsymbol{p}} \psi_{\boldsymbol{p}}(\boldsymbol{x}) + ..., \qquad (4.15)$$

$$\psi_{\boldsymbol{p}}(\boldsymbol{x}) = \prod_{i=1}^{N} \psi_{i,p_i}(x_i), \quad \beta_{\boldsymbol{p}} = \int_{\Gamma} y(\boldsymbol{x}) \psi_{\boldsymbol{p}}(\boldsymbol{x}) \rho_{\Gamma}(\boldsymbol{x}) d\boldsymbol{x},$$

Here $\boldsymbol{p} = \{p_1, p_2, ..., p_N\} \in \mathbb{N}^N$ is a multi-index expressing the degree of each univariate Legendre polynomial, $\psi_{i,p_i}(x_i)$, employed to construct the multivariate orthogonal Legendre polynomial $\psi_{\boldsymbol{p}}(\boldsymbol{x})$, $\beta_{\boldsymbol{p}}$ is the associated polynomial coefficient, and $\Im_i$ contains all indices such that only the *i*-th component does not vanish, i.e., $\Im_i = \{\ p_i \neq 0, p_k = 0 \ \ for \ k \neq i\}$.

Considering (4.10)-(4.15) allows deriving the equivalence between the Sobol' indices and the coefficients $\beta_{\boldsymbol{p}}$ of the gPCE representation of $f(\boldsymbol{x})$, i.e.

$$S_{x_{i_1},...,x_{i_s}} = \frac{1}{V_y} \sum_{\boldsymbol{p}\in\Im_{i_1,...,i_s}} \beta_{\boldsymbol{p}}^2 \quad ; \qquad y_0 = \beta_0 \quad ; \qquad V_y = \sum_{\mathbf{p}\in\mathbb{N}^N} \beta_{\mathbf{p}}^2 \qquad (4.16)$$

Equation (4.16) can be rendered workable upon truncation of the summation to a set of polynomials with total degree w, i.e., $\sum_i p_i \leq w$. Other possible truncation schemes are discussed by Bäck et al. (2011). The accuracy of the resulting gPCE approximation increases with the regularity of $y(\boldsymbol{x})$ and as $w \to \infty$. This aspect is explored in Section 4.4.

4.4 Test Case description and Numerical Implementation

4.4.1 Complete Numerical Model

We solve the coupled flow and transport problem defined by (4.1)-(4.5) by means of the widely tested numerical code SUTRA, Voss and Provost (2002) within a homogeneous anisotropic porous medium with porosity ϕ = 35%. We set the height and length of the domain respectively to d = 1 m and l = 2 m (see Figure 4.1). The density of fresh and sea water are given respectively by ρ_f = 1000 kg/m^3 and ρ_s = 1025 kg/m^3, while the fluid viscosity is constant and equal to μ = 10^{-3} kg/m s. Freshwater enters the system with a Darcy velocity q_f = 6.6×10^{-5} m/s and the concentration of salt in seawater, C_S, is set equal to the standard value 35.7×10^{-3} kg/kg. As highlighted in Section 3, we treat N_g, r_k, Pe_L, and Pe_T as uncertain parameters. In this work we do not investigate the impact of the uncertainty of the geometrical setting, boundary conditions, and fresh and sea water density and viscosity. The intervals of variability of the four dimensionless uncertain parameters are listed in Table 4.1. The lower and upper bounds for each range of parameter variability have been selected on the basis of available information on the dimensional parameters involved in their definition. In our work the variability of N_g arises from the uncertainty in the horizontal permeability, having fixed the fluid properties and the inland freshwater flux. Since Pe_L, and Pe_T affect solute spreading (e.g. Volker and Rushton, 1982; Werner et al, 2013;), the large range of variability we consider attempts to cover several situations encountered in real scenarios. Note that the selected range of variability for r_k enables one to consider both isotropic and strongly anisotropic aquifers.

The computational domain depicted in Figure 4.1 is discretized through a grid with uniform square elements with side $\Delta = \Delta x = \Delta y$. We performed a set of preliminary simulations aimed at testing the influence of grid discretization on the quantification of the global quantities of interest defined in Section 2. We found no appreciable difference between the numerical results associated with grids formed by 200 × 100 (i.e., Δ = 10^{-2} m), 256 × 128 (i.e., Δ = 7.8×10^{-3} m) or 400 × 200 (i.e., Δ = 5×10^{-3} m) elements (details not shown). On these bases, all results reported in the following are associated with a uniform grid of 256 × 128 elements. To ensure numerical stability (e.g., Voss and Provost, 2002;), all numerical simulations have been performed using a grid Péclet number $Pe_m = \Delta / \alpha_L < 4$, while keeping $\Delta < \alpha_T$. Equations (4.1)-(4.5) are solved until steady-state conditions are reached. The latter are attained after a total simulated time of about 17 hours. The effect of different time steps has been tested and a uniform time discretization Δt = 60 s has been found to render accurate results. With these settings, a single simulation via SUTRA is associated with a computational cost of about 30 minutes. All numerical results reported here have been obtained on an Intel® Core™ i5-2410M CPU @ 2.30GHz processor. The target global quantities *LT, LS, WD* and *LY* are then analyzed at steady-state. This study is consistent with the original formulation of Henry's solution (Henry, 1964; Dentz et al., 2006;) and with the way the saltwater intrusion scenario is characterized in most environmental applications (e.g. Abarca et al., 2007; and references therein).

Table 4.1. Range of variability of the dimensionless uncertain parameters.

	$\Gamma_n = [x_{n,min}, x_{n,max}]$
Γ_{N_g}	[3.04; 5.06]
Γ_{r_k}	[10^{-8}; 1.0]
Γ_{Pe_L}	[3.33; 10]
Γ_{Pe_T}	[10; 100]

4.4.2 Construction and validation of the gPCE approximation of the global quantities

As described in Section 4.3, constructing the gPCE of a target system response entails solving the complete system model (4.1)-(4.5) for diverse combinations of the selected random parameters N_g, r_k, Pe_L, and Pe_T. The number of these combinations depends on the total degree *w* selected for the polynomial representation. In this section we assess the robustness of the gPCE approximations with diverse degrees *w*, in terms of their ability to provide accurate representations of the (random) global quantities *LT, LS, WD* and *LY*. We base our analysis on comparisons between values of each GQ obtained via the solution of the full model (4.1)-(4.5), $y(\boldsymbol{x})_{FM}$, against corresponding gPCE approximations, $y(\boldsymbol{x})_{gPCE}$. The coefficients $\beta_{\boldsymbol{p}}$ are calculated by solving the multidimensional integral in (4.15) through the sparse grids interpolation technique (e.g., Formaggia et al., 2013;) (i.e., the so-called non-intrusive spectral projection). We do so by using Legendre-Gauss points. Figure 4.3 depicts the results of such an analysis in terms of the relative error, defined as $e_y = \left(y(\boldsymbol{x})_{gPCE} - y(\boldsymbol{x})_{FM} \right) \big/ y(\boldsymbol{x})_{FM}$ (with *f* = *LT, LS, WD* and *LY*) resulting from *NMC* = 100 random MC realizations of the system parameters drawn from the parameter space. Note that these simulations do not coincide with those employed for the construction of the gPCE. The gPCE approximations have been evaluated using two values of *w*, i.e., *w* = 2, 3, for which the sparse grid is formed by 41 and 137 collocation points in the parameter space and the associated computational costs are about 20 and 68 hours, respectively. A very good agreement can be seen between both gPCE approximations and the full system model solution, the maximum absolute values of e_y being smaller than 18% or 9%, while the mean absolute values of e_y is smaller than 2.0% or 1.1%, respectively for *w* = 2 or *w* = 3.

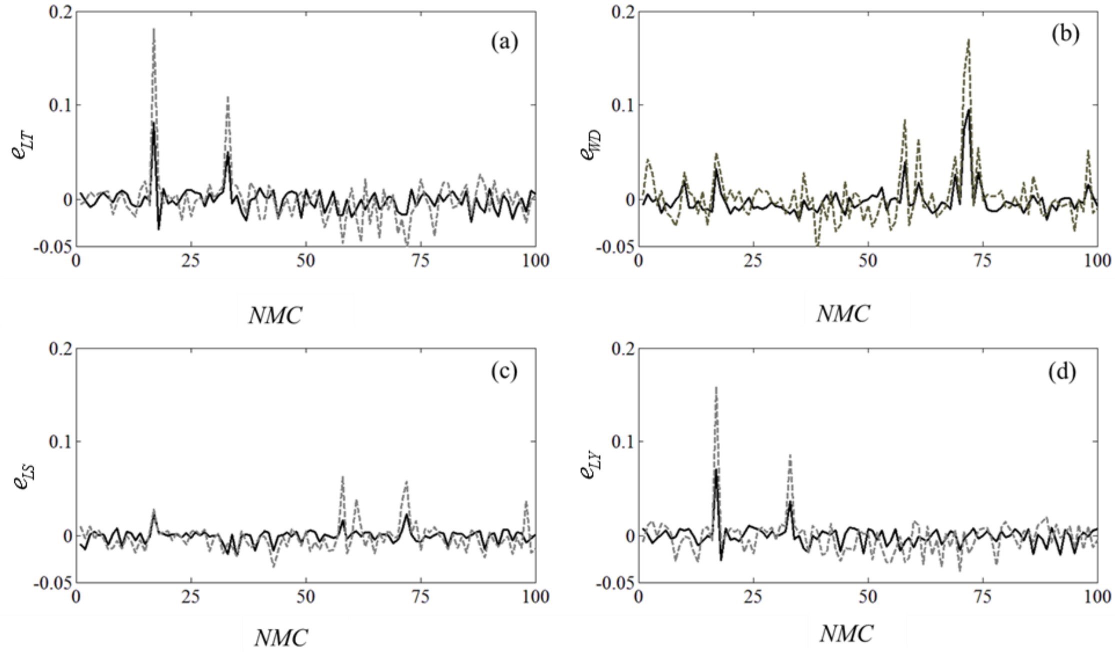

Figure 4.3. Relative error, e_y, between values of the GQs obtained via the solution of the full model (4.1)-(4.5), and the corresponding gPCE approximations associated with $w = 3$ (solid curves) and $w = 2$ (dashed curves) for *y* = (a) *LT*, (b) *WD*, (c) *LS*, (d) *LY*.

It is worthwhile to note that once expressions of the gPCE approximations are available, a large number of Monte Carlo iterations can be obtained at a very low additional computational cost upon sampling the random input parameter space. This allows grounding the analysis of the statistics of the target GQs on a very large sample of Monte Carlo realizations of the gPCE approximations. Figures 4.4 and 4.5 respectively depict the dependence of the sample mean, μ_y, and variance, σ_y^2, of the GQs on the number *NMC* of MC realizations obtained via gPCE with $w = 3$. The 95% estimated confidence intervals (CIs) are also graphically reported (see, e.g. Balio and Guadagnini, 2004;). Also depicted in the figures are corresponding results obtained via (*i*) 100 MC simulations of the complete model (performed independent of the simulations upon which the gPCE construction is based) and the gPCE using the same set of random input parameters, and (*ii*) analytical values of μ_y and σ_y^2 evaluated directly by (4.16) without resorting to the MC procedure. The latter values coincide with their Monte Carlo estimates with NMC $\approx 10^5$, as expected. The results embedded in these figures clearly demonstrate that stabilization of the statistical moments of interest (and in particular of σ_y^2) can be reached only at very large values of *NMC* (larger than 10^4). Note that such analysis would be unfeasible by solving the complete model (4.1)-(4.5). Our analysis also indicates that (*i*) all moments and the associated 95% CIs evaluated via the full model and via the gPCE approximations practically coincide for the *NMC* = 100 random parameters realizations considered independent of those employed for the construction of the gPCE; (*ii*) these moments lie within the 95% CIs obtained by independent gPCE realizations (dashed line); (*iii*) the estimates of the mean, μ_f, and variance, σ_f^2, obtained via gPCE and $NMC = 5\times10^5$ and the 95% CIs lie within the full model-based CIs evaluated by *NMC* = 100.

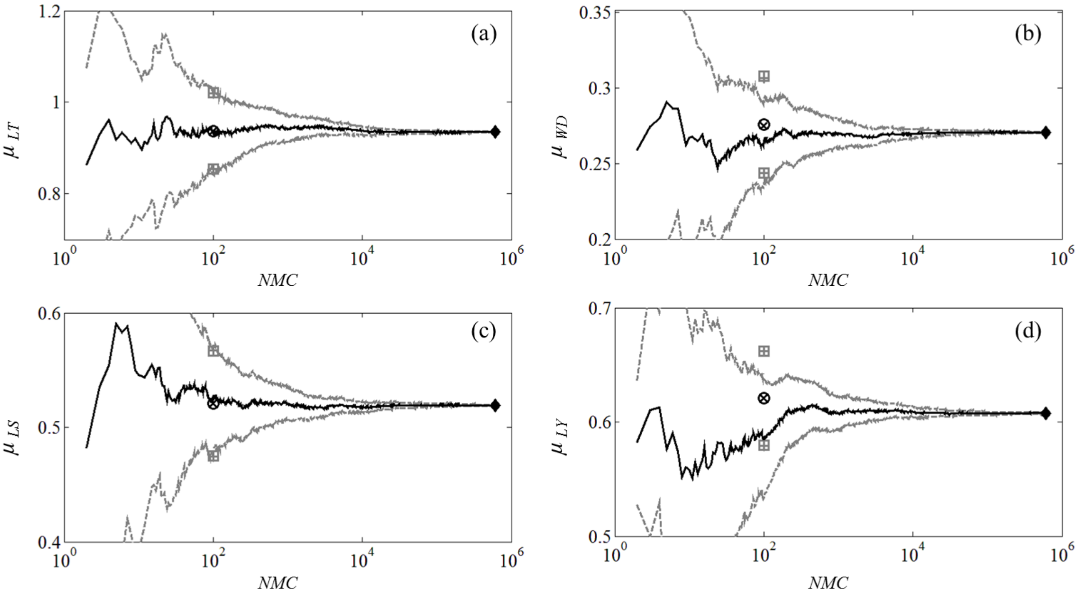

Figure 4.4. Convergence of sample mean, μ_y (solid black curve), and associated 95% CIs (grey dashed curves) with the number of Monte Carlo simulations (*NMC*) for *y* = (a) *LT*, (b) *WD*, (c) *LS*, and (d) *LY* obtained through a gPCE with $w = 3$. Corresponding results obtained via 100 independent MC simulations of (*i*) the complete model (μ_y - black circle - and 95% CIs - grey square) and (*ii*) the gPCE (μ_y - black cross - and 95% CIs - grey cross) based on the same set of input random parameters are also depicted. The black diamond represents the analytical solution of (4.16) with $w = 3$.

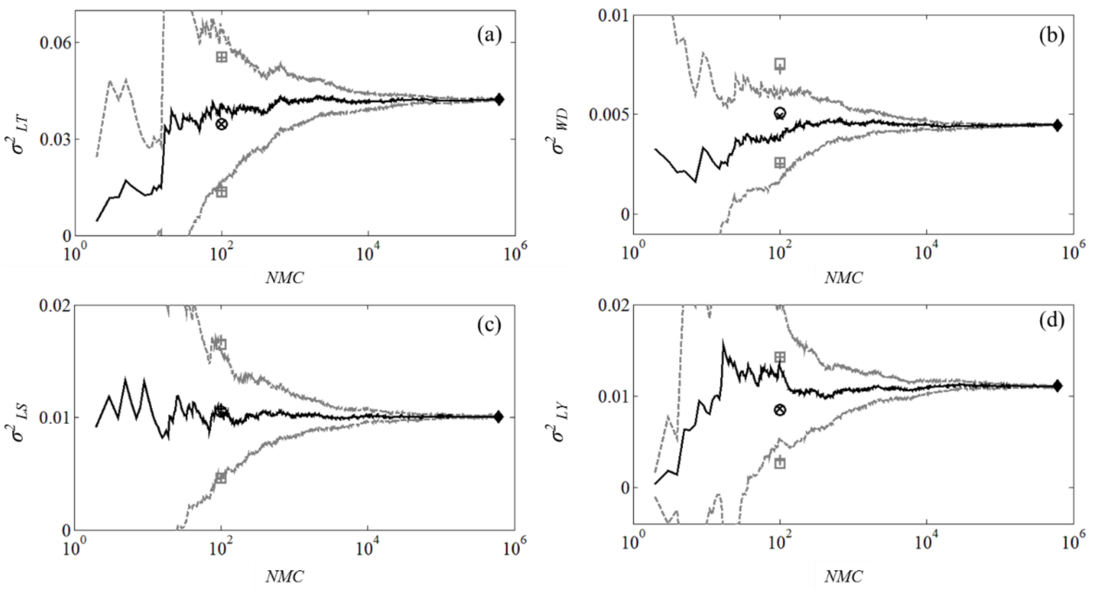

Figure 4.5. Convergence of sample variance, σ_y^2 (solid black curve) and associated 95% CIs (grey dashed curves) with the number of Monte Carlo simulations (*NMC*) for y = (a) *LT*, (b) *WD*, (c) *LS*, and (d) *LY* obtained through a gPCE with $w = 3$. Corresponding results obtained via 100 independent MC simulations of (*i*) the complete model (σ_y^2 - black circle - and 95% CIs - grey square) and (*ii*) the gPCE (σ_y^2 - black cross – and 95% CIs - grey cross) based on the same set of input random parameters are also depicted. The black diamond represents the analytical solution of (4.16) with w = 3.

To further explore the reliability of our gPCE approximations, we perform a two-sample Kolmogorov-Smirnov (K-S) test (Papoulis, 1991;) to compare the marginal probability distribution of the GQs obtained via the full model and their gPCE-based counterparts evaluated with $w = 3$. The null hypothesis that the samples belong to the same population is not rejected by the K-S test at a significance level of 0.05 (p-values always being larger than 0.9, details not reported), thus supporting the use of the gPCE surrogate models not only for the analysis of the statistical moments of the global quantity but also their probability distributions.

Finally, we analyze the level of correlation between two GQs of interest, e.g., $y(\mathbf{x})$ and $g(\mathbf{x})$, by relying on the Pearson' correlation coefficient, ρ_p. It is worthwhile to note that, when the gPCEs of $y(\mathbf{x})$ and $g(\mathbf{x})$ are available, ρ_p can be evaluated analytically making use of (4.15)-(4.16) as

$$\rho_p = \frac{\operatorname{cov}\left(y(\mathbf{x}), g(\mathbf{x})\right)}{\sqrt{V_y V_g}} = \frac{\sum_{i=1}^{N} \sum_{\mathbf{p},\mathbf{q}\in\Im_i} \beta_{\mathbf{p}}\beta_{\mathbf{q}} + \sum_{i,j=1}^{N} \sum_{\mathbf{p},\mathbf{q}\in\Im_{i,j}} \beta_{\mathbf{p}}\beta_{\mathbf{q}} + \ldots}{\sqrt{V_y V_g}} \qquad (14.7)$$

Table 4.2 lists the Pearson' correlation coefficients evaluated via (4.17) with $w = 3$ and the corresponding values obtained on the basis of the above mentioned 100 MC realizations of the full model. Once again, it can be noted that the agreement between the full model- and the gPCE-based results is quite remarkable, especially for the highly (positively or negatively) correlated quantities. On these bases, the analyses presented in the following section are grounded on gPCE approximations of order $w = 3$ for all of the global quantities of interest.

Table 4.2. Pearson' correlation coefficient of the GQs evaluated via gPCE, (black fonts) and 100 MC random realizations of the full model (grey fonts).

	WD	*LT*	*LS*	*LY*
WD	1	-0.49	0.75	-0.21
LT	-0.51	1	-0.02	0.80
LS	0.76	-0.18	1	-0.03
LY	-0.13	0.77	-0.08	1

4.5 Results and Discussion

4.5.1 Variance-based Sobol' Indices

Principal, S_{x_n}, and total, $S_{x_n}^T$, Sobol indices, together with linear contributions, $S_{x_n}^L$, are listed in Table 4.3 for all global quantities of interest and considering all of the random input dimensionless variables (i.e., in Table 4.3 x_n = N_g, r_k, Pe_L, and Pe_T). Values of $S_{x_n}^L$, S_{x_n} and $S_{x_n}^T$ coincide (or are very close to each other) indicating that non-linear terms and joint interaction between the uncertain parameters are almost negligible for all GQs with the exception of *LY*. The results embedded in Table 4.3 show that non-linear terms including r_k cannot be neglected for the evaluation of *LY*.

The uncertainty associated with the intrusion of the toe of the wedge, as represented by *LT*, is mainly controlled by $N_g = g\Delta\rho k_x / q_f \mu$ (which has about 50% weight in directing the total variance of *LT*). The nature of N_g allows recognizing that increasing $k_x / q_f \mu$ causes a reduction of the pressure drop required by a given q_f to flow towards the sea and the ensuing retreat of the wedge. On the other hand, an increase of $\Delta\rho$ results in an increased capability of seawater to intrude the aquifer. The wedge intrusion is also strongly affected by Pe_T. This is so because mixing of fresh and salt water tends to be reduced with increasing Pe_T so that a high density contrast can be sustained, leading to an increase of *LT*.

Spreading of solute at the bottom of the wedge, as described by *LS*, is mainly affected by Pe_L and to a less extent by Pe_T. This result is consistent with the previous observation of Abarca et al. (2007) that longitudinal dispersivity controls the distribution of concentrations in the lowest (bottom) part of the domain.

The roles of Pe_L and Pe_T are then reversed in governing the variability of *WD*, describing the extension of the mixing zone. Abarca et al. (2007) suggested a linear relationship between *WD* and $\sqrt{\alpha_L \alpha_T}$, thus implying that α_L and α_T contribute in equal measure to *WD*. Our results, which are based on independence between Pe_L and Pe_T, show that Pe_T (i.e., α_T) plays the main role in controlling the uncertainty of *WD*. Our finding that *WD* is almost insensitive to N_g or r_k suggests that for given values of Pe_L and Pe_T the spatial distribution of the entries of the dispersion tensor remains essentially unaltered within the transition zone. Therefore, changes in N_g and r_k only cause a horizontal (inland or seaward) and vertical shift of the transition region whose extension remains practically constant.

Finally, variations of r_k only affect variability of *LY* and *LT*. This result is consistent with the observation that decreasing r_k (i.e., decreasing the vertical permeability) causes the vertical component of the freshwater velocity to decrease so that the capability of the horizontal freshwater flux to contrast the intrusion of the saltwater is augmented. As a consequence, *LY* and *LT* tend to decrease with r_k.

Table 4.3. Principal (S_{x_n}) and total ($S_{x_n}^T$) Sobol indices (x_n = N_g, r_k, Pe_L, Pe_T), together with the linear component $S_{x_n}^L$ of S_{x_n}.

	LT	*LS*	*WD*	*LY*
$S_{N_g}^L ; S_{N_g} ;\ S_{N_g}^T$	0.49; 0.50; 0.51	0.16; 0.17; 0.19	0.00; 0.00; 0.00	0.16; 0.16; 0.20
$S_{r_k}^L ; S_{r_k} ;\ S_{r_k}^T$	0.10; 0.14; 0.14	0.01; 0.02; 0.02	0.03; 0.04; 0.04	0.60; 0.70; 0.70
$S_{Pe_L}^L ; S_{Pe_L} ;\ S_{Pe_L}^T$	0.05; 0.05; 0.05	0.51; 0.51; 0.51	0.27; 0.27; 0.28	0.00; 0.00; 0.00
$S_{Pe_T}^L ;\ S_{Pe_T} ;\ S_{Pe_T}^T$	0.29; 0.31; 0.32	0.25; 0.27; 0.28	0.65; 0.67; 0.69	0.13; 0.13; 0.13

4.5.2 Probability Distributions of Global Quantities of interest

This Section is devoted to the analysis of the marginal and joint probability distributions, *pdfs*, of the global quantities we analyze. These results are relevant for management of coastal aquifers as they can be assist in the quantification of the probability of failure of the system (i.e., the probability to exceed a given threshold values of the GQ).

We construct these sample *pdfs* by relying on the gPCE representation. The latter is employed to perform 5 × 10^5 Monte Carlo simulations of the target system states at a remarkably low computational cost (about 68 hours for the construction of the gPCE approximations, plus about 2 hours for the generation of the MC realizations), as opposed to standard Monte Carlo simulations performed with the complete model which would be unfeasible (the estimated CPU time is about 1.7×10^5 hours). Uniform sampling of the parameter space is here employed.

Once a gPCE representation is constructed, it is also possible to derive an analytical expression of the marginal probability distribution (marginal *pdf*) of the GQ, without resorting to numerical MC sampling. The procedure is detailed in Appendix A.4. Appendices A.4.1-A.4.3 show that, when the gPCE approximation (4.15) can be truncated to the first order Legendre polynomials of the parameters which are identified as relevant on the basis of the associated Sobol indices (see Table 4.3), as in the case of our analysis for *WD*, *LT*, and *LS*, the related marginal *pdfs* are fully determined by the coefficients of the Legendre polynomial of orders zero and one. When non-linear terms are relevant in the gPCE (i.e., for *LY*, as described in Section 4.5.1), the complexity of the analytical expression of the marginal *pdf* increases. Details for this case are illustrated in Appendix A.4.4 for completeness.

Figure 4.6 juxtaposes the MC-based marginal *pdfs* of the GQs with the corresponding analytical formulations. The agreement between the numerical and analytical results is remarkable. The marginal *pdfs* of *LT*, *WD* and *LS*, for which non-linear effects can be neglected, are symmetric around the mean. Otherwise, the marginal *pdf* of *LY*, where non-linear effects due to r_k are relevant, is negatively skewed, its long tail being associated with settings characterized by low values of the vertical permeability.

Figure 4.6 also depicts contour plots of the joint *pdf* of all pairs of the global variables. A negative correlation between LT and *WD* is evident. The latter is mainly due to the contrasting effects that Pe_T has on these quantities. While increasing Pe_T (i.e., decreasing α_T) causes the mixing zone to decrease, the inland intrusion of seawater increases. The joint *pdf* of *WD* and *LS* is characterized by a clear positive correlation. This is related to the observation that both quantities are primarily affected by the longitudinal and transverse Péclet numbers and they both decrease with Pe_L and Pe_T. Note also that the joint *pdf* of *LT* and *LY* shows a marked elongation in the region corresponding to relatively low values of both global variables. This behavior is representative of settings characterized by low values of the vertical permeability, i.e. by small values of r_k. The joint *pdfs* reported in Figure 4.6 are also in agreement with the picture offered by the Pearson' correlation coefficients introduced in Section 4.4.2 and listed in Table 4.2. In particular, these confirm the lack of correlation between *WD* and *LY* and between *LS* and all global variables with the exception of *WD*.

In practical applications, some of the global quantities here considered can be known through experimental campaigns. A relevant question in the management of coastal aquifers is therefore how can the knowledge of one global quantity affect the probability distribution (and therefore the predictability) of the remaining GQs. An answer to this question can be directly obtained by applying Bayes' theorem to the joint *pdfs* described above and then deriving the conditional *pdf* of the GQs of interest.

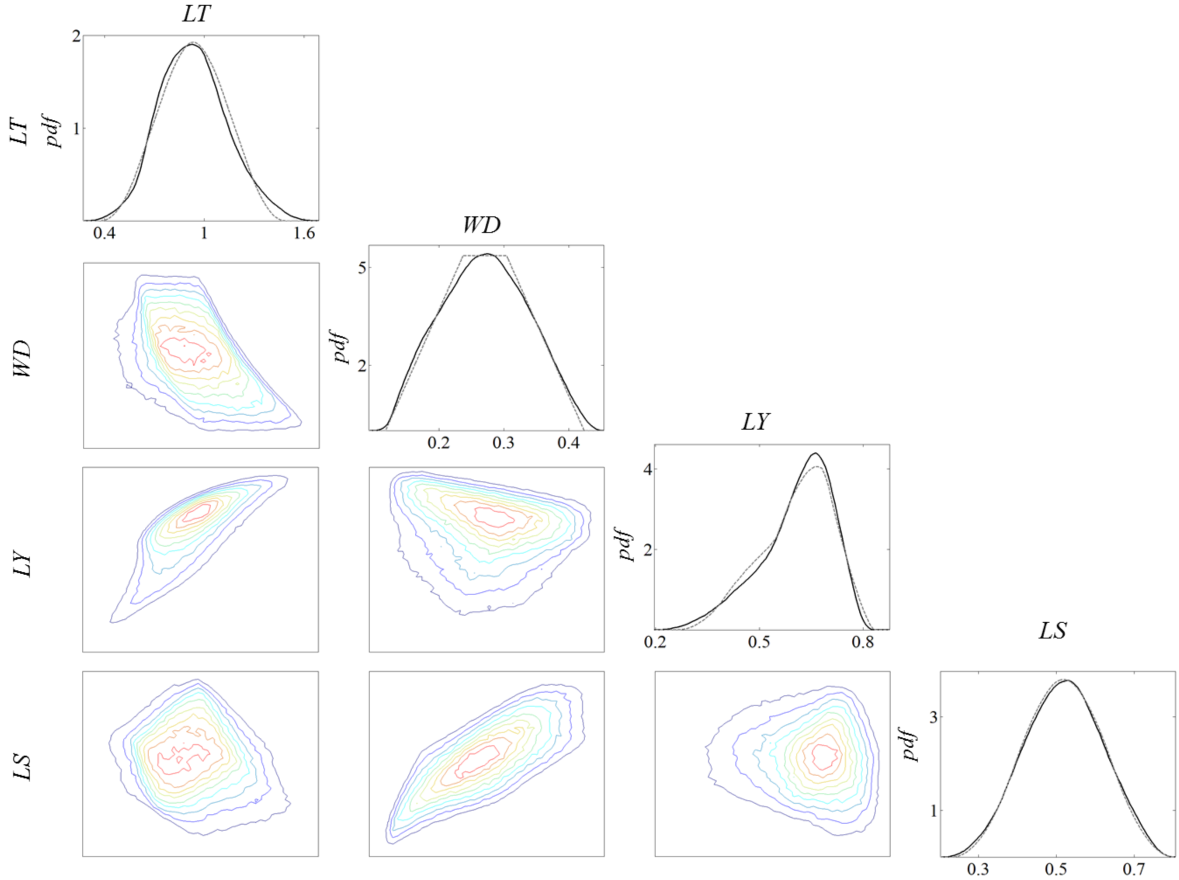

Figure 4.6. Numerical (black continuous) and analytical (grey dashed) marginal *pdf* for *LT*, *WD*, *LY* and *LS*. Contours of joint *pdf* for all pairs of GQs are also shown (color curves). For rendering purposes, the iso-probability curves in each subplot are normalized by the corresponding maximum *pdf* value.

For the problem here considered, while measurements of *LY* can be obtained with relatively modest efforts (e.g., through electrical conductivity profiles), acquiring data on the remaining GQs (and in particular of *LT* and *LS*) is problematic. It is therefore of interest to analyze the way the availability of *LY* data would affect predictions of the remaining GQs. On the basis of Figure 4.6, one can anticipate that while *LY* measurements would affect the predictability of *LT*, these data would not influence markedly the marginal *pdf* of *WD* and *LS* because of their weak level of correlation with *LY*. As an example of the type of results which one can obtain, Figure 4.7a depicts the marginal *pdf* of *LT* conditioned to the mean value of *LY*, i.e., μ_{LY} = 0.61. In Figure 4.7a we consider a measurement error with amplitude equal to ± 1% μ_{LY} and condition the marginal *pdf* of *LT* on the range of *LY* values [$\mu_{LY} - 6.1\times10^{-3}$, $\mu_{LY} + 6.1\times10^{-3}$]. The unconditional *pdf* is also depicted for comparison. Corresponding results for *WD* and *LS* are depicted in Figures 7b and 7c, respectively. These results clearly show the reduction of the variability of *LT*, which is, e.g., quantified by its variance that decreases from 4.2×10^{-2} for the unconditional case to 1.8×10^{-2} for the conditional one. On the other hand, knowledge of *LY* practically does not affect the *pdf* of *WD* and *LS*, as expected by the reasoning illustrated above.

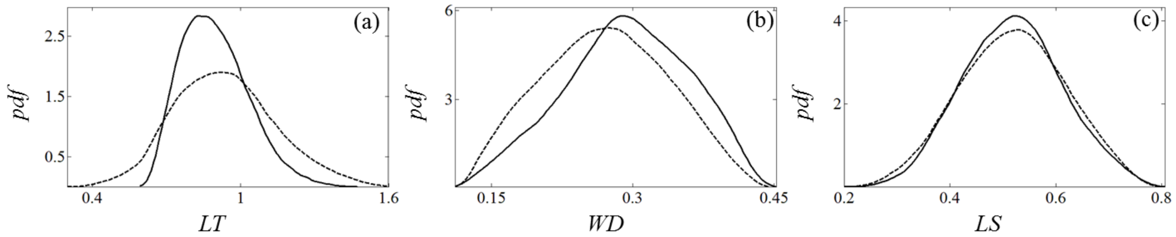

Figure 7. Marginal pdf of (a) *LT* , (b) *WD* and (c) *LS* conditioned to *LY*= μ_{LY} $\underline{+}$ 6.1×10^{-3} (solid curves). Corresponding unconditional *pdfs* are also depicted (dashed curves).

4.6 Conclusion

We analyze the way key global dimensionless quantities (GQs) characterizing the saltwater wedge in the dispersive Henry's problem are affected by the incomplete knowledge of system properties, as encapsulated in the gravity number (N_g), the anisotropic ratio of permeability (r_k), the transverse (Pe_T) and longitudinal (Pe_L) Péclet number. The analysis is based on the generalized Polynomial Chaos Expansion (gPCE) of the following GQs: the median toe penetration (LT), the spread of solute around the toe (LS), the mean width of the mixing zone (WD) and the sinking of the wedge at the seaside boundary (LY). These kinds of analyses can be useful to assist coastal aquifer management and risk assessment procedures as they lead to an appropriate probabilistic characterizations of the saltwater wedge.

Our uncertainty quantification procedure relies on the variance-based Sobol indices. We found that the variability of the gravity number greatly influences LT, while uncertainty of the permeability anisotropy ratio chiefly controls LY. On the other hand, transverse and longitudinal Péclet number respectively affects mainly the variance of the width of the mixing zone and of the spread of solute around the toe.

We then compute the joint and marginal probability density functions (*pdfs*) of the target global descriptors. We remark these tasks are computationally unaffordable by making use of the complete system model, while they can be performed with a relatively modest computational effort by means of the constructed gPCE surrogate model. We also derive analytical expressions for the marginal *pdf* of the global quantities on the basis of the gPCE approximations. The study of the joint *pdfs* allows us to highlight the degree of correlation between the GQs. This analysis is relevant to management and assessment of quality of coastal aquifers because it enables us to identify the way information on one state variable impacts on the reduction of uncertainty associated with other target quantities, thus ultimately constituting a potential driver to planning required experimental campaigns.

Future extensions of this study comprise the study of seawater intrusion processes in randomly heterogeneous systems, the inclusion of additional uncertain quantities such as porosity, inland freshwater flux and salt concentration at the sea boundary. The investigation of flow scenarios of increased complexity, such as those involving pumping and recharge wells in coastal aquifers is also envisioned.

Appendix A.4 Analytical derivation of the marginal pdf of the target global variables

In this Appendix we detail our derivations conducive to the analytical expressions of the marginal probability density function, *pdf*, of the target global variables we consider. For illustration purposes, in the following we retain in (4.15)-(4.16) all terms which allow representing at least 90% of the total variance of each state variable.

Appendix A.4.1: Marginal *pdf* of *WD*

Within the range of variability of the uncertain parameters listed in Table 4.1, one can note that 91% of the total variance of *WD* can be retained upon truncating (4.15) up to the first order Legendre polynomials ξ_{Pe_T} and ξ_{Pe_L}, defined as

$$\xi_{Pe_T} = \sqrt{3}\ \frac{2Pe_T - g - h}{h - g}; \qquad \xi_{Pe_L} = \sqrt{3}\ \frac{2Pe_L - e - f}{f - e} \tag{A.4.1}$$

where $Pe_T \in \Gamma_{Pe_T} = [g, h]$ and $Pe_L \in \Gamma_{Pe_L} = [e, f]$ (see Table 4.1). Therefore, (4.15) becomes

$$WD' = WD - \beta_{WD;0} = \beta_{WD;Pe_T}\xi_{Pe_T} + \beta_{WD;Pe_L}\xi_{Pe_L} \tag{A.4.2}$$

where $\beta_{WD;0}$ is the mean of *WD*, $\beta_{WD;Pe_T}$ and $\beta_{WD;Pe_L}$ are the coefficients of the Legendre polynomial of order one in Pe_T and Pe_L, respectively.

Equation (A.4.2) can be rewritten as

$$WD' = A_{WD} + B_{WD}Pe_T + C_{WD}Pe_L \tag{A.4.3}$$

where

$$A_{WD} = -\sqrt{3}\left(\beta_{WD;Pe_T}\frac{h+g}{h-g} + \beta_{WD;Pe_L}\frac{f+e}{f-e}\right); \ B_{WD} = \frac{2\sqrt{3}\beta_{WD;Pe_T}}{h-g}; \ C_{WD} = \frac{2\sqrt{3}\beta_{WD;Pe_L}}{f-e} \tag{A.4.4}$$

The probability density function, of Pe_T and Pe_L are respectively given by

$$pdf_{Pe_T} = \frac{1}{h-g}\left[H(Pe_T - g) - H(Pe_T - h)\right]; \quad pdf_{Pe_L} = \frac{1}{f-e}\left[H(Pe_L - e) - H(Pe_L - f)\right] \tag{A.4.5}$$

H being the Heaviside step function. Since Pe_T and Pe_L are two independent random variables, the marginal *pdf* of *WD* is given by the convolution of pdf_{Pe_T} and pdf_{Pe_L} as

$$pdf_{WD}\left(wd'\right) = \frac{1}{B_{WD}}\int_{-\infty}^{+\infty} pdf_{Pe_T}\left(\frac{wd' - A_{WD} - C_{WD}Pe_L}{B_{WD}}\right)pdf_{Pe_L}\left(Pe_L\right)dPe_L \tag{A.4.6}$$

Making use of (A.4.5), (A.4.6) becomes

$$
\begin{aligned}
pdf_{WD}\left(wd'\right) = \frac{1}{B_{WD}(h-g)(f-e)} \int_{-\infty}^{+\infty} \Bigg\{ & -H\left(\frac{wd'-A_{WD}-C_{WD}Pe_L}{B_{WD}}-h\right) H(Pe_L-e) \\
& + H\left(\frac{wd'-A_{WD}-C_{WD}Pe_L}{B_{WD}}-h\right) H(Pe_L-f) \\
& + H\left(\frac{wd'-A_{WD}-C_{WD}Pe_L}{B_{WD}}-g\right) H(Pe_L-e) \\
& - H\left(\frac{wd'-A_{WD}-C_{WD}Pe_L}{B_{WD}}-g\right) H(Pe_L-f) \Bigg\} dPe_L
\end{aligned}
\tag{A.4.7}
$$

The first integral appearing in (A.4.7) can be evaluated as

$$
\begin{aligned}
I_{1,WD} &= \int_{-\infty}^{\infty} H\left(\frac{wd'-A_{WD}-C_{WD}Pe_L}{B_{WD}}-h\right) H(Pe_L-e)\,dPe_L = \int_{e}^{\infty} H\left(\frac{wd'-A_{WD}-C_{WD}Pe_L}{B_{WD}}-h\right) dPe_L \\
&= \frac{B_{WD}}{C_{WD}}\left(\frac{wd'-A_{WD}-C_{WD}e}{B_{WD}}-h\right) H\left(\frac{wd'-A_{WD}-C_{WD}e}{B_{WD}}-h\right)
\end{aligned}
\tag{A.4.8}
$$

All remaining terms in (A.4.7) can be evaluated in a similar way, so that (A.4.7) becomes

$$
\begin{aligned}
pdf_{WD}\left(wd'\right) = \frac{1}{C_{WD}(h-g)(f-e)} \Bigg\{ & -\left(\frac{wd'-A_{WD}-C_{WD}e}{B_{WD}}-h\right) H\left(\frac{wd'-A_{WD}-C_{WD}e}{B_{WD}}-h\right) \\
& + \left(\frac{wd'-A_{WD}-C_{WD}f}{B_{WD}}-h\right) H\left(\frac{wd'-A_{WD}-C_{WD}f}{B_{WD}}-h\right) \\
& + \left(\frac{wd'-A_{WD}-C_{WD}e}{B_{WD}}-g\right) H\left(\frac{wd'-A_{WD}-C_{WD}e}{B_{WD}}-g\right) \\
& - \left(\frac{wd'-A_{WD}-C_{WD}f}{B_{WD}}-g\right) H\left(\frac{wd'-A_{WD}-C_{WD}f}{B_{WD}}-g\right) \Bigg\}
\end{aligned}
\tag{A.4.9}
$$

Finally, after some manipulations and making use of (A.4.3)-(A.4.4), (A.4.9) can be rewritten as

$$
pdf_{WD}\left(wd\right) = \frac{1}{12\beta_{WD;Pe_L}\beta_{WD;Pe_T}} \sum_{i=0}^{1} \sum_{j=0}^{1} (-1)^{i+j} \xi_{wd,ij}\, H\left[\frac{\xi_{wd,ij}}{\beta_{WD;Pe_T}}\right]
\tag{A.4.10}
$$

with $\xi_{wd,ij} = wd - \beta_{WD;0} + \sqrt{3}\left((-1)^i \beta_{WD;Pe_L} + (-1)^j \beta_{WD;Pe_T}\right)$

Appendix A.4.2: Marginal *pdf* of *LT*

Within the range of variability of the uncertain parameters listed in Table 4.1, one can note that 93% of the total variance of *LT* can be retained upon truncating (4.15) up to the first order Legendre polynomials ξ_{Pe_T} introduced in (A.4.1) and ξ_{N_g} and ξ_{r_k} defined as

$$\xi_{N_g} = \sqrt{3}\ \frac{2N_g - a - b}{b - a}; \qquad \xi_{r_k} = \sqrt{3}\ \frac{2r_k - c - d}{d - c}; \tag{A.4.11}$$

where $N_g \in \Gamma_{N_g} = [a,b]$ and $r_k \in \Gamma_{r_k} = [c,d]$. Therefore, (4.15) can be simplified as

$$LT' = LT - \beta_{LT;0} = \beta_{LT;N_g}\xi_{N_g} + \beta_{LT;r_k}\xi_{r_k} + \beta_{LT;Pe_T}\xi_{Pe_T} \tag{A.4.12}$$

where $\beta_{LT;0}$ is the mean of *LT*, $\beta_{LT;N_g}$, $\beta_{LT;r_k}$ and $\beta_{LT;Pe_T}$ are the coefficients of the Legendre polynomial of order one in N_g, r_k, and Pe_T, respectively.

Equation (A.4.12) can be rewritten as

$$LT' = A_{LT} + B_{LT}N_g + C_{LT}r_k + D_{LT}Pe_T \tag{A.4.13}$$

where

$$\begin{aligned} A_{LT} &= -\sqrt{3}\left(\beta_{LT;N_g}\frac{a+b}{b-a} + \beta_{LT;r_k}\frac{c+d}{d-c} + \beta_{LT;Pe_T}\frac{h+g}{h-g}\right); \\ B_{LT} &= \frac{2\sqrt{3}\beta_{LT;N_g}}{b-a};\ C_{LT} = \frac{2\sqrt{3}\beta_{LT;r_k}}{d-c};\ D_{LT} = \frac{2\sqrt{3}\beta_{LT;Pe_T}}{h-g} \end{aligned} \tag{A.4.14}$$

The *pdfs* of N_g and r_k are given respectively by

$$pdf_{N_g} = \frac{1}{b-a}\left[H(N_g - a) - H(N_g - b)\right]; \quad pdf_{r_k} = \frac{1}{d-c}\left[H(r_k - c) - H(r_k - d)\right] \tag{A.4.15}$$

Since N_g, r_k and Pe_T are independent random variables, the marginal *pdf* of *LT* is

$$pdf_{LT}\left(lt'\right) = \frac{1}{B_{LT}}\int_{-\infty}^{+\infty}\int_{-\infty}^{+\infty} pdf_{N_g}\left(\frac{lt' - A_{LT} - C_{LT}r_k - D_{LT}Pe_T}{B_{LT}}\right) pdf_{r_k}(r_k)pdf_{Pe_T}(Pe_T)dr_k dPe_T \tag{A.4.16}$$

Making use of (A.4.5) and (A.4.15) and following the same strategy adopted in Appendix A.4.1, (A.16) can be evaluated as

$$pdf_{LT}\left(lt\right) = \frac{1}{48\sqrt{3}\beta_{LT;r_k}\beta_{LT;Pe_T}\beta_{LT;N_g}}\sum_{k=0}^{1}\sum_{i=0}^{1}\sum_{j=0}^{1}(-1)^{k+i+j}\left(\xi_{lt,ijk}\right)^2 H\left[\frac{\xi_{lt,ijk}}{\beta_{LT;N_g}}\right] \tag{A.4.17}$$

with $\xi_{lt,ijk} = lt - \beta_{LT;0} + \sqrt{3}\left((-1)^i\beta_{LT;N_g} + (-1)^j\beta_{LT;r_k} + (-1)^k\beta_{LT;Pe_T}\right)$.

Appendix A.4.3: Marginal *pdf* of *LS*

Within the range of variability of the uncertain parameters listed in Table 4.1, one can note that 95% of the total variance of *LS* can be retained upon truncating (4.15) up to the first order Legendre polynomials ξ_{Pe_L} , ξ_{Pe_T} introduced in (A.4.1) and ξ_{N_g} , given by (A.4.11). Therefore, (4.15) can be simplified as

$$LS' = LS - \beta_{LS;0} = \beta_{LS;Pe_L}\xi_{Pe_L} + \beta_{LT;Pe_T}\xi_{Pe_T} + \beta_{LS;N_g}\xi_{N_g} \qquad \text{(A.4.18)}$$

where $\beta_{LS;0}$ is the mean of *LS*, $\beta_{LS;Pe_L}$, $\beta_{LS;Pe_T}$ and $\beta_{LT;N_g}$ are the coefficients of the Legendre polynomial of order one in Pe_L , Pe_T and N_g respectively. Following the same procedure outlined in Appendix A.4.2, we obtain the following expression for the marginal *pdf* of *LS*

$$pdf_{LS}\left(ls\right) = \frac{1}{48\sqrt{3}\beta_{LS;Pe_L}\beta_{LS;Pe_T}\beta_{LS;N_g}} \sum_{k=0}^{1}\sum_{i=0}^{1}\sum_{j=0}^{1}(-1)^{k+i+j}\left(\xi_{ls,ijk}\right)^2 \ H\left[\frac{\xi_{ls,ijk}}{\beta_{LS;Pe_L}}\right] \qquad \text{(A.4.19)}$$

with $\xi_{ls,ijk} = ls - \beta_{LS;0} + \sqrt{3}\left((-1)^i\beta_{LS;Pe_L} + (-1)^j\beta_{LS;Pe_T} + (-1)^k\beta_{LS;N_g}\right)$.

Appendix A.4.4: Marginal *pdf* of *LY*

Within the range of variability of the uncertain parameters listed in Table 4.1, one can note that 97% of the total variance of *LY* can be retained upon truncating (4.15) up to the first order Legendre polynomials ξ_{Pe_T} , ξ_{N_g} and ξ_{r_k} defined by (A.4.1) and (A.4.11) and to the second order Legendre polynomial

$$\xi_{r_k^2} = \frac{\sqrt{5}}{2}\left(3\left(\frac{2r_k - c - d}{d - c}\right)^2 - 1\right) \qquad \text{(A.4.20)}$$

Therefore, (4.15) can be written as

$$LY' = LY - \beta_{LY;0} = \beta_{LY;N_g}\xi_{N_g} + \beta_{LY;Pe_T}\xi_{Pe_T} + \beta_{LY;r_k}\xi_{r_k} + \beta_{LY;r_k^2}\xi_{r_k^2} \qquad \text{(A.4.21)}$$

where $\beta_{LY;0}$ is the mean of *LY*, $\beta_{LY;N_g}$, $\beta_{LY;Pe_T}$ and $\beta_{LY;r_k}$ are the coefficient of the Legendre polynomial of order one in N_g , Pe_T and r_k , respectively, and $\beta_{LY;r_k^2}$ is the coefficient of the Legendre polynomial of order two in r_k. Equation (A.4.21) can be rewritten as

$$LY' = A_{LY} + B_{LY}N_g + C_{LY}Pe_T + D_{LY}r_k + E_{LY}r_k^2 \qquad \text{(A.4.22)}$$

where

$$A_{LY} = -\sqrt{3}\left(\beta_{LY;N_g}\frac{a+b}{b-a} + \beta_{LY;r_k}\frac{c+d}{d-c} + \beta_{LY;Pe_T}\frac{g+h}{h-g}\right) + \beta_{LY;r_k^2}\frac{\sqrt{5}}{\left(d-c\right)^2}\left(c^2 + d^2 + 4cd\right);$$

$$B_{LY} = \frac{2\sqrt{3}\beta_{LY;N_g}}{b-a}\ ;\ C_{LY} = \frac{2\sqrt{3}\beta_{LY;Pe_T}}{h-g};\ D_{LY} = \frac{2\sqrt{3}\beta_{LY;r_k}}{d-c} - \frac{6\sqrt{5}\beta_{LY;r_k^2}(c+d)}{(d-c)^2};\ E_{LY} = \frac{6\sqrt{5}\beta_{LY;r_k^2}}{(d-c)^2} \qquad \text{(A.4.23)}$$

Since N_g , r_k and Pe_T are independent random variables, the marginal *pdf* of *LY* is

$$pdf_{LY}\left(ly'\right)=\frac{1}{B_{LY}}\int_{-\infty}^{+\infty}\int_{-\infty}^{+\infty}pdf_{N_g}\left(\frac{ly'-A_{LY}-C_{LY}Pe_T-D_{LY}r_k-E_{LY}r_k{}^2}{B_{LY}}\right)pdf_{Pe_T}\left(Pe_T\right)pdf_{r_k}\left(r_k\right)dPe_Tdr_k \tag{A.4.24}$$

Equation (A.4.24) can be evaluated as

$$\begin{aligned}pdf_{LY}\left(ly'\right)=&\frac{1}{C_{LY}(b-a)(h-g)(d-c)}\int_{-\infty}^{+\infty}\left\{H\left[r_k-c\right]-H\left[r_k-d\right]\right\}\\&\left\{\left(Ar_k{}^2+Br_k+C_1\right)H\left[Ar_k{}^2+Br_k+C_1\right]-\left(Ar_k{}^2+Br_k+C_2\right)H\left[Ar_k{}^2+Br_k+C_2\right]\right.\\&\left.-\left(Ar_k{}^2+Br_k+C_3\right)H\left[Ar_k{}^2+Br_k+C_3\right]+\left(Ar_k{}^2+Br_k+C_4\right)H\left[Ar_k{}^2+Br_k+C_4\right]\right\}dr_k\end{aligned} \tag{A.4.25}$$

where

$$A=-\frac{E_{LY}}{B_{LY}}\,;B=\frac{-D_{LY}}{B_{LY}}\,;C_1=\frac{ly'-A_{LY}-C_{LY}g-aB_{LY}}{B_{LY}}\,;\;C_2=\frac{ly'-A_{LY}-C_{LY}g-bB_{LY}}{B_{LY}}\,;$$

$$C_3=\frac{ly'-A_{LY}-C_{LY}h-aB_{LY}}{B_{LY}}\,;C_4=\frac{ly'-A_{LY}-C_{LY}h-bB_{LY}}{B_{LY}} \tag{A.4.26}$$

Equation (A.4.26) can be rewritten as

$$pdf_{LY}(ly')=I_{1,LY}-I_{2,LY}-I_{3,LY}+I_{4,LY} \tag{A.4.27}$$

where

$$I_{i,LY}=A\int_c^d\left(v-v_{1;i}\right)\left(v-v_{2;i}\right)H\left[A\left(v-v_{1;i}\right)\left(v-v_{2;i}\right)\right]dv \tag{A.4.28}$$

and

$$v_{1;i}=\frac{-B-\sqrt{B^2-4AC_i}}{2A}\qquad;\qquad v_{2;i}=\frac{-B+\sqrt{B^2-4AC_i}}{2A} \tag{A.4.29}$$

Since A > 0 in our case, the integral expression (A.4.28) can be evaluated as

$$\begin{aligned}\frac{I_{i,LY}}{A}=&H\left[v_{1;i}-c\right]H\left[d-v_{2;i}\right]\left(\frac{v_{2;\mathrm{i}}{}^3-v_{1;\mathrm{i}}{}^3}{6}-v_{1;i}v_{2;i}\frac{v_{2;i}-v_{1;i}}{2}\right)\\&+\left\{H\left[v_{1;i}-d\right]+H\left[c-v_{2;i}\right]+H\left[v_{1;i}-c\right]H\left[d-v_{2;i}\right]\right\}\left(\frac{d^3-c^3}{3}-\frac{v_{1;i}+v_{2;i}}{2}\left(d^2-c^2\right)+v_{1;i}v_{2;i}\left(d-c\right)\right)\\&+H\left[d-v_{2;i}\right]H\left[c-v_{1;i}\right]H\left[v_{2;i}-c\right]\left(\frac{d^3}{3}-\frac{v_{1;i}+v_{2;i}}{2}d^2-\frac{v_{2;i}{}^2}{2}v_{1;i}+\frac{v_{2;\mathrm{I}}{}^3}{6}+v_{1;i}v_{2;i}d\right)\\&+H\left[v_{1;i}-c\right]H\left[d-v_{1;i}\right]H\left[v_{2;i}-d\right]\left(\frac{v_{1;i}{}^2}{2}v_{2;i}-\frac{v_{1;i}{}^3}{6}-\frac{c^3}{3}+\frac{v_{1;i}+v_{2;i}}{2}c^2-v_{1;i}v_{2;i}c\right)\end{aligned} \tag{A.4.30}$$

Appendix B.4 Variance-based Global Sensitivity Analysis for Hydraulic Fracturing, a preliminary study.

Hydraulic fracturing operation consist in the injection of fracking fluid at high pressure in compact formation, containing gas and oil, in order to increase the overall permeability and connectivity of the formation (Hyman et al., 2016). This last goal is reached by promoting the aperture and extension of already existing fracture or by creating new ones. Only through this, an extraction of gas is economically feasible. The increased reservoir production achieved through fracking operation led to a widespread diffusion of the technology (see e.g. Arthur et al. 2009; USEPA 2012). The fluid used for fracturing is typically water mixed with proppants and a varying number of chemicals depending on the characteristics of a geological site. The proppants keep the fractures open after the fracturing process to make sure that desired flow rates can be achieved, while the added chemicals can range from friction reducers to biocides.

Despite the benefits, concerns has been raised about the environmental impact of hydraulic fracturing operations (Heinecke et al. 2014; Jabbari et al. 2015b; Kargbo et al. 2010). Three potential issue of main concern are the induced earthquakes (Aminzadeh et al. 2014) , air pollution (McKenzie et al. 2012; Moore et al. 2014) and water contamination (Osborn et al. 2011; Kissinger et al. 2013; Jabbari et al. 2015a; Llewellyn et al. 2015). The recently started research project FracRisk (funded within the EU Horizon 2020, see www.frackrisk.eu) seeks to identify the potential risks of the technology as well as corresponding mitigation and monitoring strategies. A well-established approach in the regulatory risk assessment procedures regarding sources (hydrocarbon bearing formation), pathways (e.g. fault zones, abandoned wells) and targets/receptors (e.g. a groundwater reservoir) is used, which will be applied to six focused scenarios (see Fig. 4.8). They are designed to capture a whole range of features, events and processes (FEPs) associated with unconventional gas production. Scenario 1-3 of the six focused scenarios (see Fig. 4.8) take a closer look at the source, i.e. the hydrocarbon bearing formation to be fracked, while Scenarios 4-6 consider larger spatial and temporal scales and focus rather on the intermediate- to long-term fate of a contaminant that has escaped from the source rock. Naturally, the scenarios are interconnected and the results and findings of one scenario can be used as an input for others. Scenario 1 attempts to identify the main processes occurring during the fracturing operations, such as the release of gas molecules, formation of pathways, increase of permeability, etc. The main focus lies on the mechanical description of the hydraulic fracturing process, i.e. the accurate description of fracture propagation, the creation of the fracture network and the occurrence of microseismic events. Findings on the fracture network characteristics can then be embedded into Scenario 2, where the interest is on pressure propagation in the reservoir and on the flow and transport processes through the fracture network and the surrounding porous matrix. The hydrocarbon-bearing formation is represented in detail and the temporal scale of investigation is short. Scenario 3 is an extension of Scenario 2, additionally considering reactive transport phenomena. This will allow investigations on the chemical interaction of the fracturing-fluid components with the reservoir fluids and the rock minerals, e.g. for an evaluation of the flow-back composition. Scenario 4 investigates the fate of a potential leakage in the overburden in the presence of e.g. fault zones or poorly sealed abandoned wells. In comparison to Scenario 4, which considers mid-term processes on the field-scale, Scenario 5 addresses the long-term regional-scale (tens of kilometers) flow and transport of gas, fracturing fluids, or saline water. The last scenario, S6, looks at long-term (tens of years) diffusive transport of methane through the overburden.

Numerical models are used in order to perform sensitivity analyses of certain FEPs on the severity of the consequences. Results will then be embedded into an FEP-based evaluation of risk and counteractive measures. The collection of data on selected sites across Europe & USA will allow the definition of parameter ranges to be scanned in the sensitivity analyses, and it provides necessary baseline data for a future application of the monitoring strategies developed in the project.

The main objective of this work is the introduction of a workflow for the determination of the parameter sensitivities as mentioned above. We show the procedure using an exemplary showcase (see Appendix B.4.1), which does not claim to be a realistic representation of a hydraulic fracturing operation. In particular the showcased example belong to previously defined Scenario 2. A numerical investigation of the environmental impact of hydraulic fracturing can also be found in Reagan et al., 2015, where numerical simulations were performed for a range of parameters. The procedure is somewhat similar to the one presented in this paper; however, in this work we base our analysis on a global sensitivity analysis (GSA) grounded on variance-based Sobol' indices. The extensive numerical modeling that will be carried out in the project and subsequent statistical analysis will pave the way to an abstracted model for risk evaluation. This work has been conducted in collaboration with D. Gläser, H. Class, R. Helmig (Dept. of Hydromechanics and modelling of Hydrosystems, University of Stuttgart), A. Tatomir (Dept. of applied Geology, University of Göttingen), M. Sauter (EWRE Environmental and Water Resources Engineering, Israel) and M. Sauter (School of Geosciences, University of Edinburg).

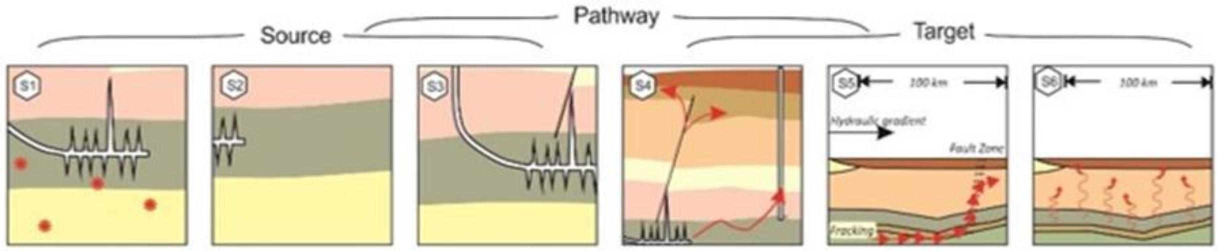

Figure 4.8. Illustration of the six focused modelling scenarios. S1: modelling of the fracture growth; S2: Pressure propagation around the fracked source; S3: geochemical modelling; S4: Flow and transport in faults and abandoned wells; S5: Regional transport of displaced fluid; S6: Diffusive transport through the overburden overlying formations and aquifers. Source: www.fracrisk.eu.

Appendix B.4.1: Showcase Scenario

The showcase presented in this work has been elaborated in order to test a general workflow and the tools being used and developed within the FracRisk project. Based on Scenario 2 (see Fig. 4.8), the showcase looks at the potential contamination of a target aquifer with a fracturing-fluid component due to the injection of such fluid at high pressure into an underlying formation (see Fig. 4.9). Highly conductive pathways through the lower formation are present by means of a fracture network, which are directly connected to the target aquifer, i.e. there is no sealing layer between the source and the target. An injection is imposed on a section of the lower boundary and the overall mass accumulated in the target formation is evaluated at the end of the simulation, i.e. after six hours of injection

In this showcase, single-phase flow and transport phenomena through porous media are considered, for which the governing system of equations can be found in e.g. Flemish et al., 2011. A vertex-centered finite volume method (box) is used for the spatial discretization, see Heling, 1997, in which control volumes are constructed around the vertices of a grid connecting the midpoints of the element edges and faces around a node with the barycenters of the surrounding elements. The conservation equation is integrated over the finite volume; thus, local conservation of the considered quantity is guaranteed. Fluxes are computed on the bounding faces of these control volumes using the finite element basis functions of the elements that intersect with the box to evaluate the necessary quantities and their gradients at the flux computation points. The model used for the simulations in this paper extends the box formulation to account for discrete fractures. Element entities of codimension 1 (faces in 3d, edges in 2d) can herein be identified as fracture entities. In control volumes that are intersected by fracture entities, the flux and storage terms of the system of equations are split into contributions from fracture and matrix respectively. A detailed description of this can be found in Tatomir, 2012. An implicit Euler method has been chosen for the time discretization and the Newton-Raphson method is used to handle the non-linear dependencies of the water-phase density and of the viscosity on pressure and temperature, for which the IAPWS 97 formulation of Wagener et al., 2000 was used. For simplicity, the fluid density and viscosity do not depend on the concentration of the transported component. The numerical model is implemented in the free open-source numerical simulator DuMu^x (Flemish et al., 2011) and works in two and three dimensions. However, the presented showcase is two-dimensional.

The fracture network as an input for the simulations can be obtained from measurements or by using a geostatistical fracture network creator as e.g. Frac3D (see Assteerawat , 2008; Silberhorn-Hemminger, 2013;). As the model presented in this paper does not solve for the geomechanical deformations of the rock, fracture propagation is not simulated and the fracture network is assumed to be static throughout the entire simulation. The fracture network geometry for this showcase has been obtained from a scan of a limestone outcrop in Bristol (Belayneh at al., 2006; Tatomir et al., 2011;) scaled by a factor of five. Even though it is not representative for shale, the geometry has been chosen to show that the numerical model does not impose any geometrical restrictions.

The injection length of approximately 20m on the lower boundary (see Fig. 4.9) is designed to represent one stage during a hydraulic fracturing operation. Injection occurs at five discrete positions representing the perforated parts of the stage. These five injection points were chosen to be at the intersections of fractures with the boundary to ensure maximum injection rates directly into the fracture network. The injection is simulated by a Cauchy-type boundary condition, where the pressure at the boundary is specified and the resulting mass flux into the domain is calculated via Darcy's law:

$$q_{inj} = -a_f \rho_w(p_{inj}) \frac{\boldsymbol{k}_f}{\mu_w} \left(\frac{\boldsymbol{x}_{inj} - \boldsymbol{x}_f}{\| \boldsymbol{x}_{inj} - \boldsymbol{x}_f \|^2} \left(p_{inj} - p_f \right) - \bar{\rho}_w \boldsymbol{g} \right) \boldsymbol{n} \qquad \text{(B.4.1)}$$

Here, p_f is the actual pressure in the fracture when evaluating the boundary condition with the specified injection pressure p_{inj}, $\boldsymbol{x}_{inj}$ is the position of the injection point, i.e. the intersection of a fracture with the boundary, $\boldsymbol{x}_f$ is the center of the fracture entity and a_f is its aperture, $\boldsymbol{n}$ is the unit outer normal vector of the boundary face. The averaged water phase density $\bar{\rho}_w = (\rho_w(p_{inj}) + \rho_w(p_f))/2$ is used to evaluate the gravitational forces, where $\boldsymbol{g}$ is the gravitational acceleration. A fully-upwind approach is applied for the density ρ_w and the viscosity μ_w outside of the brackets. $\boldsymbol{k}_f$ is the intrinsic permeability of the fracture. For the transport equation of the component the boundary influx q_{inj} has to be multiplied by the specified concentration of the component in the fracturing fluid to be injected. This has been set to $X^c = 0.01$. The remaining parts of the lower, as well as the two lateral boundaries were set to Neumann no-flow. As initial and Dirichlet boundary conditions on the upper boundary a hydrostatic pressure distribution and a component concentration of zero were applied. We assumed a constant and fixed geothermal gradient of 30 K/km throughout the simulations.

The authors are aware of the fact that the scenario setup at this early stage of the project is not a realistic representation of an actual hydraulic fracturing operation. The fracture network geometry, obtained from a limestone, does not adequately represent a shale formation. Furthermore, the fracture network does not evolve during the simulations but is already fully developed prior to the injection.

A reduction of the problem to two dimensions and no-flow boundaries on the lateral sides both contribute to an overestimation of the pressure and, thus, to higher flow rates towards the target formation. The absence of a sealing layer above the source rock and the relatively long injection time of six hours further increase the likelihood and the level of a contamination within the target aquifer. However, the showcase has not been designed to actually evaluate the potential risks of the technology, which is a final aim of the project. As mentioned before, it aims for a testing of the workflow and the tools involved. For the actual modelling of the scenarios within the project, more realistic setups will be created and a larger set of parameters will be included in the sensitivity analysis.

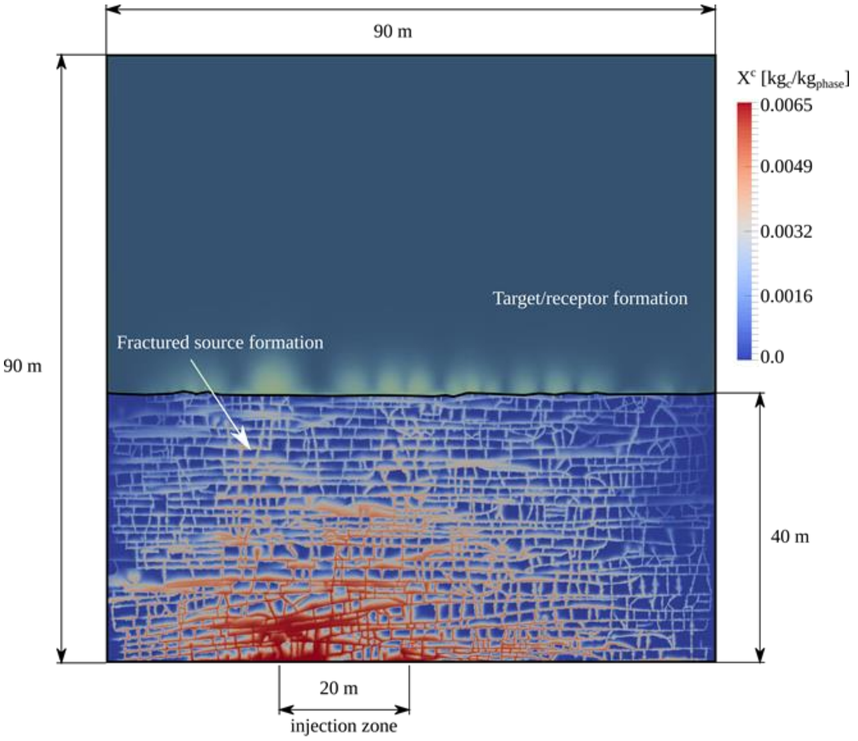

Figure 4.9. Snapshot of a simulation result edited to illustrate the model domain, its dimensions and the features included.

Appendix B.4.2: Definition of global quantity of interest and GSA results

In this study, as global quantity of interest we focus on the accumulated mass of contaminant in the target aquifer, Ω_{TA} ,at the end of the injection period

$$\overline{\mathrm{M}} = \int_{\Omega_{TA}} \rho_w X^c \Phi_{TA} d\Omega_{TA} \tag{B.4.2}$$

We investigate the sensitivity of $\overline{\mathrm{M}}$ with respect to the permeability of the target aquifer, $\boldsymbol{k}_{TA}$, the aperture of the fracture, a_f, and the pressure of injection of the fracturing fluid, p_{inj} . The first two represent our lack of knowledge about aquifer properties, whereas p_{inj} represents varying operational conditions. The parameters $\boldsymbol{k}_{TA}$, a_f, and p_{inj} are treated as independent uniformly distributed random variable, which interval of variation are listed in Table 4.4.

Table 4.4. Parameter value for the showcase.

Parameter	Unit	Value
Fracture aperture, a_f	m	[1e-5 – 1e-3]
Injection pressure, p_{inj}	bar	[150 - 350]
Intrinsic permeability of the target formation, $\boldsymbol{k}_{TA}$	m^2	[1e-11 – 1e-13]
Intrinsic permeability of the source matrix, $\boldsymbol{k}_S$	m^2	1e-14
Intrinsic permeability of the source fractures, $\boldsymbol{k}_F$	m^2	1e-8
Porosity of the target formation, Φ_{TA}	-	0.25
Porosity of the source matrix, Φ_s	-	0.1
Porosity of the source fractures, Φ_f	-	0.7

We perform a GSA grounded on variance-based Sobol indices computed through a gPCE representation (see Section 4.3) of $\overline{\mathrm{M}}$. The quality of the gPCE representation is ensued by comparing resulting values of $\overline{\mathrm{M}}$ obtained with (a) the full mathematical-numerical model with those (b) resulting from the gPCE surrogate model for 20 random combination of input parameters drawns in the parameter space. Figure 4.10 depicts a scatter plot of values of $\overline{\mathrm{M}}$, where the continuous line represents the full model results while crosses, circles and diamonds are the corresponding results based on a gPCE representation of total degree (see Section 4.3) w = 2, 3, 4 respectively. A satisfactory agreement is reached.

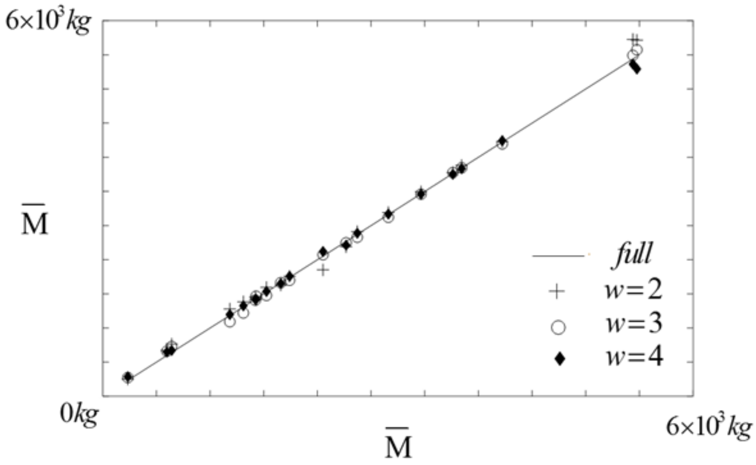

Figure 4.10. Scatter plot of the total accumulated mass of contaminant in the target aquifer obtained by the full model (x-axis) vs. the corresponding gPCE representations. Continuous line: results for the full model of section 3. gPCE of total degree w = 2, crosses; w = 3, circles; w = 4, diamonds. Twenty simulations randomly selected in parameter space.

Table 4.5 lists the mean value, $\mu_{\overline{\mathrm{M}}}$, variance, $V_{\overline{\mathrm{M}}}$, coefficient of variation, $CV_{\overline{\mathrm{M}}} = V_{\overline{\mathrm{M}}}^{0.5} / \mu_{\overline{\mathrm{M}}}$ and principal, S_{x_i}, and total, $S_{x_i}^{T}$, Sobol' Indices, for $x_i = \mathbf{k}_{TA}, a_f, p_{inj}$, for $\overline{\mathrm{M}}$ and for the different level of accuracy of the gPCE representation, i.e w = 2, 3, 4. Inspection of Tab. 4. suggests that the investigated statistical moment of $\overline{\mathrm{M}}$ and both principal and total Sobol' indices reached convergence with respect to the gPCE accuracy, i.e. w. In the following, we will refer to the results for w = 4. A look at both $S_{\mathbf{k}_{TA}}$ and $S_{\mathbf{k}_{TA}}^{T}$ indicates that the uncertainty affecting $\mathbf{k}_{TA}$ practically does not contribute to the output variance $V_{\overline{\mathrm{M}}}$. Instead, the major contribution to $V_{\overline{\mathrm{M}}}$ comes from a_f, as can be seen by looking at S_{a_f} and $S_{a_f}^{T}$, indicating that the uncertainty in the fracture aperture determines more than the seventy per cent of output variance. The examination of $S_{p_{inj}}$ and $S_{p_{inj}}^{T}$ suggests that more than twenty per cent of the output variance is dictated by the variation of p_{inj}. It is also noted that the principal and total Sobol' indices values are relatively close, indicating a small level of interaction between parameters. The GSA results suggest that, for the showcase here considered, the aperture of the fracture and the pressure of injection of fracturing fluid plays key roles in determining the level of contamination of the target aquifer, while the permeability of the last in uninfluential. This can be explained by considering that it is mainly through the fracture network and with an intensity proportional to the imposed pressure of injection, that contaminant travels throughout the production aquifer reaching the overlaying target formation.

Table 4.5. Mean, $\mu_{\overline{\mathrm{M}}}$, variance, $V_{\overline{\mathrm{M}}}$, coefficient of variation, $CV_{\overline{\mathrm{M}}}$, principal, S_{x_i}, and total, $S_{x_i}^{T}$, Sobol' indices for $x_i = \mathbf{k}_{TA}, a_f, p_{inj}$.

	w = 2	w = 3	w = 4
$\mu_{\overline{\mathrm{M}}}$	2.28 x10^{3}	2.25 x10^{3}	2.23x10^{3}
$V_{\overline{\mathrm{M}}}$	2.63 x10^{6}	2.40 x10^{6}	2.27x10^{6}
$CV_{\overline{\mathrm{M}}}$	0.71	0.69	0.68
$S_{\mathbf{k}_{TA}}$	1.9 x10^{-6}	1.0 x10^{-5}	9.1 x10^{-5}
S_{a_f}	0.70	0.70	0.71
$S_{p_{inj}}$	0.25	0.25	0.24
$S_{\mathbf{k}_{TA}}^{T}$	2.4 x10^{-6}	4.3 x10^{-5}	2.5x10^{-4}
$S_{a_f}^{T}$	0.75	0.75	0.77
$S_{p_{inj}}^{T}$	0.30	0.31	0.29

Appendix B.4.3: Summary and Outlook

A variance-based GSA for the determination of parameter sensitivities, to be embedded into an FEP-based risk assessment of hydraulic fracturing operations, has been presented on an exemplary showcase. This showcase considers a naturally fractured reservoir into which the injection of a fluid carrying a potentially hazardous component leads to a contamination in an overlying aquifer (target). The contamination is identify with the total mass of accumulated contaminant in the overlaying target aquifer. The first two statistical moments of the accumulated mass of contaminant has been evaluated and its sensitivities with respect to model input parameters has been determined by means of variance-based Sobol' indices. The current procedure is an essential tool for investigating all six focused modelling scenarios defined in the FracRisk project. However, the current work is only a very first step towards an extensive investigation of the potential environmental impact of hydraulic fracturing by applying this approach to a number of different scenarios with a large number of different setups and parameter ranges to be evaluated. This will be carried out within the scope of the project together with the development of an FEP-based model for risk assessment.

Reference

Abarca, E., Carrera, J., Sanchez-Vila, X. and Dentz, M.: Anisotropic dispersive Henry problem, Adv. Water Resour., 30(4), 913-926, 2007.

Al-Bitar, A., Ababou, R.: Random field approach to seawater intrusion in heterogeneous coastal aquifers: unconditional simulations and statistical analysis, In: Renard, P., Demougeot-Renard, H. and Froidevaux, R. editors. Proceedings of the fifth European conference for environmental applications, Geostatistics for Environmental Applications, Springer Verlag New York, 232-247, 2005.

Aminzadeh, F., Tiwari, A. and Walker, R.: Correlation between induced seismic events and hydraulic fracturing activities in California, In: American Geophysical Union Fall Meeting, San Francisco, 2014.

Archer, G. E. B., Saltelli, A. and Sobol, I. M.: Sensitivity measures, anova-like techniques and the use of bootstrap, J. Stat. Comput. Simulation, 58, 99-120, 1998.

Arthur, J. D., Bohm, B. and Coughlin, B. J.: Evaluating implications of hydraulic fracturing in shale gas reservoirs, SPE Americas E&P environmental and safety conference, Society of Petroleum Engineers, doi:10.2118/121038-MS, 2009.

Assteerawat, A.: Flow and transport modelling of fractured aquifers based on a geostatistical approach, PhD thesis, Universitätsbibliothek der Universität Stuttgart, October 2008.

Bäck, J., Nobile, F., Tamellini, L. and Tempone, R.: Stochastic spectral Galerkin and collocation methods for PDEs with random coefficients: a numerical comparison, In: Hesthaven, J. S. and Ronquist, E. M. editors, Lecture Notes in Computational Science and Engineering, Spectral and High Order Methods for Partial Differential Equations, Springer-Verlag, Berlin Heidelberg, 76, 43-62, 2011.

Ballio, F. and Guadagnini, A.: Convergence assessment of numerical Monte Carlo simulations in groundwater hydrology, Water Resour. Res., 40, W04603, 2004.

Bear, J., Cheng, A. H. D., Sorek, S., Ouazar, D. and Herrera, I.: Seawater Intrusion in Coastal Aquifers – Concepts, Methods, and Practices, Kluwer Academic Publisher, 1999.

Bear, J. and Cheng, A. H. D.: Modeling groundwater flow and contaminant transport, Springer, 2010.

Belayneh, M., Geiger, S. and Matthai, S. K.: Numerical simulation of water injection into layered fractured carbonate reservoir analogs, AAPG Bulletin, 90, 1473-1493, doi: 10.1306/05090605153, 2006.

Boso, F., de Barros, F. P. J., Fiori, A. and Bellin, A.: Performance analysis of statistical spatial measures for contaminant plume characterization toward risk-based decision making, Water Resour. Res., 49, 3119-3132, doi: 10.1002/wrcr.20270, 2013.

Bruggeman, G.A.: Analytical solutions of geohydrological problems, Developments in water science, Elsevier Amsterdam 46, 1999.

Chang, C. M. and Yeh, H.D.: Spectral approach to seawater intrusion in heterogeneous coastal aquifers, Hydrol. Earth Syst. Sci., 14, 719-727, doi:10.5194/hess-14-719-2010, 2014.

Ciriello, V., Di Federico,V., Riva, M., Cadini, F., De Sanctis, J., Zio, E. and Guadagnini, A.: Polynomial chaos expansion for global sensitivity analysis applied to a model of radionuclide migration in a randomly heterogeneous aquifer, Stoch. Environ. Res. Risk. Assess., 27,945-954, doi: 10.1007/s00477-012-0616-7, 2013.

Crestaux, T., Le Maître, O. and Martinez, J. M.: Polynomial chaos expansion for sensitivity analysis, Reliab. Eng. Syst. Safety, 94(7), 1161-1172, doi:10.1016/j.ress.2008.10.008, 2009.

Dagan, G. and Zeitoun, D. G.: Seawater-freshwater interface in a stratified aquifer of random permeability distribution, J. Cont. Hydrol., 29, 185-203, 1998.

Dentz, M., Tartakovsky, D. M., Abarca, E., Guadagnini, A., Sanchez-Vila, X. and Carrera, J.: Variable-density flow in porous media, J. Fluid Mech., 561, 209-235, doi:10.1017/S0022112006000668, 2006.

Fajraoui, N., Ramasomanana, F., Younes, A., Mara, T., Ackerer, P. and Guadagnini, A.: Use of global sensitivity analysis and polynomial chaos expansion for interpretation of nonreactive transport experiments in laboratory-scale porous media, Water Resour. Res., 47, W02521, doi:10.1029/2010WR009639, 2011.

Fetter, C. W.: Contaminant Hydrogeology, Second Edition, Prentice Hall, Upper Saddle River, New Jersey, 1999.

Flemisch, B., Darcis, M. and Erbertseder K.: DuMux: DUNE for multi-{phase, component, scale, physics, …} flow and transport in porous media. Adv. Water Resour., 34, 1102-1112, doi: 10.1016/j.advwatres.2011.03.007, 2011.

Formaggia, L., Guadagnini, A., Imperiali, I., Lever, V., Porta, G., Riva, M., Scotti, A. and Tamellini, L.: Global sensitivity analysis through polynomial chaos expansion of a basin-scale geochemical compaction model, Comput. Geosci., 17, 25-42, doi: 10.1007/s10596-012-9311-5, 2013.

Gautschi, W.: Orthogonal Polynomials: Computation and Approximation, Oxford University Press, Oxford, 2004.

Ghanem, R. G. and Spanos, P.D.: Stochastic finite elements: a spectral approach, Springer Berlin, 1991.

Heinecke, J., Jabbari, N. and Meshkati, N.:The role of human factors considerations and safety culture in the safety of hydraulic fracturing (Fracking), J. Sustain. Energy Eng., 2, 130–151, doi:10. 7569/JSEE.2014.629509, 2014.

Held, R., Attinger, S. and Kinzelbach, W.: Homogenization and effective parameters for the Henry problem in heterogeneous formations, Water Resour. Res., 41, 1-14, doi:10.1029/2004WR003674, 2005.

Helmig, R.: Multiphase flow and transport processes in the subsurface: a contribution to the modeling of hydrosystems, Springer-Verlag, 1997.

Henry, H. R.: Effects of dispersion on salt encroachment in coastal aquifers,Water-Supply Paper 1613-C, U. S. Geological Survey, 1964.

Hyman, J. D., Jimenéz-Martìnez, J., Viswanathan, H. S., Carey, J. W., Porter M. L., Rougier, E., Karra, S., Kang, Q., Frash, L., Chen, L., Lei, Z., O'Malley, D. and Makedonska, N.: Understanding hydraulic fracturing: a multi-scale problem, Phil. Trans. R. Soc. A, 374:20150426, http://dx.doi.org/10.1098/rsta.2015.0426

Jabbari, N., Aminzadeh, F. and de Barros F. P. J.:Assessing the groundwater contamination potential from a well in a hydraulic fracturing operation, J. Sustain. Energy Eng., 3, 66-79, doi:10.7569/ JSEE.2015.629507, 2015a.

Jabbari, N., Ashayeri, C. and Meshkati, N.: Leading safety, health, and environmental indicators in hydraulic fracturing, In: SPE Western Regional Meeting, Garden Grove, CA, 2015b.

Jiang, Z., Raiber, M., Bian, J. and Malcolm, M.: On the effective hydraulic conductivity and macrodispersivity for density-dependent groundwater flow, Environ. Fluid. Mech., 14, 157-171, doi 10.1007/s10652-013-9281-8, 2013.

Kargb, D. M., Wilhelm, R. G. and Campbell, D. J.: Natural gas plays in the Marcellus Shale: challenges and potential opportunities, Environ. Sci. Technol., 44, 5679-5684, doi:10.1021/es903811p, 2010.

Kerrou, J. and Renard., P.: A numerical analysis of dimensionality and heterogeneity effects on advective dispersive seawater intrusion processes, Hydrol. Journal, 18, 55-72, 2010.

Kempers, L. T. J. M. and Haas, H.: The dispersion zone between fluids with different density and viscosity in a heterogeneous porous medium, J. Fluid Mech., 267, 299-324, 1994.

Kissinger, A., Helmig, R., Ebigbo, A., Class, H., Lange, T., Sauter, M., Heitfeld, M., Klünker, J. and Jahnke, W.: Hydraulic fracturing in unconventional gas reservoirs: risks in the geological system, part 2, Environ. Earth Sci., 70, 3855-3873, doi:10.1007/s12665-013-2578-6, 2013.

Kretz, V., Berest, P., Hulin J. P. and Salin, D.: An experimental study of the effects of density and viscosity contrasts on macrodispersion in porous media, Water Resour. Res., 39(2), 1032, doi:10.1029/2001WR001244, 2003.

Laloy, E., Rogiers, B., Vrugt, J. A., Mallants, D. and Jacques, D.: Efficient posterior exploration of a high-dimensional groundwater model from two-stage MCMC simulation and polynomial chaos expansion, Water Resour. Res., 49, 2664-2682, doi:10.1002/wrcr.20226, 2013.

Le Maître, O.P. and Knio, O. M.: Spectral methods for uncertainty quantification, Scientific Computation, Springer, 2010.

Llewellyn, G. T., Dorman, F. and Westland, J. L.: Evaluating a groundwater supply contamination incident attributed to Marcellus Shale gas development, Proc. Natl. Acad. Sci., 112, 6325-6330, doi:10.1073/pnas.1420279112, 2015.

Li, W., Lu, Z. and Zhang D.: Stochastic analysis of unsaturated flow with probabilistic collocation method, Water Resour. Res., 45, W08425, doi:10.1029/2008WR007530, 2009.

McKenzie, L. M., Witter, R. Z., Newman, L. S. and Adgate, J. L.: Human health risk assessment of air emissions from development of unconventional natural gas resources, Sci. Total. Environ., 424, 79-87, 2012.

Menand, T. and Woods, A. W.: Dispersion, scale, and time dependence of mixing zones under gravitationally stable and unstable displacements in porous media, Water Resour. Res., 41, W05014, doi:10.1029/2004WR003701, 2005.

Moore, C. W., Zielinska, B., Pétron, G. and Jackson, R. B.: Air impacts of increased natural gas acquisition, processing, and use: a critical review, Environ Sci Technol., doi:10.1021/es4053472, 2014.

Osborn, S. G., Vengosh, A., Warner, N. R. and Jackson, R. B.: Methane contamination of drinking water accompanying gas-well drilling and hydraulic fracturing, Proc. Natl. Acad. Sci. USA, 108, 8172-8176, doi:10.1073/pnas.1100682108, 2010.

Papoulis, A.: Probability, random variables, and stochastic process, Third Edition, McGraw-Hill series in electrical engineering, 1991.

Porta, G., Lever, V., Tamellini, L. and Riva, M.: Characterization of sedimentary basins through Polynomial Chaos Expansion in the presence of mechanical and geochemical compaction, Water Resous. Res., 50, 9414-9431, 2014.

Reagan, M. T., Moridis, J. G., Keen, N. D. and Johnson, J. N.: Numerical simulation of the environmental impact of hydraulic fracturing of tight/shale gas reservoirs on near-surface groundwater: Background, base cases, shallow reservoirs, short-term gas, and water transport, Water Resour. Res., 51, 2543–2573, doi:10.1002/2014WR016086, 2015.

Reilly, T. E. and Goodman, A. S.: Quantitative analysis of saltwater-freshwater relationships in groundwater systems-A historical perspective, J. Hydrol., 80, 125-160, doi: 10.1016/0022-1694(85)90078-2, 1985.

Rubin, Y.: Applied stochastic hydrogeology, Oxford University Press, New York, 2003.

Saltelli, A., Ratto, M., Tarantola, S. and Campolongo, F.: Sensitivity analysis practices: strategies for model-based inference, Reliab. Eng. & Syst. Saf., 91, 1109-1125, doi:10.1016/j.ress.2005.11.014, 2006.

Silberhorn-Hemminger, A.: Modellierung von Kluftaquifersystemen. Geostatistische Analyse und deterministisch stochastische Kluft-generierung, PhD thesis, Universitätsbibliothek der Universität Stuttgart, January 2013.

Simpson, M. J. and Clement, T. P.: Theoretical analysis of the worthiness of Henry and Elder problems as benchmarks of density-dependent groundwater flow models, Adv. Water Resous., 26, 17-31, 2004.

Sobol, I. M.: Sensitivity estimates for nonlinear mathematical models, Mathematical Modeling and Computational Experiment, 1, 407-417, 1993.

Sobol, I. M.: Global sensitivity indices for nonlinear mathematical models and their Monte Carlo estimates, Mathematics and Computers in Simulations, 55, 271-280, 2001.

Sudret, B.: Global sensitivity analysis using polynomial chaos expansions, Reliab. Eng. & Syst. Safety, 93, 964-979, doi:10.1016/j.ress.2007.04.002, 2008.

Tatomir, A. B., Szymkiewicz, A., Class, H. and Helmig, R.: Modeling two phase flow in large scale fractured porous media with an extended multiple interacting continua method, C. M. E. S., 77, 81-111, 2011.

Tatomir, A.: From discrete to continuum concepts of flow in fractured porous media, PhD thesis, Universitätsbibliothek der Universität Stuttgart, http://dx.doi.org/10.18419/opus-476, 2012.

Volker, R. E. and Rushton, K. R.: An assessment of the importance of some parameters for seawater intrusion in aquifers and a comparison of dispersive and sharp-interface modelling approaches, J. Hydrol., 56, 239-250, 1982.

Voss, C. I. and Provost, A. M.: SUTRA, a model for saturate-unsaturated variable density ground-water with solute or energy transport, Reston USA: US Geological Survey Open-File Report 02-4231, 250 p., 2002.

Wagner, W., Cooper, J. R. and Dittmann, A.: The IAPWS Industrial Formulation 1997 for the Thermodynamic Properties of Water and Steam, J. Eng. Gas Turb. Pow. 122(1), 150-184, 2000.

Werner, A.D., Bakker, M., Post, V. E. A., Vandenbohede, A., Lu, C., Ataie-Ashtiani, B., Simmons, C. T. and Barry, D. A.: Seawater intrusion processes, investigation and management: Recent advances and future challenges, Adv. Water Resour., 51, 3-26, 2013.

Xiu, D. and Karniadakis, G. E. M.: The Wiener-Askey polynomial chaos for stochastic differential equations, SIAM J. Sci. Comput., 24(2), 619-644, 2002.

5 Moment-based Metrics for Global Sensitivity Analysis of Hydrogeological Systems

In this chapter we propose new metrics/indices to assist Global Sensitivity Analysis (GSA) of hydrogeological systems. We quantify sensitivity of model uncertain parameters through the use of indices based on the first four (statistical) moments of the probability density function (*pdf*) of a model output of interest. Evaluating parameter sensitivity in terms of multiple statistical moments leads to the assessment of the impact of model parameters on main features governing the shape of the *pdf* of target model outputs. These include the expected value of the output as well as the spread around the mean (as quantified by the variance), and the degree of symmetry and tailedness of the *pdf* of interest.

Since reliable assessment of higher order statistical moments can be computationally demanding for complex models, we couple our GSA approach with the construction of a surrogate model, approximating the full model response at a reduced computational cost. Here, we consider the generalized Polynomial Chaos Expansion (gPCE), other model reduction techniques being fully compatible with our theoretical framework.

We demonstrate our approach through three test cases, including a popular analytical benchmark, a simplified scenario mimicking pumping in a coastal aquifer, and a laboratory-scale conservative transport experiment. Our results allow discriminating which parameters can be more influential to some moments of the model output *pdf* while being uninfluential to others. We also investigate the error associated with the evaluation of our sensitivity metrics by replacing the original system model through the selected surrogate model. In general, our results indicate that the construction of a surrogate model with increasing level of accuracy might be required depending on the statistical moment considered in the GSA. Our approach is fully compatible with (and can assist the development of) analysis techniques employed in the context of model calibration, design of experiment, uncertainty quantification and risk assessment.

5.1 Introduction

Our improved understanding of basic mechanisms governing hydrological processes at multiple space and time scales and the ever increasing power of modern computational resources are at the heart of the formulation of conceptual models characterized by unprecedented levels of sophistication and complexity. This is typically transparent when one considers the spectrum of mathematical formulations and ensuing level of model parametrization rendering our conceptual understanding of given environmental scenarios (Grauso et al., 2007; Wagener and Montanari, 2011; Hostache et al., 2011; Koutsoyiannis, 2010; Wagener et al., 2010; Paniconi and Putti, 2015; Markstrom et al. 2016; Alzraiee et al., 2014; Hartmann et al., 2013; Herman et al., 2013; Willmann et al., 2006; Lee et al., 2012; Elshorbagy et al., 2010a,b; Förster et al., 2014). Model complexity can in turn exacerbate challenges associated with the need to quantify the way uncertainty associated with parameters of a given model propagate to target state variables.

In this context, approaches based on rigorous sensitivity analysis are valuable tools to improve our ability to (*i*) quantify uncertainty, (*ii*) enhance our understanding of the relationships between model input and outputs, and (*iii*) tackle the challenges of model- and data- driven design of experiments in hydrological sciences. These also offer critical insights to guide model simplification, e.g., by identifying model input parameters that have limited effects on a target output. The variety of available sensitivity analysis methodologies can be roughly subdivided into two broad categories, i.e., local and global approaches. Local sensitivity analyses consider the variation of a model output against variations of model input solely in the neighbourhood of a given set of parameters values. Otherwise, global sensitivity analysis (GSA) quantifies model sensitivity across the complete support within which model parameters can vary. Error measurements and/or lack of knowledge about parameters can be naturally accommodated in a GSA by specifying appropriate parameter intervals and evaluating sensitivity over the complete parameter space. A review of the diverse available sensitivity analysis approaches and of the various interpretations of the concept of model sensitivity is outside the scope of this study. Recent works providing extended appraisals of these issues include, e.g., the studies of Pianosi et al. (2016), Sarrazin et al. (2016), and Razavi and Gupta (2015).

Our study is framed in the context of GSA approaches. A broadly recognized strategy to quantify global sensitivity of uncertain model parameters to model outputs relies on the evaluation of the Sobol' indices (Sobol, 1993). These quantify the relative amount of the variance of a target model output that is apportioned to the variability of one parameter alone or in conjunction with other parameters across the domain (support) of parameter definition (i.e., across the parameter space). Sobol' indices are typically referred to as variance-based sensitivity measures because the output variance is taken as the metric upon which sensitivity is quantified. A key limitation of a variance based- GSA is that the uncertainty of the output is implicitly considered to be fully characterized by the variance. Relying solely on this criterion can provide an incomplete picture of a system response to model parameters, also considering that probability densities of typical hydrological quantities can be characterized by higher order (statistical) moments, e.g., in the presence of highly skewed distributions (e.g., Borgonovo, 2011). Some studies introduce a sensitivity metric grounded on the complete probability density function (*pdf*) of the model output (see, e.g., Krykacz-Hausmann, 2001; and Borgonovo, 2007). These so-called moment-independent analyses may suffer from operational constraints for complex and computationally demanding problems, because a robust evaluation of the complete probability distribution may require a number of model runs which is unaffordable. The PAWN method introduced by Pianosi and Wagener (2015) attempts to overcome this limitation introducing a sensitivity metric based on the cumulative density function, which can potentially be estimated more robustly than its associated *pdf* for a given sample size.

A comparison between variance-based and moment-independent GSA suggests that (*a*) the meaning of the former and the relationship between variance and spread of the *pdf* around the mean are straightforward information to convey, albeit incomplete to fully characterize the variability of a model response; and (*b*) in the case of the latter it is hard to extract quantitative information about the way variations of a parameter can affect the main features of the *pdf*. It is then clear that while a variance-based GSA can be favored for its (conceptual and implementation) simplicity and variance can be considered in several cases as an adequate proxy of the spread around the mean, it does not yield a forthright quantification of the way variations of a parameter can affect the structure of the *pdf* of a target model output. Otherwise, moment-independent methodologies condense the entire *pdf* in only one index, somehow clouding our understanding of how the structure of the *pdf* is affected by variations of each uncertain model parameter.

Our distinctive objective is to contribute to bridge the gap between these two types of GSA. We do so by introducing theoretical elements and an implementation strategy which enable us to appraise parameter sensitivity through the joint use of sensitivity indices based on the first four (statistical) moments of the probability distribution of the model output of interest, i.e., (*i*) expected value, (*ii*) variance, (*iii*) skewness and (*iv*) kurtosis. The key idea at the basis of this strategy is that linking parameter sensitivity to multiple statistical moments leads to improved understanding of the way a given uncertain parameter can govern important features of the shape of the *pdf* of desired model outputs. As such, our strategy yields a quantification of the effects of uncertain model parameters in terms of the selected statistical moments, that have well-known properties in controlling elements of the shape of the *pdf* which are of interest in modern applications of hydrological sciences.

Variance-based GSA has also been applied (*a*) to guide reduction of model complexity, e.g., by setting the value of a parameter which is deemed as uninfluential to the variance of a target model output (see, e.g., Fu et al., 2011; Chu et al., 2015; Punzo et al., 2015), and (*b*) in the context of uncertainty quantification (Saltelli et al., 2008; Pianosi et al., 2014; Colombo et al., 2016). Only limited attention has been devoted to assess the relative effects of uncertain model parameters to the expected value of the desired model output. This information would complement a model complexity analysis by introducing a quantification of the impact that conditioning the process on prescribed parameter values would have on the expected value of the output. Our approach is based on the joint use of multiple (statistical) moments for GSA. It enables us to address the following critical questions: When can the variance be considered as a reliable proxy for characterizing model output uncertainty? Which model parameter mostly affects asymmetry and/or the tailing behavior of a model output *pdf*? Does a given model parameter have a marked role in controlling some of the first four statistical moments of model output *pdf*, while being uninfluential to others?

Even as the richness of information content that a GSA grounded on the first four statistical moments might carry can be a significant added value to our system understanding, it may sometimes be challenging to obtain robust and stable evaluation of the proposed metrics for complex and computationally demanding models. This can be especially true when considering higher-order moments such as skewness and kurtosis. To overcome this difficulty, we cast the problem within a computationally tractable framework by relying on the use of surrogate models, which mimic the full model response with a reduced computational burden. Amongst the diverse available techniques to construct a surrogate model (see, e.g., Razavi et al., 2012a,b), we exemplify our approach by considering the generalized Polynomial Chaos Expansion (gPCE) that has been successfully applied to a variety complex environmental problems (Riva et al., 2015; Ciriello et al., 2013; Formaggia et al., 2013; Sudret, 2008; Gläser et al. 2016 and references therein), other model reduction techniques being fully compatible with our GSA framework. In this context, we also investigate the error associated with the evaluation of the sensitivity metrics we propose by replacing the original (full) system model through the selected surrogate model for three test cases, including a widely employed analytical benchmark, a simplified pumping scenario in a coastal aquifer, and a laboratory-scale transport setting. The rest of the work is organized as follow. Section 5.2 presents our theoretical developments; Section 5.3 illustrates our results for the three diverse test cases indicated above, our conclusions being drawn in Section 5.4.

5.2 Theoretical Framework

The widely used variance-based Sobol' indices employed as metrics for GSA are described in previous Section 4.3. Details about the generalized Polynomial Chaos Expansion (gPCE) technique which we use to construct a surrogate of the full system model and to evaluate analytically the Sobol' indices can be found in Section 4.3 and are not repeated here. Sobol' indices allow quantifying the contribution of each uncertain parameter to the total variance of a state variable of interest, y. We then illustrate in Section 5.2.1 the theoretical developments underlying our approach and introduce new global sensitivity indices. Our novel metrics enable us to quantify the impact of model uncertain parameters on the first four statistical moments of the probability density function (*pdf*) of y.

5.2.1 New metrics for multiple-moment GSA

We introduce new metrics to quantify the expected relative change of main features of the *pdf* of $y(\boldsymbol{x})$ due to variability of model input parameters. In contrast with traditional variance-based GSA techniques of the kind described in Section 4.3, we quantify changes in the *pdf* of $y(\boldsymbol{x})$ through its first four statistical moments, i.e., mean, variance, skewness, $\gamma[y]$, and kurtosis, $k[y]$. The latter is an indicator of the behavior of the tails of the *pdf* of y and is particularly useful in the context of risk analysis, $\gamma[y]$ quantifying the asymmetry of the *pdf*.

We consider a target system state variable, y, which depends on N random parameters collected in vector $\boldsymbol{x}$ = (x_1 , x_2 , …, x_N) and defined in the parameter space $\Gamma = \Gamma_{x_1} \times \Gamma_{x_2} \times ... \Gamma_{x_N}$, $\Gamma_i = [x_{i,\min}, x_{i,\max}]$ being the support of the *i*-th random variable x_i .The effect of changes of $\boldsymbol{x}$ on the mean of y cannot be systematically analysed by the metrics currently available in the literature. Assessment of the effect of variations of x_i on the mean value of $y(\boldsymbol{x})$ is achieved through the following quantity

$$AMAE_{x_i} = \begin{cases} \dfrac{1}{|y_0|} \displaystyle\int_{\Gamma_{x_i}} \left|y_0 - E[y \,|\, x_i]\right| \rho_{\Gamma_{x_i}}(x_i)\, dx_i = \dfrac{1}{|y_0|} E\left[\left|y_0 - E[y \,|\, x_i\right|]\right] & if \quad y_0 \neq 0 \\ \displaystyle\int_{\Gamma_{x_i}} \left|E[y \,|\, x_i]\right| \rho_{\Gamma_{x_i}}(x_i)\, dx_i = E\left[\left|\mathrm{E}[y \,|\, x_i]\right|\right] & if \quad y_0 = 0 \end{cases} \tag{5.1}$$

y_0 being the unconditional expected value of y and the symbol $| \, x_i$ indicates conditioning the process y on knowledge of x_i . Extension of (5.1) to consider the joint effect of $x_{i_1}, x_{i_2}, ..., x_{i_s}$ is straightforward, leading to the following index

$$AMAE_{x_{i_1},x_{i_2},\dots,x_{i_s}} = \begin{cases} \dfrac{1}{|y_0|} \displaystyle\int_{\Gamma_{x_{i_1},x_{i_2},\dots,x_{i_s}}} \left| y_0 - E[y \mid x_{i_1}, x_{i_2}, \dots, x_{i_s}] \right| \rho_{\Gamma_{x_{i_1},x_{i_2},\dots,x_{i_s}}}(\boldsymbol{x}) dx_{i_1} \dots dx_{i_s} \\ \qquad = \dfrac{1}{|y_0|} E\left[\left| y_0 - E[y \mid x_{i_1}, x_{i_2}, \dots, x_{i_s}] \right| \right] \quad if \quad y_0 \neq 0 \\ \displaystyle\int_{\Gamma_{x_{i_1},x_{i_2},\dots,x_{i_s}}} \left| E[y \mid x_{i_1}, x_{i_2}, \dots, x_{i_s}] \right| \rho_{\Gamma_{x_{i_1},x_{i_2},\dots,x_{i_s}}}(\boldsymbol{x}) dx_{i_1} \dots dx_{i_s} \\ \qquad = E\left[\left| E[y \mid x_{i_1}, x_{i_2}, \dots, x_{i_s}] \right| \right] \quad if \quad y_0 = 0 \end{cases} \tag{5.2}$$

Note that index $AMAE_{x_i}$ quantifies the expected relative variation of the mean of *y* due to variations of only x_i, while $AMAE_{x_{i_1},x_{i_2},\dots,x_{i_s}}$ also includes all interactions amongst parameters $x_{i_1}, x_{i_2}, \dots, x_{i_s}$.

Along the same lines, we introduce the following index

$$AMAV_{x_i} = \frac{1}{V[y]} \int_{\Gamma_{x_i}} \left| V[y] - V[y \mid x_i] \right| \rho_{\Gamma_{x_i}}(x_i) dx_i = \frac{E\left[\left| V[y] - V[y \mid x_i] \right| \right]}{V[y]} \tag{5.3}$$

quantifying the relative expected discrepancy between unconditional, $V[y]$, and conditional (on x_i) process variance. Note that (5.3) does not generally coincide with the principal Sobol' index $S_{x_i} = E\left[V[y] - V[y \mid x_i]\right] / V[y]$ that quantifies the expected relative reduction of the variance due to knowledge of x_i alone, without interaction with other parameters (or, in other words, the relative contribution to the variance arising from uncertainty in x_i). Index $AMAV_{x_i}$ reduces to S_{x_i} only if the conditional variance, $V[y \mid x_i]$, is always (i.e., for each value of x_i) smaller than (or equal to) its unconditional counterpart $V[y]$. The difference between $AMAV_{x_i}$ and S_{x_i}, as well as advantages of using $AMAV_{x_i}$, will be elucidated through the numerical examples illustrated in Section 5.3. Note that equivalent writings for the principal Sobol' index are $S_{x_i} = V\left[E[y \mid x_i]\right] / V[y] = E\left[\left| y_0 - E[y \mid x_i] \right|^2 \right] / V[y]$ (see Borgonovo 2007), which highlight a relevant similarity with $AMAE_{x_i}$. This observation suggest that the resulting parameters ranking (i.e. parameters relevancy is assigned according to the values of the sensitivity index) based on (5.1) or (5.3) will be the same, but the reader should bear in mind that they are convening different information. Extension of (5.3) to consider the joint effect of $x_{i_1}, x_{i_2}, \dots, x_{i_s}$ reads

$$\begin{aligned} AMAV_{x_{i_1},x_{i_2},\dots,x_{i_s}} &= \frac{1}{V[y]} \int_{\Gamma_{x_{i_1},x_{i_2},\dots,x_{i_s}}} \left| V[y] - V[y \mid x_{i_1}, x_{i_2}, \dots, x_{i_s}] \right| \rho_{\Gamma_{x_{i_1},x_{i_2},\dots,x_{i_s}}}(\boldsymbol{x}) dx_{i_1} \dots dx_{i_s} \\ &= \frac{1}{V[y]} E\left[\left| V[y] - V\left[y \mid x_{i_1}, x_{i_2}, \dots, x_{i_s} \right] \right| \right] \end{aligned} \tag{5.4}$$

Index $AMAV_{x_{i_1},x_{i_2},\dots,x_{i_s}}$ quantifies the expected relative discrepancy between $V[y]$ and the variance of the process conditional to joint knowledge of $x_{i_1}, x_{i_2}, \dots, x_{i_s}$.

We then quantify the relative expected discrepancy between unconditional ($\gamma[y]$) and conditional ($\gamma[y \mid x_i]$) skewness through the index

$$
AMA\gamma_{x_i} = \begin{cases} \dfrac{1}{\gamma[y]} \displaystyle\int_{\Gamma_{x_i}} \left|\gamma[y]-\gamma[y \mid x_i]\right| \rho_{\Gamma_{x_i}}(x_i)dx_i = \dfrac{1}{|\gamma[y]|} E\left[\left|\gamma_y - \gamma[y \mid x_i]\right|\right] & if \ \gamma_y \neq 0 \\ \displaystyle\int_{\Gamma_{x_i}} \left|\gamma[y \mid x_i]\right| \rho_{\Gamma_{x_i}}(x_i)dx_i = E\left[\left|\gamma[y \mid x_i]\right|\right] & if \ \gamma_y = 0 \end{cases} \tag{5.5}
$$

Extension of (5.5) to consider the joint effect of $x_{i_1}, x_{i_2}, \ldots, x_{i_s}$ gives

$$
AMA\gamma_{x_{i_1}, x_{i_2}, \ldots, x_{i_s}} = \begin{cases} \dfrac{1}{|\gamma[y]|} \displaystyle\int_{\Gamma_{x_{i_1}, x_{i_2}, \ldots, x_{i_s}}} \left|\gamma[y]-\gamma[y \mid x_{i_1}, x_{i_2}, \ldots, x_{i_s}]\right| \rho_{\Gamma_{ix_{i_1}, x_{i_2}, \ldots, x_{i_s}}}(\boldsymbol{x})dx_{i_1} \ldots dx_{i_s} & \\ \quad = \dfrac{1}{|\gamma[y]|} E\left[\left|\gamma[y]-\gamma\left[y \mid x_{i_1}, x_{i_2}, \ldots, x_{i_s}\right]\right|\right] & if \ \gamma[y] \neq 0 \\ \displaystyle\int_{\Gamma_{x_{i_1}, x_{i_2}, \ldots, x_{i_s}}} \left|\gamma[y \mid x_{i_1}, x_{i_2}, \ldots, x_{i_s}]\right| \rho_{\Gamma_{x_{i_1}, x_{i_2}, \ldots, x_{i_s}}}(\boldsymbol{x})dx_{i_1} \ldots dx_{i_s} & \\ \quad = E\left[\left|E[y \mid x_{i_1}, x_{i_2}, \ldots, x_{i_s}]\right|\right] & if \ \gamma[y] = 0 \end{cases} \tag{5.6}
$$

The relative variation of the kurtosis ($k[y]$) of $y(\boldsymbol{x})$ due to variations of a parameter x_i or of the set $x_{i_1}, x_{i_2}, \ldots, x_{i_s}$ can be respectively quantified through

$$
AMAk_{x_i} = \frac{1}{k[y]} \int_{\Gamma_{x_i}} \left|k[y]-k[y \mid x_i]\right| \rho_{\Gamma_{x_i}}(x_i)dx_i = \frac{1}{k[y]} E\left[\left|k[y]-k[y \mid x_i]\right|\right] \tag{5.7}
$$

$$
\begin{aligned} AMAk_{x_{i_1}, x_{i_2}, \ldots, x_{i_s}} &= \frac{1}{k[y]} \int_{\Gamma_{x_{i_1}, x_{i_2}, \ldots, x_{i_s}}} \left|k[y]-k[y \mid x_{i_1}, x_{i_2}, \ldots, x_{i_s}]\right| \rho_{\Gamma_{x_{i_1}, x_{i_2}, \ldots, x_{i_s}}}(\boldsymbol{x})dx_{i_1} \ldots dx_{i_s} \\ &= \frac{1}{k[y]} E\left[\left|k[y]-k\left[y \mid x_{i_1}, x_{i_2}, \ldots, x_{i_s}\right]\right|\right] \end{aligned} \tag{5.8}
$$

Relying jointly on (5.1)-(5.8) enables one to perform a comprehensive GSA of the target process $y(\boldsymbol{x})$ quantifying the impact of $\boldsymbol{x}$ on the first four (statistical) moments of the *pdf* of $y(\boldsymbol{x})$. This strategy yields information about the way important elements of the distribution of $y(\boldsymbol{x})$, such as mean, spread around the mean, symmetry, and tailedness, are affected by model uncertain parameters collected in $\boldsymbol{x}$. This analysis is not feasible through a classical variance- based GSA.

Calculation of the indices we propose entails evaluation of conditional moments of $y(\boldsymbol{x})$. This step can be computationally very demanding. Along the lines of our discussion about Sobol' indices in Section 4.3, the new metrics (5.1)-(5.8) can be evaluated via a surrogate model, as we illustrate in Section 5.3.

5.3 Illustrative Examples

The theoretical framework introduced in Section 5.2 is here applied to three diverse testbeds: (*a*) the Ishigami function, which constitutes an analytical benchmark typically employed in GSA studies; (*b*) a pumping scenario in a coastal aquifer, where the state variable of interest is the critical pumping rate, i.e. the largest admissible pumping rate to ensure that the well is still not contaminated by seawater; and (*c*) a laboratory-scale setting associated with non-reactive transport in porous media. In the first two examples the computational costs associated with the complete mathematical description of the targeted outputs are low. This enables us to assess the error associated with the evaluation of the sensitivity indices (5.1), (5.3), (5.5) and (5.7) through a gPCE representation of the output. In the third case, due to the complexity of the problem and the associated computational costs, we solely relay on the gPCE representation for the target quantity of interest. We emphasize that the use of a gPCE as a surrogate model is here considered only as an example, our GSA approach being fully compatible with a model order reduction technique of choice.

In all of the above scenarios, uncertain parameters x_i collected in $\boldsymbol{x}$ are considered as independent and identically distributed (*i.i.d.*) random variables, each characterized by a uniform distribution within the interval $\Gamma_{x_i} = \left[x_{i,\min}, x_{i,\max}\right]$. All results are grounded on 5×10^5 Monte Carlo realizations, enabling convergence of all statistical moments analysed. Series appearing in the gPCE (4.15) are evaluated up to a given order of truncation in all three examples. Here, we apply the total-degree rule and construct a polynomial of order *w* through a sparse grid technique (see, e.g., Formaggia et al., 2013 and references therein). We then analyze the way the selected order *w* influences the results. Note that the optimal choice of the polynomial $\psi_{\boldsymbol{p}}(\boldsymbol{x})$ in (4.15) depends on the *pdf* of the random variables collected in $\boldsymbol{x}$ (Xiu and Karniadakis, 2002;). In our exemplary settings we use the multidimensional Legendre polynomials which are orthonormal with respect to the uniform *pdf*.

5.3.1 Ishigami function

The non-linear and non-monotonic Ishigami function

$$y(\boldsymbol{x}) = ISH = \sin(2\pi x_1 - \pi) + a\sin^2(2\pi x_2 - \pi) + b\left(2\pi x_3 - \pi\right)^4 \sin(2\pi x_1 - \pi) \tag{5.9}$$

is widely used in the literature (e.g., Homma and Saltelli, 1996; Chun et al., 2000; Borgonovo, 2007, 2011; Sudret, 2008; Crestaux et al., 2009) to benchmark GSA methods. Here, x_i (i = 1, 2, 3) are *i.i.d.* random variables uniformly distributed within the interval [0, 1]. Unconditional mean $E\left[ISH\right]$, variance, $V\left[ISH\right]$, skewness, $\gamma\left[ISH\right]$, and kurtosis, $k\left[ISH\right]$, of (5.9) can be evaluated analytically as

$$E\left[ISH\right] = \frac{a}{2};\;\; V\left[ISH\right] = \frac{1}{2} + \frac{a^2}{8} + b\pi^4\left(\frac{1}{5} + \frac{b\pi^4}{18}\right);\;\; \gamma\left[ISH\right] = 0 \tag{5.10a}$$

$$k\left[ISH\right] = \frac{1}{2V^2\left[ISH\right]} \left\{\frac{3}{4} + b\pi^4\left(\frac{3}{5} + b\pi^4\left(\frac{1}{2} + 3b\pi^4\left(\frac{1}{13} + \frac{\pi^4}{68}b\right)\right)\right) + \frac{3}{2}a^2\left(\frac{1}{2} + \frac{a^2}{32} + \pi^4 b\left(\frac{1}{5} + \frac{\pi^4}{18}b\right)\right)\right\} \tag{5.10b}$$

Equation (5.10) reveals that the unconditional *pdf* of *ISH* is symmetric with tails that increase with |*b*| and decrease with |*a*|, as quantified by $k\left[ISH\right]$ (5.10b). The conditional mean $E\left[ISH \mid x_i\right]$, variance $V\left[ISH \mid x_i\right]$, skewness $\gamma\left[ISH \mid x_i\right]$ and kurtosis $k\left[ISH \mid x_i\right]$ can be evaluated analytically as

$$E\left[ISH \mid x_1\right] = \frac{a}{2} + \frac{1}{5}\left(5 + b\pi^4\right)\sin\left(2\pi x_1 - \pi\right);\;\; E\left[ISH \mid x_2\right] = a\sin^2\left(2\pi x_2\right);\;\; E\left[ISH \mid x_3\right] = \frac{a}{2} \tag{5.11}$$

$$\begin{gathered} V\left[ISH \mid x_1\right] = \frac{a^2}{8} + \frac{8b^2\pi^8}{225}\left(1 - \cos\left(4\pi x_1\right)\right);\qquad V\left[ISH \mid x_2\right] = \frac{1}{2} + b\pi^4\left(\frac{1}{5} + \frac{b}{18}\pi^4\right); \\ V\left[ISH \mid x_3\right] = \frac{a^2}{8} + \frac{1}{2}\left(1 + b\pi^4\left(1 - 2x_3\right)^4\right)^2 \end{gathered} \tag{5.12}$$

$$\gamma\left[ISH\mid x_1\right]=\frac{128b^3\pi^{12}\sin^3\left(2\pi x_1-\pi\right)}{4875\left(V\left[ISH\mid x_1\right]\right)^{3/2}};\qquad \gamma\left[ISH\mid x_2\right]=0;\qquad ISH\left[y\mid x_3\right]=0 \tag{5.13}$$

$$\begin{aligned}
k\left[ISH\mid x_1\right]&=\frac{1}{V^2\left[ISH\mid x_1\right]}\left\{\frac{3}{128}a^4+\frac{4}{75}b^2\pi^8\sin^2\left(2\pi x_1\right)\left[a^2+\frac{1849}{5525}b^2\pi^8\sin^2\left(2\pi x_1\right)\right]\right\}\\
k\left[ISH\mid x_2\right]&=\frac{1}{2V^2\left[ISH\mid x_2\right]}\left\{\frac{3}{4}+b\pi^4\left(\frac{3}{5}+b\pi^4\left(\frac{1}{2}+3b\pi^4\left(\frac{1}{13}+\frac{1}{68}b\pi^4\right)\right)\right)\right\}\\
k\left[ISH\mid x_3\right]&=\frac{3}{128V^2\left[ISH\mid x_3\right]}\left\{a^4+16\left(1+b\pi^4\left(1-2x_3\right)^4\right)^2\left[a^2+\left(1+b\pi^4\left(1-2x_3\right)^4\right)^2\right]\right\}
\end{aligned} \tag{5.14}$$

For the sole purpose of illustrating our approach, here and in the following we set a = 5 and b = 0.1, which corresponds to $E\left[ISH\right]=2.50$, $V\left[ISH\right]=10.84$ and $k\left[ISH\right]=4.18$. Figure 5.1 depicts the first four moments of *ISH* conditional to values of x_1 (blue curves), x_2 (red curves) and x_3 (green curves) within the parameter space. The corresponding unconditional moments (black curves) are also depicted for completeness.

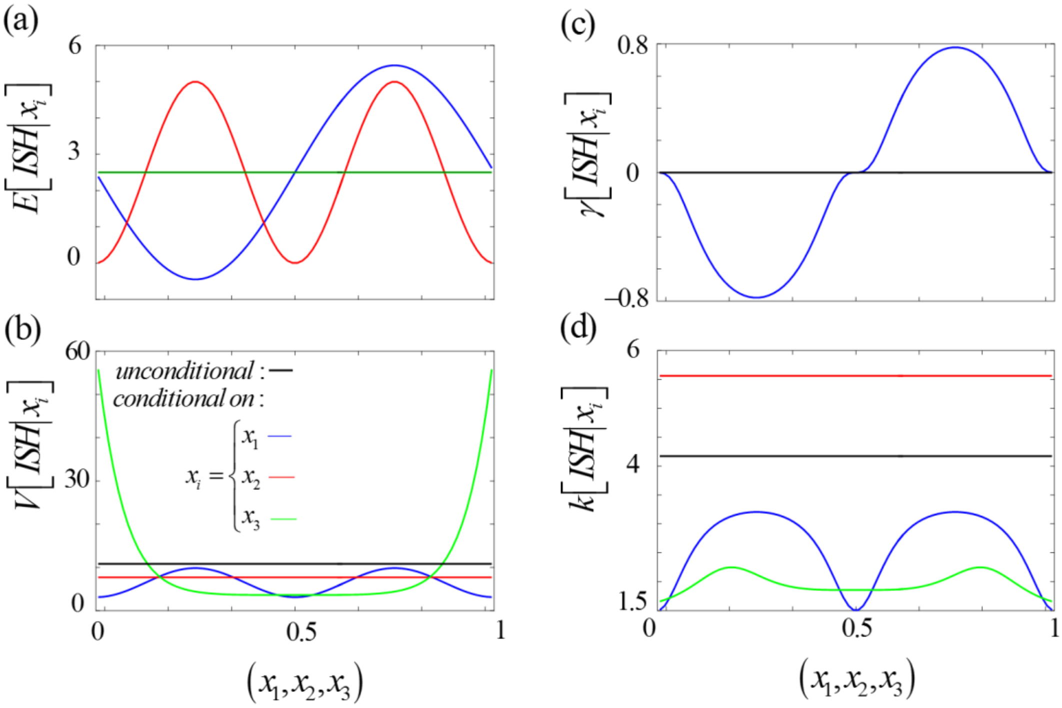

Figure 5.1. Variation of the first four moments of *ISH* (5.9) conditional to values of x_1 (blue curves), x_2 (red curves) and x_3 (green curves) within the parameter space: (a) expected value, $E\left[ISH\mid x_i\right]$, (b) variance, $V\left[ISH\mid x_i\right]$, (c) skewness, $\gamma\left[ISH\mid x_i\right]$, and (d) kurtosis, $k\left[ISH\mid x_i\right]$, ($i$ = 1, 2, 3). The corresponding unconditional moments (black curves) are also depicted.

Comparing (5.10a) and (5.11), it is seen that $E\left[ISH\mid x_3\right]$ coincides with its unconditional counterpart $E\left[ISH\right]$, indicating that conditioning on any value of x_3 does not impact the mean of *ISH*. Otherwise, setting x_1 or x_2 to a given value clearly affects the mean of *ISH* in a way which is governed by (5.11) and shown in Fig. 5.1a. It is clear from (5.11) that $E[ISH \mid x_2]$ has a higher frequency of oscillation within Γ_{x_2} than has $E[ISH \mid x_2]$ within Γ_{x_1}. The new global index (5.1) can be evaluated analytically as

$$AMAE_{x_1} = \frac{4}{a\pi}\left|1 + \frac{b}{5}\pi^4\right|; \qquad AMAE_{x_2} = \frac{2}{\pi}; \qquad AMAE_{x_3} = 0 \tag{5.15}$$

Note that $AMAE_{x_2}$ does not depend on specific values of *a* and *b*. Table 5.1 lists the values of $AMAE_{x_i}$ ($x_i = x_1, x_2, x_3$) corresponding to the *a* and *b* values selected for our demonstration.

Equation (5.12) shows that all random model parameters influence the variance of *ISH*, albeit to different extents, as also illustrated in Fig. 1b. Note that $V[ISH \mid x_2]$ is always smaller than $V[ISH]$ (compare (5.10a) and (5.12)) and does not depend on x_2, i.e., conditioning ISH on x_2 reduces the process variance regardless the conditioning value. Otherwise, $V[ISH \mid x_3]$ can be significantly larger or smaller than its unconditional counterpart. Tab. 1 lists values of $AMAV_{x_i}$ ($x_i = x_1, x_2, x_3$) computed via (5.3) with the *a* and *b* values selected for our demonstration. The principal Sobol' indices (Sudret, 2008)

$$S_{x_1} = \frac{\left(5 + b\pi^4\right)^2}{50\,V[ISH]}; \qquad S_{x_2} = \frac{a^2}{8\,V[ISH]}; \qquad S_{x_3} = 0 \tag{5.16}$$

are also listed for completeness. As expected, values of $AMAV_{x_i}$ listed in Tab. 5.1 suggest that conditioning on x_3 has the strongest impact on the variance of *ISH*, followed by x_2 and x_1. Note that S_{x_3} = 0, a result which might be interpreted as a symptom that *ISH* is insensitive to x_3. The apparent inconsistency between the conclusions which could be drawn by analyzing $AMAV_{x_3}$ and S_{x_3} is reconciled by the observation that the function $V[ISH] - V[ISH \mid x_3]$ can be positive and negative in a way that its integration over Γ_{x_3} vanishes (see also Fig. 5.1b). As a consequence, the mean reduction of the variance of *ISH* due to knowledge of (or conditioning on) x_3 is zero. It is remarked that this observation does not imply that that the variance of *ISH* does not vary with x_3, as clearly highlighted by Fig. 5.1b and quantified by $AMAV_{x_3}$.

The symmetry of the *pdf* of *ISH* is not affected by conditioning on x_2 or x_3, as demonstrated by (5.13). Otherwise, $\gamma[ISH \mid x_1]$ is left (or right) skewed when x_1 is smaller (or larger) than 0.5, as dictated by (5.13) and shown in Fig. 5.1c for our test showcase. Tab. 5.1 lists the resulting $AMA\gamma_{x_i}$ ($x_i = x_1, x_2, x_3$) for the selected *a* and *b* values.

The conditional kurtosis $k[ISH \mid x_2]$ does not depend on the conditioning value x_2 and on the value of *a* (see (5.14)). We then note that it is always larger than (or equal to) its unconditional counterpart $k[ISH]$, regardless the particular values assigned to *b*, as we verified through extensive numerical tests. This result implies that the *pdf* of *ISH* conditional on x_2 is characterized by tails which are heavier than those of its unconditional counterpart. Fig. 1d reveals that $k[ISH \mid x_1]$ and $k[ISH \mid x_3]$ are smaller than $k[ISH]$ for the values of *a* and *b* implemented in this example. Tab. 5.1 lists the resulting $AMAk_{x_i}$ ($x_i = x_1, x_2, x_3$) for the selected *a* and *b* values.

Table 5.1. Global sensitivity index $AMAE_{x_i}$ (5.1), $AMAV_{x_i}$ (5.3), $AMA\gamma_{x_i}$ (5.5), and $AMAk_{x_i}$ (5.7) associated with the Ishigami function (5.9). Principal Sobol' indices, S_{x_i} , are also listed; $x_i = x_1, x_2$, x_3.

	$AMAE_{x_i}$	$AMAV_{x_i}$	S_{x_i}	$AMA\gamma_{x_i}$	$AMAk_{x_i}$
x_1	0.75	0.40	0.40	0.45	0.37
x_2	0.64	0.29	0.29	0.00	0.33
x_3	0.00	0.84	0.00	0.00	0.53

We close this part of the study by investigating the error which would arise when one evaluates our GSA indices by replacing *ISH* through a gPCE surrogate model. We do so on the basis of the absolute relative error

$$e_j = \begin{cases} \left| \dfrac{j_{gPCE} - j_{full\,model}}{j_{full\,model}} \right| & if \quad j_{full\,model} \neq 0 \\ \left| j_{gPCE} - j_{full\,model} \right| & if \quad j_{full\,model} = 0 \end{cases} \tag{5.17}$$

where j = $AMAE_{x_i}$, $AMAV_{x_i}$, $AMA\gamma_{x_i}$ or $AMAk_{x_i}$ ($x_i = x_1, x_2, x_3$); the subscripts *full model* and gPCE respectively indicate that quantity j is evaluated via (5.9) or through a gPCE surrogate model, constructed as outlined in Section 4.3.1. Figure 5.2 depicts (5.17) versus the total degree *w* of the gPCE. Note that the lower limit of the vertical axis of Fig. 5.2 is set to 0.001% for convenience of graphical representation. Approximation errors associated with GSA indices related to the mean, $AMAE_{x_i}$, rapidly approach zero as *w* increases. Note that $e_{AMAE_{x_3}}$ is smaller than 0.001% for all tested values of *w*. Values of e_j linked to $AMAV_{x_i}$, $AMA\gamma_{x_i}$ and $AMAk_{x_i}$ do not show a consistently decreasing trend until $w \geq 5$, which is consistent with the presence of a fourth power exponent in (5.9). Values of e_j associated with the variance, skewness and kurtosis decrease with approximately the same average linear rate (in log-log scale) for the largest *w* considered (Fig. 5.2b, c, d). This example reinforces the need to reliably test the accuracy of a gPCE-based model approximation as a function of the total degree desired, depending on the statistical moment of interest.

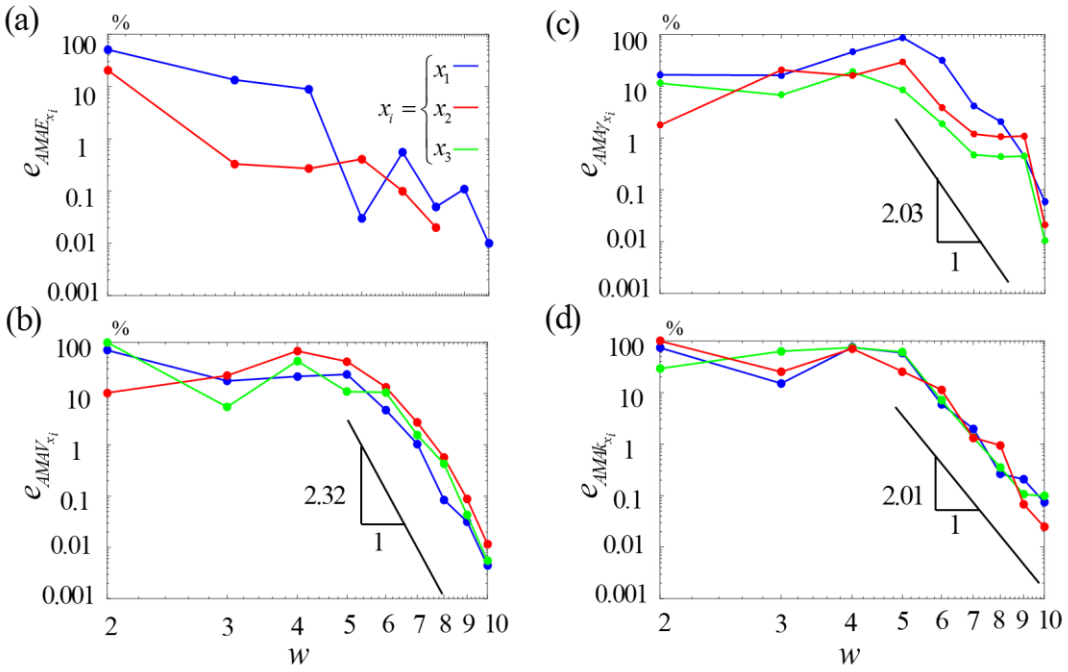

Figure 5.2. Error e_j (5.17) versus the total degree w of the gPCE; j = (a) $AMAE_{x_i}$, (b) $AMAV_{x_i}$, (c) $AMA\gamma_{x_i}$ and (d) $AMAk_{x_i}$, with $x_i = x_1$ (blue curves), x_2 (red curves), x_3 (green curves). Note that $AMAE_{x_3}$ is always smaller than 0.01%. Average slope of the rate of decrease of e_j associated with the variance, skewness and kurtosis are indicated as a reference.

5.3.2 Critical Pumping Rate in Coastal Aquifers

The example we consider here is taken from the study of Pool and Carrera (2011) related to the analysis of salt water contamination of a pumping well operating in a homogenous confined coastal aquifer of uniform thickness $b^{'}$. The setting is sketched in Figure 3 and is that of an imposed constant freshwater flux ($q_f^{'}$ [L T^{-1}]) flowing from the inland to the coastline and pushing against invading saltwater advancing from the seaside boundary. A constant discharge, $Q_w^{'}$ [L^3 T^{-1}], is pumped from a fully penetrating well located at a distance $x_w^{'}$ [L] from the coastline. Pool and Carrera (2011) introduced a dimensionless well discharge $Q_w = Q_w^{'} / (b^{'} x_w^{'} q_f^{'})$ and defined the critical pumping rate Q_c as the value of Q_w at which a normalized solute concentration monitored at the well exceeds 0.1%. A key result of the study of Pool and Carrera (2011) is that Q_c can be approximated through the following implicit equation

$$\lambda_D = 2\left[1-\frac{Q_c}{\pi}\right]^{1/2} + \frac{Q_c}{\pi}\ln\frac{\left[1-\left(1-Q_c/\pi\right)^{1/2}\right]}{\left[1+\left(1-Q_c/\pi\right)^{1/2}\right]} \tag{5.18}$$

where

$$\lambda_D = \varepsilon^{*}\frac{1}{x_w}\frac{1}{J}\,;\ \varepsilon^{*} = \varepsilon\left[1-\left(Pe_T\right)^{-1/6}\right];\ \varepsilon = \Delta\rho^{'} / \rho_f^{'} \tag{5.19}$$

Here, $x_w = x_w^{'} / b^{'}$; $J = q_f^{'} / K$; $Pe_T = b^{'} / \alpha_T^{'}$; K [L T^{-1}] is the uniform hydraulic conductivity; $\alpha_T^{'}$ [L] is transverse dispersivity; $\Delta\rho^{'}$ is the density difference between fresh and saltwater; and $\rho_f^{'}$ is freshwater density. Here, Pe_T is a measure of the intensity of dispersive effects, *J* is the natural head gradient of the incoming freshwater, and x_w is the dimensionless distance of the well from the coastline. Pool and Carrera (2011) suggest that (25) holds for $\lambda_D \in (0-10]$. Additional details about the problem setting, boundary and initial conditions, as well as geometrical configuration of the system can be found in Pool and Carrera (2011). Here, we focus on the main results (5.18)-(5.19) which represent the complete mathematical description of the problem we analyze. We perform a sensitivity analysis of Q_c with respect to Pe_T, *J*, and x_w. While the first two quantities are difficult to characterize experimentally in practical applications, the well location can be considered as an operational/design variable. Table 2 lists the intervals of variation we consider for Pe_T, *J* and x_w. These are designed to (*a*) resemble realistic field values and (*b*) obey the constraint about λ_D.

Table 5.2. Intervals of variations of Pe_T, *J*, x_w.

	$\Gamma_n = [x_{n,\min} - x_{n,\max}]$
Γ_{Pe_T}	$[0.01 - 0.1]$
Γ_J	$[8e^{-4} - 2.5e^{-3}]$
Γ_{x_w}	$[10 - 33]$

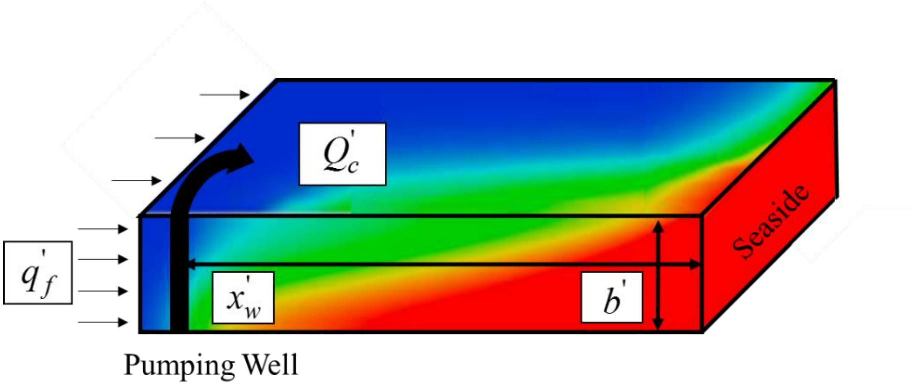

Figure 5.3. Sketch of the critical pumping scenario taking place within a coastal aquifer of thickness $b^{'}$. A constant freshwater (in blue) flux ($q_f^{'}$) flows from the inland to the coastline; invading saltwater (in red) comes from the seaside boundary. A constant discharge, $Q_w^{'}$, is pumped from a fully penetrating well located at a distance $x_w^{'}$ from the coastline. Color scale indicating variable concentration of saltwater is only qualitative and for illustration purposes.

Numerical evaluation of the first four unconditional statistical moment of Q_c yields a mean value $E[Q_c]=1.65$, variance $V[Q_c]=0.17$, skewness $\gamma[Q_c]=-0.30$ (which indicates a light asymmetry in the pdf), and kurtosis $k[Q_c]=2.51$ (i.e., pdf tails decrease faster than for Gaussian distributions). Figure 5.4 depicts the first four moments of Q_c conditional to values of Pe_T (blue curves), J (green curves), and x_w (red curves) within the parameter space. The corresponding unconditional moments (black curves) are also depicted for completeness. Note that each parameter interval of variation has been normalized to span the range [0, 1] for ease of graphical comparison. Table 5.3 lists the values of $AMAE_{x_i}$, $AMAV_{x_i}$, S_{x_i}, $AMA\gamma_{x_i}$ and $AMAk_{x_i}$ (x_i = Pe_T, J, x_w) associated with Q_c. As in our first example, it is clear that sensitivity of Q_c with respect to Pe_T, J, x_w depends on the statistical moment of interest.

Table 5.3. Global sensitivity index $AMAE_{x_i}$ (5.1), $AMAV_{x_i}$ (5.3), $AMA\gamma_{x_i}$ (5.5), and $AMAk_{x_i}$ (5.7) associated with the critical pumping rate Q_c (5.18). Principal Sobol' indices, S_{x_i}, are also listed; x_i = Pe_T, J, x_w.

	$AMAE_{x_i}$	$AMAV_{x_i}$	S_{x_i}	$AMA\gamma_{x_i}$	$AMAk_{x_i}$
Pe_T	0.07	0.14	0.09	0.35	0.09
J	0.14	0.41	0.41	0.88	0.12
x_w	0.15	0.48	0.48	0.78	0.11

Inspection of Fig. 5.4a reveals that the mean of Q_c is more sensitive to conditioning on J or x_w than to conditioning on Pe_T. Note that increasing Pe_T, i.e., considering advection-dominated scenarios, leads to an increase of the mean value of Q_c. This is so because the dispersion of the intruding saltwater wedge is diminished and the travel time of solutes to the well tends to increase. High values of the natural head gradient of the incoming freshwater, J, are associated with high mean values of Q_c. This is consistent with the observation that the inland penetration of the wedge is contrasted by the effect of freshwater which flows in the opposite direction. As expected, increasing x_w (moving the pumping well towards the coast) leads to a reduction of the mean value of Q_c. Figure 5.4a shows that mean Q_c varies with x_w and J in a similar way. This outcome is consistent with (5.19) where Q_c depends on the product $x_w J$, i.e. increasing x_w or J has the same effect on Q_c. It can be noted (see Table 5.3) that $AMAE_{Pe_T}$ is smaller than $AMAE_J$ and $AMAE_{x_w}$, consistent with the results of Fig. 5.4a. Fig. 5.4b shows that the variance of Q_c decrease as Pe_T, J, or x_w increase. This trend suggests that the uncertainty on Q_c, as quantified by the variance, decreases as (*i*) the intruding wedge sharpens or is pushed toward the seaside boundary by the incoming freshwater or (*ii*) the well is placed at increasing distance from the coastline. Inspection of Fig. 4c, d shows that conditioning on Pe_T, J, or x_w causes the *pdf* of Q_c to become less asymmetric and less heavy tailed than its unconditional counterpart. This behavior suggests that the relative frequency of occurrence of (high or low) extreme values of Q_c tends to decrease as additional information about the model parameters become available.

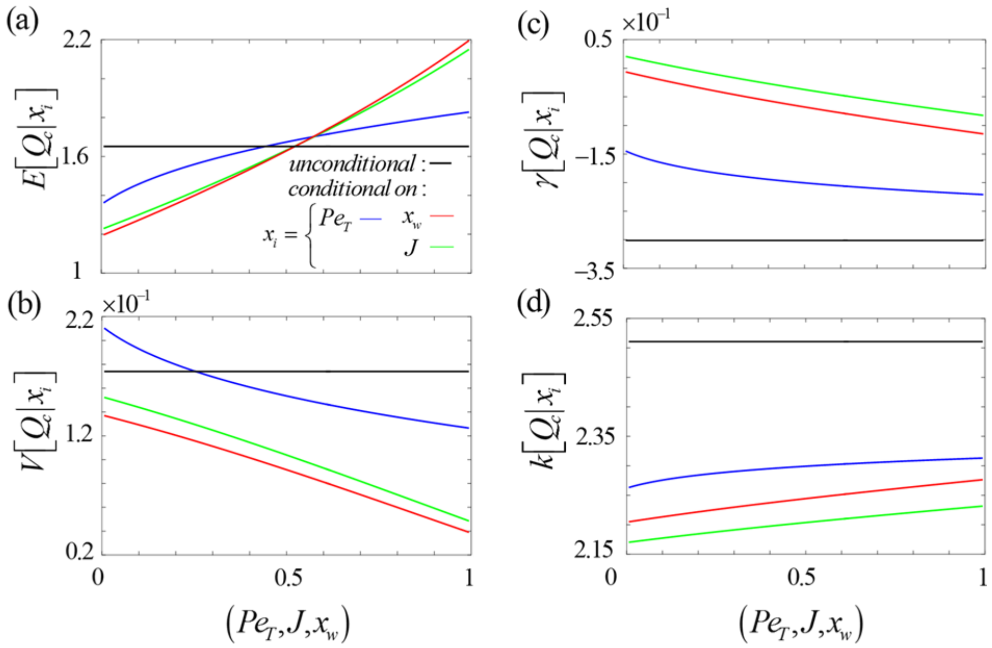

Figure 5.4. First four moments of Q_c conditional to values of Pe_T (blue curves), J (green curves), and x_w (red curves) within the parameter space: (a) expected value, $E[Q_c \mid x_i]$, (b) variance, $V[Q_c \mid x_i]$, (c) skewness, $\gamma[Q_c \mid x_i]$, and (d) kurtosis, $k[Q_c \mid x_i]$, ($x_i = Pe_T$, J, x_w). The corresponding unconditional moments (black curves) are also depicted. Intervals of variation of Pe_T, J and x_w has been rescaled between zero and one for ease of comparison (see Table 5.2).

Figure 5.5 depicts the dependence of the error e_j (5.17) on the total degree *w* of the gPCE representation of Q_c, for *j* = (*a*) $AMAE_{x_i}$, (*b*) $AMAV_{x_i}$, (*c*) $AMA\gamma_{x_i}$ and (*d*) $AMAk_{x_i}$ ($x_i = Pe_T$ (blue curves), J (red curves), x_w (green curves)). These results indicate that: (*i*) e_j associated with $AMAE_{x_i}$ is not significant even in the worst case considered, where it is about 1%; (*ii*) $e_{AMAV_{Pe_T}} \approx 10\%$ for *w* = 2 and rapidly decreases to values below 1% for increasing *w*; (*iii*) values of e_j for $AMAV_{x_i}$ (x_i = *J*, x_w) are always smaller than 1%; and (*iv*) the trend of $e_{AMA\gamma_{x_i}}$ is similar to that of $e_{AMAk_{x_i}}$ for all x_i, with values of the order of 10% or higher for *w* = 2 and displaying a slow decrease with increasing *w* to then stabilize around values smaller than 1% when *w* ≈ 4 or 5. It is then clear from Fig. 5 that attaining a given acceptable level of accuracy for the gPCE-based approximation of our moment-based GSA indices for Q_c requires increasing the total order *w* of the gPCE with the order of the statistical moment considered. As such, following the typical practice of assessing the reliability of a gPCE surrogate model solely on the basis of the variance or of a few random model realizations does not guarantee a satisfactory accuracy of the uncertainty analysis of a target model output which should consider higher-order statistical moments.

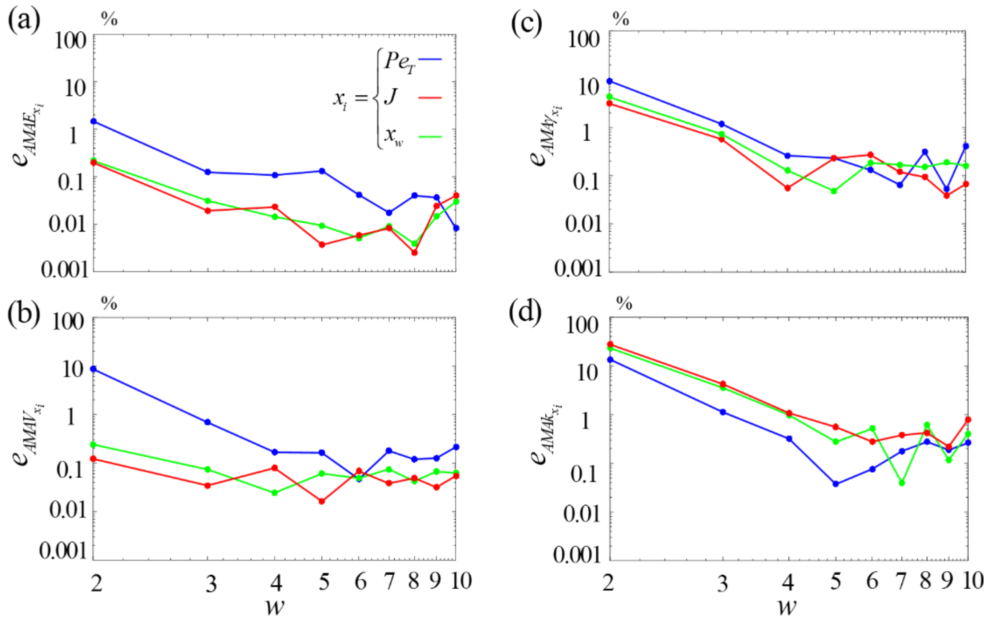

Figure 5.5. Dependence of the error e_j (5.17) on the total degree *w* of the gPCE representation of Q_c, for *j* = (a) $AMAE_{x_i}$, (b) $AMAV_{x_i}$, (c) $AMA\gamma_{x_i}$ and (d) $AMAk_{x_i}$ ($x_i = Pe_T$ (blue curves), J (red curves), x_w (green curves)).

5.3.3 Solute transport in a laboratory-scale porous medium with zoned heterogeneity

As a last exemplary showcase, we consider the laboratory-scale experimental analysis of nonreactive chemical transport illustrated by Esfandiar et al. (2015). These authors consider tracer transport within a rectangular flow cell filled with two types of uniform sands. These were characterized by diverse porosity and permeability values, which were measured through separate, standard laboratory tests. A sketch of the experimental set-up displaying the geometry of the two uniform zones respectively formed by coarse and fine sand is illustrated in Figure 5.6.

After establishing fully saturated steady-state flow, a pulse injection of a solution containing a constant tracer concentration takes place at the cell inlet. The tracer breakthrough curve is then measured at the outlet. Esfandiar et al. (2015) modeled the temporal evolution of normalized concentration at the outlet, $\overline{C}(t)$ (t denoting time), by numerically solving within the flow domain the classical Advection-Dispersion Equation (ADE) (e.g., Bear and Cheng, 2011) implementing an original and accurate space-time grid adaptation technique. Longitudinal dispersivities of the two sands ($a_{L,i}$, i = 1, 2 respectively denoting the coarse and fine sand) were considered as uncertain system parameters to be estimated against the available experimental solute breakthrough data. To minimize the computational costs in the model calibration process, Esfandiar et al. (2015) relied on a gPCE approximation of $\overline{C}(t)$. The authors constructed a gPCE of total degree $w = 3$ by considering $\log_{10}\left(a_{L,i}\right)$ (i = 1, 2) to be two *i.i.d.* random variables uniformly distributed within $\Gamma_{\log_{10}\left(a_{L,i}\right)}$ = [-6, -2] (i = 1, 2; $a_{L,i}$ being expressed in [m]). Further details about the problem set-up, numerical discretization and grid adaptation technique as well of the construction of the gPCE representation can be found in Esfandiar et al. (2015). Here, we ground the application of our new GSA metrics on the gPCE surrogate model already constructed by Esfandiar et al. (2015) to approximate $\overline{C}(t)$.

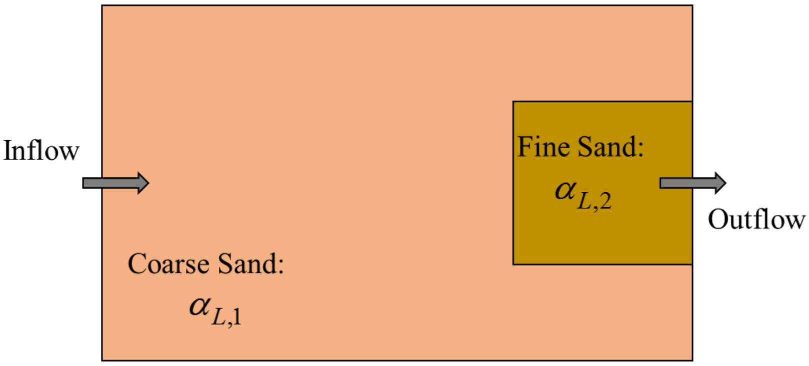

Figure 5.6. Sketch of the solute transport setting considered by Esfandiar et al. (2015). The laboratory-scale porous medium is formed by two zones filled with coarse or fine sand.

Figure 5.7 depicts the temporal evolution of the unconditional expected value, $E\left[\overline{C}(t)\right]$, variance, $V\left[\overline{C}(t)\right]$, skewness, $\gamma\left[\overline{C}(t)\right]$, and kurtosis, $k\left[\overline{C}(t)\right]$, of normalized $\overline{C}(t)$. Time steps $t_{0.4}$, $t_{0.02}$ and $t_{0.96}$, i.e., the times at which $E\left[\overline{C}(t)\right]$ = 0.02, 0.4, and 0.96, respectively, are highlighted in Fig. 5.7a, for the sake of the discussion presented in the following.

Fig. 5.7a reveals a pronounced tailing of $E\left[\overline{C}(t)\right]$ at late times, the short time mean breakthrough being associated with a rapid increase of $E\left[\overline{C}(t)\right]$. A local minimum at $t_{0.4}$ and two local peaks and are recognized in $V\left[\overline{C}(t)\right]$ (Fig. 5.7b). The variance peaks at times approximately corresponding to the largest values of the local concavity of $E\left[\overline{C}(t)\right]$, as expressed by $\partial^2 E\left[\overline{C}(t)\right]/\partial t^2$. This outcome is consistent with the results of numerical Monte Carlo (MC) simulations depicted in Figure 8 of Esfandiar et al. (2015) where the largest spread of the MC results is observed around these locations. The local minimum displayed by $V\left[\overline{C}(t)\right]$ suggests that $\overline{C}(t)$ at observation times close to $t_{0.4}$ is mainly driven by advection, consistent with the observation that advective transport components are the main driver of the displacement of the center of mass of a solute plume. The late time variance $V\left[\overline{C}(t)\right]$ tends to vanish because the normalized breakthrough curve is always very close to unity irrespective of the values of $a_{L,1}$ and $a_{L,2}$. Joint inspection of Fig.s 5.7c, d reveals that the *pdf* of $\overline{C}(t)$ tends to be symmetric around the mean (Fig. 5.7c) and characterized by light tails (Fig. 5.7d) at about $t_{0.4}$. Otherwise, the *pdf*s of $\overline{C}(t)$ tend to display heavy right or left tails, respectively for observation times shorter and longer than $t_{0.4}$. These observations suggest that the relative frequency of rare events (i.e., very low or high solute concentrations, which can be of some concern in the context of risk assessment) is lowest at intermediate observation times across the duration of the experiment.

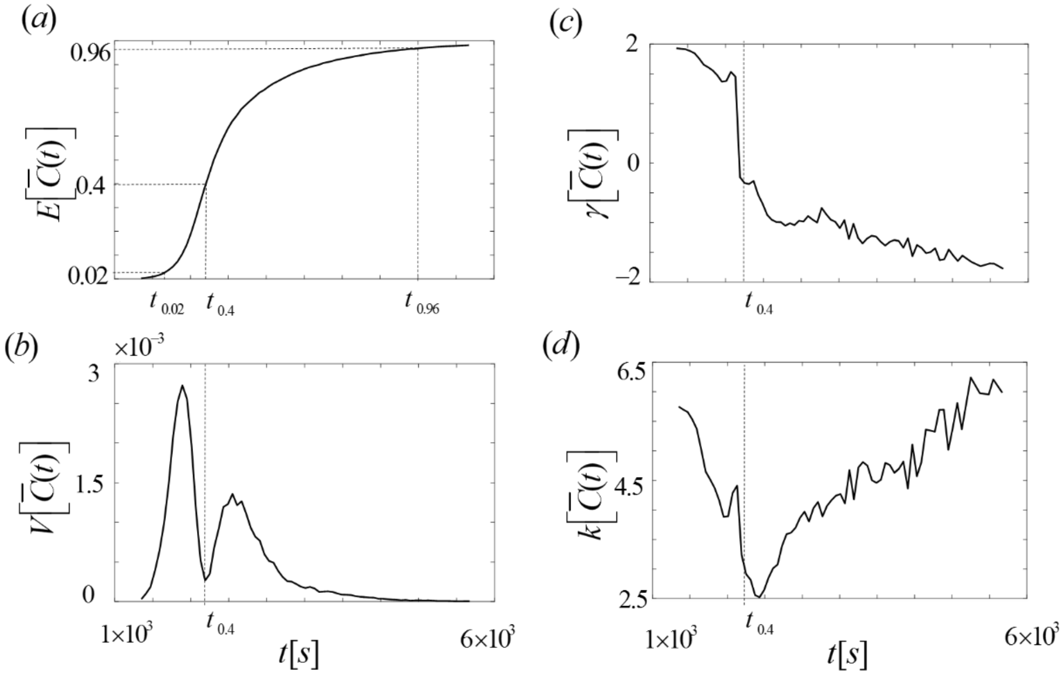

Figure 5.7. Temporal evolution of the unconditional (*a*) expected value, $E\left[\overline{C}(t)\right]$, (*b*) variance, $V\left[\overline{C}(t)\right]$, (*c*) skewness, $\gamma\left[\overline{C}(t)\right]$, and (*d*) kurtosis, $k\left[\overline{C}(t)\right]$, of normalized $\overline{C}(t)$. Vertical lines in (a) correspond to time steps $t_{0.4}$, $t_{0.02}$ and $t_{0.96}$, i.e., the times at which $E\left[\overline{C}(t)\right]$ = 0.02, 0.4, and 0.96, respectively.

Figure 5.8 depicts the temporal evolution of (*a*) $AMAE_{x_i}$, (*b*) $AMAV_{x_i}$, (*c*) $AMA\gamma_{x_i}$, and (*d*) $AMAk_{x_i}$ (x_i = $\log_{10}(a_{L,1})$, $\log_{10}(a_{L,2})$) of $\overline{C}(t)$. These results suggest that $\overline{C}(t)$ (*i*) is more sensitive to $\log_{10}(a_{L,1})$ than to $\log_{10}(a_{L,2})$ at early times, (*ii*) is almost equally sensitive to both dispersivities for $t \approx t_{0.4}$, and (*iii*) is more sensitive to the dispersivity of the fine sand (i.e., to $\log_{10}(a_{L,2})$) at late times. Our set of results suggests that the overall early time pattern of solute breakthrough is mainly dictated by the value of $a_{L,1}$, the late time behavior being chiefly influenced by $a_{L,2}$.

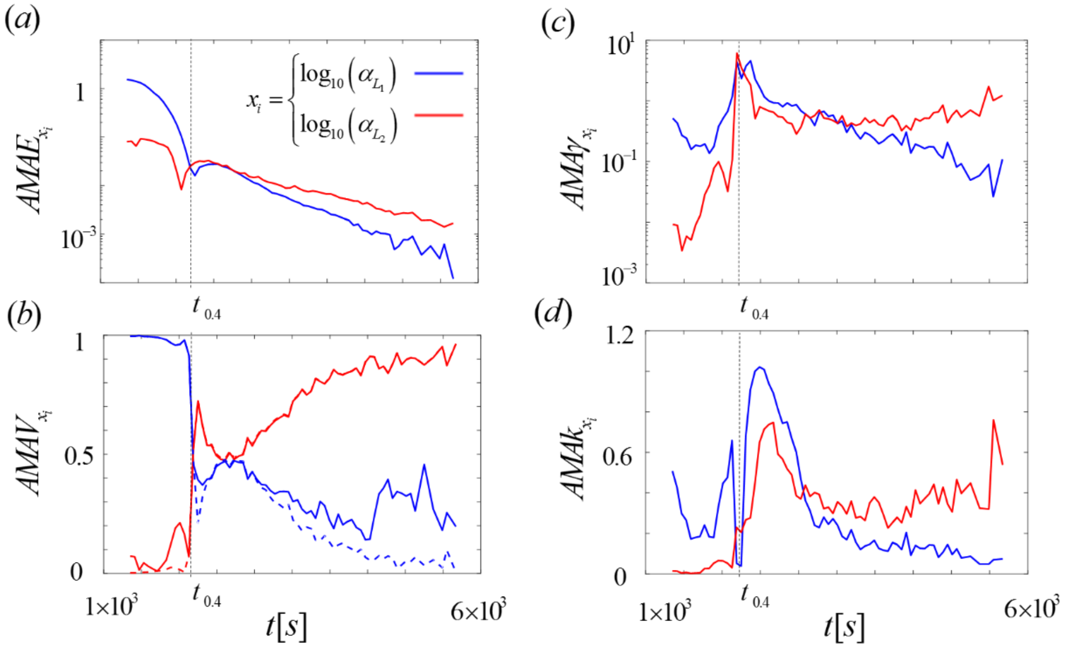

Figure 5.8. Time evolution of the global sensitivity index (a) $AMAE_{x_i}$, (b) $AMAV_{x_i}$ and S_{x_i} (dashed curves), (c) $AMA\gamma_{x_i}$, and (d) $AMAk_{x_i}$ of $\overline{C}(t)$ (x_i = $\log_{10}(a_{L,1})$ (blue), or $\log_{10}(a_{L,2})$ (red)).

These conclusions are supported by the results of Figures 5.9-5.11, where we depict the expected value, variance, skewness, and kurtosis of $\overline{C}\ (t)$ conditional to $\log_{10}(a_{L,1})$ (blue curves) and $\log_{10}(a_{L,2})$ (red curves), at times t = $t_{0.02}$ (Fig. 5.9), $t_{0.4}$ (Fig. 5.10), and $t_{0.96}$ (Fig. 5.11). The corresponding unconditional moments are also depicted (black curves) for ease of comparison. Fig. 5.9 shows that the first four statistical moments of $\overline{C}\left(t_{0.02}\right)$ are practically insensitive to the value of the fine sand dispersivity, $a_{L,2}$. As one could expect by considering the relative size and geometrical pattern of the two sand zones, Fig. 5.9a shows that the average amount of solute reaching the cell outlet at early times increases with $a_{L,1}$, because dispersion of solute increases through the coarse sand which resides in the largest portion of the domain. Fig. 5.9b shows that knowledge of $a_{L,1}$ causes a marked reduction of $V\left[\overline{C}(t_{0.02})\right]$, which attains an essentially constant value across the overall range of values of $a_{L,1}$. Consistent with this result, Fig.s 5.9c, d respectively show a reduction in the asymmetry and in the tailing behavior of the *pdf* of $\overline{C}\left(t_{0.02}\right)$ when $a_{L,1}$ is fixed. These results are a symptom of a reduced process uncertainty, which is in line with the observation that the bulk of the domain is filled with the coarse sand whose dispersive properties become deterministic when $a_{L,1}$ is known.

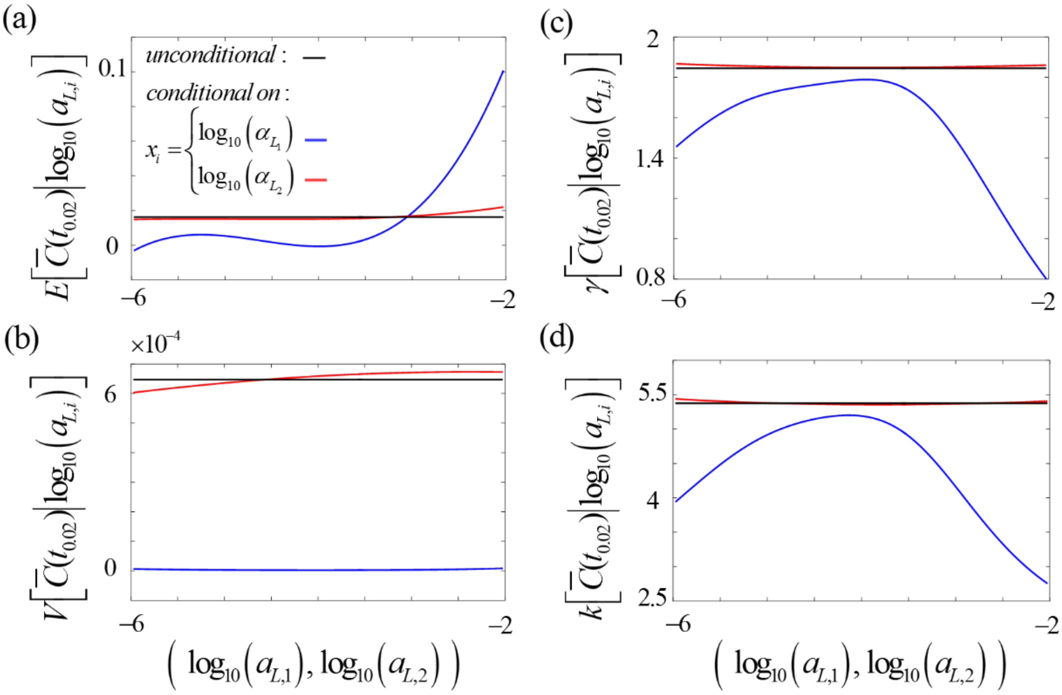

Figure 5.9. First four moments of $\overline{C}(t = t_{0.02})$ conditional on $\log_{10}(a_{L,1})$ (blue curves) and $\log_{10}(a_{L,2})$ (red curves), at time t = $t_{0.02}$: (a) expected value, $E\left[\overline{C}(t_{0.02})\middle|\log_{10}\left(a_{L,i}\right)\right]$, (b) variance, $V\left[\overline{C}(t_{0.02})\middle|\log_{10}\left(a_{L,i}\right)\right]$, (c) skewness, $\gamma\left[\overline{C}(t_{0.02})\middle|\log_{10}\left(a_{L,i}\right)\right]$, and (d) kurtosis, $k\left[\overline{C}(t_{0.02})\middle|\log_{10}\left(a_{L,i}\right)\right]$ (i = 1, 2). The corresponding unconditional moments are also depicted (black curves).

Inspection of the first four unconditional statistical moments of $\overline{C}\left(t_{0.4}\right)$ (black curves in Fig. 5.10) indicates that the unconditional *pdf* of $\overline{C}$ at this intermediate time is closely resembling a Gaussian distribution. The very act of conditioning $\overline{C}\left(t_{0.4}\right)$ on dispersivity causes a variance reduction, an increase of the tailing and the appearance of a negative (left) or positive (right) skewness, respectively when conditioning is performed on $a_{L,1}$ or $a_{L,2}$. The latter behavior suggests that in the type of experimental setting analyzed the variability of $a_{L,1}$ promotes the appearance of values of $\overline{C}\left(t_{0.4}\right)$ larger than the mean, the opposite occurring when solely $a_{L,2}$ is considered as uncertain.

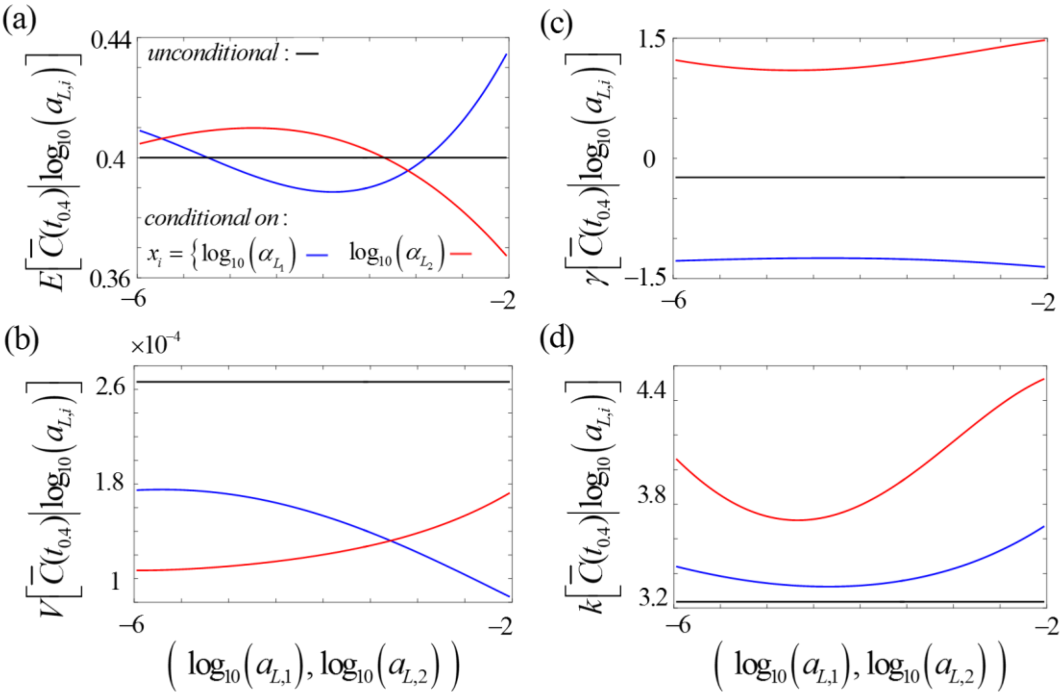

Figure 5.10. First four moments of $\overline{C}(t = t_{0.4})$ conditional on $\log_{10}(a_{L,1})$ (blue curves) and $\log_{10}(a_{L,2})$ (red curves), at time $t = t_{0.02}$: (a) expected value, $E\left[\overline{C}(t_{0.4})\middle|\log_{10}\left(a_{L,i}\right)\right]$, (b) variance, $V\left[\overline{C}(t_{0.4})\middle|\log_{10}\left(a_{L,i}\right)\right]$, (c) skewness, $\gamma\left[\overline{C}(t_{0.4})\middle|\log_{10}\left(a_{L,i}\right)\right]$, and (d) kurtosis, $k\left[\overline{C}(t_{0.4})\middle|\log_{10}\left(a_{L,i}\right)\right]$ (i = 1, 2). The corresponding unconditional moments are also depicted (black curves).

Fig. 5.11 shows that all the four statistical moment of $\overline{C}\left(t_{0.96}\right)$ are chiefly sensitive to the dispersivity of the fine sand box, which is placed near the cell outlet. One can note that knowledge of $a_{L,2}$ yields a diminished variance of $\overline{C}\left(t_{0.96}\right)$, which drops almost to zero, an increased degree of symmetry and a reduce tailing of the *pdf* of $\overline{C}\left(t_{0.96}\right)$, all these evidences being symptoms of uncertainty reduction.

Results depicted in Fig. 5.9-5.11 and our earlier observations about Fig. 5.7 are consistent with the expected behavior of transport in the system and the relative role of the dispersivities of the two sand regions. The high level of sensitivity of $\overline{C}(t)$ to $a_{L,1}$ at the early times of solute breakthrough is in line with the observation that solute are mainly advected and dispersed through the coarse sand. Both dispersivities affect the behavior of $\overline{C}(t)$ at intermediate times, when solute is traveling through both sands (see Figure 4*c* of Esfandiar et al., 2015). The dispersivity of the coarse sand plays a minor role at late times, because virtually no concentration gradients arise in this portion of the domain. Otherwise, concentration gradients persist in the fine sand zone close to the outlet and the solute breakthrough is clearly controlled by the dispersive properties of the fine sand.

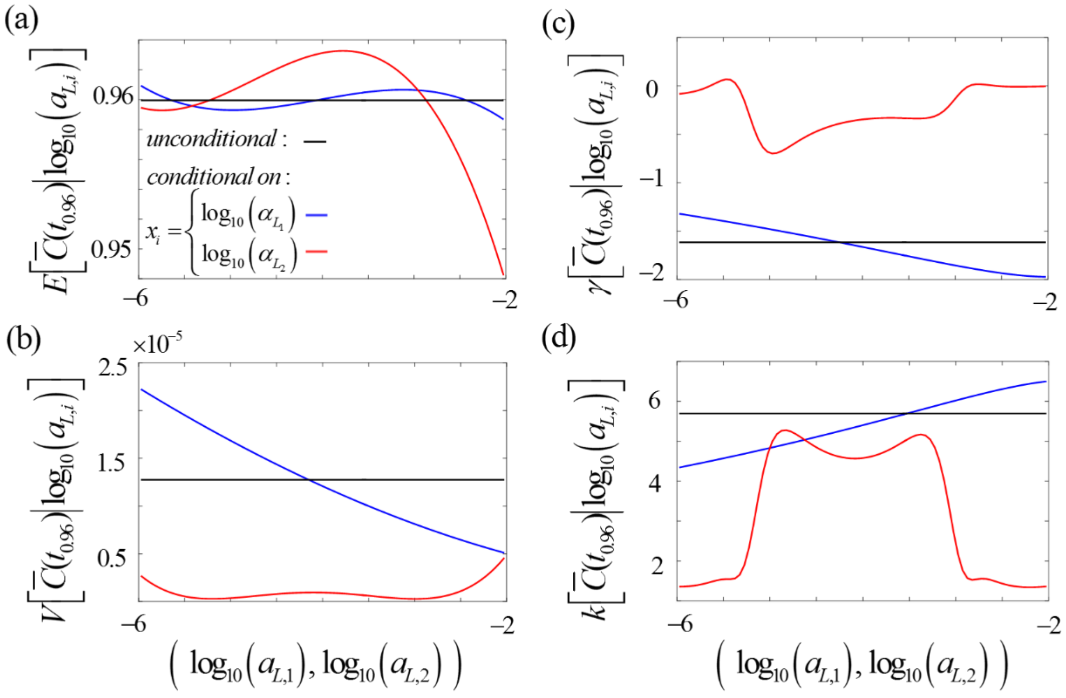

Figure 5.11. First four moments of $\overline{C}(t = t_{0.96})$ conditional on $\log_{10}(a_{L,1})$ (blue curves) and $\log_{10}(a_{L,2})$ (red curves), at time t = $t_{0.02}$: (a) expected value, $E\left[\overline{C}(t_{0.96})\middle|\log_{10}\left(a_{L,i}\right)\right]$, (b) variance, $V\left[\overline{C}(t_{0.96})\middle|\log_{10}\left(a_{L,i}\right)\right]$, (c) skewness, $\gamma\left[\overline{C}(t_{0.96})\middle|\log_{10}\left(a_{L,i}\right)\right]$, and (d) kurtosis, $k\left[\overline{C}(t_{0.96})\middle|\log_{10}\left(a_{L,i}\right)\right]$ ($i = 1, 2$). The corresponding unconditional moments are also depicted (black curves).

5.4 Conclusions

We introduce a set of new indices to be employed in the context of global sensitivity analysis, GSA, of hydrological and Earth systems. These indices consider the first four (statistical) moments of the probability density function, pdf, of a desired model output, y. As such, they quantify the expected relative variation, due to the variability in one (or more) model input parameter(s) of the expected value (5.1)-(5.2), variance (5.3)-(5.4), skewness (5.6)-(5.7) and kurtosis (5.8)-(5.9) of y. When view in the current research trend, our work is intended to bridge the gap between variance-based and pdf-based GSA approaches since it embeds the simplicity of the former while allowing for a higher-order description of how the structure of the pdf of y is affected by variations of uncertain model parameters. We cope with computational costs which might be high when evaluating higher-order moments by coupling our GSA approach with techniques approximating the full model response through a surrogate model. For the sake of our study, we consider the generalized Polynomial Chaos Expansion (gPCE), other model reduction techniques being fully compatible with our approach. Our new indices can be of interest in applications in the context of current practices and evolution trends in factor fixing procedures (i.e., assessment of the possibility of fixing a parameter value on the basis of the associated output sensitivity), design of experiment, uncertainty quantification and environmental risk assessment, due to the role of the key features of a model output pdf in such analyses.

We test and exemplify our methodology on three testbeds: (*a*) the Ishigami function, which is widely employed to test sensitivity analysis techniques, (*b*) the evaluation of the critical pumping rate to avoid salinization of a pumping well in a coastal aquifer and (*c*) a laboratory-scale nonreactive transport experiment. Our theoretical analyses and application examples lead to the following major conclusions.

1. The sensitivity of a model output, y, with respect to a parameter depends on the selected global sensitivity index, i.e., variability of a model parameter affects statistical moments of y in different ways and with different relative importance. Relying on the indices we propose allows enhancing our ability to quantify how model parameters affect features of the model output pdf, such as mean and degree of spread, symmetry and tailedness, in a straightforward and easily transferrable way.
2. Joint inspection of our moment-based global sensitivity indices and of the first four statistical conditional and unconditional moments of y increases our ability to understand the way the structure of the model output pdf is controlled by model parameters. As demonstrated in our examples, classical variance-based GSA methods cannot be used for this purpose, leading, in some cases, to the false conclusion that a given parameter have a limited impact on a target output.
3. Analysis of the errors associated with the use of a surrogate model for the evaluation of our moment-based sensitivity indices suggests that the construction of a surrogate model with increasing level of accuracy (as rendered, in our examples, by the total degree w of gPCE approximation) might be required depending on the statistical moment considered in the GSA, i.e. on the target statistical moment of y.

Reference

Alzraiee, A. H., Baú, D. and Elhaddad A.: Estimation of heterogeneous aquifer parameters using centralized and decentralized fusion of hydraulic tomography data, Hydrol. Earth Syst. Sci., 18, 3207–3223, doi:10.5194/hess-18-3207-2014, 2014

Bear, J. and Cheng, A. H. D.: Modeling groundwater flow and contaminant transport, Springer, 2010.

Borgonovo, E.: A new uncertainty importance measure, Reliability Eng. Syst. Safety, 92, 771–784, 2007.

Borgonovo, E., Castaings, W., and Tarantola, S.: Moment Independent Importance Measures: New Results and Analytical Test Cases, Risk Anal., 31, 404–428, 2011.

Chu, J., Zhang, C., Fu, G., Li, Y. and Zhou, H.: Improving multi-objective reservoir operation optimization with sensitivity-informed dimension reduction, Hydrol. Earth Syst. Sci., 19, 3557-3570, doi:10.5194/hess-19-3557-2015, 2015.

Chun, M. H., Han, S. J. and Tak, N. I. L.: An uncertainty importance measure using a distance metric for the change in a cumulative distribution function, Reliab. Eng. Syst. Saf., 70, 313-321, 2000.

Ciriello, V., Di Federico, V., Riva, M., Cadini, F., De Sanctis, J., Zio, E. and Guadagnini A.: Polynomial chaos expansion for global sensitivity analysis applied to a model of radionuclide migration in a randomly heterogeneous aquifer, Stoch. Environ. Res. Risk. Assess., 27, 945-954, http://dx.doi.org/10.1007/s00477-012-0616-7, 2013.

Colombo, I., Porta, G.M., Ruffo, P. and Guadagnini, A.: Uncertainty quantification of overpressure buildup through inverse modeling of compaction processes in sedimentary basins, Hydrogeol. J., doi:10.1007/s10040-016-1493-9, 2016.

Crestaux, T., Le Maître, O. and Martinez, J. M.: Polynomial chaos expansion for sensitivity analysis, Reliab. Eng. Syst. Safety, 94(7), 1161-1172, http://dx.doi.org/10.1016/j.ress.2008.10.008, 2009.

Elshorbagy, A., Corzo, G., Srinivasulu, S., and Solomatine, D. P.: Experimental investigation of the predictive capabilities of data driven modeling techniques in hydrology - Part 1: Concepts and methodology, Hydrol. Earth Syst. Sci., 14, 1931–1941, doi:10.5194/hess-14-1-2010, 2010.

Elshorbagy, A., Corzo, G., Srinivasulu, S. and Solomatine D. P.: Experimental investigation of the predictive capabilities of data driven modeling techniques in hydrology - Part 2: Application, Hydrol. Earth Syst. Sci., 14, 1943–1961, doi:10.5194/hess-14-1943-2010, 2010.

Esfandiar, B., Porta, G., Perotto, S. and Guadagnini, A.: Impact of space-time mesh adaptation on solute transport modeling in porous media, Water Resour. Res., 51, 1315-1332, doi:10.1002/2014WR016569, 2015.

Formaggia, L., Guadagnini, A., Imperiali, I., Lever, V., Porta, G., Riva, M., Scotti, A. and Tamellini, L.: Global sensitivity analysis through polynomial chaos expansion of a basin-scale geochemical compaction model, Comput. Geosci., 17, 25-42, http://dx.doi.org/10.1007/s10596-012-9311-5, 2013.

Förster, K., Meon, G., Marke, T. and Strasser U.: Effect of meteorological forcing and snow model complexity on hydrological simulations in the Sieber catchment (Harz Mountains, Germany), Hydrol. Earth Syst. Sci., 18, 4703-4720, doi:10.5194/hess-18-4703-2014, 2014.

Fu, G., Kapelan, Z. and Reed, P.: Reducing the complexity of multiobjective water distribution system optimization through global sensitivity analysis, J. Water Resour. Plann. Manage., 38(3), 196-207, doi:0.1061/(ASCE)WR.1943-5452.0000171, 2012.

Ghanem, R. G and Spanos, P. D.: Stochastic finite elements: a spectral approach, Berlin: Springer; 1991.

Gläser, D., Dell'Oca, A., Tatomir, A., Bensabat, J., Class, H., Guadagnini, A., Helmig, R., McDermott, C., Riva, M., and Sauter, M., An approach towards a FEP-based model risk assessment for hydraulic fracturing operations, Energ. Procedia, 97, 387-394, 2016.

Grauso, G., Fattoruso, G., Crocetti C. and Montanari, A.: A spatially distributed analysis of erosion susceptibility and sediment yield in a river basin by means of geomorphic parameters and regression relationships, Hydrology and Earth System Sciences Discussions, 4, 627-654, 2007.

Hartmann, A., Weiler, M., Wagener, T., Lange, J., Kralik, M., Humer, F., Mizyed, N., Rimmer, A., Barbera, J. A., Andreo, B., Butscher, C. and Huggenberger P.: Process-based karst modelling to relate hydrodynamic and hydrochemical characteristics to system properties, Hydrol. Earth Syst. Sci., 17, 3305-3321, doi:10.5194/hess-17-3305-2013, 2013.

Herman, J. D., Kollat, J. B., Reed, P. M. and Wagener T.: From maps to movies: high-resolution time-varying sensitivity analysis for spatially distributed watershed models. Hydrol. Earth Syst. Sci., 17, 5109-5125, doi:10.5194/hess-17-5109-2013, 2013.

Homma, T. and Saltelli, A.: Importance measures in global sensitivity analysis of nonlinear models, Reliab. Eng. Syst. Saf., 52, 1-17, 1996.

Hostache, R., Matgen P., Montanari, A., Montanari, M., Hoffmann, L. and Pfister L.: Propagation of uncertainties in coupled hydro-meteorological forecasting systems: A stochastic approach for the assessment of the total predictive uncertainty, Atmospheric Research, 100, 263–274, doi:10.1016/j.atmosres.2010.09.014, 2011.

Iman, R.L. and Hora, S. C.: A robust measure of uncertainty importance for use in fault tree system analysis, Risk Anal., 10(3), 401-406, 1990.

Koutsoyiannis, D.: "A random walk on water", Hydrol. Earth Syst. Sci., 14, 585–601, 2010.

Krykacz-Hausmann, B.: Epistemic sensitivity analysis based on the concept of entropy, In: Prado, P., Bolado, R. (Eds.), Proceedings of SAMO2001, Madrid, pp. 31-35, 2001.

Le Maître, O. P. and Knio, O. M.: Spectral methods for uncertainty quantification, Scientific computation, Springer, 2010.

Lee, H., Seo, D.J., Liu, Y., Koren, V., McKee, P. and Corby R.: Variational assimilation of streamflow into operational distributed hydrologic models: effect of spatiotemporal scale of adjustment, Hydrol. Earth Syst. Sci., 16, 2233–2251, doi:10.5194/hess-16-2233-2012, 2012.

Paniconi, C. and Putti M.: Physically based modeling in catchment hydrology at 50: survey and outlook, Water Resour. Res., 51, 7090–7129, doi:10.1002/ 2015WR017780, 2015.

Pianosi, F. and Wagener, T.: A simple and efficient method for global sensitivity analysis based on cumulative distribution functions, Environ. Model. Softw., 67, 1-11, http://dx.doi.org/10.1016/j.envsoft.2015.01.004, 2015.

Pianosi, F., Wagener, T., Beven, K., Freer, J., Hall, J.W., Rougier, J. and Stephenson, D.B.: Sensitivity Analysis of Environmental Models: a Systematic Review with Practical Workflow, Environmental Modelling & Software, 79, 214-232, http://dx.doi.org/10.1016/j.envsoft.2016.02.008, 2016.

Pool, M. and Carrera, J.: A correction factor to account for mixing in Ghyben-Herzberg and critical pumping rate approximations of seawater intrusion in coastal aquifers, Water Resour. Res., 47, W05506, doi:10.1029/2010WR010256, 2011.

Punzo, V., Marcello, M. and Biagio, C.: Do we really need to calibrate all the parameters? Variance-based sensitivity analysis to simplify microscopic traffic flow models, Intel. Trans. Sys. IEEE Trans., 16(1), 184-193, 2015.

Rajabi, M. M., Ataie-Ashtiani, B. and Simmons, C. T.: Polynomial chaos expansions for uncertainty propagation and moment independent sensitivity analysis of seawater intrusion simulations, J. Hydrol., 520, 101-122, http://dx.doi.org/10.1016/j.jhydrol.2014.11.020, 2015.

Razavi, S. and Gupta H. V.: What do we mean by sensitivity analysis? The need for comprehensive characterization of “global” sensitivity in Earth and Environmental systems models, Water Resour. Res., 51, doi:10.1002/2014WR016527, 2015.

Razavi, S., Tolson, B.A. and Burn, D.H.: Numerical assessment of metamodelling strategies in computationally intensive optimization, Environ. Model. Softw., 34(0), 67-86, http://dx.doi.org/10.1016/j.envsoft.2011.09.010, 2012a.

Razavi, S., Tolson, B.A. and Burn, D.H.: Review of surrogate modeling in water resources. Water Resour. Res. 48 (7), W07401, http://dx.doi.org/10.1029/ 2011WR011527, 2012b.

Saltelli, A., Ratto, M., Andres, T., Campolongo, F., Cariboni, J., Gatelli, D., Saisana, M., Tarantola, S.: Global Sensitivity Analysis. The Primer. Wiley, 2008.

Sarrazin, F., Pianosi, F. and Wagener, T.: Global sensitivity analysis of enviromental models: convergence and validation, Environ. Model. Softw., 79, 135-152, http://dx.doi.org/10.1016/j.envsoft.2016.02.005, 2016.

Sobol, I. M.: Sensitivity estimates for nonlinear mathematical models, Math. Model. Comput. Exp., 1, 407–417, 1993.

Song, X., Zhang, J., Zhan, C., Xuan, Y., Ye, M. and Chonggang, X.: Global sensitivity analysis in hydrological modeling: Reviews of concepts, methods, theoretical frameworks and applications, J. Hydrol., 523, 739-757, http://dx.doi.org/10.1016/j.jhydrol.2015.02.013, 2015.

Wagener, T. and Montanari, A.: Convergence of approaches toward reducing uncertainty in predictions in ungauged basins, Water Resour. Res., 47, W060301, doi:10.1029/2010WR009469, 2011.

Wagener, T., Sivapalan, M., Troch, P. A., McGlynn, B. L., Harman, C. J., Gupta, H. V., Kumar, P., Rao, P. S. C., Basu, N. B., and Wilson, J. S.: The future of hydrology: An evolving science for a changing world, Water Resour. Res., 46, W05301, doi:10.1029/2009WR008906, 2010.

Willmann, M., Sanchez-Vila, X., Carrera, J. and Guadagnini, A.: Block-upscaling of transport in heterogeneous aquifers, Calibration and Reliability in Groundwater Modelling: From Uncertainty to Decision Making, Proceedings of ModelCARE 2005, The Hague, The Netherlands, June 2005, IAHS Publ. 304, 2006.

Xiu, D. and Karniadakis, G. E. M.: The Wiener-Askey polynomial chaos for stochastic differential equations, SIAM J. Sci. Comput., 24(2), 619-644, http://dx.doi.org/10.1137/S1064827501387826, 2002.